

**Optimal design of energy storage flywheel rotors**

by

Vaishnavi Kale

A thesis submitted in partial fulfillment of the requirements for the degree of

Doctor of Philosophy

Department of Mechanical Engineering  
University of Alberta

© Vaishnavi Kale, 2022

# Abstract

Flywheels are mechanical devices that store energy as the inertia of a rotating disk. Flywheel Energy Storage Systems (FESS) can combat the challenges of intermittency and unreliability that prevent effective integration of renewable energy sources into the electric grid. They have long lifespans, can undergo deep discharge without degradation, and are made of environmentally safe materials, however, their cost and storage capacity limit their large-scale deployment.

The use of optimization methods with mathematical models of the system can considerably shorten design time, and minimize costly ‘hardware-in-the-loop’ design iterations. The energy capacity of FESS rotors can be improved by choosing the optimal rotor geometry, operation conditions, rotor materials and by tailoring the material properties. Depending on the complexity of the design goals, the model used to represent the system may range from a fairly simple analytical model to a complex 3D finite element model. In this thesis, an open-source optimization framework with shape and topology optimization capabilities was developed for the design of optimal FESS rotors. A suite of 1D, 2D axisymmetric and 3D linear elastic numerical rotor models were developed for use with the optimizer.

FESS are broadly categorized as low-speed metal rotor and high-speed composite rotor systems, and although both systems have been analyzed and optimized in literature, there is no consensus on which system is better suited to grid applications. The first contribution of this thesis was to perform a quantitative comparison of the two FESS technologies. Results showed that the total kinetic energy of both composite and metal constant thickness rotors was comparable. Multi-rim composite rotors

with certain material sequences could outperform single-rim composite and metal flywheels in terms of total or specific energy, but offered no significant cost advantage over single rim metal rotors.

The second contribution of this thesis was to offer holistic metal rotor FESS design guidelines by establishing the correlation between rotor shape, speed and radius and their combined effect on FESS energy capacity. Choosing the best combination of rotor shape, speed and radius resulted in 21% to 46% improvements in the energy storage capacity of two different FESS designs, indicating a strong correlation between these parameters. A study on the self discharge of optimally shaped flywheels indicated that low-speed rotors with a large radius had a lower self discharge than high-speed rotors with a smaller radius and the same weight, which could be an important consideration during the FESS design process.

Stress-constrained topology optimization was used to further optimize energy storage characteristics of the FESS by using complex geometries that could not be analyzed with shape optimization. This thesis proposed a novel specific energy formulation with a global stress constraint, which allowed the optimizer to choose the topology volume fraction that led to the best specific energy improvement. The proposed formulation consistently achieved better design improvements than conventional kinetic energy formulations for various operating speeds and rotational symmetries. A post-optimality analysis on the effect of acceleration related stresses on the optimal topologies determined these to be significant only when considering extremely short duration charge-discharge cycles of less than 0.1 s.

Two approaches were used to improve the discreteness and convergence of the specific energy topology formulation. Local stress constraints with an Augmented Lagrangian formulation were shown to achieve designs with a more uniform stress distribution compared to P-norm aggregated global stress constraints, where undesirable local stress concentrations could be seen at narrow bottleneck regions. A modified robust approach improved design discreteness and allowed for 3D topology

optimization with the specific energy formulation. Two distinct 3D rotor designs with similar energy capacities were seen to emerge when two different ranges of density filter radius were used for design, with one design being similar to shape optimized rotors, and the other design having spokes connecting the central shaft with an outer rim.

The developed optimization framework will serve as a comprehensive design tool for FESS rotors. The open-source nature of the tool will allow for further extensions to the library in terms of materials or analysis of non-linear or transient behaviour.

**Keywords:** *FESS, energy storage, rotor materials, shape optimization, topology optimization, Augmented Lagrangian approach, local stress constraints, robust topology optimization*

# Preface

Parts of Chapter 1 have been published as Kale, V., and Secanell, M. (2022). "Rotor Design and Optimization of Metal Flywheels". In: Luisa F. Cabeza (eds.), *Encyclopedia of Energy Storage*; Oxford: Elsevier; pp. 41-56 (available online at <https://doi.org/10.1016/B978-0-12-819723-3.00075-5>). I was responsible for review, manuscript writing and revision. M. Secanell was the supervisory author, and helped with manuscript concept, writing and review. License 5420611067336 was obtained on 01 November 2022 from the publisher (Elsevier) for reproduction in this thesis.

Parts of Chapters 1 and 2 have been published as Kale, V., and Secanell, M. (2018). "A comparative study between optimal metal and composite rotors for flywheel energy storage systems". In: *Energy Reports*, 4, 576-585 (available online at <https://doi.org/10.1016/j.egy.2018.09.003>). I was responsible for review, model development and implementation, data processing and analysis, and manuscript writing and revision. M. Secanell was the supervisory author, and helped with manuscript concept, writing and review. Permission was obtained under the Creative Commons Attribution License (CC BY) from the publisher (Elsevier) for reproduction in this thesis.

Parts of Chapters 1 and 3 have been published as Kale, V., Thomas, M., and Secanell, M. (2021). "On determining the optimal shape, speed, and size of metal flywheel rotors with maximum kinetic energy". In: *Structural and Multidisciplinary Optimization*, 64(3), 1481-1499 (available online at <https://doi.org/10.1007/s00158->

021-02935-x). I was responsible for review, model development and implementation, data processing and analysis, and manuscript writing and revision. M. Thomas was responsible for parametrized mesh generation and manuscript review. M. Secanell was the supervisory author, and helped with manuscript concept, writing and review. License 5446320277168 was obtained on 12 December 2022 from the publisher (Springer) for reproduction in this thesis.

Parts of Chapters 1 and 4 have been submitted for publication as Kale, V., Aage, N., and Secanell, M. (2022). "Stress constrained topology optimization of energy storage flywheels using a specific energy formulation". In: *Journal of Energy Storage*. I was responsible for review, model development and implementation, data processing and analysis, and manuscript writing and revision. N. Aage was a collaborator who provided technical perspectives and helped with manuscript review. M. Secanell was the supervisory author, and helped with manuscript concept, writing and review.

*To my family*

# Acknowledgements

First and foremost, I would like to extend my sincere thanks to my Ph.D. supervisor, Dr. Marc Secanell, whose mentorship, advice and support was vital to the success of this dissertation. I admire his work ethic and his sincere commitment to sustainability that reflects in his persona. I hope to emulate his systematic and scientific approach to solving problems in my own career. I would also like to convey my heartfelt gratitude to my supervisory committee, Dr. John Doucette and Dr. Pierre Mertiny, for their valuable inputs to this work.

Moving to a new country for an education was a big transition that was always somewhat daunting, but it was made easier by the amazing people that I met and interacted with at the ESDLab. A big thank you to all the past and present group members - and a special shoutout to Ambuj Punia, Dr. Aslan Kosakian, Elena Ezquerro, Dr. Manas Mandal, Michael Moore, Mohamad Ghadban, and Dr. Alex Jarauta. Some of my favourite memories have been the morning runs, beers, dinners and Tim's coffees we enjoyed together.

I briefly visited the TopOpt group at DTU, Denmark in order to work on my topology optimization framework for this dissertation. Although my trip was cut short due to COVID, I was able to get some valuable discussions and feedback from my time spent there, and I would like to thank Dr. Niels Aage and his research group for graciously hosting me at DTU.

I would also like to acknowledge the research funding from NSERC Energy Storage Technology Network (NESTNet) and NSERC Discovery Grant, and access to high performance computing clusters provided by the Digital Research Alliance of

Canada (previously Compute Canada) and WestGrid, which were critical resources that enabled me to complete my work.

This thesis would not have been possible without the love and support of my parents - Suman and Bhaskar Kale, my brother Koustubh, who kept my spirits high, and my childhood friend Sindhu, who never let me forget how much she missed me. My big family - Neeru and Deepak Sabharwal, Pallavi, Aman, Astha, Sohil, and so many others, were so far away, yet always in my heart. Thank you to my friends in Edmonton who were always with me - Shobha, Tanushree, Abhishek, Jayeeta, Raj, Nibedita, Benazir, Siddharth, Meenal, Chintan, Dimitra, Mahima - for all the good times and the wonderful company. Finally, thank you to the person who encouraged and inspired me to do a Ph.D. - my husband, Mayank. Your faith in my ability has been unwavering and it really helped me reach the end of this journey.

# Table of Contents

<b>1</b>	<b>Introduction</b>	<b>1</b>
1.1	Motivation . . . . .	1
1.2	Background . . . . .	4
1.3	Literature review . . . . .	7
1.3.1	Flywheel rotor modeling . . . . .	7
1.3.2	Optimal rotor design . . . . .	13
1.3.2.1	Rotor materials . . . . .	17
1.3.2.2	Shape optimization . . . . .	23
1.3.2.3	Topology optimization . . . . .	31
1.4	Objectives . . . . .	41
1.5	Thesis Outline . . . . .	43
<b>2</b>	<b>Optimal selection of rotor materials by FESS application</b>	<b>45</b>
2.1	Methodology . . . . .	47
2.1.1	Flywheel structural model . . . . .	47
2.1.1.1	Governing equations . . . . .	48
2.1.1.2	Boundary conditions . . . . .	48
2.1.1.3	Implementation . . . . .	49
2.1.2	Optimization problem . . . . .	49
2.1.2.1	Formulation . . . . .	49
2.1.2.2	Implementation . . . . .	51
2.2	Model and framework validation . . . . .	52
2.3	Results and discussion . . . . .	54
2.3.1	Optimal flywheels using maximum kinetic energy criterion . . . . .	57
2.3.2	Optimal flywheels using maximum specific energy criterion . . . . .	60
2.3.3	Optimal flywheels using maximum energy per cost criterion . . . . .	62
2.4	Summary . . . . .	63

<b>3</b>	<b>Shape optimization of grid scale FESS</b>	<b>65</b>
3.1	Methodology . . . . .	66
3.1.1	Flywheel numerical model . . . . .	66
3.1.2	Post-processing, input parameters and shape parameterization	69
3.1.3	Optimization . . . . .	71
3.2	Results and discussion . . . . .	76
3.2.1	Flywheel rotor model validation . . . . .	76
3.2.2	Initial design analysis . . . . .	76
3.2.3	Convergence of shape optimization studies . . . . .	77
3.2.4	Effect of operating speed and rotor radius on the optimal rotor shape . . . . .	79
3.2.5	Effect of power losses . . . . .	84
3.2.6	Interdependence of rotor material, operating speed and outer radius of optimally shaped rotors . . . . .	85
3.2.7	Post optimality analysis . . . . .	87
3.2.7.1	Effect of gravity loads . . . . .	89
3.3	Summary . . . . .	90
<b>4</b>	<b>Topology optimization of grid-scale FESS</b>	<b>94</b>
4.1	Methodology . . . . .	95
4.1.1	Flywheel numerical model . . . . .	96
4.1.2	Post-processing and adjoint sensitivity analysis . . . . .	99
4.1.2.1	Post-processing . . . . .	99
4.1.2.2	Sensitivity Analysis . . . . .	101
4.1.3	Filtering . . . . .	105
4.1.3.1	Density filtering . . . . .	105
4.1.3.2	Projection filtering . . . . .	105
4.1.3.3	Filtered sensitivities . . . . .	106
4.1.4	Optimization . . . . .	106
4.1.5	Implementation . . . . .	107
4.2	Results and discussion . . . . .	107
4.2.1	Flywheel rotor model validation . . . . .	107
4.2.2	Benchmarking of the topology framework . . . . .	110
4.2.3	Rotor topology optimization for kinetic energy maximization under volume fraction and stress constraints . . . . .	111
4.2.3.1	Effect of maximum stress limit . . . . .	117
4.2.3.2	Effect of maximum volume fraction . . . . .	117

4.2.4	Rotor topology optimization for maximum specific energy under stress constraints . . . . .	119
4.2.4.1	Effect of rotor material . . . . .	124
4.2.4.2	Effect of operating speed . . . . .	125
4.2.4.3	Effect of rotational symmetry . . . . .	129
4.3	Summary . . . . .	129
<b>5</b>	<b>Augmented Lagrangian approach for locally stress constrained rotor topology optimization</b>	<b>134</b>
5.1	Methodology . . . . .	134
5.1.1	Optimization formulation . . . . .	135
5.1.2	Augmented Lagrangian function . . . . .	136
5.1.3	Sensitivity analysis . . . . .	137
5.1.4	Optimization solver . . . . .	139
5.1.5	Implementation . . . . .	139
5.2	Results and Discussion . . . . .	139
5.2.1	Pareto-optimal solutions . . . . .	141
5.2.2	Local vs global stress constraints . . . . .	146
5.3	Summary . . . . .	148
<b>6</b>	<b>Modified robust approach for 3D topology optimization</b>	<b>149</b>
6.1	Methodology . . . . .	150
6.1.1	Modified robust formulation . . . . .	152
6.1.2	3D numerical model . . . . .	154
6.1.3	Solver . . . . .	156
6.2	Results and discussion . . . . .	156
6.2.1	2D robust design compared to conventional design . . . . .	156
6.2.2	3D Rotor topology . . . . .	159
6.2.2.1	Effect of density filter radius . . . . .	161
6.2.2.2	Effect of domain size . . . . .	163
6.2.2.3	Effect of operating speed on optimal topology . . . . .	167
6.2.2.4	Effect of rotor height on optimal topology . . . . .	168
6.2.3	3D topology vs shape optimization . . . . .	169
6.3	Summary . . . . .	170
<b>7</b>	<b>Conclusions and future work</b>	<b>173</b>
7.1	Contributions . . . . .	177
7.2	Future work . . . . .	179

<b>Bibliography</b>	<b>180</b>
<b>Appendix A: Literature data</b>	<b>190</b>
A.1 Literature on flywheel rotor sizing and material optimization . . . . .	190
A.2 Literature on FESS rotor shape optimization . . . . .	192
A.3 Literature on FESS rotor topology optimization . . . . .	194
A.4 Literature on topology optimization of rotors used in other applications	195
<b>Appendix B: Rotor Materials</b>	<b>196</b>
B.1 Material Properties . . . . .	196
<b>Appendix C: Shape optimization</b>	<b>198</b>
C.1 Mesh independence of axisymmetric rotor model . . . . .	198
C.2 Optimal solutions for parametric studies to determine the effect of operating speed and rotor radius on the rotor design . . . . .	200
C.3 Optimal designs for parametric studies to determine the effect of op- erating speed and rotor radius on the rotor design . . . . .	201
<b>Appendix D: Topology optimization</b>	<b>206</b>
D.1 Weak form of linear elastic flywheel numerical model . . . . .	206
D.2 Adjoint sensitivity analysis . . . . .	209
D.3 Finite difference tests for topology optimization responses . . . . .	210
D.4 Benchmarking of 2D rotor topology reported by Jiang and Wu [68] .	212
D.5 Effect of bore size on optimal topology . . . . .	214
D.6 Post-optimality analysis on body fitted meshes . . . . .	216

# List of Tables

1.1	Flywheel storage solutions deployed at utility scale applications . . .	13
1.2	Shape factor K of some typical flywheel geometries, reproduced with permission from reference [12] . . . . .	24
2.1	Optimal glass/epoxy and carbon/epoxy composite rotors for varying cost ratios. . . . .	55
2.2	Optimal composite rotors with different binding constraints . . . . .	55
2.3	Comparison of optimal flywheel designs based on kinetic energy criterion	59
3.1	Flywheel numerical model and mesh input parameters . . . . .	70
3.2	Specifications of flywheels used as the case studies for optimization .	72
3.3	Flywheel shape optimization parameters . . . . .	75
3.4	Computational requirements for hybrid sequential shape optimization of design-1 at $\omega = 6000$ rpm, $r_{out} = 1.0$ m and design-2 at $\omega = 6000$ rpm, $r_{out} = 1.0$ m . . . . .	78
3.5	Comparison of the two original designs with optimal designs obtained from the parametric study w.r.t $\omega$ , $r_{out}$ . . . . .	83
3.6	Individual contributions of shape, operating speed and rotor radius to design improvements obtained using the parametric study based shape optimization approach . . . . .	84
3.7	Temporal rotor design specifications used in the study to determine the effect of rotor material on optimal shapes . . . . .	87
3.8	Sensitivity of optimal solution to design parameters and mesh refinement	89
4.1	Parameters used to validate 2D plane stress numerical flywheel model using 1D solution . . . . .	109
4.2	Comparison of literature and simulated rotor designs for constant thickness and topology optimized designs . . . . .	111
4.3	Topology optimization parameters for kinetic energy maximization of flywheel rotor using 2D plane stress numerical model . . . . .	112

4.4	Comparison of original uniform thickness disk-type and optimal topology flywheels . . . . .	114
4.5	Comparison of stresses developed in the original uniform thickness disk-type and optimal topology flywheels under acceleration loads . . . . .	116
4.6	Comparison of optimal rotor topologies for various maximum stresses	118
4.7	Comparison of optimal rotor topologies for various prescribed volume fractions . . . . .	120
4.8	Comparison of optimal topologies at 5000 rpm, obtained with kinetic energy and specific energy formulations . . . . .	121
4.9	Comparison of optimal topologies for different rotor materials at 5000 rpm . . . . .	125
4.10	Comparison of optimal rotor topologies for various operating speeds .	128
4.11	Comparison of optimal rotor topologies for various circular symmetries	131
5.1	Optimization parameters for Augmented Lagrangian approach for local stress-constrained topology optimization of flywheel . . . . .	142
5.2	Comparison of non-dominated optimal rotor designs obtained with different objective function weights for the multi-objective Augmented Lagrangian formulation . . . . .	145
5.3	Comparison of optimal 2D rotor designs obtained using global P-norm and local (Augmented Lagrangian) stress constraints . . . . .	147
6.1	Topology optimization parameters for specific energy maximization of flywheel rotor using modified robust approach . . . . .	158
6.2	Comparison of optimal 2D rotor designs obtained using a) the robust approach and b) the volume preserving approach, with the specific energy formulation . . . . .	159
6.3	Comparison of optimal 2D and 3D rotor topologies obtained with the robust specific energy formulation in Eq. (6.1) . . . . .	160
6.4	Effect of density filter radius on the optimal 3D rotor topology obtained with the robust specific energy formulation . . . . .	161
6.5	Effect of rotational symmetry on the optimal 3D rotor topology obtained with the robust specific energy formulation . . . . .	165
6.6	Effect of rotational symmetry on the optimal 3D rotor topology obtained with the robust specific energy formulation . . . . .	165
6.7	Effect of Z-direction symmetry on the optimal 3D rotor topology obtained with the robust specific energy formulation . . . . .	165

6.8	Effect of operating speed and choice of density filter radius on the optimal 3D rotor topology obtained with the robust specific energy formulation . . . . .	168
6.9	Effect of rotor height on the optimal 3D rotor topology obtained with the robust specific energy formulation . . . . .	168
6.10	Comparison of optimal rotor geometry obtained using topology optimization, and shape optimization . . . . .	170
A.1	Literature on optimal rotor design for FESS using tailored material properties . . . . .	191
A.2	Literature on optimal metal rotor design using shape optimization . .	192
A.3	Literature on topology optimization of flywheels used in energy storage applications . . . . .	194
A.4	Literature on topology optimization of axisymmetric disks used in other applications . . . . .	195
B.1	Composite material properties [110] . . . . .	196
B.2	Isotropic material properties [127] . . . . .	197
C.1	Kinetic energy in kWh for the optimal shaped rotors based on design-1	200
C.2	Kinetic energy in kWh for the optimal shaped rotors based on design-2	201
C.3	Shape design parameters $h(r)$ for optimal rotors in the parametric studies based on design-1 . . . . .	201
C.4	Shape design parameters $h(r)$ for optimal rotors in the parametric studies based on design-2 . . . . .	203
D.1	Topology optimization parameters for kinetic energy maximization of 2D rotor design reported in reference [68] . . . . .	213
D.2	Comparison of optimal topologies for various rotor radius ratios . . .	214

# List of Figures

1.1	Schematic of a typical FES system, reproduced with permission from Skinner [16]. . . . .	5
1.2	A comparison of the energy capacity and maximum operating speed of existing metal and composite rotor FESS . . . . .	14
1.3	Steel wire bare filament flywheel used in spin tests by Genta [78], reproduced with permission from authors. . . . .	32
2.1	Block diagram of flywheel rotor . . . . .	52
2.2	Schematic of the Python-DAKOTA interface . . . . .	53
2.3	Comparison of simulated and literature results [17] for a) Radial and b) Hoop stress distributions in 2-rim and 1-rim composite flywheels . . . . .	54
2.4	Rim detachment failure as a a) non-binding constraint, and b) binding constraint. . . . .	56
2.5	Maximum kinetic energy criterion : Radial (top) and hoop (bottom) stress distributions for optimal a) 1-rim metal, b) 1-rim composite, c) 2-rim composite, d) 2-rim hybrid rotors . . . . .	58
2.6	Comparison of Kinetic Energy and Specific Energy of a) Metal, b)Composite rotor materials . . . . .	61
2.7	Comparison of kinetic energy and specific energy of optimal 2-rim and 1-rim rotors . . . . .	61
2.8	Comparison of Kinetic Energy and Specific Energy of a) Metal, b)Composite rotor materials . . . . .	62
2.9	Comparison of kinetic energy and energy per cost of optimal 2-rim and 1-rim rotors . . . . .	63
3.1	Boundary conditions for the 2D axisymmetric rotor model with symmetry about the $r$ -axis . . . . .	68
3.2	a) Parameterized geometry and b) mesh with symmetry about the $r$ -axis for the 2D Axisymmetric rotor model . . . . .	71
3.3	Block diagram of the shape optimization framework . . . . .	74

3.4	Comparison of mid-plane values of a) $u_r$ , b) stresses $\sigma_{rr}$ , $\sigma_{\theta\theta}$ and c) strains $\varepsilon_{rr}$ , $\varepsilon_{\theta\theta}$ obtained from numerical and analytical rotor models .	76
3.5	Stress distribution $\sigma_{vm}$ in FESS rotors of type a) design-1 (Temporal steel) at 10000 rpm and b) design-2 (Amber Kinetics) at 8500 rpm . .	77
3.6	Convergence history of the hybrid sequential shape optimization algorithm for a) design-1 at $\omega = 6000$ rpm, $r_{out} = 1.0$ m and b) design-2 at $\omega = 6000$ rpm, $r_{out} = 1.0$ m . . . . .	79
3.7	3D contour plot of the kinetic energy obtained with the optimal shaped flywheels at various operating speeds and rotor radii, given specifications of rotors from design-1 (left), and design-2 (right) . . . . .	80
3.8	Optimal flywheel shapes (for maximum kinetic energy) obtained at various operating speeds and rotor radii, given specifications of rotors from design-1 (top) and design-2 (bottom) . . . . .	81
3.9	Optimal steel (left) and aluminium (right) rotors with a),b) $\omega=10000$ rpm, $r_{out}=0.5$ m, c),d) $\omega=8000$ rpm, $r_{out}=0.7$ m, and e),f) $\omega=7000$ rpm, $r_{out}=0.8$ m. . . . .	86
3.10	Plots of energy-per-cost ratio vs cost ratio of optimal steel and aluminium rotors with design specifications shown in Table 3.7 . . . . .	87
3.11	Stress distribution at standstill in optimal rotors for design-1 (left) at $\omega=0$ rpm, $r_{out}=1$ m and design-2 (right) at $\omega=0$ rpm, $r_{out}=0.5$ m (right)	90
3.12	Stress distribution with gravity in optimal rotor for design-1 (left) at $\omega=6000$ rpm, $r_{out}=1$ m and design-2 (right) at $\omega=10000$ rpm, $r_{out}=0.5$ m . . . . .	91
4.1	a) 2D rotor domain and boundary conditions and b) unstructured mesh using rotational symmetry of $N=6$ . . . . .	97
4.2	Flowchart of the rotor topology optimization framework . . . . .	108
4.3	Validation of 2D plane stress numerical model of the rotor by comparison to 1D solutions of a) radial deformation $u_r$ , b) radial stress $\sigma_{rr}$ , and c) circumferential stress $\sigma_{\theta\theta}$ . . . . .	109
4.4	Validation of rotor topology optimization framework, a) literature design (reproduced from ref [68] with permission) and b) simulated design	110
4.5	a) Optimal topology, b) full rotor topology, and c) stress distribution in the topology optimized energy storage flywheel . . . . .	113
4.6	Convergence histories of a) kinetic energy, b) P-norm stress, c) volume fraction, and d) % gray region in the optimal energy storage flywheel topology . . . . .	113

4.7	Optimal rotor topology obtained with mesh element sizes of a) 6 mm (coarse mesh), b) 3 mm (medium mesh), and b) 1.5 mm (fine mesh) .	114
4.8	Shear stress distributions $\sigma_{r\theta}$ in constant speed operation of uniform thickness rotors with a) $\dot{\omega}=0$ rad/s <sup>2</sup> , b) $\dot{\omega}=5235.9$ rad/s <sup>2</sup> , and optimal topology rotors with c) $\dot{\omega}=0$ rad/s <sup>2</sup> , d) $\dot{\omega}=5235.9$ rad/s <sup>2</sup> . . . . .	116
4.9	Optimal rotor topologies and corresponding stress distributions obtained at different maximum stresses: a) 55 MPa, b) 65 MPa, c) 75 MPa, and d) 85 MPa . . . . .	118
4.10	Optimal rotor topologies and corresponding stress distributions obtained at different prescribed volume fractions of a) 60%, b) 65%, c) 70%, d) 75% and e) 80% . . . . .	119
4.11	a) Location of mesh elements used for density sweep, and variation of b) specific energy and c) kinetic energy with density of the chosen mesh element . . . . .	121
4.12	Stress distribution in the optimal rotor topology at 5000 rpm using steel with a) max $E_{kin}$ , d) max $e_{kin}$ , formulations, using aluminium with b) max $E_{kin}$ , e) max $e_{kin}$ formulations, and using PEEK with c) max $E_{kin}$ , f) max $e_{kin}$ formulations . . . . .	122
4.13	Convergence of the topology based on the specific energy formulation using a Heaviside filter with a) fixed threshold, and b) volume preserving threshold obtained with a line search . . . . .	124
4.14	Optimal rotor topology and corresponding stress distributions obtained with kinetic energy and specific energy formulations respectively at different operating speeds: a),f) 4000 rpm, b),g) 4500 rpm, c),h) 5000 rpm, d),i) 5500 rpm and e),j) 6000 rpm . . . . .	127
4.15	Optimal rotor topologies and corresponding stress distributions obtained with kinetic energy and specific energy formulations respectively using different circular symmetries: a),f) N=5, b),g) N=6, c),h) N=7, d),i) N=8, and e),j) N=9 . . . . .	130
5.1	Flowchart of the Augmented Lagrangian approach for rotor topology optimization . . . . .	140
5.2	Optimal topologies obtained using the multi-objective (max energy, min mass) and the Augmented Lagrangian approach with local stress constraints, using several combinations of objective function weights $w_{ke}$ and $w_m$ . . . . .	143

5.3	Stress distributions in the optimal rotors obtained using the multi-objective (max energy, min mass) and the Augmented Lagrangian approach with local stress constraints, using several combinations of objective function weights $w_{ke}$ and $w_m$ . . . . .	144
5.4	Pareto optimal designs for the multi-objective rotor design problem using the Augmented Lagrangian approach . . . . .	146
5.5	Comparison of stress distributions and flywheel topologies for designs obtained with a),d) global stress constrained $E_{kin}$ formulation, b),e) global stress constrained $e_{kin}$ formulation, and c),f) local stress constrained MOO formulation . . . . .	148
6.1	Flowchart of the modified robust approach for rotor topology optimization . . . . .	151
6.2	Projected density maps for an example 2D topology depicting: a) eroded ( $\hat{\rho}^e$ ), b) blueprint ( $\hat{\rho}^b$ ), and c) dilated ( $\hat{\rho}^d$ ) designs . . . . .	153
6.3	a) 3D rotor domain using a) half the rotor height $H/2$ , b) full rotor height $H$ , and c) unstructured hexahedral mesh using rotational symmetry ( $N=6$ ), with corresponding boundary conditions . . . . .	155
6.4	Convergence plots of the a) specific energy objective, b) stress constraint and c) convergence criterion in the modified robust approach .	157
6.5	Optimal topology obtained using a) the robust approach and b) the volume preserving approach . . . . .	157
6.6	a) Full 3D topology, b) optimal topology ( $\rho > 0.5$ ), c) stress distribution, d) clipped view of 3D topology , e) $r$ - $z$ plane slice of 3D topology, f) $r$ - $\theta$ plane slice of 3D topology . . . . .	160
6.7	Optimal stress distribution in the 3D topology and corresponding $r - z$ plane rotor profiles obtained using filter radius of a) 10 mm, b) 15 mm, c) 20 mm, d) 25 mm, e) 30 mm, f) 35 mm. . . . .	162
6.8	Optimal 3D topologies obtained using rotational symmetry of a) $N = 6$ , and b) $N = 9$ . . . . .	164
6.9	Optimal 3D topology ( $N=9$ ) and $r - z$ plane views obtained using a),d) $lc=1.5$ mm and $r_{filt}=10$ mm, b),e) $lc=2.0$ mm and $r_{filt}=10$ mm, and c),f) $lc=2.0$ mm and $r_{filt}=15$ mm, . . . . .	165
6.10	Optimal 3D topologies obtained using $Z$ -direction symmetry of a) $H/2$ , and b) $H$ . . . . .	166

6.11	Optimal 3D topologies and $r - z$ plane views obtained using two different density filter radii of 15 and 25 mm, with operating speeds of a),e) $\omega = 4000$ rpm, b),f) $\omega = 5000$ rpm, c),g) $\omega = 5500$ rpm, and d),h) $\omega = 6000$ rpm . . . . .	167
6.12	Optimal 3D topologies and $r - z$ plane views obtained with different rotor heights of a) $H = 40$ mm, b) $H = 50$ mm, and c) $H = 60$ mm .	169
6.13	Comparison of optimal rotor geometry obtained using a) topology optimization, and b) shape optimization . . . . .	170
C.1	Axisymmetric constant thickness rotor mesh for a) annular disk geometry with 20x6 elements and b) solid disk geometry with 40x6 elements	198
C.2	Convergence of displacement $u_r^{max}$ in the axisymmetric rotor model with a) h-refinement (first order approximations) and b) p-refinement (mesh with 120 elements). . . . .	199
C.3	Convergence of stress $\sigma_r^{max}$ in the axisymmetric rotor model with a) h-refinement (first order approximations) and b) p-refinement (mesh with 120 elements). . . . .	200
D.1	Finite difference tests to validate the analytical sensitivity of a) kinetic energy and b) P-norm aggregated stress response . . . . .	211
D.2	a) 2D mesh, b) optimal topology and c) optimal stress distribution for the benchmarking problem described in Equation D.26 . . . . .	214
D.3	Convergence histories of a) kinetic energy, b) P-norm stress, c) volume fraction, d) convergence criterion and e) % gray region in the topology for the benchmarking problem described in Equation D.26 . . . . .	215
D.4	Stress distributions in the optimal rotor topology obtained using different radius ratios, with inner radius of a) 25 mm, b) 30 mm, and c) 35 mm . . . . .	216
D.5	Effect of using a body fitted mesh to analyze design with remnant gray regions: a-c) optimal topologies with visible gray regions, d-f) stress distribution in post-processed meshes with density threshold of 50%, and g-i) stress distribution in post-processed meshes with density threshold of 90%. . . . .	217

# List of Symbols

## Latin

$E$	Young's Modulus,	Pa
$E_{\text{kin}}$	kinetic energy,	kJ
$e_{\text{kin}}$	specific energy,	kJ/kg
$H$	height,	m
$h$	projection filter threshold	
$I$	moment of inertia,	kg m <sup>2</sup>
$K$	shape factor,	dimensionless
$m$	mass,	kg
$M_{nd}$	measure of discreteness,	%
$N$	rotational symmetry	
$n$	normal unit vector	
$P$	power,	W
$p$	SIMP penalty for material interpolation	
$q$	SIMP stress relaxation parameter	
$r$	radius,	m
$u$	displacement vector,	m
$V$	volume,	m <sup>3</sup>

## Greek

$\beta$	projection filter slope	
$\dot{\omega}$	angular acceleration,	rad/s <sup>2</sup>
$\lambda_j$	Lagrange multipliers for AL formulation	
$\mu$	penalty for AL formulation	

$\nu$	Poisson's ratio,	dimensionless
$\omega$	angular velocity,	rad/s
$\rho$	density,	kg/m <sup>3</sup>
$\sigma$	stress,	Pa
$\varepsilon$	strain,	dimensionless

### **Subscripts and superscripts**

kin	kinetic
pn	P-normalized
ult	ultimate
vm	von Mises
y	yield

# Abbreviations

**AL** Augmented Lagrangian.

**BLDC** brushless direct current.

**CAMD** continuous approximation of material distribution.

**EA** evolutionary algorithm.

**ESS** energy storage system.

**FEM** finite element method.

**FESS** flywheel energy storage system.

**GA** genetic algorithm.

**GC-MMA** globally convergent method of moving asymptotes.

**IIGA** injection island genetic algorithm.

**KKT** Karush–Kuhn–Tucker.

**K-S** Kreisselmeier Steinhauser.

**MADS** mesh adaptive direct search.

**MBB** Messerschmitt-Bölkow-Blohm.

**MFD** method of feasible directions.

**MMA** method of moving asymptotes.

**MPGS** modified generalized plane strain.

**NIPM** nonlinear interior point method.

**NSGA-ii** non-dominated sorting genetic algorithm ii.

**PEEK** polyetheretherketone.

**PMSM** permanent magnet synchronous machine.

**SA** simulated annealing.

**SIMP** solid isotropic material with penalization.

**SQP** sequential quadratic programming.

# Chapter 1

## Introduction<sup>†</sup>

### 1.1 Motivation

With current policy and energy trends, global warming is expected to raise the average world temperature by 4.1 - 4.8°C above pre-industrial levels by the end of the century [1]. This is well above the Paris Agreement's long term goal of limiting the temperature rise to 1.5°C above pre-industrial levels [1]. The world is still grappling with the implications of the Paris Agreement on its existing and planned energy infrastructure. For example, in the European Union (EU), the success of the plan to scale up climate action relies on reducing emissions in three main areas - electricity supply, residential buildings, and transportation; with the success of the transportation sector relying on a parallel de-carbonization of the electricity sector. In order to achieve the 1.5°C benchmark, the EU would have to increase the share of renewable power from 30% in 2017 to 55% in 2030 [2]. Similarly, 20% of the total installed power capacity in India is from renewable sources, which would have to be doubled to achieve its Paris agreement goals[3]. Nearly 60% of the electricity produced in Canada comes from hydro power, and 5.2% from other renewable sources [4]. However, as hydro power is constrained by geography (half of the world's hydro power installed capacity is in just three countries), other renewable energy sources must also be deployed.

---

<sup>†</sup>Parts of this chapter have been published in: Vaishnavi Kale, and Marc Secanell. *Luisa F. Cabeza (eds.), Encyclopedia of Energy Storage* Oxford: Elsevier, 2022; pp. 41-56.

As an increasing number of renewable energy production technologies, such as wind and solar farms, are integrated into the grid, the associated challenges, such as intermittency and power quality, must be dealt with. Long-term and short-term energy storage technologies are increasingly being deployed to solve this problem and hence improve the reliability and robustness of a renewable energy based grid [5, 6]. As of 2017, the world total installed energy storage capacity was 176.5 GW, of which 97% was pumped hydro power [7]. The International Energy Agency's sustainable development scenario target estimates an additional 80 GW of overall storage capacity must be added by 2030. Thus, alternative energy storage technologies such as batteries, flywheels, supercapacitors and compressed air storage are also being tested and commercialized. As per the Canadian National Electricity Board's market snapshot, Canada is in the early testing stages with about 61.7 MW of installed energy storage capacity (excluding pumped hydro), of which batteries constitute 81%, followed by 11% flywheels, with the remainder being a mix of technologies [8].

Energy storage systems (ESS) can help to better integrate intermittent sources like solar and wind into the electric grid, by enabling storage at times of low demand and use at times of peak demand [5]. Besides, they can also improve the grid's power quality by performing voltage and frequency regulation, thereby improving the system reliability and robustness [6]. Flywheel energy storage (FES) systems, which are an old innovation, have seen a resurgence in modern times, mainly because advancements in technology have made high-strength materials, rotor manufacturing processes and power electronics more economically viable, which in turn, has increased their efficiency significantly. FES systems typically have a high energy capacity, deep-discharge capability, a long lifetime ( $> 20$  years) and are made of environmentally safe materials [9–12]. Due to their rapid charge-discharge characteristics, they are best suited for short duration storage applications.

The capital cost per unit power of different FESS configurations was reported to be between 600 and 2400 \$/kW, and the cost of operation and maintenance was reported

to be 5.56-5.80 \$/kW-yr [13]. Another source reported that an FESS system, with a power rating of 250 kW and a maximum expected storage duration of 15 minutes, had a capital cost per unit power of 250-350 \$/kW and a corresponding per unit energy cost of 1000-5000 \$/kWh [14]. The International Renewable Energy Agency estimated that by 2030 the per unit energy installation costs of FESS would fall by 35%, from the current estimated 1500 - 6000 \$/kWh to 1000 - 3900 \$/kWh [15]. Although the overall capital cost of this technology is high, it is comparable to that of ultracapacitors, which are the direct competitors to the FESS for short duration storage, making FESS a serious contender in commercial storage applications, such as grid stability and reliability.

The design of energy storage systems often requires multi-objective, multi-variable optimization to improve the efficiency and thereby, the usability of the system. Optimization using mathematical models of the physical system can reduce the design time by months, and can result in fewer ‘hardware-in-the-loop’ iterations during the initial design stages. Depending on the complexity of the energy system and design goals, the complexity of the model used to represent the system may range from a fairly simple analytical model to a complex 3D finite element model. Most physical systems have non-linear characteristics, and their optimal design may necessitate the use of sophisticated non-linear optimization algorithms and strategies. Consequently, the optimization of FES systems can be used to improve their performance, reduce system losses or improve the overall cost effectiveness. Thus, the application of optimization strategies to the mathematical models of FES systems can provide insight into their design for commercial applications.

The overall objective of this thesis is to develop numerical optimization techniques to maximize the performance of FES systems for short-duration grid-scale energy storage, while minimizing their cost by improving on FESS design parameters such as the rotor materials and geometry.

## 1.2 Background

FES systems store energy in the form of kinetic energy, which is related to the rotational speed and moment of inertia of the rotor. The energy stored in a rotating flywheel,  $E$ , which depends on the operating speed,  $\omega$ , and the moment of inertia,  $I$ , is computed using the relation,

$$E = \frac{1}{2}I\omega^2 \quad (1.1)$$

A flywheel rotor can be connected to the grid via an electric machine. When excess energy from the grid needs to be stored in the flywheel, it is ‘charged’ by the electric machine, working as a motor, which speeds up the flywheel rotor. When the grid needs to use the stored energy, the flywheel is ‘discharged’, or used to drive the electric machine as a generator, which converts kinetic energy to electricity. In the ‘standby’ mode, the flywheel is uncoupled from the grid, and in some cases, the electric machine as well, and it simply stores the energy by rotating until the next grid command. Over time, the flywheel rotor experiences self discharge because of mechanical and electrical losses. Because of this, the FESS is ideal for short-duration storage applications. The flywheel is operated in a vacuum enclosure to minimize mechanical losses due to air friction and windage.

The main components of an FES system are: 1) a flywheel rotor to store kinetic energy, 2) an electric machine and controller, which transfers energy between the flywheel and the grid as needed, 3) bearings, on which the rotor rests, 4) a mechanism to couple the rotating shafts of the flywheel rotor and the electric machine, 5) a vacuum enclosure for the flywheel rotor, which also acts as a containment unit in case of failure, and 6) peripheral devices such as speed and strain gauges that provide feedback to the control system. Figure 1.1 shows a schematic of the FES system, along with the main components.

The flywheel rotor is the energy storage component of the FESS, and determines its energy capacity. Flywheel rotors used in FES systems can be classified as low speed

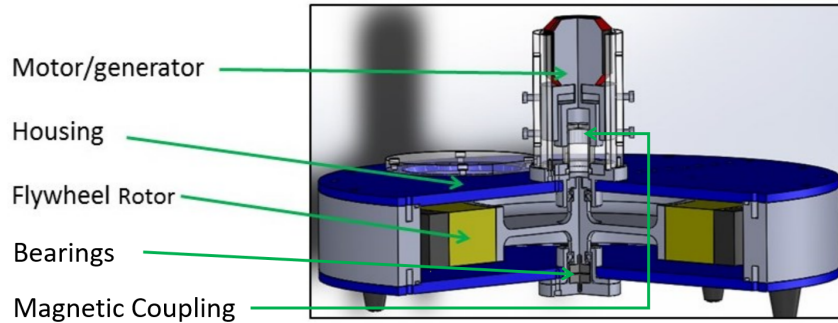


Figure 1.1: Schematic of a typical FES system, reproduced with permission from Skinner [16].

or high speed rotors. Low speed flywheels store kinetic energy primarily in the form of moment of inertia and are operated at relatively low speeds up to 10,000 rpm. Their rotors are made from isotropic materials such as metals, alloys or concrete. High speed flywheels, on the other hand, are designed with lightweight, high strength materials such as composites, and usually operate at very high speeds typically between 10,000 and 30,000 rpm.

The performance of the flywheel rotor can be quantified by its energy capacity, efficiency and cost. The energy capacity of the flywheel depends on a number of factors such as the size and overall geometry of the rotor, the material used in the construction of the rotor and the operating speed at which energy is stored. The mechanical energy losses, on the other hand, occur primarily due to air friction and windage, which are influenced by the operating speed and air pressure in the flywheel housing. These mechanical losses are mitigated by operating the FESS in a vacuum enclosure. This also acts as a physical barrier to ensure safe high speed operation. Besides the vacuum enclosure, another layer of safety is usually provided by a containment chamber, which is built to handle the maximum impact of the rotor in case of catastrophic failure. The overall cost of the FESS rotor is affected by the cost of materials used to construct the rotor as well as its manufacturing complexity.

The electric machine is used to transfer energy between the grid and the flywheel rotor and vice versa. When excess energy from the grid needs to be stored, the

electric machine is operated as a motor which accelerates the flywheel rotor by using the energy from the grid. When the grid needs to use the stored energy from the flywheel, the electric machine is used as a generator which uses energy from the deceleration of the flywheel to produce electrical energy which is sent to the grid. There is a third mode, called the standby mode, wherein the electric machine does nothing, and simply waits for the next grid command.

The power rating and energy capacity of the FESS are separable, since the rotor determines the energy capacity, whereas the specifications of the electric machine ultimately determine the power rating of the FESS. For energy storage applications where it is critical to store or provide frequent short bursts of energy, an electrical machine with a high power rating must be chosen. Over time, the FESS experiences self discharge because of energy losses both during operation and standby, and the electrical machine contributes to these losses in the form of copper losses during operation and no-load losses due to eddy currents and hysteresis during standby. Some common examples of electrical machines used in FESS are brushless DC (BLDC) machine, induction machine and permanent magnet synchronous machine (PMSM).

Several different coupling mechanism configurations can be used to connect the rotating flywheel and the electric machine. The mechanism shown in Figure 1.1 is a magnetic coupling, which is used when the flywheel is operated in a vacuum enclosure, and the electric machine is outside the enclosure [17]. Other configurations include a flywheel which is directly built on the rotating component of the electric machine, or a mechanically coupled flywheel and electric machine [12].

Bearings used in FESS can be categorized as passive and active bearings. Various bearings such as passive ceramic or steel bearings, active electromagnetic bearings and superconducting bearings have been studied in literature [18–20]. Passive bearings are usually radial bearings, and can be made of steel, ceramic (roller / ball). Active bearings need additional controllers to provide axial / radial control. Losses occurring in the bearings depend on the type of bearings used, such as eddy currents in magnetic

bearings and friction in passive radial bearings. The bearings are the most frequently replaced component in the FESS due to wear, therefore their cost contributes to the operational cost of the FESS.

This thesis will focus mainly on FESS rotor design, with the aim of improving its energy capacity while minimizing cost in the form of material used.

## **1.3 Literature review**

### **1.3.1 Flywheel rotor modeling**

#### **Quasi static rotor models**

The flywheel rotor is the energy storage component of the FES system. Several analytical and numerical models of the rotor have been proposed in literature. The quasi-static rotor model is predominantly used for stress and failure analysis in the rotor [21]. Flywheel rotor models are typically developed in a cylindrical coordinate system for convenience. Depending on the geometry of the rotor, certain assumptions can be made to simplify the governing equations and make it possible to determine an exact analytical solution for the model. For instance, if a relatively thin disk with a constant thickness profile is used as the rotor, a plane-stress assumption can be made [21]. If there are no external forces acting on the flywheel rotor and it is perfectly balanced, it can be assumed to be axisymmetric [21]. The linear elastic constitutive law is an excellent predictor of the response of materials, such as steel and concrete, that undergo small deformations under large loads.

Optimal composite rotor designs described in literature predominantly use analytical rotor models [22, 23]. This is because composite rotors are typically designed in literature as thin, cylindrical, annular disks, press-fitted or temperature fitted onto a metallic hub. Axisymmetric flywheel models with the plane stress assumption are thus good approximations and have been used in references [24, 25] whereas the plane strain assumption was used in reference [22]. A modified generalized plane

strain (MGPS) assumption was proposed in reference [26]. The authors showed that the MGPS assumption allowed the analytical results to better match 3D FEM results. While the use of the MGPS assumption could not account for edge effects at the top and bottom surfaces of the rotor, the mid-plane results for axial stresses were in agreement with FEM results. Some researchers also used numerical models to account for axial or shear stresses in the rotor [24, 27]. Design considerations that are unique to composite rotor design, such as tailored orthotropic material properties, fiber winding angles used during the filament winding manufacturing process, the choice of fibers and matrix materials are relatively easy to incorporate into these analytical or 1D models [21].

The geometry of the flywheel rotor can affect the specific energy of the FESS, and using optimal shapes can improve their performance [21]. Thus, researchers have also developed models to represent variable thickness rotors using analytical expressions. Holland [28] proposed an analytical model to determine the radial displacement and radial and circumferential stresses in a rotating disk with a hyperbolic profile. The authors improved on the original model proposed by Stodola for turbine blades [29] by including a solution for an indeterminate case. However, these analytical solutions were limited to hyperbolic profiles which may not be ideal for the purpose of energy storage. Manna [30] proposed a generic analytical model of a variable thickness rotating disk, with linear, hyperbolic or exponential thickness profiles. Yeh and Han [31] developed mathematical models of rotating disks with variable thickness and inhomogeneity. Singh and Chaudhary [32, 33] used the Runge-Kutta method to solve a piecewise two-point boundary value problem for the variable thickness flywheel rotor. However this method was only able to capture radial and tangential stress components.

When researchers found that the geometry of variable thickness rotors could not be adequately represented by analytical models [34, 35], or when the axial or shear stresses in thick rotors were significant [27, 36], they developed numerical rotor models

based on linear elasticity, which could capture details that the analytical models could not, such as gravity and acceleration loads which were previously neglected. Most numerical models of flywheels used for optimal rotor design have been developed using commercial finite element packages, which are capable of generating meshes, imposing the necessary boundary conditions, and have post processing tools to determine the three-dimensional stress state in the rotor. 2D axisymmetric, 2D plane stress and complete 3D numerical models have been used in literature.

Since this thesis aims to design optimal low-cost flywheel rotors for stationary grid-scale applications, it is expected that low-cost isotropic metals would be used in the rotor, which can be accurately modeled using the linear elastic assumption. Since flywheel rotors can be balanced after being manufactured, and as there is little risk of gyroscopic effects in the rotor due to the influence of external forces in stationary applications, the axisymmetric assumption is a reasonably good one for grid-scale flywheels. The plane-stress assumption may not hold always, especially for variable thickness rotors or rotors with high aspect ratios ( $h \gg r$ ). Additionally, the effect of gravity loads is also ignored under the plane-stress assumption, which may be necessary to determine the maximum rotor size at standstill or low speeds. As a result, this thesis will use a 2D axisymmetric numerical rotor model, which can accommodate gravity and rotational loads, as well as account for variable shape rotors and thick rotors. Also, to study the influence of the rotor topology and acceleration loads on its performance and stress distribution, it is necessary to use either a 2D plane stress or a 3D numerical rotor model. Thus, 2D axisymmetric numerical models will be used to design the rotor shape, whereas 2D plane stress and 3D quasi-static, linear elastic numerical rotor models will be used for the optimal rotor topology.

### **Transient models**

Transient rotor models can predict the stresses due to acceleration and deceleration of the rotor during charging or discharging operations. These acceleration stresses

can affect the overall rotor design as well as define the limits of safe transient operating characteristics [37–41]. This is important for short to medium duration storage applications such as power quality, frequency regulation or voltage regulation, where the ESS is frequently and rapidly charged and discharged in the order of seconds.

Tang [38] simulated a plane-stress analytical model of a rotor centrally mounted on a circular shaft, subjected to rotational and acceleration loads. The angular velocity contributed to the body force in the radial direction, and the angular acceleration contributed to the tangential component of the body force. As a result, the angular acceleration was seen to affect the shear stress  $\sigma_{r\theta}$  developed in the rotor. The author found that the maximum shear stress occurred at the inner periphery of the disk at the interface with the shaft, and the maximum tangential displacement occurred at the outer periphery of the disk. The maximum shear stress was seen to increase drastically as the ratio of the inner and outer radii of the disk was reduced. However, the results of this article were later demonstrated to hold only when the rotor was at rest and just beginning to accelerate. Phillips and Schrock [39] analyzed the effect of acceleration stresses on variable thickness disks. They found a significant reduction in the maximum shear stress due to acceleration when the disk was tapered. They also found the thickness profile for which the shear stress was uniform throughout the disk.

Reid [40] determined a method to find the least time in which a uniform thickness flywheel could be accelerated from zero to maximum speed without any plastic deformation. The author considered the effect of centrifugal radial and hoop stresses as well as shear stresses due to acceleration. They found that, for an annular disk with zero radial stress at the inner and outer rims, as the ratio of outer to inner radii ( $m = \frac{b}{a}$ ) was increased, the maximum angular acceleration decreased very rapidly compared to the maximum angular velocity. If angular accelerations are expected to be within  $3000 \text{ rad/s}^2$ , then the ratio  $m$  can be of the order of 9 or 10 before yield takes place. Thus, the importance of considering acceleration stress effects was seen

to depend on the disk geometry and the magnitude of acceleration required in the application. Similarly, the minimum time to ramp-up the speed from zero to maximum speed was seen to increase cubically with the ratio of outer to inner radii,  $m$ . For a steel disk with inner and outer radii of 50 and 200 mm respectively, the minimum run-up time was found to be 0.16 s, whereas typical run-up times are of the order of 1.5 s, so these were determined as unlikely to cause yield. On the other hand, sudden removal of load (fault conditions) could result in high enough accelerations to cause yield. Reddy and Srinath [41] devised a similar method to determine the yield behavior of centrally mounted uniform and variable thickness disks using von Mises criterion. They used a hyperbolic function to capture the rotor shape and used a different, fixed radial displacement boundary condition at the inner rim. Both studies [40, 41] established that the effects of acceleration stresses could become significant depending on the disk geometry and the minimum time to ramp-up the speed of the FESS.

The effect of transient behaviour on the rotor stress distribution can affect the transient operating characteristics such as the maximum ramp rate of the FES system. Previous studies have been performed on uniform and variable thickness flywheels. The addition of acceleration loads in the numerical rotor model can give useful insights into how the transient behaviour of the flywheel affects the optimal rotor design. This thesis will use a quasi-static approach to study acceleration related stresses on the optimal rotor designs. Since the acceleration loads mainly affect in-plane shear stresses in the rotor, these will be investigated using the 2D plane stress or 3D rotor models.

### **Standby losses**

The flywheel rotor specifications such as choice of operating speed and rotor geometry also influence the total standby losses which contribute to self-discharge and can impact the overall efficiency of the FESS. These standby losses can be mainly

attributed to mechanical losses due to bearing friction and windage, and electrical losses due to eddy currents and core losses. Literature studies have used simulations based on analytical models [42] and empirical models based on experiments [16, 43] to characterize standby losses, as well as run-time losses occurring while charging or discharging the FESS [44].

Gurumurthy et al. [43] quantified the mechanical and electrical losses in the FESS by performing tests at atmospheric pressure on an experimental flywheel setup. They accelerated the FESS to 15000 rpm and then allowed the system to decelerate under various loaded and no-load conditions. Their experiments determined that the mechanical losses, specifically the drag losses, dominated the losses especially at very high speeds of 15000 rpm, where they accounted for 72% of the total power loss. On the other hand, switching losses in the power converter accounted for a very high fraction (11%) of the total losses at the lowest speed of 2670 rpm due to the high input current. Skinner et al. [16] performed experiments on a cylindrical composite rotor FESS accelerated to speeds up to 5000 rpm to characterize the mechanical and no-load electrical losses occurring as a result of self discharge of the rotor during standby. Empirical models of the power losses developed using a curve-fitting approach showed that the mechanical losses were strongly dependent on the operating speed and vacuum pressure inside the FESS enclosure. Amiryar and Pullen [42] performed simulations using analytical and empirical models respectively to estimate the windage and bearing friction losses in a cylindrical steel flywheel operating at various low pressures and at speeds between 10000 and 20000 rpm. They determined that while the windage losses increased non-linearly with the operating speed, they could be strongly controlled by changing the vacuum pressure and the gap between the rotor and the enclosure. However, the bearing losses, which could be attributed to speed dependent and load dependent loss components, could not be influenced greatly by the air pressure. Further, the speed dependent losses were seen to increase much more than the load dependent losses with an increase in operating speed, therefore the

Table 1.1: Flywheel storage solutions deployed at utility scale applications

Flywheel model	Rotor type	Power Capacity	Energy Storage	Mass	Specific Energy	Speed	Self-discharge	$\eta$	Ref
		kW	kWh	kg	Wh/kg	rpm	W	%	
Beacon Power, LLC (BP400)	Carbon composite	100	25	1133	22.06	8000-16000	4500	85	[45]
LEVISYS	Carbon composite	10-40	10	-	-	-	- <sup>a</sup>	-	[46]
Stornetic GmbH (EnWheel)	Carbon composite	22-80	3.6	-	-	<45000	-	-	[47]
Flywheel Energy Systems Inc.	Composite	50	0.75	135	5.55	15500-31000	500-1000	86	
Powerthru / Pentadyne	Carbon composite	190	0.528	590	0.89	30000-53000	250-300	-	[48]
Calnetix (VDS-XE)	4340 Aerospace steel	300	1.11	821	1.35	24500-36750	-	-	[49]
Amber Kinetics (M32)	Low-carbon Steel	8	32	2268	14.10	<8500	65	88	[50]
Temporal Power	Steel	100-500	50	3500	14.28	<10000	500	85	[51]
ActivePower	Steel	50-250	0.958	272	3.55	7700	2500	-	[52]
ABB (PowerStore)	Steel	100-1500	5	2900	1.72	1800-3600	12000	-	[53]
Piller	-	2400	5.833	-	-	1500-3600	-	-	[54]
Energiestro	Concrete	5	5	1700	2.94	-	-	-	[55]

<sup>a</sup>Three weeks standby time

choice of operating speeds during FESS design could affect these losses significantly.

The above studies established a strong influence of the FESS design parameters such as operating speed, air gap and vacuum pressure on the total standby losses in the system. The empirical models proposed by Skinner et al. [16] will be used to determine the effect of the chosen operating speed on the standby losses in the optimized rotor designs.

### 1.3.2 Optimal rotor design

A number of studies have optimized the flywheel rotor, which is the energy storage component of the FESS. Two broad categories of materials are used in the construction of the flywheel rotor: orthotropic composites and isotropic metals. The choice of rotor material is seen to significantly affect the rotor design, as composite rotors are light and high-speed systems, whereas metal rotors are heavy and operate at relatively lower speeds. Table 1.1 depicts the specifications, including choice of rotor materials, of flywheels manufactured for commercial applications. There is an even mix of metal and composite rotors, which indicates that they might both be suited to different applications.

Figure 1.2 compares the energy capacity of several existing low speed metal rotor

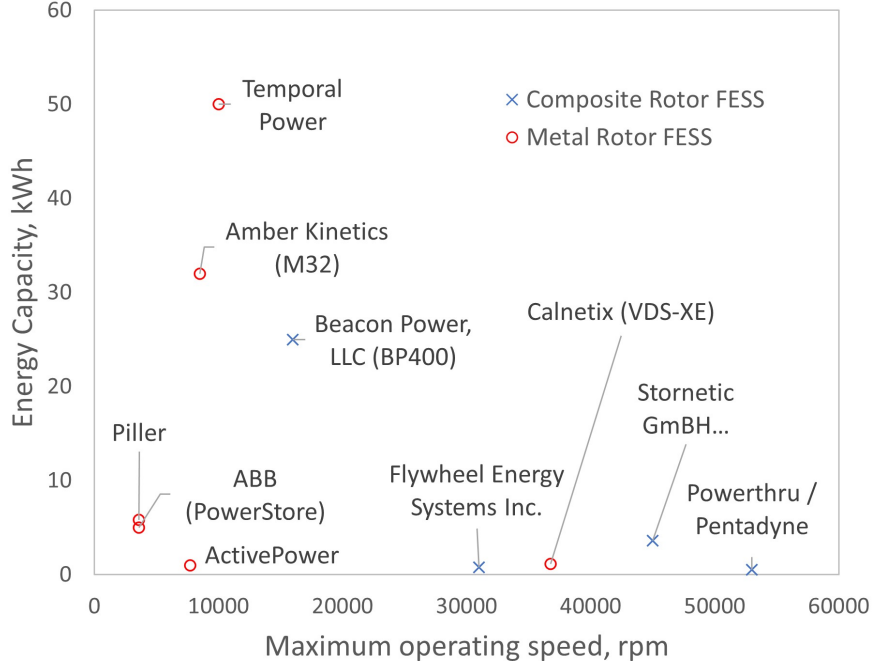


Figure 1.2: A comparison of the energy capacity and maximum operating speed of existing metal and composite rotor FESS

and high speed composite rotor FESS. Metal rotor FESS are usually employed in grid or electric utility applications, whereas composite rotor FESS are more prevalent in transportation and mobile applications. This difference in the application could explain the generally large energy capacity of the low speed FESS compared to the high speed composite FESS.

Researchers have predominantly used specific energy as a performance measure to compare flywheel designs. Genta [21] compared flywheel materials using their specific energy at burst speeds, which is given by the relation:

$$e = \frac{E}{m} = K \left( \frac{\sigma_u}{\rho} \right) \quad (1.2)$$

where  $e$  is the specific energy,  $E$  is the total energy,  $m$  is the mass of the rotor,  $\sigma_u$  is the ultimate strength and  $\rho$  is the density of the material. The shape factor  $K$  depends mainly on the flywheel geometry. Using equation (1.2), the specific strengths of some isotropic materials, Carbon Steel (Fe 34), Aluminium Alloy 2024, Titanium Alloy and Maraging Steel were found to be 12, 46, 63 and 66 Wh/kg respectively,

and those of composites such as unidirectional Glass, Kevlar and Graphite reinforced plastics were 180, 230 and 240 Wh/kg respectively. This indicated that the theoretical maximum specific energy of composites was greater than that of metals, by a factor of 4-5 on average.

As described by Genta, however, there are some precautions to be taken when using this method to compute the specific energy. When orthotropic materials such as composites are used to fabricate flywheel rotors, the ultimate strength,  $\sigma_u$ , must be indicative of the failure mode of the composite rotor. Also, rotor designs with shape factors  $> 0.5$  have bi-directional stress distributions, which cannot be handled by filament wound composite rotors with unidirectional laminates, since their tensile strengths transverse to the fiber direction (i.e., in the radial direction) are very low. Thus, designs with shape factors  $\leq 0.5$  must be chosen, or an alternative manufacturing method must be used, which would result in a multi-directional composite, with a better transverse tensile strength, albeit a lower hoop strength. Metal rotors, on the other hand, can be fabricated to have high shape factors, leading to improved performance. Thus, the shape factor depends on the choice of rotor material.

Liu et al. [56] estimated the theoretical maximum energy density of different flywheel rotors using (1.2), and found the specific energy of Maraging steel, Kevlar and T700-Graphite fiber composite flywheels to be 47, 370 and 545 Wh/kg respectively, when using a fixed shape factor of 0.5, corresponding to a rotor of constant thickness. The flywheel shape used for this comparison is unfavorable for metal rotors, since they can be manufactured with complex shapes to improve the shape factor  $K$ . Bitterly et al. [9], calculated the specific energy of the flywheel using the relation:

$$e = 1.57 \times 10^{-5} \left( \frac{\sigma_\theta}{\rho} \right) \xi_{Stress} \xi_{Design} \quad (1.3)$$

where,  $\sigma_\theta$  is the hoop stress,  $\rho$  is the material density,  $\xi_{Stress}$  and  $\xi_{Design}$  are safety factors for stress and design. They reported the theoretical maximum energy density  $e^{max}$  of 4340-Steel and Kevlar-49 flywheels to be 31.7 and 350 Wh/kg, using (2),

with safety factors of 100% to estimate the energy density. Neither of these methods accounted for the different failure modes in composites, and thus could not be used to reliably compare the specific energy of metal and composite rotors.

Arnold et al. [23] modified the shape factor to account for material anisotropy and stress-state multiaxiality and compared the specific energy of a slightly anisotropic and a strongly anisotropic material using the original and modified shape factors. They found that, for the strongly anisotropic material with a volume fraction of 40%, the calculated specific energy varied from 327.86 to 113.74 and to 115.36 Wh/kg when using the original ‘hoop only’, a modified ‘radial-only’ and ‘multi-axial’ shape factors respectively. Thus, the use of multi-axial shape factors could account for the geometry and operating conditions of the rotor more accurately. Also, this study showed that the shape factor of the type used in previous literature resulted in an over-prediction of the specific energy in the case of anisotropic materials such as composites.

The data from Table 1.1 indicates that there is a balanced mix of composite and metal flywheels currently being manufactured, despite evidence from previously published work that the specific energy of composites is much higher than that of metals. Literature studies aimed towards the design of optimized flywheel rotors can be broadly categorized under the following groups:

- Studies that improve the energy capacity by use of optimal materials or combinations of materials by multiple rim assembly or by tailoring material properties,
- Studies that design variable thickness axisymmetric rotors with optimized shapes, and
- Studies that design rotors with spokes, holes or features using topology optimization approaches.

In this thesis, optimization techniques will be developed to address each of these problems. Therefore, a description of the optimization objectives, constraints, design

variables and optimization strategies used in literature for these three broad areas of optimal flywheel design is provided below.

### 1.3.2.1 Rotor materials

Appendix A.1 contains the optimization formulations used in FESS rotor design studies that are focused on improving the FESS energy capacity by using different material combinations or tailored material properties. The objectives, design variables, constraints and optimization strategies used in these studies are discussed below.

#### Objectives

Several objective functions have been used in the optimization of rotors for FES systems that focused on material design or combinations. Most studies focus on the energy storage capacity of the FES system, either characterized by the maximum kinetic energy or the specific energy of the rotor. A few studies have included the cost of the rotor materials and manufacturing process.

References [26, 57] maximized the total kinetic energy of the rotor. Ha et al. [26, 57] maximized the kinetic energy of the rotor by tailoring the number of rims used in the rotor, the combination of composite materials used in the rims and the thickness of the rims. They found that the kinetic energy of the rotor was directly influenced by the chosen composite materials and their combinations. Increasing the number of rims increased the kinetic energy, but also the size of the rotor. Since the size of the flywheels was not fixed in these studies, the performance index (kinetic energy) could not be used to compare designs obtained using a single rim with those obtained with multiple rims.

Ha et al. [22] maximized the specific energy of a composite multi-rim rotor of fixed size, by varying the interference between rings and the fiber winding angles. They obtained a 29% and 145% increase in the specific energy by designing with optimal ply angles and optimal interferences between the ten rims of the flywheel respectively.

Ha et al. [58] also optimized a multi-rim composite flywheel by allowing the thickness of rims and interference between rims to vary. The inner radius and operating speed were fixed. They were able to achieve higher specific energies with an increase in the number of rims, but as the outer radius was allowed to vary, this came with a corresponding increase in the total size and mass.

Krack et al. [17, 24, 27] maximized the energy-per-cost of the rotor by tailoring various properties of the composite materials used in two-rim rotors. They allowed the relative thickness of the two rims to vary while the outer radius was kept constant, and found that the optimal design was subjective to the cost ratio of the two materials used in the rims [17]. They also found that the use of a split hub with optimal thickness could improve the objective by about 20% [27]. The authors also tried an approach where two distinct composite materials were used to construct the rotor, and the number of rims of each material, their interferences and ply angles could be varied to maximize the energy-per-cost of the rotor. They obtained increases of 12% and 13% in the objective function when the number of rims per material were increased from one to two and four respectively. The use of energy-per-cost as a performance metric can be useful when the overall size of the rotor is fixed and a combination of materials with varying cost ratios are used in the rotor. It may also be useful in determining the optimal rotor material from a set of candidate rotor materials. Mittelstedt et al. [25] solved a multi-objective problem which maximized the energy and manufacturing productivity while minimizing the cost of the rotor, by tailoring properties of the composite materials used in the rotor. The use of multi-objective formulations provided these studies with insights into the trade-offs between competing objectives, albeit at the cost of increased complexity of the optimization algorithm.

This thesis will perform a comparison of the three predominantly used different performance indices, i.e., kinetic energy, specific energy or energy density and energy-per-cost, to determine how the choice of performance metric or objective varied with

the choice of rotor material

### **Design variables**

While some studies on optimal composite rotors were performed at a prescribed operating speed [59], most studies also allowed the maximum operating speed to vary [17, 24, 27, 60]. The optimal operating speeds were found to be limited only by the material failure, and thus, the optimal speed was typically the highest possible speed allowed by the properties of the chosen material.

The multi-rim composite rotor has been extensively studied and optimized in fly-wheel design. The effect of the optimal thickness of composite rims on the kinetic energy or the specific energy of the rotor has been established [17, 24–27, 58, 60]. While some authors designed rotors with a fixed overall size and only varied the relative thickness of composite rims [17, 24, 27, 60], others chose to vary the overall dimensions such as the inner radius [25], or the outer radius [58]. Studies which varied the relative thickness of composite rims while keeping the overall dimension fixed, found that the optimal rim thickness was dependent on the optimization objective. When the specific energy or kinetic energy was maximized, the optimal relative thickness of each rim depended on materials used and the effective stress distribution in the rotor. When the energy-per-cost of the rotor was maximized, the optimal thickness ratio also depended on the cost ratio of the materials.

The effect of the number of press-fitted rims on the performance of the rotor was studied by Ha et al. [58], who allowed the outer radius to vary, and found a significant increase in the specific energy with every additional rim up to three rims, when only carbon composite materials were used in the rims. Mittelstedt et al. [25] varied the number of rims as a parameter and optimized the rim materials, speed, interference and thickness, while keeping the overall size of the rotor fixed. Their Pareto-front helped to better analyze the trade-offs between an increase in specific energy and an increase in the cost that came with increasing number of composite rims. Krack et

al [24] studied the effect of cost ratios on the optimal number of rims. When there was a significant difference in the prices of the composite materials being used for the rims, single rim optimal solutions were obtained. The increase in objective with increased rims was not significant beyond two rims, and the authors felt the increased manufacturing complexity was not justified.

When multiple rim rotors were found to improve the performance, other related properties such as the combination and choice of materials used in the rims [25, 26, 59], the interference between the rims [22, 24, 59], the fibre winding angles [22, 24], and the manufacturing and assembly method [59] were also explored.

This thesis will perform a comparison of several metal and composite rotor materials using several different objective functions or performance indices. The multi-rim rotor using different material combinations will also be evaluated. The design of hybrid metal-composite rotors has not been explored previously, and could yield designs which combine the best traits of both rotor types. However, as the energy as well as the cost of the rotor are the two main objectives of this thesis, tailored material properties or multi-rim rotors with more than two rims are not investigated in greater depth.

## **Constraints**

Flywheel rotor design optimization is typically performed by imposing constraints or bounds on the size of the rotor, which can influence the energy capacity of the FESS, and constraints on stress or strain measures which prevents material failure in the system.

Constraints to prevent material failure were used in almost all the rotor optimization studies, with appropriate failure criteria for the chosen rotor material. Several failure theories have been proposed and used in literature, each with its own merits. The Puck failure criterion, which can capture fibre failure and matrix failure due to transverse and shear loads in unidirectional composites, was used in reference [61].

The Tsai Wu failure criterion, capable of predicting overall failure but not the direction or the mode, was used in references [22, 24, 26]. A combination of all three criteria was used in reference [25].

When multi-rim rotors are used in the FESS, the use of additional failure criteria such as detachment of press-fitted rings as optimization constraint could be useful. While the optimization studies discussed above all checked for rim detachment as a post-processing step, they did not explore the use of a detachment failure constraint.

### **Optimization strategies**

The optimization of FESS rotors is a non-linear constrained optimization problem, and several different optimization strategies have been presented in literature. Traditional methods such as parametric studies, local methods and global gradient free algorithms have been used in some studies mainly due to their prevalence in commercial optimization packages and their ease of use. Global methods, such as simulated annealing [62], and gradient-based methods, such as the modified method of feasible direction with the golden section line search method [22, 57] and sequential quadratic programming (SQP) [59, 63], have been used in rotor design.

Traditional gradient based optimization methods have been used to a certain extent in rotor optimal design. However, in scenarios where the optimization domain was non-convex, hybrid optimization methods, such as multi-start or sequential strategies, were used to avoid getting stuck in local minima. Global methods were also used when categorical design variables, such as number of rims, rotor material combinations and design configurations, needed to be selected. When the trade-offs between multiple conflicting optimization objectives needed to be compared and analyzed, approaches such as multi-objective genetic algorithms have been used to solve the multi-objective problem as discussed below.

Several hybrid optimization strategies have also been used in literature, mainly in an effort to find a compromise between the robustness and convergence of global

methods and the speed of local methods. A multi-start strategy with Newton type method was used in reference [24] to ensure global convergence of the local method. A surrogate strategy was used in references [24, 27], where a simple 1D surrogate model of the rotor was used in the optimization iterations, with a 2D FEM model, run less frequently, used to provide corrections to the surrogate solutions. A variation of the local Newton method was used for optimization. A multi-strategy scheme was proposed in references [24, 27], where an evolutionary algorithm was used to move close to the vicinity of the optimal, after which a local gradient based Newton method could be used to quickly converge to the optimal solution. In another case, the rotor material was a design variable and the mixed integer nonlinear optimization problem was solved using a hybrid GA-SQP strategy [25]. The GA was used to solve the mixed integer problem where the rim materials could be chosen, with the SQP algorithm used to solve the non-linear constrained optimization sub-problem of selecting the best speed and rim thickness once the material, interference fit and number of rims had been chosen. The GA-SQP hybrid optimization strategy resulted in a reduced computational effort.

In this thesis, a mesh adaptive direct search (MADS) algorithm was used to compare rotor materials. The MADS algorithm is a local, gradient-free method, hence it converges faster than global methods, and it does not need any analytical gradient calculations that are necessary for gradient-based methods. It also allows for global convergence by using a variable neighborhood search strategy to escape local minima.

## **Discussion**

Most recent research on flywheel rotors has focused on high-speed composite rotors as the storage element of the flywheel energy storage system (FESS). Literature research indicates that this is primarily due to the high specific energy of composites compared to metals. However, a quantitative comparison of the performance of flywheels made from these materials has not been conducted. The first objective of this

thesis aims to answer the question - 'Are composite flywheels better suited for energy storage than metal flywheels?'. This study uses three different performance indices: kinetic energy; specific energy; and, energy per cost, to compare the corresponding rotor designs. A plain-stress, linear elastic mathematical model of the flywheel rotor described by Krack et al. [17] is used for analysis. Different optimization formulations corresponding to performance indices chosen based on the FESS application are then solved to study optimal FESS designs. Several metal and composite materials are evaluated. Multi-rim designs with two rims made with different combinations of composite materials as well as hybrid metal-composite materials are also evaluated and compared. A rim-detachment failure constraint is introduced for multi-rim rotor optimization formulations.

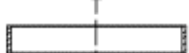
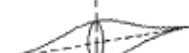
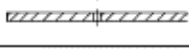
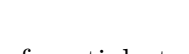
### **1.3.2.2 Shape optimization**

The shape factors of some common rotor geometries are shown in Table 1.2, with higher shape factors resulting in a more uniform stress distribution in the rotor. The shape of the flywheel rotor is known to affect its stress distribution and moment of inertia [21], and can therefore be optimized to achieve a uniform stress distribution, or a higher specific energy. However, shape optimization is employed mostly in the design of rotors made of isotropic materials. Composite rotors, which are manufactured by filament winding, are typically constant thickness rim-type rotors. Due to their orthotropic material properties, variable thickness rotors made of composites do not have very high shear and axial strength and are not prevalent [21], hence the design of variable shape rotors is focused on metal rotor FESS optimization. The optimization formulations used in shape optimization studies are recorded in Appendix A.2.

### **Objectives**

Kress [35] and Bhavikatti and Ramakrishnan [64] tried to achieve a uniform stress distribution in the rotor by minimizing the variation in the developed rotor stresses.

Table 1.2: Shape factor  $K$  of some typical flywheel geometries, reproduced with permission from reference [12]

Fly wheel geometry	Cross section	Shape factor $K$
Disc		1.000
Modified constant stress disc		0.931
Conical disc		0.806
Flat unpierced disc		0.606
Thin firm		0.500
Shaped bar		0.500
Rim with web		0.400
Single bar		0.333
Flat pierced bar		0.305

Kress [35] tried to reduce the high circumferential stresses at the inner rim of an annular shaft-mounted rotor by optimizing its shape. However, they used a modified 1D rotor model with spheres of variable radii at the inner and outer rotor rims to approximate the shape of the rotor, and this model could not accurately predict the rotor shape for annular disks with large ratios of inner to outer radii. Moreover, the study was performed only at a fixed, predetermined operating speed. Bhavikatti and Ramakrishnan [64] evaluated three different stress levelling objectives, including a weighted objective function which minimized the volume and levelled the stress distribution and found slight differences in the obtained optimal rotor shapes. Both of the above studies chose stress levelling optimization objectives, and their results did not indicate whether the energy storage capacity of the optimal disks was improved.

References [34, 65–69] maximized the specific energy of variable thickness rotors by optimizing the shape of the rotor, subject to stress constraints. Jiang et al. [67] maximized the specific energy of an FESS with an integrated rotor-shaft design subject to stress constraints by varying the rotor shape and studied how the maximum allowable stress affected the optimal design. With different allowable stresses, 14 to

23.2% improvements in the specific energy of integrated-shaft optimally shaped rotors were achieved compared to the constant thickness design. The study was conducted at a single operating speed of 1800 rpm, and resulted in similar rotor profiles, with a slight thickening of the inner region near the hub as the maximum allowable stress was reduced. Berger and Porat [34] maximized the specific energy of the rotor subject to radial and tangential stress constraints by using non-smooth piece-wise functions to approximate the inner, middle and outer regions of the rotor. The convergence of specific energy based formulations without any mass or volume constraints to physically viable designs was achieved in these studies either by the use of fixed aspect ratios resulting from the use of a fixed rotor radius or narrow bounds imposed on the height of the variable rotor thickness.

Singh and Chaudhary [70] on the other hand, maximized the energy capacity, i.e. kinetic energy, of the rotor subject to mass and stress constraints, by using a finite difference rotor model with cubic B-splines to approximate the rotor shape. Their choice of an extremely low operating speed resulted in an optimal shape that tried to maximize the moment of inertia of the disk by concentrating most of the rotor mass in the outer rim of the rotor. They were able to obtain a 36.55% increase in the stored energy over a constant thickness flywheel. Pedrolli et al. [71] designed optimally shaped flywheels using an evolutionary method with a fitness function which was a weighted combination of the mass, the standard deviation of the stress, the polar moment of inertia target, and maximum allowable stress target. Effectively, this formulation minimized the mass of the rotor subject to constraints on the stress, total energy and deviation of the stress distribution. Uyar et al. [72] also used a multi-objective formulation to maximize the kinetic energy and minimize the mass of the flywheel, subject to constraints on the maximum stress and speed.

Ghotbi and Dhingra [73] solved a multi-objective problem of maximizing the kinetic energy of the rotor while minimizing the cost, by optimizing the shape of the flywheel rotor. They used a bi-level game theoretic approach and assumed that the cost was

a function of how much the optimal shape deviated from the uniform thickness rotor shape.

### **Design Variables / Shape parametrization**

Several researchers used analytical functions to represent the variable thickness of the rotor. Ghotbi and Dhingra [73] represented the rotor thickness by a Fourier series approximation, Bhavikatti and Ramakrishnan [64] used 5<sup>th</sup> order polynomial approximations, and references [32, 33, 67, 70, 71] used cubic B-spline approximations. Alternatively, the variable thickness of the rotor was controlled by mesh element re-sizing in references [35, 65, 66]. Here, z-direction coordinates of the mesh were varied to control the height at any given radius. Berger and Porat [34] proposed the use of a non-smooth or piecewise initial rotor shape to find the optimal shape, based on a rough idea of the optimal material distribution along the radius. Liu et al. [74] proposed a metamorphic development approach to optimize the shape of continuum structures using axisymmetric numerical models. The metamorphic development approach sought an optimal  $r$ - $z$  plane domain shape through simultaneous growth and degeneration, i.e., nodes and elements could be added or removed from the structure as needed. ‘Growth cones’ defined how elements were added to boundary regions with high strain energy, and elements carrying small loads were considered inefficient and were removed from the domain. The optimization procedure did not need gradient information, as only surface stress distributions were relevant.

Most studies which optimized the shape of the rotor designed them at a fixed operating speed [32, 67, 70, 73]. While a few authors performed parametric studies to determine the optimal shape for different ranges of operating speeds [34, 64, 71], and only one study used the speed as a design variable [72]. This can be attributed to the fact that the operating speed in shape or topology optimization problems is essentially a categorical design variable, and can make the optimization problem very complex. Bhavikatti and Ramakrishnan [64] performed parametric studies to

determine the influence of operating speed on the optimal shape and found that the operating speed had no impact on the shape if there was zero fit pressure at the interface to the hub. However, as the fit pressure was increased, lesser thickening was needed near the hub with increasing speeds. Berger and Porat [34] conducted a parametric study to determine how the operating speeds influenced the optimal rotor shape and obtained three distinct optimal flywheel shapes for low, medium and high speeds of operation. They observed that as the operating speed was increased, mass was redistributed from the outer to the inner regions of the rotors. Depending on the speed of operation, the optimally shaped rotors achieved 30 to 52% improvements over constant thickness disks and 41 to 65 % improvements over exponential profile disks rotating at similar speeds. Thus this study established that the range of operating speed had a strong influence on the obtained optimal rotor shape and specific energy.

Pedrolli et al. [71] studied the effect of varying different parameters such as maximum speed, material density, allowable stress, outer radius, and maximum kinetic energy on the optimal profile, and found that, as the maximum operating speed or the density of the rotor material was increased, the rotor material was redistributed from the outer rim to the central axis. A similar effect was observed while increasing the rotor radius at a fixed operating speed. Increasing the material's strength while keeping all other parameters fixed resulted in material being redistributed from the central axis to the outer rim of the rotor. Based on the results of the parametric study, the authors concluded that including the operating speed, rotor outer radius and material properties in the optimization problem with appropriate cost functions or constraints could be used to further improve the rotor design. Despite the parametric studies performed however, the interdependence of these parameters was not studied.

Huang and Fadel [75] and Uyar et al [72] investigated the use of heterogeneous material models to design optimally shaped flywheels using two or more materials, operating at a low operating speed. While the manufacturing technologies that utilize

heterogeneous materials are still not fully mature, the study demonstrated the advantages of using optimal material placement and variable volume fractions to achieve flywheels with better stress distributions or moment of inertia.

Several shape approximation alternatives are described in literature, but the B-spline approximation is easily implemented in open-source meshing tools, and does not need elaborate mesh modification or resizing algorithms. This thesis will use the B-spline shape approximation function in rotor shape optimization studies. Also, based on recommendations by Pedrolli et al. [71], design parameters like operating speed, rotor outer radius and material properties will be included in the analysis.

### **Constraints**

Shape optimization literature on metal rotor design that used an energy maximization objective typically enforced constraints on the maximum mass of the rotor [70, 73], and conversely, mass minimization objectives had a constraint on the minimum energy capacity of the rotor [71]. These studies typically constrained the rotor mass [32, 33, 70] or the energy capacity [71] in order to fix the scale of the rotor being optimized. Mass or energy constraints were also imposed on rotor shape optimization problems to accommodate for other design considerations such as design of bearings or the starting torque limitations of the electric machine.

The total size of the rotor was constrained in some optimization formulations which maximized the specific energy content of the metal rotor using shape optimization [65, 67]. These shape optimization studies usually applied bounds on the maximum rotor radius or height and thus ensured that the optimization problem was bounded [67].

Constraints to prevent material failure were used in almost all the rotor optimization studies, with appropriate failure criteria for the chosen rotor material. Studies that designed isotropic metal rotors predominantly used the maximum von Mises stress to predict material failure [67, 71–73].

## Optimization strategies

Some studies used traditional methods such as parametric studies, local or global algorithms to design optimally shaped rotors. Arslan et al. [69] conducted parametric studies to compare the specific energy and maximum speeds of six different flywheel shapes, represented using an axisymmetric numerical model. However, they did not optimize the shape of the flywheel. Local methods such the method of feasible directions (MFD) [35], improved move limit sequential linear programming (SLP) [64], and downhill simplex [67], as well as global methods such as evolutionary algorithm [71, 76], non dominated sorting GA-II [72] have been used in some shape optimization studies. Singh and Chaudhary [70] used the Jaya global algorithm [77], and compared their designs to those obtained using GA and particle swarm optimization (PSO) global methods.

Predominantly, hybrid optimization strategies have been used in literature, mainly due to the complex nature of the shape optimization problem and in an effort to find a compromise between the robustness and convergence of global methods and the speed of local methods. Ghotbi and Dhingra [73] used a bi-level game theoretic approach to optimize the kinetic energy and cost simultaneously. The cost was assumed to be proportional to the deviation of the shape from a constant thickness profile. The problem of maximizing the kinetic energy was assumed to be the leader, and the minimization of cost was the follower problem. The seven shape related design variables were divided among the leader and follower problems. For different variable partitioning cases, the authors obtained different optimal shapes. Eby et al. [65] introduced the use of island injection GA (iiGA) to optimize the shape of flywheels for maximum specific energy. In the island injection GA, a plane stress 1D axisymmetric and a 2D axisymmetric model were both used. The flywheel was assumed to be composed of concentric rings of varying thickness. Initially, the 1D model, which was accurate when the gradient of the thickness was small, was used to determine a rough optimal shape, using varying levels of mesh refinement. Then, these rough

estimates were used as the initial population in the optimization using a 2D model, with increasing levels of mesh refinement. This helped the authors to save some time by generating a good initial shape using the inexpensive 1D model at the beginning.

## **Discussion**

Most of the studies discussed so far that used flywheel rotor shape optimization to achieve improvements in the energy storage characteristics of the FESS focused solely on improving the shape of the rotor at a fixed operating speed and rotor radius. As a result, the improvements in the design were mainly attributed to the improved stress distribution in the rotor achieved by tuning the rotor shape in a limited range. The optimization formulations in these studies further limited the extent to which the rotor geometry could be varied, either by means of imposing a mass constraint and fixing the rotor radius or by enforcing strict bounds on the variables that controlled the shape of the rotor. As a result, a major part of the optimal rotor design space remained unexplored. Even though a few parametric studies [34, 71] showed that the problem of finding the optimal rotor shape, size and speed is fully coupled, none of them studied the simultaneous influence of multiple design parameters such as speed, rotor material or rotor size on the optimal rotor shape and its energy capacity. The impact of FESS design parameters such as operating speed and vacuum pressure on the standby losses due to self discharge has been established by some literature studies using a combination of simulations based on analytical models and experimental characterization using curve-fitting. However, the effect of choosing a specific operating speed on the energy storage characteristics as well as the standby losses has not been evaluated previously.

It is essential to understand the correlation between important rotor design parameters such as rotor shape, radius, speed and choice of material, in order to design optimal FESS rotors with improved energy storage characteristics. The aim of this thesis is firstly to determine the effects of simultaneously varying multiple design

parameters, such as operating speed and rotor size on the rotor shape optimization problem and to understand if such an approach can offer a significant improvement in the energy storage characteristics of the FESS as compared to an optimally shaped rotor with an arbitrarily chosen radius and speed. This will allow for the exploration of a much larger part of the rotor design space, which is expected to yield better optimal rotor designs, and more importantly, to help visualize the nature of the optimization response surface. Secondly, the effect of the rotor material on the optimal shape and energy capacity is evaluated, while also studying how the operating speed and rotor size affect the choice of rotor material. Lastly, since standby losses occurring in the FESS are known to scale with the operating speed, and a few empirical and analytical models of the standby losses have been determined, this thesis will also use one of the existing empirical models [16] to determine how the chosen operating speed and optimal rotor design can influence the standby losses in the system. The three studies proposed above will result in an overall better understanding of the importance of several rotor design parameters and can also be used as an optimal FESS rotor design tool.

### **1.3.2.3 Topology optimization**

Shape optimization methods attempted to find the optimal flywheel shape in the axial cross section. This is important for metal flywheels where the manufacturing of the rotor can be adapted to produce complex shapes [21]. However, these formulations do not allow for variations in the circular cross section using shapes where the thickness could vary along the circumference and the radius, which can be visualized as spokes or perforations in the rotor. Topology optimization can be used to explore more of the rotor design space compared to shape optimization methods that use analytical shape functions such as B-Splines and Fourier series to approximate the rotor shape. While shape optimization can be used to determine the best rotor shape in the  $r$ - $z$  plane, topology optimization can allow for the addition of features, such as spokes or

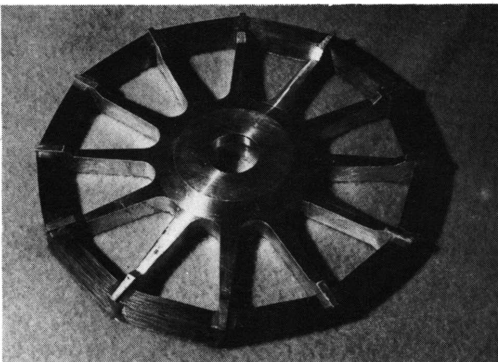


Figure 1.3: Steel wire bare filament flywheel used in spin tests by Genta [78], reproduced with permission from authors.

holes, in the design and enhance the performance of the design further, by seeking designs that might be too complex to achieve with shape optimization. The rotor structure in the  $r$ - $\theta$  plane or the entire 3D domain can be designed with topology optimization. Prototypes of rotors with such features were tested in the experimental studies performed by Genta [78], who conducted spin tests on 56 flywheels made of composites material laminates, composite rim flywheels, and quasi-circular flywheels consisting of a metal hub with spokes and a bare filament or steel wire wound around it. Their objective was to develop prototypes of low-cost advanced flywheels in the medium-energy density range. They concluded from their tests that the energy densities obtained with steel wire bare-filament flywheels, along with their associated cost and safety, were adequate for most applications. Figure 1.3 shows one of the steel wire bare filament flywheels used in the spin tests.

Moreover, the topology can be optimized to account for variations in the geometry to better handle tangential loads due to the acceleration or deceleration of the rotor, which is not possible with shape optimization. Even though the application of topology optimization algorithms to structural problems, such as truss design, is well understood and established [79], only a limited number of studies have reported the use of topology optimization for flywheel rotor design [68, 80, 81]. The optimization formulations used in topology optimization studies that designed energy storage fly-

wheels are recorded in Appendix A.3. Formulations used in rotor topology studies in other applications such as the design of motors, turbines and compressors can be found in Appendix A.4.

## Objectives

Tsai and Cheng [81] optimized the 2D  $r$ - $\theta$  plane rotor topology, for several different optimization objectives such as torsional frequency, moment of inertia considering centrifugal loads, and quasi-static compliance considering both centrifugal and acceleration loads on the flywheel at a fixed operating speed. Their compliance minimized rotor design study showed that acceleration loads strongly influenced the topology at standstill by resulting in a bending in the rotor spokes, whereas centrifugal loads dominated at higher speeds and resulted in straight spokes between the shaft and outer rim. The acceleration loads were approximated as point forces applied at eight equally distributed locations on the outer rim, and the relation between the transient operation of the flywheel and the corresponding value of the angular acceleration loads was not discussed. On the other hand, the moment of inertia maximized rotor design was reported to be a practically infeasible detached-rim rotor, because the study only used a volume fraction constraint, and did not use any stress constraints to enforce the formation of ribs or spokes between the central shaft and the fixed outer rim. Moreover, a fixed volume fraction limit of 50% was used in the study, without any background or parametric studies to establish why this volume fraction was chosen.

Jiang and Wu [68] found the optimal rotor topology using a 2D  $r$ - $\theta$  plane numerical model operating at a fixed angular speed of 2250 rpm, by maximizing the moment of inertia of the rotor, subjected to volume fraction and maximum stress constraints. They used a density-based approach with the SIMP power law, and a ‘minimum member size’ for length scale control. The study demonstrated a 14% improvement in the specific energy of the rotor by removing 30% of the material from a constant

thickness rotor design. They tested the sensitivity of the design to parameters including minimum member size, rotational symmetry, maximum volume fraction and maximum allowable stress, and found that a rotational symmetry of 6 (i.e.,  $60^\circ$  circular section), and a volume fraction limit of 70% achieved the best specific energy for the chosen design. This study did not study the influence of acceleration induced stresses or variations in the operating speed on the rotor topology.

Lottes et al. [82] used a combination of shape selection and topology optimization to design the flywheel. They initially used a parametric study with four selection criteria (mass, Rankine stress criterion, mass-specific angular momentum and form factor) to rank and select the best rotor shape or contour from among 15 different shapes, using axisymmetric 2D numerical models for analysis. Next, the selected shape was used as the initial design to perform topology optimization only on the inner structure of the rotor using a 3D numerical model, by effectively hollowing out the rotor to minimize its compliance subject to a 40% volume fraction constraint. The study reported a 16% increase in the specific energy over the reference flywheel obtained from the initially selected optimal shape, but this was accompanied by a 74% increase in the developed stresses. This was attributed to the limited choice of optimization objectives and constraints available in the software used for topology optimization, which could not incorporate energy capacity or stress criteria in the topology optimization problem. Details about the topology optimization approach, solver, filters and other implementation details used to generate the results in the article were not reported.

Hinterdorfer et al. [61] optimized specific energy by varying the r-z plane shape of axisymmetric metal and composite rotors by discretization of the rotor thickness along the radius. Although variable thickness composite rotor designs were determined, the optimal shapes were highly irregular and the manufacturing feasibility of these designs was not demonstrated. Bugada et al. [76] used a combination of shape and topology optimization to get the optimal r- $\theta$  plane geometry of the flywheel. The

author initially obtained an initial ‘optimal’ topology using a topology optimization routine, and then found the best smooth outline of the flywheel spokes using separate shape approximation functions for each curved boundary.

Lopes et al. [80] optimized the topology of a hydro generator shaft using 2D and 3D FEM models of the shaft. They used the standard SIMP model with an optimality criterion to find the optimal designs, by minimizing the compliance of the shaft subject to volume constraints. Both gravity loads and inertial loads due to rotation at a constant speed were considered. Initially, they tried optimizing the 2D topology (top view) under gravity only, and then added the inertial load. They found that at low volume fraction constraints, the optimal design had intermediate densities at the center of the structure, indicating that a 3D analysis would be needed. The optimal topology using 3D models seemed to have converged to a feasible design; however, no data was presented to indicate how the optimal design fared better than the original. Also, the stress distribution in the model was not checked or reported.

### **Design variables**

Density-based topology optimization techniques typically utilize the mesh element or cell densities as the optimization design variables [83], although a few literature studies have utilized nodal design variables, such as the continuous approximation of material distribution (CAMD) approach used by Tsai and Cheng [81].

The use of element densities as topology design variables leads to unwanted checkerboard patterns in the topology. Filtering techniques are used to ensure the convergence of the problem to an optimal design without any checkerboard patterns, as well as provide length scale control, which can be used to meet manufacturing requirements such as minimum size of the features in the optimal topology. The sensitivity filtering approach proposed by Sigmund [84] filters the objective function sensitivities. This filtering approach may not be ideal if the sensitivity data does not represent a descent direction. Thus, the success of this scheme can be subject to the

nature of the objective function. The density filter proposed by Bruns et al. [85] is a more robust approach and is also commonly used in topology optimization. Here, the element densities are filtered in a given neighbourhood, and the filtered densities are used as design variables for the optimization problem. Le et al. [86] used this approach to minimize the volume of an L-bracket subject to stress constraints.

In addition to the density filter, a Heaviside or projection filter stage is also sometimes necessary to allow convergence to a discrete design. Sigmund [87] used image morphology techniques as a post-processing step on the optimal topology to remove the gray regions and obtain purely black-and-white designs. They used sequences of ‘erosion’ and ‘dilation’ operations on the image to preserve the volume constraints of the optimal design. Here, erosion and dilation referred to forcing pixels to take values of 0 or 1 based on certain neighbourhood criteria.

## **Constraints**

The flywheel topology studies reported so far utilized a fixed volume fraction constraint to remove material from the initial domain, whereas in reality, the volume fraction that achieves the best energy capacity is not known, and should be determined during the optimization process. Thus, this constraint was artificially imposed in order to remove material from the domain.

Based on energy storage flywheel topologies reported in literature, the use of a stress-constraint in the optimization formulation is seen to be essential for two reasons - it provides a means of predicting and preventing material failure, and it drives the convergence of the design to a physically feasible design without any detachment of the rotor rim from the inner shaft. Previous FESS topology studies have either neglected or not discussed in detail the type of stress constraint used, despite stress-constrained topology optimization being an established branch of topology problems that have been tackled in great detail in literature for a variety of benchmarking problems [86, 88–90]. Imposing stress constraints on a topology optimization prob-

lem may make the feasible domain singular, thereby making it extremely difficult for gradient-based optimization techniques to converge to the optimal solution. Several stress constraint relaxation techniques have been proposed in literature to ensure convergence. Collet et al.[91] used a q-p relaxation scheme to relax the stress constraint. The sensitivities of the local stress constraints were computed using an adjoint formulation. Alternatively, the  $\epsilon$ -relaxation scheme by Cheng et al. [92] was also used in several studies. Literature studies have reported the use of global stress constraints aggregated using functions such as P-norm [88] or Kresselmeier–Steinhauser (K-S) functions [93], as well as local stress constraints using the Augmented Lagrangian (AL) approach [90].

Global stress constraints have been employed in the topology optimization of other types of rotating machinery such as hydrogenerator shafts [94], compressor and turbine rotors [95, 96], and synchronous reluctance machine rotors [97, 98]. While the optimization objectives used for these rotors are different from the energy storage flywheels, some of these studies used a global stress constraint in the optimization formulation, computed as the P-norm aggregated relaxed von Mises stresses, which can also be utilized in flywheel rotor design. In this method, the local stress constraints at each mesh element are combined into a single maximum constraint. Since the ‘maximum’ function is not differentiable, an analytical function such as the P-norm can be used to approximate the  $\max$  function. References [96, 97] reported that the use of a global stress constraint for compressor and synchronous reluctance motor design made the optimization problem difficult to converge, especially since they used projection filters with continuous updates on the slope to improve the discreteness of design, and that the computed stresses would see large oscillations for large values of the projection slope. They used an additional constraint on the strain energy or compliance to try and prevent instabilities. Several strategies have been reported in topology literature to ensure convergence of the design with a projection filter, such as modified  $\beta$ -continuation schemes [99], volume preservation by performing line-search

on the filter threshold [100] and morphology based filtering methods [87].

The global stress constraints described above are not very effective when the topology domain is large or complicated. They can either be very difficult to converge, or generate topologies with localized stress concentrations, which might be sub-optimal or locally optimal. The use of regional or local stress constraints can offer more control over the stress distribution in the entire domain, resulting in better convergence to an optimal design. Collet et al. [91] computed the local stress constraints and their sensitivities using an ‘active set selection’ strategy, which effectively eliminated the need to check some of the stress constraints based on a heuristically determined threshold value. Le et al. [86] used region-normalized stress constraints instead of local stress constraints. They divided the domain into several smaller regions and used the normalized p-norm of the maximum stress constraint over each region. This was done to provide better control over the local stress than the maximum stress approach. Other studies have used local stress constraints in their optimization formulations [101–103], which resulted in an optimization problem with as many constraints as the number of mesh elements. Since the calculation of sensitivities for local stress constraints comes with a high computational cost, strategies such as Augmented Lagrangian formulation [103, 104] have been used in literature to reduce this expense.

### **Optimization strategies**

Density-based topology optimization techniques applied to numerical models treat the density of each mesh element as a design variable. Thus, every element may have a density of zero or one, indicating the absence or presence of material at that location. This is essentially a discrete design problem with a very large number of design variables that scales with mesh refinement. Although some studies have solved this discrete problem using global optimization algorithms [61, 105], the majority of topology optimization strategies relax the problem by allowing the element densities to take intermediate, real values between zero and one. The solid isotropic material

with penalization (SIMP), or ‘power law’ approach proposed by Bendsøe [83] does this by imposing a penalty on the material properties of elements with intermediate densities, thus allowing the optimization routine to converge to nearly black-and-white designs.

The method of moving asymptotes (MMA) by Svanberg [106], which is specifically developed for structural optimization, was used by Tsai and Cheng [81] and Lottes et al. [82] to find the optimal flywheel topology. Other rotor design studies have used the MMA method [80, 95, 96], Optimality criterion [107], and the globally convergent MMA (GC-MMA) [97] for topology optimization. These methods require information about the gradients of the objectives and constraints, which can be computationally expensive for topology optimization problems, with a typical range of 10,000 to millions of design variables. Predominantly, adjoint approaches have been used for the calculation of the optimization response sensitivities in topology optimization literature [86, 88, 91].

## **Discussion**

Out of the few studies which were aimed at improving the energy capacity of FESS rotors using topology optimization, only one was successful in obtaining manufacturable energy maximized rotor designs. The other studies either used compliance minimization formulations because these are readily available in commercial tools, or were unable to converge to physically feasible designs due to the lack of stress constraints in their formulation, and further, all the studies assumed a fixed, relatively low operating speed. Moreover, the results reported so far utilized a fixed volume fraction constraint to remove material from the initial domain, whereas in reality, the volume fraction that achieves the best energy capacity is not known, and should be determined during the optimization process. A robust topology framework is needed in order to investigate different topology optimization formulations to improve the energy storage performance of FESS. While kinetic energy and compliance have been

used as objectives, the use of specific energy or energy-per-cost-ratios, as discussed in references [17, 27] is hypothesized to be a more adequate objective as doing so will drive the optimization algorithm to determine the most desirable volume fraction. This approach has, however, not been evaluated thus far in topology optimization based design of energy storage flywheels.

Although stress constraints have been used in rotor topology studies, they were mostly global stress constraints, which suffer from problems such as localized stress concentrations, which can cause the optimization problem to get stuck in a local minima or suboptimal design. The use of local stress constraints with an Augmented Lagrangian framework can help achieve better stress distributions while driving the flywheel design towards a higher energy capacity.

Further, most existing flywheel topology optimization literature optimizes the 2D topology of the rotor, as seen from the top, i.e, in the  $r-\theta$  plane. To fully use the capabilities of topology optimization algorithms, they need to be implemented on the 3D geometry to allow flexibility in the topology in all three dimensions. The additional computational expense can be reduced by the use of innovative optimization strategies to reduce stress constraint and sensitivity information computations. These modifications are not easily implemented while using commercial software, and the implementation of an in-house numerical model and topology optimization algorithm for this purpose is justified. The implementation of a specific-energy based, stress-constrained 3D topology optimization framework is therefore an integral part of this thesis. The optimal 3D rotor designs can be compared to, or combined with shape optimized rotor designs, to further improve the specific energy by removing additional unnecessary material from the interior regions of the rotor.

Grid-scale FESS are typically used in short duration energy storage applications mainly related to grid reliability. At times, the system could be required to quickly store or discharge energy by accelerating or decelerating the flywheel. Tsai and Cheng [81] studied the effect of combined centrifugal and acceleration loads on the

optimal rotor topology at various speeds for a compliance minimized formulation, where the acceleration loads were incorporated by applying equally eight tangential point loads distributed along the outer rim of the rotor. However, they did not study the relation between ramp times and acceleration loads, and the corresponding effect on the shear and von Mises stresses in the flywheel topology. This thesis will therefore also discuss acceleration loads.

## 1.4 Objectives

Some gaps were identified in the literature on optimal FES rotor design, which will be investigated in this thesis in order to assess and potentially improve the design methodology of flywheel rotors. While there has been abundant literature on optimizing composite rotors for flywheels, and some on optimal metal rotors, there was no unified study that performed a quantitative comparison between composites and metals that could help the designer choose the rotor material for a specific storage application. It was essential to understand this before trying to design optimal rotors for grid-scale FES systems. Hence, such a study was performed as a preliminary objective of this thesis, which formed the basis for the subsequent research goals outline below. Based on this preliminary study, it was found that metal rotors, with a higher energy-per-cost than composite rotors, were better suited to grid-storage applications. Thus, the following goals aim to further optimize metal rotors based on literature findings.

Studies have optimized the geometry of the rotor by using either shape or topology optimization methods. Shape optimization studies have reported the effects of design parameters, such as operating speed, on the optimal rotor shape and indicated that the problem of determining the optimal rotor shape, size and speed is a fully couple one. **However, the simultaneous influence of multiple design parameters including the rotor shape on the energy capacity has not been investigated.** So far, the optimal rotor design has aimed at maximizing the performance, usually

quantified by the storage capacity of the rotor. **This design approach does not take into account the standby losses occurring in the system, which are also influenced by design parameters such as operating speed.** In order to perform the above studies, 2D axisymmetric numerical models of the rotor with rotational and gravity loads will be developed using an open-source software. The model will be integrated with a parameterized mesh generator for shape optimization. An empirical model of the standby losses in the FES system, based on experimental findings, will be used to study the influence of standby losses on the optimal operating speed, rotor shape.

Topology optimization techniques utilized to define the optimal 2D flywheel topology have either used compliance formulations that are readily available in commercial tools but do not address the key objective of rotor design, i.e., maximizing the energy capacity, or have used artificial volume fraction constraints to remove material from the domain. **The removal of the dependence of the topology optimization formulation on a volume fraction constraint has not been explored previously.** The use of local stress constraints instead of global constraints can yield better topology optimized designs through greater control over the stress distribution in the entire rotor. However, imposing local stress constraints can result in an optimization problem with as many constraints as mesh elements, and needs to be handled using approaches such as the Augmented Lagrangian formulation. **A local stress constrained problem with an Augmented Lagrangian formulation and its comparison to global stress constrained formulations has not been previously performed for rotor topology design.** Further, the use of a 3D numerical model to find the optimal rotor topology could greatly improve and change the optimal topology by exploring a larger design space. Topology optimization with a 3D rotor model is computationally expensive, and therefore requires novel optimization strategies to reduce the computational effort. In order to perform the above studies, a numerical optimization framework will be developed to conduct the proposed

topology optimization studies.

In summary, the overall objective of this thesis is to develop numerical optimization techniques to maximize the energy storage of FES systems for short-duration grid-scale energy storage, while minimizing their cost by improving on FESS design parameters such as the rotor materials and geometry. Based on the identified gaps in literature the specific goals of this thesis are:

- To determine the optimal FES system and rotor materials based on different performance indices such as maximizing the kinetic energy, specific energy or energy-per-cost, that reflect the type of storage application.
- To improve the performance of low-cost metal flywheels by simultaneously optimizing the rotor shape and multiple operating conditions, such as operating speed, rotor size and rotor materials, and studying the influence of the optimal design on standby losses in the system
- To improve the performance of low-cost metal flywheels by optimizing the rotor topology through the use of a optimization formulation that removes dependence on the artificial volume fraction constraint, and to study the effect of acceleration loads on the optimal design
- The use of topology optimization with local stress constraints using an Augmented Lagrangian formulation for greater control over the stress distribution and 3D simulations for exploring a larger design space.

## 1.5 Thesis Outline

This thesis is divided into six chapters. This chapter provides a motivation and a literature review which form the basis for the objectives of the work. The literature review discusses the state-of-the-art for optimization approaches used for optimal energy storage flywheel design. Since the flywheel models, optimization framework

and solvers used for each of the objectives are different, the methodology for each objective is discussed in the corresponding chapters. Chapter 2 uses a 1D plane-stress axisymmetric quasi-static rotor model and an optimization framework to compare various isotropic metal rotors and orthotropic composite rotors. The performance of different rotor materials is compared using different optimization objectives, such as maximizing the kinetic energy, specific energy or energy-per-cost. Chapter 3 describes a 2D axisymmetric finite element model of the flywheel, which is integrated with a shape optimization framework to design optimally shaped low-speed metal flywheels. Chapter 4 uses a 2D plane-stress finite element model of the flywheel integrated with a topology optimization framework to determine the optimal topology of metal flywheels. Chapter 5 uses an Augmented Lagrangian framework with local stress constraints to determine the optimal topology of the rotor. Chapter 6 presents a modified robust formulation for performing 3D flywheel topology optimization and compares the approach with previously explored shape optimized rotor designs. The conclusions and contributions of this thesis are summarized in chapter 7.

# Chapter 2

## Optimal selection of rotor materials by FESS application<sup>†</sup>

### Preface

Most recent research on flywheel rotors has focused on high-speed composite rotors as the storage element of the flywheel energy storage system (FESS). Literature research indicates that this is primarily due to the high specific energy of composites compared to metals. However, a quantitative comparison of the performance of flywheels made from these materials has not been conducted. This study described in this chapter aims to answer the question - 'Are composite flywheels better suited for energy storage than metal flywheels?'. This study uses three different performance indices: kinetic energy; specific energy; and, energy per cost, to compare the corresponding rotor designs. A plain-stress, linear elastic mathematical model of the flywheel rotor described by Krack et al. [17] is used for analysis. Different optimization formulations corresponding to performance indices chosen based on the FESS application are then solved to study optimal FESS designs.

The first hypothesis is that the specific energy is not the only performance index which is important while selecting the rotor material, and that there might be other factors influencing the choice of materials during the design process. In utility or grid

---

<sup>†</sup>Parts of this chapter have been published in: V. Kale and M. Secanell. *Energy Reports* 4 (2018): 576-585.

applications, the total energy and cost might be the most important performance indices; whereas, in mobile applications, the weight or space occupied by the FESS might be a major constraint, and thus the specific energy or energy density might be the most important performance indices. There is, therefore, a need to compare optimal flywheel designs based on different criteria, depending on the application. Krack et al. [27], [60] optimized the energy per cost of fixed volume multi-rim composite annular disk-type flywheels, by varying the operating speed and relative thickness of the composite rims, using normalized costs of rotor materials. This approach can be extended to the current work to select the best rotor materials for the optimal flywheel for the application.

The second hypothesis is that the use of a simple geometric shape factor to estimate the specific energy of a material might not accurately predict the specific energy of a rotor made of that material, especially when anisotropic materials are used. Thus, a mathematical model of the rotor is needed, which will account for material anisotropy and failure modes. When this model is used to optimize the flywheel, a more realistic value of the specific energy of the rotor can be obtained, which can then be used to choose the appropriate rotor material. An additional advantage of using an optimization formulation to determine the performance of the rotor materials is that, practical constraints other than material failure can also be checked. For example, constraints on the radial tensile stresses at the interface of multi-rim press-fitted composite rotors ensure that the composite rims do not detach due to differences in the radial expansion of the various rims.

The optimal flywheel rotor obtained using several different rotor materials is used to compare and select rotor materials. The 1-D plane-stress axisymmetric flywheel model, proposed by Krack et al. [17], is used for the analysis. Several optimization formulations consisting of various configurations of metal and composite rotors are studied. For multiple-rim flywheels, additional interference constraints are applied, to ensure that there is no physical detachment of the rims. Comparing the optimal rotors

ensures that the theoretical limits of the rotor material are reached, while also ensuring a feasible rotor design, without other failures such as detachment of press-fitted rims from the hub. Optimization objectives, such as total kinetic energy, energy per cost and specific energy are used to compare the rotors and materials. A mesh adaptive direct search (MADS) algorithm is used to solve the optimization problem, instead of the hybrid and multi-start methods employed in [17]. The MADS algorithm is a local, gradient-free method, hence it converges faster than global methods, while being more reliable than gradient-based methods.

In Section 2.1.1, the analytical model of the flywheel is described. This model calculates the kinetic energy, stresses and deformations in the flywheel rotor at a given speed. Section 2.1.2 presents the optimization formulations, with constraints imposed on the flywheel rotor model developed in the previous section. Objectives such as kinetic energy, specific energy and energy per cost are optimized by varying the operating speed, number of rims, rim materials and relative thickness of the rims. Constraints on the material failure and rim detachment ensure that there is no failure in the flywheel. Finally, in Sections 2.3 and 2.4, the results and conclusions drawn from the studies conducted here are summarized.

## 2.1 Methodology

### 2.1.1 Flywheel structural model

The flywheel mathematical model proposed by Krack et al. [17] is used in this study. A brief overview of the model is provided below. The stored energy of the flywheel is given by

$$E = \frac{1}{2}I\omega^2 = \frac{1}{2}\rho\pi h\omega^2 \sum_{j=1}^n [(r_o^j)^4 - (r_i^j)^4] \quad (2.1)$$

where  $\omega$  is the rotational speed,  $\rho$  is the density,  $h$  is the constant rotor height,  $n$  is the number of rotor rims and  $r_o^j$ ,  $r_i^j$  are the outer and inner radii of the  $j^{th}$  rim. A linear elastic model is used to determine the developed stresses in the rotor, based on

the assumptions of plane stress, and axisymmetric rotation. Cylindrical coordinates are used for convenience.

### 2.1.1.1 Governing equations

The flywheel stresses can be found by solving Euler's equation of balance of linear momentum for a body,

$$\nabla \cdot \underline{\sigma} + \rho \mathbf{b} = \rho \mathbf{a} \quad (2.2)$$

where  $\underline{\sigma}$  is the Cauchy stress tensor,  $\mathbf{b}$  is the vector of body forces and  $\mathbf{a}$  is the linear acceleration. The strain-displacement relation for small deformations is used, along with a linear stress-strain relation, given by Hooke's law.

$$\underline{\epsilon} = \frac{1}{2}[\nabla \mathbf{u} + (\nabla \mathbf{u})^T] \quad (2.3)$$

$$\underline{\sigma} = \underline{\underline{Q}} \underline{\epsilon} \quad (2.4)$$

where  $\underline{\epsilon}$  is the strain tensor,  $\mathbf{u}$  is the displacement vector and  $\underline{\underline{Q}}$  is the stiffness tensor. The above relations are expressed in the cylindrical coordinate system, and the assumptions of plane stress and axisymmetry are used to obtain the second order equation:

$$\frac{\partial^2 u_r}{\partial r^2} + \frac{1}{r} \frac{\partial u_r}{\partial r} - \frac{Q_{11}}{Q_{33}} \frac{u_r}{r^2} = -\frac{\rho \omega^2}{Q_{33}} r \quad (2.5)$$

Here,  $u_r$  is the radial displacement,  $Q_{11}, Q_{33}$  are stiffness matrix components,  $\omega$  is the operating speed and  $\rho$  is the density of the material. The derivation and solution of this equation can be found in [17].

### 2.1.1.2 Boundary conditions

The radial stresses at the interface of the hub and the rotor, or between rims for multi-rim rotors, are continuous. Thus, the following compatibility condition is applied on the radial stresses at the interfaces:

$$\sigma_{r_i}^{j+1} = \sigma_{r_o}^j \quad (2.6)$$

where  $j = 1, 2, \dots, (n - 1)$

The radial displacements are continuous, but with an interference  $\delta^j$ , which results from the press-fitting of the rims during assembly. This results in the displacement related compatibility condition:

$$u_{r_i}^{j+1} = u_{r_o}^j + \delta^j \quad (2.7)$$

where  $j = 1, 2, \dots, (n - 1)$

The stresses at the rotor outer surface are assumed to be 0, and the stresses due to the hub, at the inner surface of the rotor, can be expressed using the model from [27]. Thus, the boundary conditions which are applied on the stresses are:

$$\sigma_{r_i}^1 = p_i = \frac{\rho_{hub} \omega^2 (r_i^3 - r_{hub}^3)}{3r_i} \quad (2.8)$$

$$\sigma_{r_o}^{Nrim} = 0 \quad (2.9)$$

### 2.1.1.3 Implementation

The above model is implemented and solved in Python. The `numpy.linalg.solve` solver, which utilizes the LAPACK routine 'dgesv', is used. The average simulation time for the analysis model is  $< 10$  ms, on a 64-bit 4-core, 3.3 GHz processor.

## 2.1.2 Optimization problem

### 2.1.2.1 Formulation

From the discussion in Section 1.3.2.1 it is clear that there is a need to formulate the optimization problem in a way that allows a meaningful comparison of the rotor materials. This means that the optimization formulation needs to have enough flexibility to find the true optimal rotor that can be made using any type of material. For example, the optimal composite rotor might have multiple thin rings press fitted together to form a high speed composite rotor, whereas the optimal metal rotor might be a single thick disk rotating at much lower speeds. Also, the performance

index used to compare the optimal rotor materials might be different depending on the application.

In order to compare the energy content of flywheel rotors made of different materials, a rotor of the type shown in Figure 2.1 is used, where the rotor height is assumed to be constant, since a thick rotor would violate the plane-stress assumption and necessitate the use of FEA simulations. The optimization problem can thus be formulated as:

**max:**  $f(\mathbf{x})$

where the objective  $f(\mathbf{x})$  may be one of the following:

$$\frac{1}{2}I\omega^2, \quad \text{kinetic energy (KE)}$$

$$\frac{KE}{Cost}, \quad \text{energy per cost}$$

$$\frac{KE}{Mass}, \quad \text{specific energy}$$

**w.r.t:**  $\mathbf{x} = \{\omega, n, \{r_{out}^1, r_{out}^2, \dots, r_{out}^{n-1}\}, \{material_1, material_2, \dots, material_n\}\}$

**subject to:**  $\frac{\sigma_i}{\sigma_i^{ult}} < 1$ , material failure constraint

$$\text{and } \sigma_{r_{in}}^{j+1} = \sigma_{r_{out}}^j \leq 0, \quad \text{rim detachment failure constraint}$$

where,

$$j = 1, 2, \dots, (n - 1) \quad ; \quad i = (r, \theta, z)$$

$\omega$  : rotor speed, rpm

$n$  : number of rims

$r_{out}^j$  : outer radius of rim  $j$ , m

$material_j$  : material used in rim  $j$

$\sigma_i$  : stress in direction  $i$  ( $i = r, \theta, z$ )

$\sigma_i^{ult}$  : ultimate strength in direction  $i$  ( $i = r, \theta, z$ )

$\sigma_{r_{in}}^j, \sigma_{r_{out}}^j$  : radial stress at inner and outer radii of rim  $j$ .

For the material failure constraint, the yield strengths of the metals are used to compute the strength ratio for the material failure constraint, to avoid plastic deformation. For composite materials, the ultimate strengths of the composite laminates are used for their strength ratios. The maximum stress failure theory (MSFT) is used to indicate failure.

There is a constraint on the maximum radial tensile stress between the press-fitted rims of a multi-rim composite rotor. The rim detachment constraint used in this study is a novel one, which can allow the optimization routine to yield better results than in the past. Previous research conducting optimization of press-fitted multi-rim flywheels used a constraint which restricted the radial stresses in the flywheel to compressive (negative) values at all points along the radius [27]. The new rim-detachment constraint only restricts the radial stresses to compressive values at the interface between rims, where the load cannot be transferred in the radial direction. Thus, other regions in the flywheel may be subjected to radial tensile stresses within the material elastic limits, which further increases the energy capacity of the optimal FESS. The number of rims in multi-rim composite rotors has been limited to two in this study, since it has been demonstrated by previous researchers [108], that a further increase in the number of rims results in a limited improvement in the performance of the flywheel.

#### **2.1.2.2 Implementation**

The optimization problem is solved using DAKOTA toolbox [109], which allows the use of its optimization algorithms as a black box, using a script interface. A schematic of the interface between DAKOTA, and the analysis code, implemented in Python is shown in Figure 2.2. A MADS algorithm is used to solve this non-linear constrained optimization problem, as it is a local, gradient free method, and is more reliable than local gradient-based methods, while being faster than global methods such as

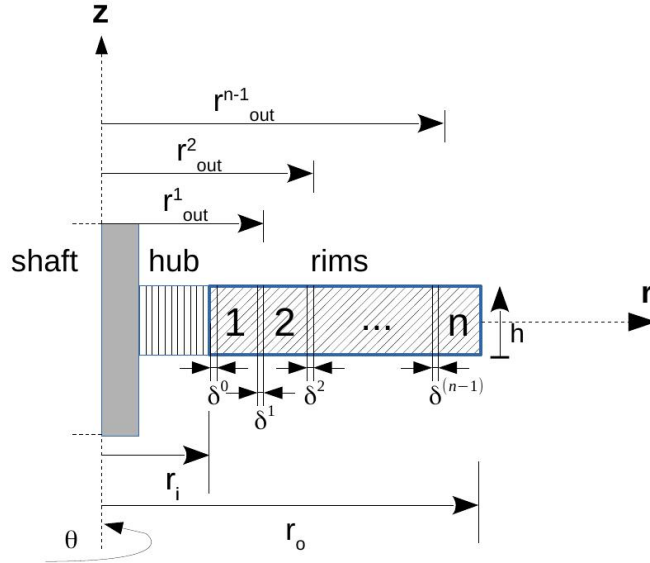


Figure 2.1: Block diagram of flywheel rotor

genetic algorithms. It has minimal dependence on the initial guess of the design variables. Also, this method can reliably solve non-convex problems, which can prove challenging for gradient-based methods because of their tendency to get stuck in local optima when the optimization problem is non-convex.

## 2.2 Model and framework validation

The flywheel mathematical model used in this study was validated against the results published by Krack et al. [17]. A 2-rim composite rotor consisting of an inner glass-epoxy rim and an outer carbon-epoxy rim was simulated. The composite material properties and flywheel dimensions from [17] were used. The radial and hoop stresses developed in the flywheel rotating at 30,000 rpm were then plotted, and compared with the stresses developed in a single rim rotor made from either of the 2 composite materials. It was found that the radial stresses developed in the rotor were reduced by introducing an extra rim. The stress distributions in the 1-rim and 2-rim composite flywheel rotors, obtained from the Python model described in Section 2.1.1 are shown in Figure 2.3. The results were in agreement with the previous publication.

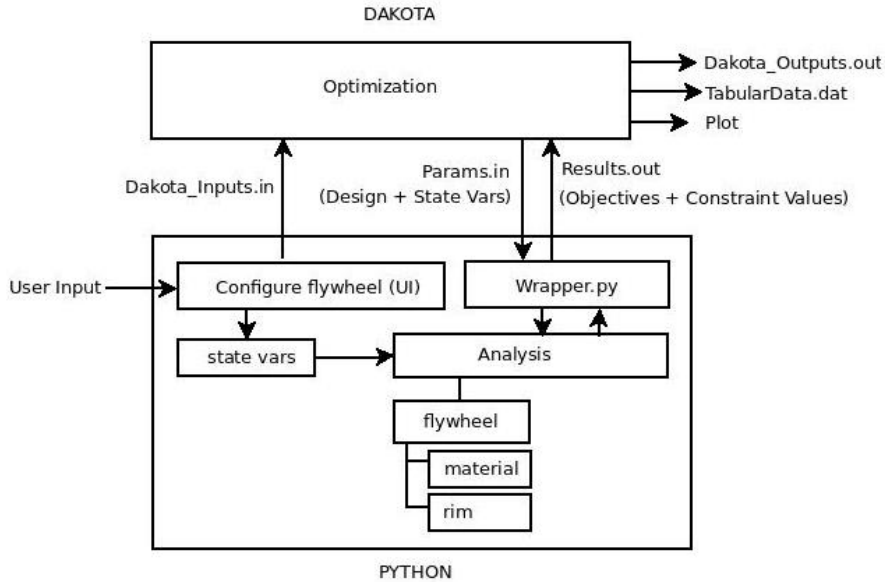


Figure 2.2: Schematic of the Python-DAKOTA interface

In order to validate the optimization framework, the design problem in [17] was also solved. The energy per unit cost of materials, for the 2-rim glass-epoxy and carbon-epoxy composite flywheel, was maximized by varying the operating speed and the relative thickness of the 2 composite rims. The optimal solution was obtained for 4 different cost ratios of the materials used in the rims. Table 2.1 shows a comparison of the optimal solution with the proposed framework and the solution obtained in [17]. The simulated results were within  $\pm 0.3\%$  of the literature results, which could be due to the use of different optimization algorithms.

The proposed optimization formulation discussed in Section 2.1.2, introduced an additional constraint on the radial stress developed at the interface of press-fit rims in multi-rim rotors. This constraint was necessary to ensure that there are no radial tensile stresses at the rim interfaces, which could result in failure due to detachment of the rims. The necessity and significance of this new constraint was investigated. This constraint was not used in [17] because the radial stress at the rim interface became more compressive at higher speeds, and there was no need of checking for the rim detachment constraint. This is because the ratio of the specific stiffnesses of

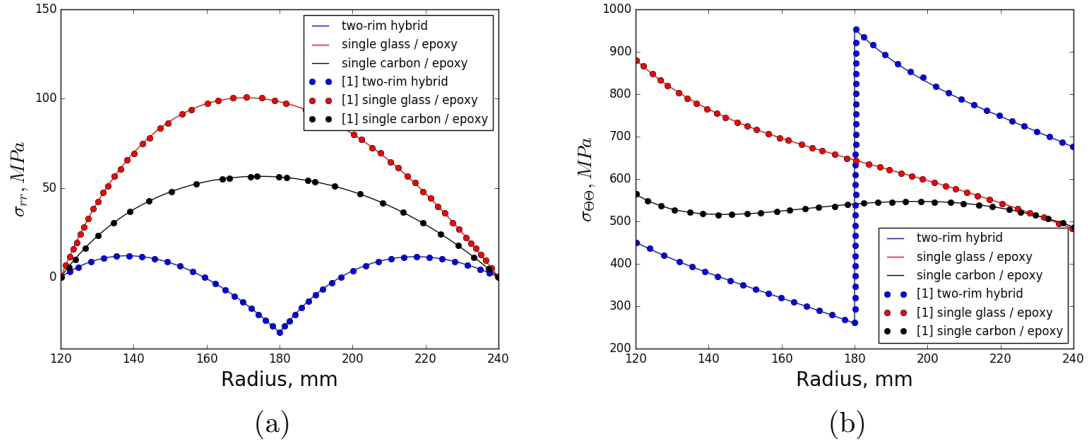


Figure 2.3: Comparison of simulated and literature results [17] for a) Radial and b) Hoop stress distributions in 2-rim and 1-rim composite flywheels

the composite materials used in the study were very similar. Figure 2.4(a) shows the feasible range of designs for the glass-epoxy and carbon-epoxy rotor used in [17]. It can be seen that the material failure constraint is the binding constraint, and the rim detachment constraint is non-binding. However, when there is a large difference in the specific stiffness of the 2 rims, the rim detachment constraint also tends to become a binding constraint. Figure 2.4(b) shows the feasible range of designs using a kevlar-epoxy and carbon-epoxy rotor, with a press-fit interference of 0.4 mm between the rims. It is clear that there is a need to check for both constraints in the latter case. The focus of this study is to select the best flywheel materials for various performance criteria. Hence, the addition of the rim detachment constraint is important, in order to evaluate all the materials and their combinations. The optimal designs for the two flywheels evaluated in this study are also depicted in Table 2.2.

## 2.3 Results and discussion

The optimization problems formulated in Section 2.1.2 were solved using a set of 18 high strength composites and metals whose material properties are in Appendix B under Tables B.1 and B.2 respectively. The 3D material properties of the composite

Table 2.1: Optimal glass/epoxy and carbon/epoxy composite rotors for varying cost ratios.

Optimization framework	$\frac{d_{\text{carbon}}}{d_{\text{glass}}}$	$E^{opt}$ , MJ	$\omega$ , rpm	$r_{out}^1$ , mm
Literature Data [17]	[11.3684 - $\infty$ )	2.205	18,661	240.0
	[2.3271 - 11.3684)	11.387	45,363	187.18
	[0.1712 - 2.3271)	12.459	48,219	166.51
	[0.0 - 0.1712)	4.672	30,137	120.0
Simulation	20	2.212	18,692	239.99
	5	11.396	45,381	187.18
	1	12.487	48,278	166.39
	0.1	4.670	30,134	120.01

Table 2.2: Optimal composite rotors with different binding constraints

Flywheel	$\delta^1$ , mm	$E^{opt}$ , MJ	$\omega$ , rpm	$r_{out}^1$ , mm	Binding Constraint
Glass-Epoxy, Carbon-Epoxy	0	12.486	48,278	166.39	Material failure
Kevlar49-Epoxy, Carbon-Epoxy	0.4	6.39	35,477	149.04	Material failure, Interface Stress

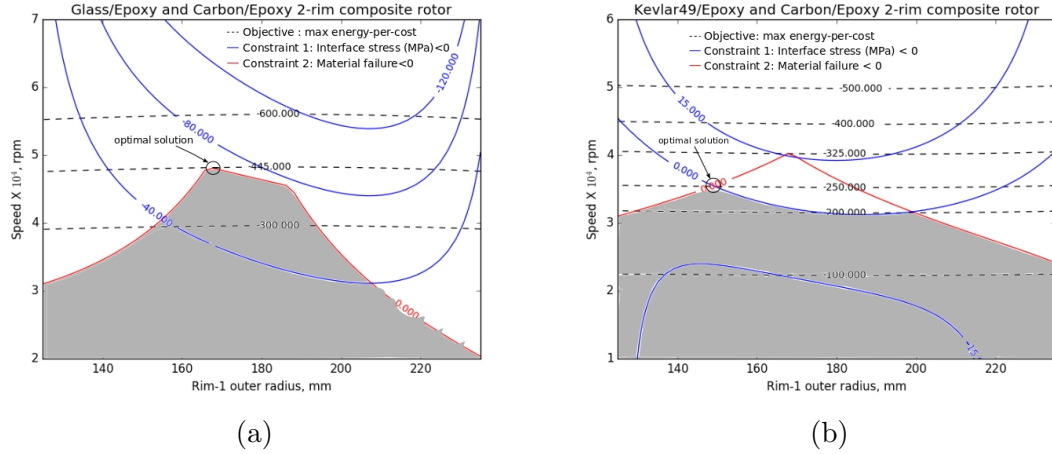


Figure 2.4: Rim detachment failure as a) non-binding constraint, and b) binding constraint.

laminates were computed using the properties of some typical laminae in Autodesk Helius Composite software [110]. The costs of the metals were based on current wholesale market prices. The costs of the composites were calculated using the volume fraction of the composite, along with market prices of the composite fiber rovings, and prices of the matrix materials such as resin and hardener. The cost of a rotor can depend on factors such as manufacturing process and complexity of design. However, this study only used the cost of the material, and did not account for manufacturing and other costs. To alleviate the impact of the uncertainty in costs on the results, all material costs were normalized before use in the optimization problem.

The performance criterion, or the objective function was maximized by varying a combination of the following design variables: rpm  $\omega$ , and relative rim thickness, which depend on  $r_{out}^1$ . The choice of optimization objective, which was used as a performance index to compare the rotor materials, was seen to affect the optimal flywheel design. A parametric study was then conducted by varying the number of press-fit rims  $n$  and the materials used in the rims  $material_j$ . The number of press-fit rims,  $n$ , was limited to a maximum of 2, and a fixed rotor height of 50 mm, inner radius of 110 mm and outer radius of 200 mm were used for the study. For multi-rim rotors, the press-fit interference was fixed at 0.4 mm.

The optimization convergence criterion was defined by the DAKOTA parameters 'function precision' and 'maximum number of black-box evaluations'. The 'function precision' parameter, which defines the resolution or accuracy of the objectives and constraints was set to  $1.e^{-10}$ , and the 'maximum number of black-box evaluations' parameter was set to 1000. The DAKOTA parameter 'variable neighborhood search' was used to escape local optima.

### **2.3.1 Optimal flywheels using maximum kinetic energy criterion**

The kinetic energy of the flywheel was maximized and the performance of the various rotor designs is presented in Table 2.3. The stress distributions in the optimal 1-rim metal, 1-rim composite, 2-rim composite and 2-rim hybrid flywheels are shown in Figure 2.5. The material failure constraint is a binding constraint in all the optimal designs. However, in some 2-rim rotor designs, the rim-detachment constraint also becomes a binding constraint. Some optimal 2 rim composite rotors where the rim-detachment is a binding constraint are Kevlar49-Epoxy/AS4-3501-6, AS4-8552/IM7-8551-7 and T300-BSL914C/T300-PR319.

The following observations can be made from the study:

1. The average kinetic energy of optimal 1-rim flywheels made from composite was around 1.5 times that of metal 1-rim flywheels. The kinetic energy was maximized by allowing the operating speed and inner radius of the rotor to vary. It was found that metal flywheels were around 3.7 times heavier than composites. However, composite flywheels were 4 times costlier and operated at 2.3 times the speed of metal flywheels
2. The kinetic energy of composite flywheels could be increased by using 2 press-fit composite rims instead of 1. The rims were chosen in increasing order of stiffness along the radius. This method allowed the kinetic energy to increase by upto 150%, accompanied by an increase in the operating speed. A similar

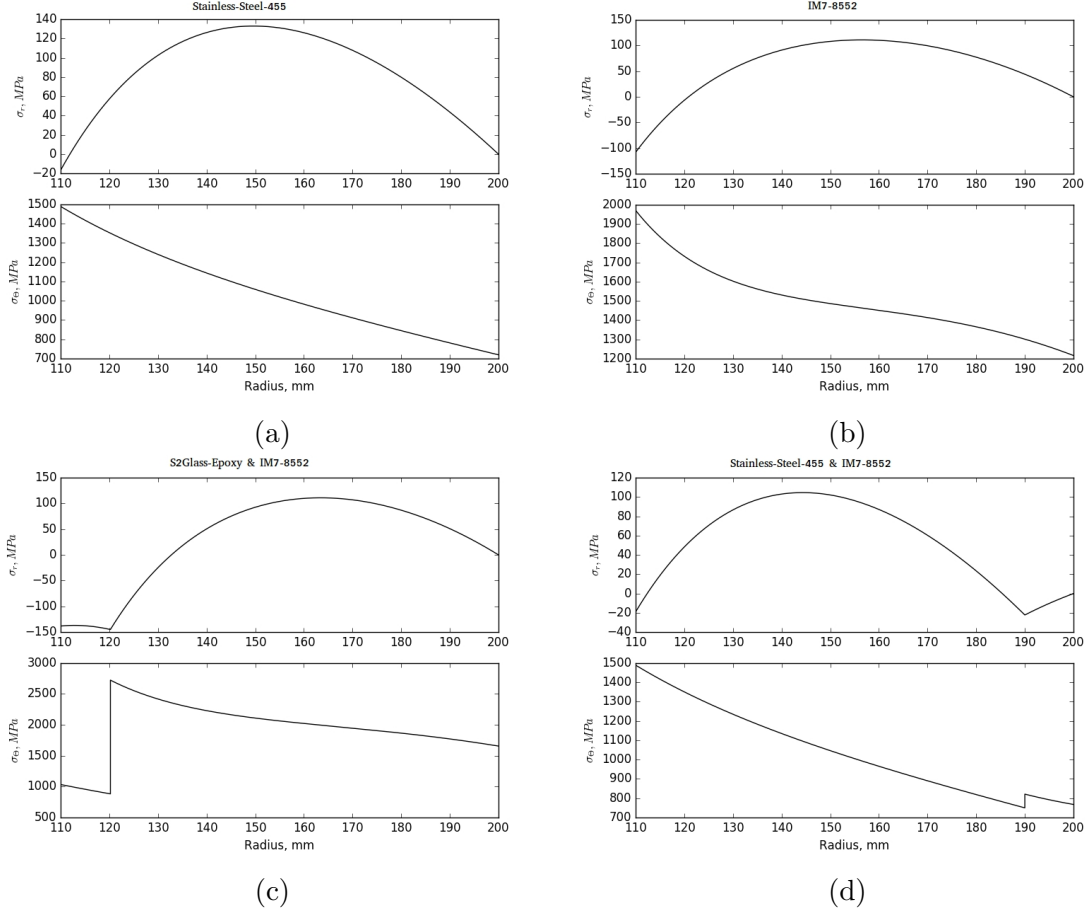


Figure 2.5: Maximum kinetic energy criterion : Radial (top) and hoop (bottom) stress distributions for optimal a) 1-rim metal, b) 1-rim composite, c) 2-rim composite, d) 2-rim hybrid rotors

study was conducted by Ha et al. [37], where Graphite/Epoxy rotors with 1 to 5 rims were optimized by varying the thickness and interference of the press-fit rims. It was found that increasing the number of rims from 1 to 2 could increase the specific energy of the rotor by 145%.

3. The use of 2 press-fit metal rims resulted in a trivial 1-rim solution.
4. The use of more than 2 composite-rim rotors could further improve the kinetic energy, but the increase was not large enough to justify the use of multiple rims, which would need a more complex manufacturing process.
5. All the above designs used a constant height rotor, corresponding to a shape

Table 2.3: Comparison of optimal flywheel designs based on kinetic energy criterion

Flywheel	Material	Kinetic energy, kJ	Speed, rpm	Rim radii, mm	Mass, kg	Relative Cost
Metal, 1-rim	Al-6061-T6	418.86	15,713	(110 - 200)	11.87	27.31
Metal, 1-rim	Al-2024	637.04	19,167	(110 - 200)	12.13	46.61
Metal, 1-rim	Carbon-Steel-1020	685.47	11,818	(110 - 200)	34.35	60.47
Metal, 1-rim	Al-7075-T6	709.56	20,156	(110 - 200)	12.22	37.53
Metal, 1-rim	Steel-4340	749.61	12,351	(110 - 200)	34.40	34.40
Metal, 1-rim	Stainless-Steel-15-7	1180.80	15,682	(110 - 200)	33.61	90.42
Metal, 1-rim	Steel-18Ni-300	1203.03	15,460	(110 - 200)	35.23	53.91
Metal, 1-rim	Stainless-Steel-440C	1947.44	20,100	(110 - 200)	33.74	42.51
Metal, 1-rim	Stainless-Steel-455	2369.82	22,087	(110 - 200)	34.00	78.21
Composite, 1-rim	T300-BSL914C	786.48	28,388	(110 - 200)	6.83	216.65
Composite, 1-rim	Kevlar49-Epoxy	885.49	31,970	(110 - 200)	6.06	164.37
Composite, 1-rim	E-Glass-Epoxy	1060.36	28,565	(110 - 200)	9.09	170.31
Composite, 1-rim	S2-Glass-Epoxy	1355.19	32,958	(110 - 200)	8.73	269.97
Composite, 1-rim	AS4-3501-6	1360.29	36,957	(110 - 200)	6.97	185.68
Composite, 1-rim	T300-PR319	1403.14	37,877	(110 - 200)	6.84	217.12
Composite, 1-rim	AS4-8552	2404.63	49,343	(110 - 200)	6.91	184.54
Composite, 1-rim	IM7-8551-7	2452.16	49,883	(110 - 200)	6.89	246.78
Composite, 1-rim	IM7-8552	3150.50	56,292	(110 - 200)	6.96	248.98
Composite, 2-rim	EGlass-Epoxy, IM7-8551-7	3154.54	56,263	(110 - 119.32 - 200)	7.06	240.92
Composite, 2-rim	EGlass-Epoxy, AS4-8552	3224.14	56,740	(110 - 120.48 - 200)	7.10	183.31
Composite, 2-rim	Kevlar49-Epoxy, T300-BSL914C	2213.79	48,459	(110 - 155.64 - 200)	6.49	193.93
Composite, 2-rim	Kevlar49-Epoxy, AS4-3501-6	2532.95	51,162	(110 - 146.72 - 200)	6.66	178.48
Composite, 2-rim	Kevlar49-Epoxy, IM7-8551-7	3716.71	61,814	(110 - 134.25 - 200)	6.72	229.28
Composite, 2-rim	S2-Glass-Epoxy, AS4-3501-6	2798.60	52,233	(110 - 133.60 - 200)	7.33	203.05
Composite, 2-rim	S2-Glass-Epoxy, IM7-8552	4072.10	63,650	(110 - 120.22 - 200)	7.11	250.75
Composite, 2-rim	AS4-8552, IM7-8551-7	3302.65	57,882	(110 - 137.42 - 200)	6.90	231.64
Composite, 2-rim	T300-BSL914C, T300-PR319	1738.68	42,169	(110 - 134.62 - 200)	6.84	217.01
Hybrid, 2-rim	Al-6061-T6, Kevlar49-Epoxy	441.64	17,006	(110 - 190 - 200)	11.06	46.47
Hybrid, 2-rim	Al-2024, IM7-8552	719.87	21,325	(110 - 190 - 200)	11.41	74.90
Hybrid, 2-rim	Steel-4340, IM7-8552	760.70	13,598	(110 - 190 - 200)	30.56	64.39
Hybrid, 2-rim	Stainless-Steel-15-7, T300-PR319	1153.48	16,937	(110 - 190 - 200)	29.87	108.13
Hybrid, 2-rim	Stainless-Steel-440C, Kevlar49-Epoxy	1804.94	21,208	(110 - 190 - 200)	29.87	59.55
Hybrid, 2-rim	Stainless-Steel-455, Kevlar49-Epoxy	2188.32	23,265	(110 - 190 - 200)	30.10	90.26
Hybrid, 2-rim	Stainless-Steel-455, IM7-8552	2274.63	23,644	(110 - 190 - 200)	30.22	102.08

factor of 0.5. Practically, metal flywheels can be fabricated with better shape factors, and thus, can store more kinetic energy than projected in these simulation results. Thus the use of rotor shape and topology as a design variable needs to be explored.

6. Burst failure is one of the main causes of concern while using metal flywheels, which fail in few, large fragments, whereas; composites fail either by delamination or due to the fibers breaking into small fragments [21]. Thus, the con-

tainment structure for composite flywheels must be designed to avoid fragment penetration, whereas, that of metal flywheels must restrict the forces or moments of the flywheel fragments from being transferred outside. To address the concern of burst safety, a hybrid metal-composite press-fit rotor was also optimized in this study. The outer composite rim had a fixed thickness of 10 mm, and was primarily for safety. The flywheel was then optimized, by allowing the rpm of the rotor to vary. It was found that the kinetic energy was nearly the same as that of 1-rim metal flywheels, with a marginal increase in the cost and operating speeds. These hybrid flywheels also provide an opportunity to optimize the shape of the inner metallic rim, which could further increase the kinetic energy and reduce the mass and the cost of the rotor.

### **2.3.2 Optimal flywheels using maximum specific energy criterion**

The specific energy of the flywheel was maximized, and a comparison of the performance of various rotor designs is presented in Figures 2.6 and 2.7. The material failure constraint is a binding constraint in all the optimal designs. However, in some 2-rim rotor designs, the rim-detachment constraint also becomes a binding constraint. Some optimal 2 rim composite rotors where the rim-detachment is a binding constraint are Kevlar49-Epoxy/AS4-3501-6, AS4-8552/IM7-8551-7 and T300-BSL914C/T300-PR319.

The following observations can be made from the study:

1. The average specific energy of optimal 1-rim composite flywheels was 5-6 times that of optimal 1-rim metal flywheels.
2. The specific energy of rotors made from isotropic metals was in the range 6-19 Wh/kg, and that of composite rotors was in the range 32-126 Wh/kg. The specific energy of composite flywheels was significantly lower than the theoretical maximum specific energy of the materials previously reported in literature. For

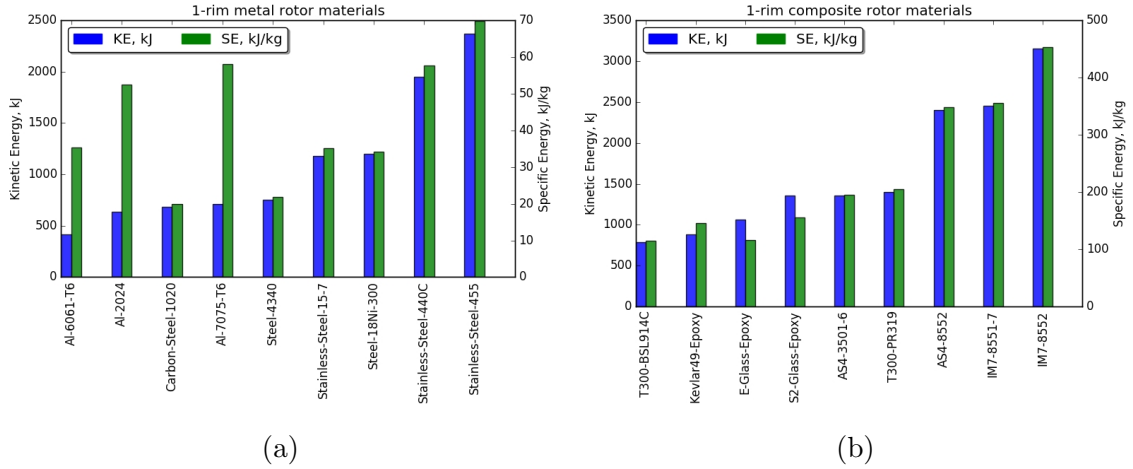


Figure 2.6: Comparison of Kinetic Energy and Specific Energy of a) Metal, b) Composite rotor materials

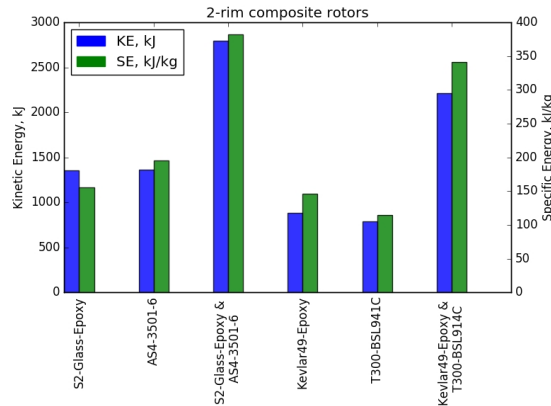


Figure 2.7: Comparison of kinetic energy and specific energy of optimal 2-rim and 1-rim rotors

example, Genta [21] reported the specific strengths of Aluminium Alloy 2024 and unidirectional Kevlar composite as 46 and 240 Wh/kg respectively. Assuming a shape factor of 0.303 corresponding to an annular constant thickness disc, the flywheels made from these materials would have theoretical specific energies of 13.938 and 72.72 Wh/kg respectively. The corresponding optimal flywheels using these materials resulted in specific energies of 14.58 and 37.26 Wh/kg. This justified the need for an optimization formulation and a rotor model that captures the physical and material failure constraints on the rotor.

- The specific energy of composite rotors could be improved by upto 150 % over 1-rim rotors, by using multiple press-fit rims.

### 2.3.3 Optimal flywheels using maximum energy per cost criterion

The energy-per-cost of the flywheel was maximized and a comparison of the performance of various rotor designs is presented in Figures 2.8 and 2.9. The material failure constraint is a binding constraint in all the optimal designs. However, in some 2-rim rotor designs, the rim-detachment constraint also becomes a binding constraint. Some optimal 2 rim composite rotors where the rim-detachment is a binding constraint are Kevlar49-Epoxy/AS4-3501-6, AS4-8552/IM7-8551-7 and T300-BSL914C/T300-PR319.

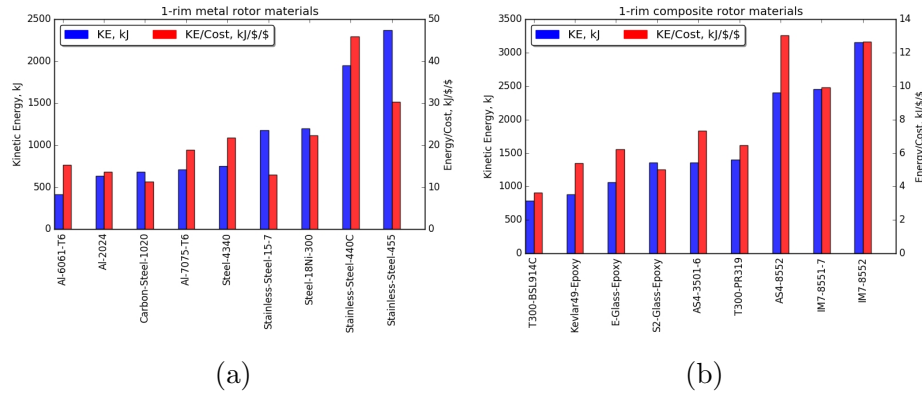


Figure 2.8: Comparison of Kinetic Energy and Specific Energy of a) Metal, b) Composite rotor materials

The following observations can be made from this study:

- The average energy-per-cost of optimal 1-rim metal flywheels was 2.7 times that of optimal 1-rim composite flywheels.
- The use of 2 press-fit composite rims increased the energy-per-cost of the composite rotor, but not enough to be competitive with high strength 1-rim metal rotors of the same dimensions.

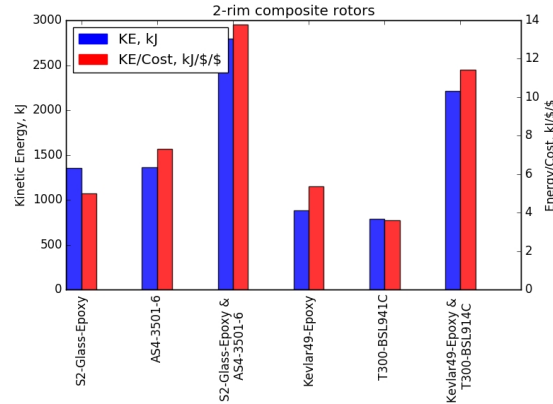


Figure 2.9: Comparison of kinetic energy and energy per cost of optimal 2-rim and 1-rim rotors

## 2.4 Summary

This study optimized 1-rim and 2-rim flywheel rotors made of various metal and composite materials to determine the optimal rotor material. It was found that the choice of optimal material depended on the performance criterion being used. Composite rotors performed better in terms of specific energy, whereas metal rotors had a better energy per cost. The total kinetic energy of both composite and metal rotors of a constant thickness were comparable. It was also shown that the specific energy of the composite rotors was significantly lower than the theoretical specific energy of the rotor materials, which only used uniaxial material failure considerations. Thus, the significance of multiaxial material failure and other physical constraints was established. The optimization model allowed us to apply constraints on the radial displacement, as well as direction-dependent failure modes, which limited the practically achievable specific energy of orthotropic materials such as composites used to construct flywheel rotors.

The means of improving the performance of the flywheels were studied, and it was shown that press-fitted multi-rim composite rotors with specific material sequences could outperform single rim composite and metal flywheels, in terms of total energy or specific energy. However, when energy-per-cost was used as the performance

criterion, 2-rim rotors offered no significant advantage over 1-rim rotors. Further improvements in the performance of metal flywheels can be achieved by optimizing the stress distributions, using variations in the shape or topology of the rotor; however, this analysis would need a 2D or 3D numerical rotor model.

# Chapter 3

## Shape optimization of grid scale FESS<sup>†</sup>

### Preface

This chapter first analyzes two commercially manufactured FESS rotors with distinct energy storage characteristics, which are then used as initial designs to perform flywheel shape optimization studies. A shape optimization framework, along with a 2D axisymmetric linear elastic numerical model of the flywheel is used to analyze the performance of several rotor designs. Results show that when rotor shape, size and speed are designed simultaneously, substantial gains in energy storage with the same amount of material can be achieved, i.e., 21 to 46%. Further, a low speed design is achieved, thereby limiting standby losses. While a few rotor shape optimization studies used local optimization methods [35, 67], most other needed to use global methods due to the complex nature of the optimization domain [70, 71]. A two-step sequential hybrid optimization strategy, which combines a genetic algorithm with a local search method, is used in this study, because it is a robust method that is seen to converge reliably in over 100 different shape optimization problems solved as part of the parametric studies conducted in this chapter. The use of the sequential hybrid strategy for rotor shape optimization is new, and is seen to offer the benefits of

---

<sup>†</sup>Parts of this chapter have been published in: Vaishnavi Kale, Mia Thomas, and Marc Secanell. *Structural and Multidisciplinary Optimization* 64.3 (2021): 1481-1499.

being more robust than a purely local method, and to allow for faster convergence to the optimum as compared to a purely global method [111], therefore resulting in an improved, open source, optimal FESS rotor design tool to be used in a variety of applications. A post-optimality analysis is also performed to determine the effect of gravity and the sensitivity of the optimal designs to manufacturing tolerances, speed variations and mesh refinement levels.

## 3.1 Methodology

### 3.1.1 Flywheel numerical model

A steady-state balance of linear momentum equation (3.1) was used to predict the stress-state of the rotor, which was assumed to rotate at a fixed operating speed,

$$\nabla \cdot \underline{\underline{\sigma}} + \mathbf{f} = 0 , \quad (3.1)$$

where  $\underline{\underline{\sigma}}$  is the second-order stress tensor and  $\mathbf{f}$  is the vector of body forces. Hooke's law (3.2) was used to capture the stress-strain relationship,

$$\underline{\underline{\sigma}} = \underline{\underline{C}} \underline{\underline{\varepsilon}} , \quad (3.2)$$

where  $\underline{\underline{C}}$  and  $\underline{\underline{\varepsilon}}$  are the fourth-order stiffness tensor and the second-order strain tensor respectively. A constitutive law for linear isotropic materials (3.3) was used to determine the components of the stiffness tensor, since low-speed isotropic metal rotors are being used in this study, i.e.,

$$\underline{\underline{C}} = \lambda \underline{\underline{I}} \otimes \underline{\underline{I}} + 2\mu \underline{\underline{I}} , \quad (3.3)$$

where  $\lambda$  and  $\mu$  are Lamé's first and second parameter respectively, and can be obtained from the material properties using (3.4),

$$\begin{aligned} \lambda &= \frac{E\nu}{(1+\nu)(1-2\nu)} , \\ \mu &= \frac{E}{2(1-\nu)} , \end{aligned} \quad (3.4)$$

where  $E$ ,  $\nu$  are the Young's modulus and Poisson's ratio, respectively. The strain-displacement relation, assuming small deformations, can be expressed as (3.5),

$$\underline{\underline{\varepsilon}} = \frac{1}{2} \left( \nabla \mathbf{u} + (\nabla \mathbf{u})^T \right) \quad (3.5)$$

where  $\mathbf{u}$  is the vector of displacements.

The weak form used to solve the numerical rotor model can be obtained by multiplying Equation (3.1) by a displacement test function,  $\bar{\mathbf{v}}$ , integrating over the domain  $\Omega$ , and using Green's formula to simplify the weak form. The weak form of the governing equation was thus reduced to

$$\int_{\Omega} (\nabla \bar{\mathbf{v}}) : \underline{\underline{\sigma}} \, d\Omega = \int_{\Omega} \bar{\mathbf{v}} \cdot \mathbf{f} \, d\Omega + \int_{\Gamma} \bar{\mathbf{v}} \cdot (\underline{\underline{\sigma}} \mathbf{n}) \, d\Gamma \quad (3.6)$$

Interpreting the test function  $\bar{\mathbf{v}}$  as a virtual displacement vector, the virtual strain form of the test function is defined as  $\bar{\underline{\underline{\varepsilon}}} = \frac{1}{2} (\nabla \bar{\mathbf{v}} + \nabla \bar{\mathbf{v}}^T)$ . Then, the weak form of the 3D linear elastic rotor model described in Equation (3.6) can be written as

$$\int_{\Omega} \bar{\underline{\underline{\varepsilon}}} : \underline{\underline{\sigma}} \, d\Omega = \int_{\Omega} \bar{\mathbf{v}} \cdot \mathbf{f} \, d\Omega + \int_{\Gamma} \bar{\mathbf{v}} \cdot (\underline{\underline{\sigma}} \mathbf{n}) \, d\Gamma \quad (3.7)$$

The domain  $\Omega$  was treated as axisymmetric about the axis of rotation of the flywheel, aligned with the  $z$ -axis. Thus, the domain was reduced from 3D to 2D (only the  $r$ - $z$  plane). Under axisymmetric loading conditions, the weak form described in Equation (3.7) can be re-written as

$$\int_r \int_z \bar{\underline{\underline{\varepsilon}}}^T \underline{\underline{\sigma}} (2\pi r) \, dr \, dz = \int_r \int_z \bar{\mathbf{v}}^T \mathbf{f} (2\pi r) \, dr \, dz + \int_{\Gamma} \bar{\mathbf{v}} \cdot (\underline{\underline{\sigma}} \mathbf{n}) \, d\Gamma \quad (3.8)$$

where the inertial load due to the rotation of the flywheel was imposed as a body force  $\mathbf{f} = \rho \omega^2 r$  over the entire domain and the surfaces of the flywheel were assumed to be traction free. Also, symmetry about the  $r$ -axis was used to reduce the domain size by half, assuming that gravity loads were negligible. Thus, the boundary conditions for this FEM problem may be represented as shown in Figure 3.1 and expressed mathematically as:

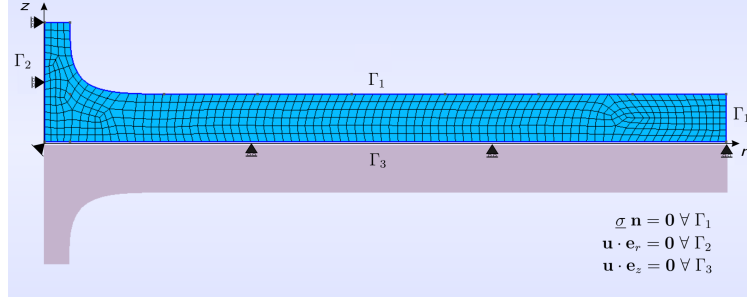


Figure 3.1: Boundary conditions for the 2D axisymmetric rotor model with symmetry about the  $r$ -axis

$$\begin{aligned}
 \underline{\sigma} \cdot \mathbf{n} &= \mathbf{0} \quad \forall \Gamma_1 \\
 \mathbf{u} \cdot \mathbf{e}_r &= 0 \quad \forall \Gamma_2 \\
 \mathbf{u} \cdot \mathbf{e}_z &= 0 \quad \forall \Gamma_3
 \end{aligned} \tag{3.9}$$

Linear Lagrange quadrilateral elements with an iso-parametric mapping were used in this study and solved using a two-point Gauss quadrature formula to determine the element-wise stiffness matrix  $k_e$  and forcing vector  $f_e$  as

$$k_e = 2\pi \sum_{i=1}^m \sum_{j=1}^n w_i w_j \underline{\overline{B}}^T \underline{C} \underline{B} r \det(J) , \tag{3.10}$$

$$f_e = 2\pi \sum_{i=1}^m \sum_{j=1}^n w_i w_j \underline{\overline{N}}^T \mathbf{f} r \det(J) , \tag{3.11}$$

where  $w_i, w_j$  are the weights corresponding to the quadrature points determined by  $i, j$ ;  $\underline{\overline{B}}, \underline{\overline{N}}$  are the solution approximations for the virtual strains and displacement, respectively,  $\det(J)$  is the determinant of the Jacobian matrix corresponding to the geometric mapping, and  $r$  is the radial distance from the axis of rotation. These equations along with the boundary conditions in (3.9) were used to assemble the global stiffness matrix  $K$  and global forcing vector  $F$ . The linear system of equations  $KU = F$  was then solved using a conjugate gradient (CG) linear solver, since the global stiffness matrix  $K$  was symmetric and positive definite. The solver was implemented in the open-source software OpenFCST [112], based on the deal.II FEM libraries [113].

### 3.1.2 Post-processing, input parameters and shape parameterization

The numerical model used in this study predicted the components of the deformation,  $\mathbf{u}$ , in the rotor. The maximum von Mises stress in the flywheel rotor was obtained *a posteriori* from the deformation solutions of the numerical model. The strain tensor components were calculated from the solution using Equation (3.5). Then, the components of the stress tensor  $\sigma$  were calculated using Equation (3.2). The local stresses and strains in the mesh elements were computed at Gauss quadrature points one order lower than the order of quadrature used for numerical integration, i.e. at element centroids instead of the nodes. This is because there are discontinuities in the stresses obtained using solution gradients at the element nodes, and the convergence of the stress solution can be improved by using optimal locations for evaluating the stresses [114]. The von Mises stresses in the rotor were computed using,

$$\sigma_{vm} = \sqrt{\frac{1}{2} [(\sigma_{rr} - \sigma_{\theta\theta})^2 + (\sigma_{\theta\theta} - \sigma_{zz})^2 + (\sigma_{zz} - \sigma_{rr})^2 + 6\sigma_{rz}^2]} \quad (3.12)$$

The optimization of flywheel rotors also requires the computation of performance indices such as the kinetic energy, specific energy, and material failure constraints. The kinetic energy of the rotor can be expressed as:

$$E = \frac{1}{2} I \omega^2 \quad (3.13)$$

where, the moment of inertia,  $I$ , can be determined using

$$I = \int_z \int_r \int_\theta \rho \|r\|^2 r \, d\theta \, dr \, dz \quad (3.14)$$

The weight of the rotor can be calculated as

$$m = \rho V , \quad (3.15)$$

where  $\rho$  is the material density and  $V$  is the volume of the rotor, which can be calculated using

$$V = \int_{z=0}^{h(r)} \int_{r=r_i}^{r_o} \int_{\theta=0}^{2\pi} 2r \, d\theta \, dr \, dz , \quad (3.16)$$

Table 3.1: Flywheel numerical model and mesh input parameters

Parameter	Value
FEM solver	Conjugate Gradient (CG)
CG tolerance	$10^{-10}$
Global mesh refinement	0.01 m
Number of B-spline points	8

where  $r_i$  and  $r_o$  are the inner and outer radii of the rotor. The input parameters used to simulate the flywheel numerical model are recorded in Table 3.1.

The open source mesh generation tool Gmsh [115] was used to generate the 2D quadrilateral mesh used for the numerical analysis. The top surface of the rotor, whose shape needs to be optimized was parameterized using a cubic B-spline function. Figure 3.2 shows the parameterized rotor geometry. The B-spline curve used to parametrize the rotor shape had one fixed control point at the coordinates  $(r_{shaft}, h_{shaft})$ , and eight variable control points which were treated as optimization design variables. The number of B-spline control points was chosen keeping in mind that the rotor radius could vary in a large range of [0.4 - 1.0] m in the parametric studies that were conducted in the study. Thus, for example, choosing too few control points resulted in a loss of detail for designs with larger radii, and choosing too many control points resulted in shape fluctuations for designs with small radii. The choice of eight control points allowed the use of the same geometry parameterization for all flywheel radii that were evaluated. The control points were spaced equally along the radius of the flywheel, and their height coordinates were changed at the optimization iterations. Due to the large physical range of the design variables, i.e., the eight B-spline control points, it was seen that the use of a fixed shaft height resulted in unusual B-spline shapes. To avoid this, the height of the shaft,  $h_{shaft}$  was made dependent on the first B-spline control point  $h_1$ . Similarly, the use of a shaft radius  $r_{shaft}$  that scaled with the flywheel radius  $r_{out}$  helped to reduce large stress concentrations

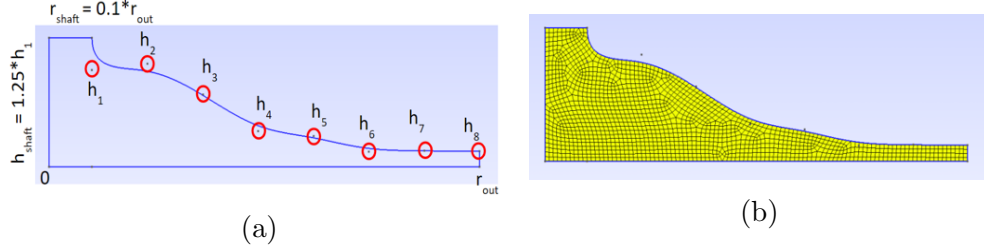


Figure 3.2: a) Parameterized geometry and b) mesh with symmetry about the  $r$ -axis for the 2D Axisymmetric rotor model

at the shaft - rim interface. Gmsh scripts were used to parameterize the geometry and python scripts were used to automatically generate the mesh with the specified rotor radius and shape at each optimization iteration. The strategy to re-mesh the entire domain at every iteration was chosen because large variations in the shape were expected in the rotor optimization process. Techniques that deform the mesh at optimization iterations without re-meshing can end up with low-quality quadrilateral mesh elements that can distort the obtained solution [116], especially when there are large variations in the shape and the size of the domain. An appropriate global mesh refinement factor was used to ensure mesh independence of the stresses predicted by the rotor model.

### 3.1.3 Optimization

In order to understand and quantify how the performance of existing rotor designs could be improved using shape optimization, the design specifications of two commercially manufactured flywheels were chosen as case studies and are shown in Table 3.2. Some of the design specifications, such as the exact dimensions and material properties, were assumed or computed using the known specifications such as energy capacity, operating speed, and rotor material, which were obtained from the manufacturer's data sheets. The following optimization formulation was used to find optimally shaped rotors with the maximum kinetic energy, having the same mass and

Table 3.2: Specifications of flywheels used as the case studies for optimization

Parameter	Design 1 (Temporal [51])	Design 2 (Amber Kinetics [50])
Energy, kWh	50.303	32.58
Mass, kg	3511.53	2280.33
Radius, m	0.434	0.510
Height, m	0.755	0.355
Material	steel	steel
$E$ , GPa	210	210
$\nu$	0.3	0.3
Density, kg/m <sup>3</sup>	7850	7850
$\sigma_y$ , MPa	755	755
Max speed, rpm	10000	8500
$\sigma_{vm}^{max}$ , MPa	657.65	719.23
Safety factor $SF^{-1}$	1.148	1.049
$u_r^{max}$ , $\mu\text{m}$	615.097	713.415

allowable stress as the two commercial designs from Table 3.2:

$$\begin{aligned}
& \underset{\mathbf{x}}{\text{maximize}} && E = \frac{1}{2} I \omega^2 \\
& \text{w.r.t} && h(r) = \{h_1, h_2, \dots, h_8\} \\
& \text{subject to} && \frac{\sigma_{VM}}{\sigma_y} \leq SF^{-1} \\
& && m \leq m_{design}
\end{aligned} \tag{3.17}$$

Initially, the operating speed  $\omega$  and rotor radius  $r_{out}$  were included as design variables along with the shape parameters  $h(r)$  for the two optimization formulations described above. However, due to the very different nature of the design variables, the problem had many local optima and did not converge reliably. A parametric study on these variables was therefore deemed suitable. Alternatively, a bi-level approach could be used to handle such an optimization problem involving both - shape related and other types of design variables [73]. The shape optimization problems described above have nonlinearities in the objectives as well as the constraints. As a result, the convergence of gradient-based methods was found to be highly dependent on the initial solution, and purely global methods such as genetic algorithms were deemed too slow to converge. A sequential optimization strategy implemented using the DAKOTA optimization toolbox [109] was chosen for this study. This optimization strategy used the `soga` genetic algorithm to converge to the vicinity of the global optimum and generate a good initial guess, followed by a local gradient based method of feasible directions, `conmin.mfd`, to converge to the exact global optimum. The sequential hybrid optimization strategy, which was used for rotor shape optimization for the first time in this study, combined the robustness of the global method in the initial search with the quick convergence of the local method in the final stage of the optimization. This ensured that the same optimization method and parameters could be used for more than 100 shape optimization problems that were solved as part of the parametric studies with respect to various FESS design parameters. The global method was seen to reliably converge to the vicinity of the global optimum when the maximum

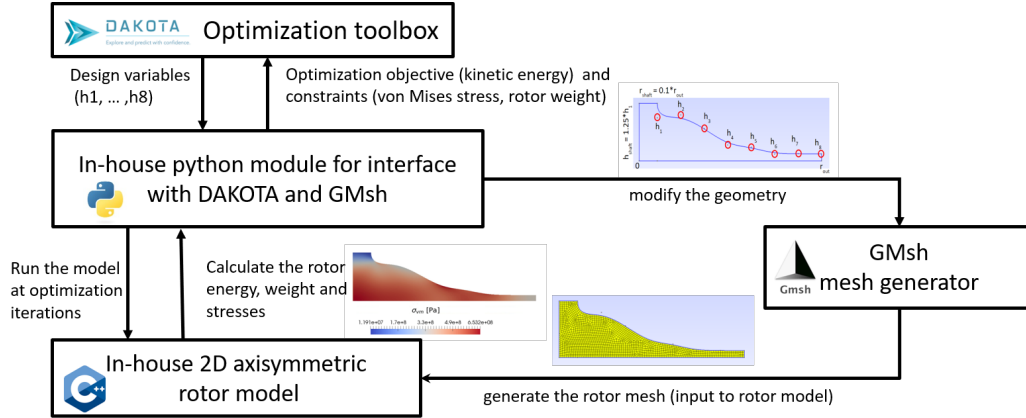


Figure 3.3: Block diagram of the shape optimization framework

difference between the average fitness function value did not exceed 10% for 5 successive generations. A maximum relative difference between objective function values in successive iterations of  $10^{-4}$  was used as the optimization convergence criterion for the local method. It was seen that up to 18% improvements in the shape optimization objective could be achieved by using the local gradient method in the second stage of the sequential optimization method, compared to only using the global method with the same convergence criterion. A corresponding 38% reduction in number of optimization iterations was achieved by using the sequential hybrid method, compared to the use of a purely global method with a stricter convergence criterion that tried to converge to the same optimum as the hybrid method. The optimization parameters used in the study are shown in Table 3.3.

A block diagram of the shape optimization framework and its integration with the mesh generator and numerical rotor model is shown in Figure 3.3. At each shape optimization iteration, the optimization algorithm generates a new guess for the shape parameters  $h_1, h_2, \dots, h_8$ . These are used to modify the parameterized rotor geometry and generate a new mesh. This new rotor mesh is used by the numerical rotor model to predict the optimization responses such as maximum stresses and kinetic energy, which are then returned to the optimizer. This process is performed iteratively until an optimal rotor shape is found.

Table 3.3: Flywheel shape optimization parameters

<b>Parameter</b>	<b>Value</b>
Opt. strategy	Hybrid sequential
Step 1 optimizer	Genetic algorithm, <code>soga</code>
fitness type	<code>merit_function</code>
convergence type	<code>average_fitness_tracker</code>
replacement type	<code>favor_feasible</code>
Crossover parameters	2-point real, crossover rate = 0.7
Mutation parameters	<code>replace_uniform</code> , mutation rate = 0.2
Convergence tolerance	$10^{-3}$
Step 2 optimizer	Method of feasible directions, <code>conmin_mfd</code>
Convergence tolerance	$10^{-4}$
Constraint tolerance	$10^{-4}$
Gradients	Numerical (central differences)
Gradient step size	$10^{-3}$

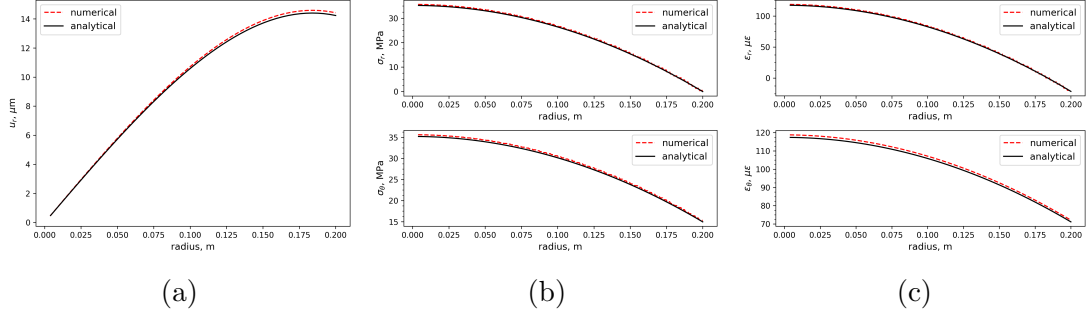


Figure 3.4: Comparison of mid-plane values of a)  $u_r$ , b) stresses  $\sigma_{rr}$ ,  $\sigma_{\theta\theta}$  and c) strains  $\epsilon_{rr}$ ,  $\epsilon_{\theta\theta}$  obtained from numerical and analytical rotor models

## 3.2 Results and discussion

### 3.2.1 Flywheel rotor model validation

The developed flywheel rotor numerical model was used to simulate a constant thickness steel disk with an integrated shaft, with outer dimensions  $r = 0.20$  m,  $h = 0.05$  m, rotating at a fixed speed of 5000 rpm, having material properties  $E = 210$  GPa,  $\nu = 0.3$ ,  $\rho = 7850$  kg/m<sup>3</sup>. The mid-plane components of the deformations, strains and stresses obtained from the numerical model were compared to those obtained from the analytical plane-stress model described in [117]. Figure 3.4, which compares the mid-plane radial deformations  $u_r$ , stresses  $\sigma_{rr}$ ,  $\sigma_{\theta\theta}$  and strains  $\epsilon_{rr}$ ,  $\epsilon_{\theta\theta}$  from the analytical and numerical models shows good agreement between the solutions obtained from the two models. The small discrepancies observed were assumed to be due to the use plane-stress assumptions in the case of the analytical model, which is only valid for thin disks ( $h \ll r$ ). Further, the axisymmetric numerical model was also determined to be mesh independent by performing mesh refinement and by using higher order solution approximations. The results of the mesh independence study can be found in Appendix C.1.

### 3.2.2 Initial design analysis

The two commercial rotors that were used as the initial designs for the shape optimization studies were simulated using the developed numerical model. The numerical

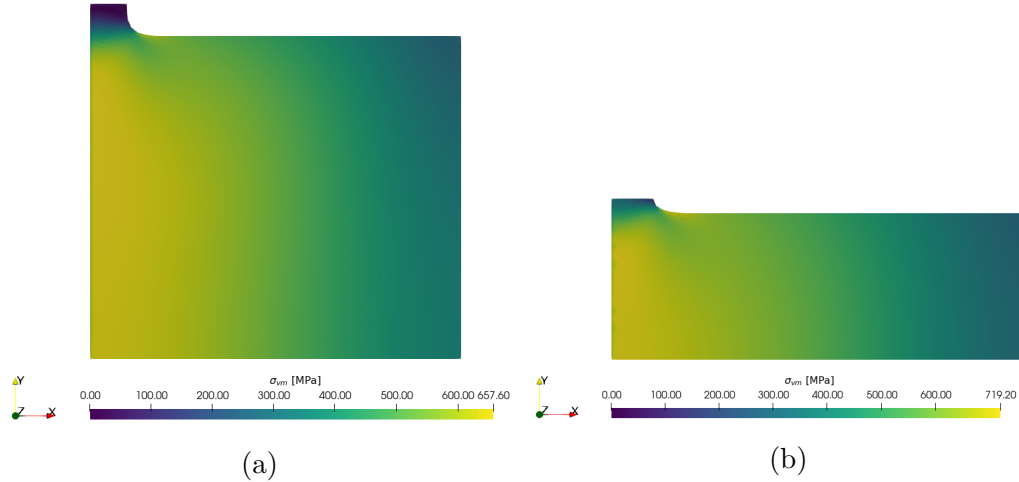


Figure 3.5: Stress distribution  $\sigma_{vm}$  in FESS rotors of type a) design-1 (Temporal steel) at 10000 rpm and b) design-2 (Amber Kinetics) at 8500 rpm

results of this simulation are shown in Figure 3.5. The two designs chosen for the case studies have different energy capacities and rotor designs. The FESS in design-1 has an energy capacity of 50 kWh and uses a tall rotor with a low aspect ratio, operating at a maximum speed of 10000 rpm. On the other hand, the FESS in design-2 can store up to 32 kWh using a rotor with a higher aspect ratio operated at a lower speed of 8500 rpm. The rotor weights and maximum von Mises stresses obtained from these designs were then used in the mass and stress constraints in the design of optimally shaped flywheels.

### 3.2.3 Convergence of shape optimization studies

The convergence histories of the hybrid sequential strategy used for rotor shape optimization of design-1 and design-2 at an operating speed of 6000 rpm and a rotor radius of 1.0 m can be seen in Figure 3.6. The plot tracks the evolution of  $\frac{f}{f_{max}}$ , which is the ratio of the maximum fitness of the population at each generation to the fitness of the optimal solution, with the optimization iterations. It also depicts the rotor shapes of the fittest candidates at some intermediate optimization iterations, where the iterations in stage-1 of the sequential strategy refer to the generations of

Table 3.4: Computational requirements for hybrid sequential shape optimization of design-1 at  $\omega = 6000$  rpm,  $r_{out} = 1.0$  m and design-2 at  $\omega = 6000$  rpm,  $r_{out} = 1.0$  m

Rotor	stage-1 $N_{iter}$	stage-1 $N_{eval}$	stage-2 $N_{iter}$ ( $N_{iter}^{grad}$ )	stage-2 $N_{eval}$	CPU time
design-1	160	17936	10 (4)	58	19 h, 48 m
design-2	166	17708	28 (8)	155	27 h

the genetic algorithm (`soga`), and those of stage-2 refer to the search steps of the gradient based method (`conmin_mfd`). The improvement offered by the second phase `conmin_mfd` gradient based method for the two examples can also be seen in the plot. Although the convergence histories in the plots indicate that the computational effort at the last few iterations of the stage-1 genetic algorithm could have been reduced by choosing a more relaxed convergence tolerance to switch from stage-1 to stage-2, the chosen criterion was found to ensure reliable convergence of all the shape optimization studies that were conducted in the parametric studies. The number of optimization iterations and function evaluations required for the two stages of the sequential optimization, as well as the total CPU time needed for the optimization procedure can be seen in Table 3.4. The number of function evaluations  $N_{eval}$  in stage-1 depend on the population size, and those in stage-2 depend on the number of design variables, because the response gradients are computed numerically using central differences.  $N_{iter}^{grad}$  is the number of iterations in stage-2 where numerical gradients were computed. Since most of the computational effort for optimization was required during the first stage of the sequential hybrid strategy which used the `soga` genetic algorithm, the computational overhead of calculating numerical gradients in the gradient-based second stage of optimization seemed justified. The number of function evaluations were reduced to an extent by making use of an evaluation cache available in the DAKOTA optimization toolbox [109] to avoid redundant computations. The optimization iterations were performed in parallel using 16 CPU cores.

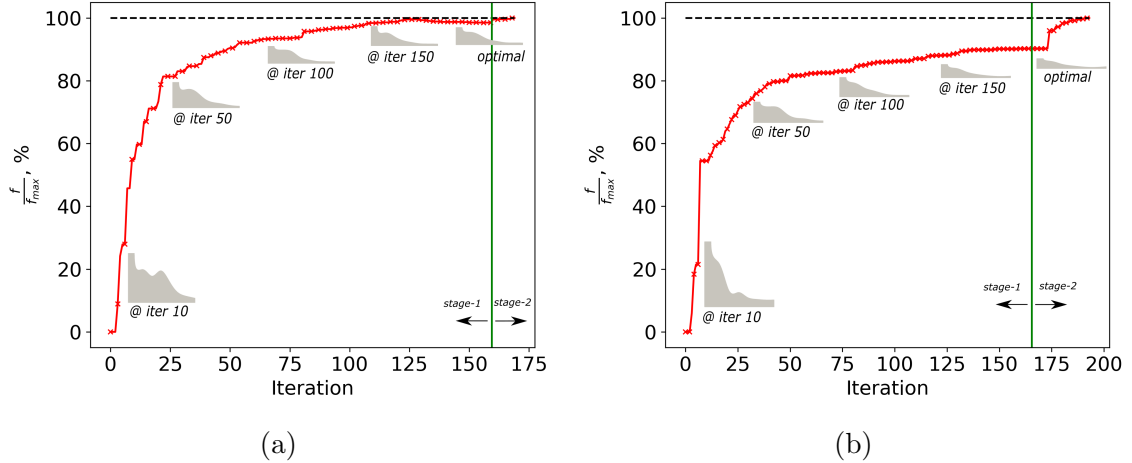


Figure 3.6: Convergence history of the hybrid sequential shape optimization algorithm for a) design-1 at  $\omega = 6000$  rpm,  $r_{out} = 1.0$  m and b) design-2 at  $\omega = 6000$  rpm,  $r_{out} = 1.0$  m

### 3.2.4 Effect of operating speed and rotor radius on the optimal rotor shape

The optimization formulation described in Equation (3.17) aimed to understand how an optimally shaped flywheel could improve the kinetic energy of the original commercial flywheel designs, and how the chosen operating speed and rotor radius specifications could influence the extent of improvement in the design. Thus, the shape of the flywheel was optimized at various combinations of operating speeds and rotor radii with the objective to maximize the energy capacity of the flywheel for a fixed mass. The results of this parametric study can be seen in Figure 3.7, where the kinetic energy of the optimally shaped rotors is plotted against the operating speed and rotor radius. The response surface shape of the two flywheel designs is quite similar, with a combination of large radii and low operating speeds achieving the highest energy storage capacity. Also, for some combinations of speed and rotor radius, especially at high speeds and with large radii, there were no feasible designs that could simultaneously adhere to the imposed mass constraint and maximum stress constraint.

The optimal shapes corresponding to various points distributed all over the re-

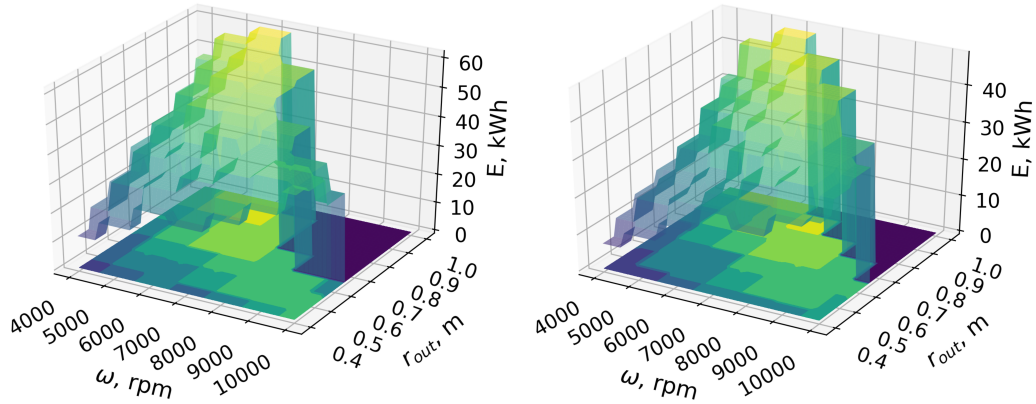


Figure 3.7: 3D contour plot of the kinetic energy obtained with the optimal shaped flywheels at various operating speeds and rotor radii, given specifications of rotors from design-1 (left), and design-2 (right)

response surface can be seen in Figure 3.8. The optimal solutions for all shape optimization studies conducted within the parametric study are available in Appendix C.2, and the corresponding optimal designs are in Appendix C.3. At low operating speeds, when the stress constraint was inactive, most of the rotor mass was distributed towards the outer rim of the flywheel. This can be seen in case of the optimal Temporal flywheel shape at an operating speed of 5000 rpm, and a rotor radius of 0.6 m. This finding was consistent with the optimal rotor shapes reported in references [67, 70], which designed optimally shaped rotors for relatively low speeds. As the operating speed increases and the stress constraint started to become active, the rotor mass was redistributed and concentrated near the central axis. This finding was also reported in the parametric studies conducted by references [34, 71]. At any operating speed, the optimal design was the one with the largest achievable radius that could minimize variations in the stress distribution. A similar trend was observed as the rotor radius was increased. As the rotor radius was increased at any fixed operating speed, the rotor material was redistributed from the outer rim to the inner rim, in agreement with the results reported by [34, 71].

Table 3.5 compares the two original rotor designs with the optimal designs obtained from the parametric study. The energy storage capacity of the original design-1

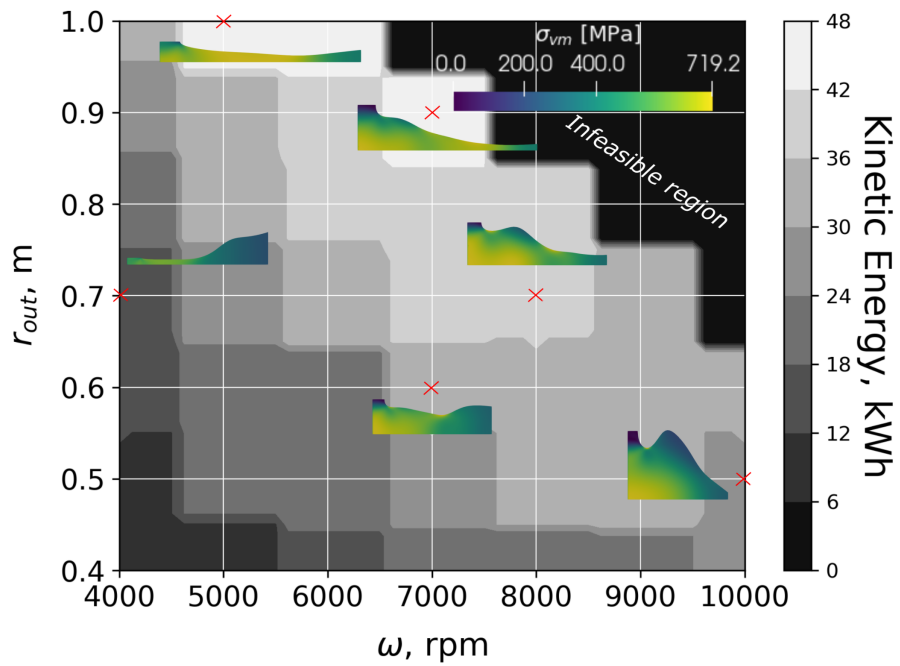
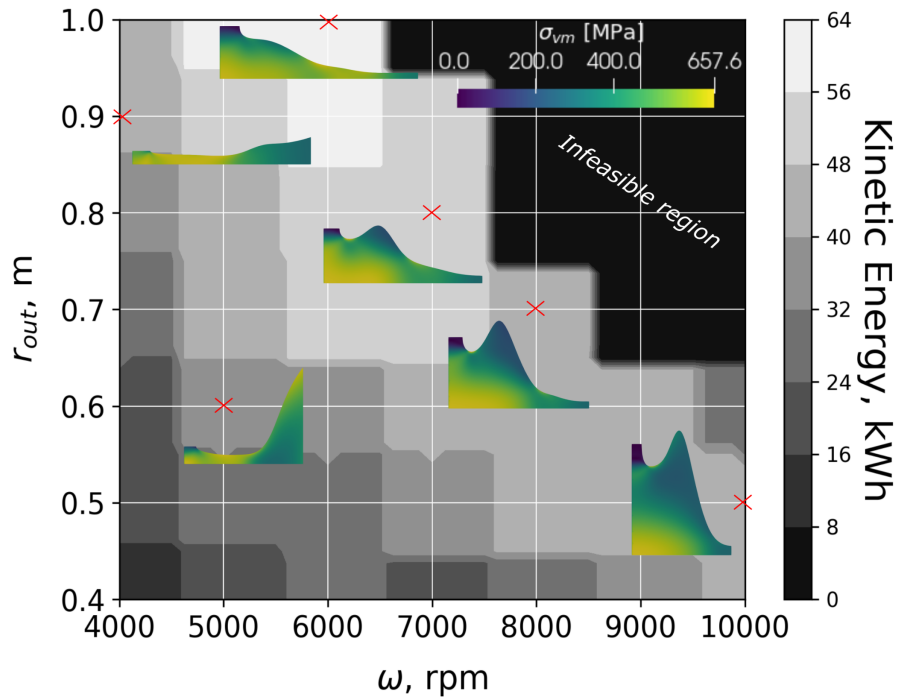


Figure 3.8: Optimal flywheel shapes (for maximum kinetic energy) obtained at various operating speeds and rotor radii, given specifications of rotors from design-1 (top) and design-2 (bottom)

(Temporal) FESS improved by 21%, from 50.3 kWh to 60.9 kWh when the rotor shape was optimized at a suitable rotor speed and radius combination ( $\omega = 6000$  rpm,  $r_{out} = 1.0$  m). Note that further improvements could be possible by including  $\omega$  and  $r_{out}$  as design variables in the optimization problem. Similarly, the energy capacity of the rotor in design-2 could be improved by 46.6% by using an optimally shaped rotor at a suitable rotor speed and radius. Thus, the choice of operating speed and rotor radius were seen to affect the optimal rotor shape as well as the energy storage characteristics. Although the aspect ratios of the two initial designs used in the study were quite different, the resulting optimal shapes obtained in the parametric studies for the two designs were quite similar. In both cases, the best optimal design was obtained using the rotors with the largest rotor radii operated at relatively low speeds. Since the kinetic energy, as seen from Equation 3.13, scales linearly with the moment of inertia and quadratically with the operating speed, the optimal rotors which were designed for lower speed rotors had a much higher contribution from the moment of inertia than the original high speed rotors.

The findings reported in Table 3.5 indicate that this parametric study based optimal design approach improved the energy capacity of the rotors in design-1 and design-2 by 21% and 46.6% respectively. To further understand how each parameter, i.e., shape parameters, operating speed and rotor radius, contributed to the improvement, a study was conducted to determine the partial design improvements offered by each of the design parameters by a) performing only shape optimization of the two original designs, and b) choosing an optimal speed or rotor radius, without any shape optimization. Table 3.6 shows the results of these studies on the two initial designs. For both designs, performing only shape optimization at the original speed and rotor radius resulted in insignificant changes in the energy capacity because the stress constraint is active thereby preventing any redistribution of material from the region near the axis to the rim as it would violate the stress constraint. Next, the operating speed was chosen as 6000 rpm (corresponding to the speed of the optimal

Table 3.5: Comparison of the two original designs with optimal designs obtained from the parametric study w.r.t  $\omega$ ,  $r_{out}$

FESS design	$E$ , kWh	$\mathbf{h}(r)$ , m	$\omega$ , rpm	$r$ , m
design-1	50.3	{0.378, 0.378, 0.378, 0.378, 0.378, 0.378, 0.378, 0.378}	10000	0.43
design-1, $\mathbf{h}^{(*)}(r)$ , $\omega^{(*)}$ , $r_{out}^{(*)}$	60.95	{0.201, 0.216, 0.153, 0.073, 0.062, 0.031, 0.035, 0.035}	6000	1.00
design-2	32.5	{0.178, 0.178, 0.178, 0.178, 0.178, 0.178, 0.178, 0.178}	8500	0.51
design-2, $\mathbf{h}^{(*)}(r)$ , $\omega^{(*)}$ , $r_{out}^{(*)}$	47.67	{0.116, 0.111, 0.068, 0.054, 0.041, 0.025, 0.028, 0.038}	6000	1.00

designs reported in Table 3.5), the rotor shape was not optimized, and the rotor radius was chosen so that it resulted in the same mass and maximum stress as the original designs. In this case, the energy capacity of design-1 reduced by 8.9% and that of design-2 increased by 2.5%. Similarly, the rotor radius was chosen as 1.0 m (to match that of the optimal designs from Table 3.5), the rotor shape was not optimized and the maximum speed was chosen so that it resulted in the same mass and stress limits and the original rotor. Here, the performance of design-1 was seen to decrease by 3.3% and that of design-2 improved by 7.9%. Thus, it was seen that when the design parameters such as shape, speed and radius were optimized or changed individually, the energy capacity changed marginally and not always for the better. On the other hand, the optimal combination of these design parameters resulted in a significant improvement in the performance. This result clearly shows the synergies that can be achieved by increasing the design space.

Since all the optimal designs obtained at various speed - radius combinations use the same rotor mass constraint, the two optimal designs also improved the specific energy of the original designs. In future, alternative optimization formulations to evaluate the performance of the FESS will be studied. One such formulation is to maximize the specific energy of the rotor without imposing constraints on the mass or the overall rotor size, which would further increase the size of the optimization search domain. This could allow the optimization problem to determine the optimal rotor aspect ratio which can maximize the specific energy of the rotor.

Table 3.6: Individual contributions of shape, operating speed and rotor radius to design improvements obtained using the parametric study based shape optimization approach

Rotor		Original design	Optimal Shape	Optimal Speed	Optimal Radius	Shape + Speed + Radius
design-1	$E$ , kWh	50.3	50.3 (0%)	45.83 (-8.9%)	48.64 (-3.3%)	60.95 (+21.1%)
	$\omega$ , rpm	10000	10000	<b>6000</b>	4265	<b>6000</b>
	$r_{out}$ , m	0.434	0.434	0.690	<b>1.0</b>	<b>1.0</b>
	Shape					
design-2	$E$ , kWh	32.5	32.47 (-0.1%)	33.31 (+2.5%)	35.08 (+7.9%)	47.67 (+46.6%)
	$\omega$ , rpm	8500	8500	<b>6000</b>	4495	<b>6000</b>
	$r_{out}$ , m	0.510	0.510	0.730	<b>1.0</b>	<b>1.0</b>
	Shape					

### 3.2.5 Effect of power losses

The choice of operating speed and optimal rotor design also influences the total standby losses, which is related to the self-discharge and overall efficiency of the FESS. These standby losses can be attributed to mechanical losses due to bearing friction and windage, and electrical losses due to eddy currents, core and copper losses. The mechanical losses are known to depend on the FESS design parameters such as operating speed, vacuum pressure and air gap between the rotor and the flywheel enclosure. An empirical model of the standby losses in the flywheel, developed by Skinner et al. [16], used curve-fitting of flywheel experimental data to characterize the standby losses. The empirical relation used to characterize the total power losses as a function of operating speed at a fixed vacuum pressure, as determined experimentally in [16] is:

$$P_{loss} = \alpha\omega^\beta \quad (3.18)$$

where  $\alpha = 2.753 \times 10^{-4}$  and  $\beta = 1.685$  are the experimentally determined fitting parameters for a constant pressure of 133 Pa inside the flywheel enclosure. Using this model of the rotor losses, the power losses for the Temporal flywheel (design-1) and the optimal design for this case were evaluated. It was found that the power losses in

the FESS reduced from 33.77 W to 14.28 W when the existing FESS rotor designed for a maximum speed of 10000 rpm was replaced with the optimal rotor designed for operation at 6000 rpm. This demonstrated the importance of considering standby losses while designing the FESS rotor.

### 3.2.6 Interdependence of rotor material, operating speed and outer radius of optimally shaped rotors

The effect of using a different rotor material, Aluminium 2024, on the optimal Temporal steel rotor design was studied. The Temporal flywheel was optimized at the three different design specifications in Table 3.7. The optimization formulation used in these studies was:

$$\begin{aligned}
 & \underset{\mathbf{x}}{\text{minimize}} && m \\
 & \text{w.r.t} && h(r) = \{h_1, h_2, \dots, h_8\} \\
 & \text{subject to} && \frac{\sigma_{VM}}{\sigma_y} \leq SF^{-1} \\
 & && E \geq E_{design}
 \end{aligned} \tag{3.19}$$

The above formulation minimized the mass of the rotor designed for a fixed energy capacity. The energy capacity  $E_{design}$  was chosen to be equal to the energy capacity of equivalent optimal steel rotors. The optimal aluminium and steel rotor shapes for the design specifications shown in Table 3.7 are shown in Figure 3.9. It was seen that the aluminium rotor had a higher specific energy than the corresponding steel rotor for lower rotor radii and vice-versa for higher rotor radii.

Rotor material selection is mainly influenced by cost and safety considerations, therefore a cost analysis was also done to understand how the cost ratio of the two rotor materials affected the energy-per-cost ratio of the flywheel. Figure 3.10 plots the energy-per-cost ratio of materials vs the cost ratio of the two materials. The plots show that aluminium rotors with smaller radii and operating at high speeds become more feasible than steel for a cost ratio  $\frac{c_{Al}}{c_{Steel}} = 1.45$ , where  $c_{Al}$ ,  $c_{Steel}$  are the cost-per-kg of the rotor materials, i.e., aluminium and steel, normalized with respect to the cost of steel. As the rotor radii were increased, steel was seen to become more

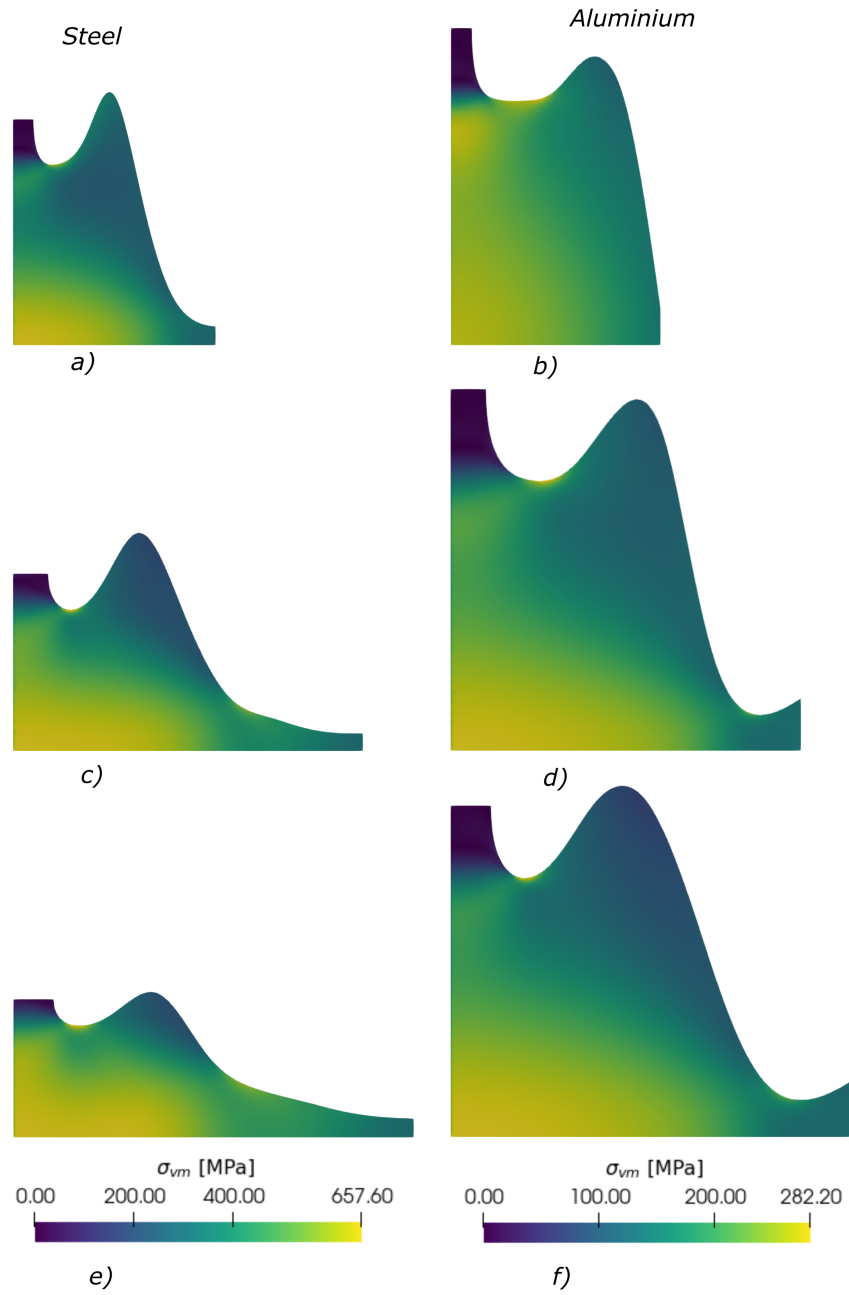


Figure 3.9: Optimal steel (left) and aluminium (right) rotors with a),b)  $\omega=10000$  rpm,  $r_{out}=0.5$  m, c),d)  $\omega=8000$  rpm,  $r_{out}=0.7$  m, and e),f)  $\omega=7000$  rpm,  $r_{out}=0.8$  m.

Table 3.7: Temporal rotor design specifications used in the study to determine the effect of rotor material on optimal shapes

Material	$E$ , kWh	$m$ , kg	$\omega$ , rpm	$r$ , m
Steel	40.32	3511	10000	0.50
Aluminium	40.33	2392	10000	0.50
Steel	45.14	3511	8000	0.70
Aluminium	45.14	3005	8000	0.70
Steel	51.63	3511	7000	0.80
Aluminium	51.63	3579	7000	0.80

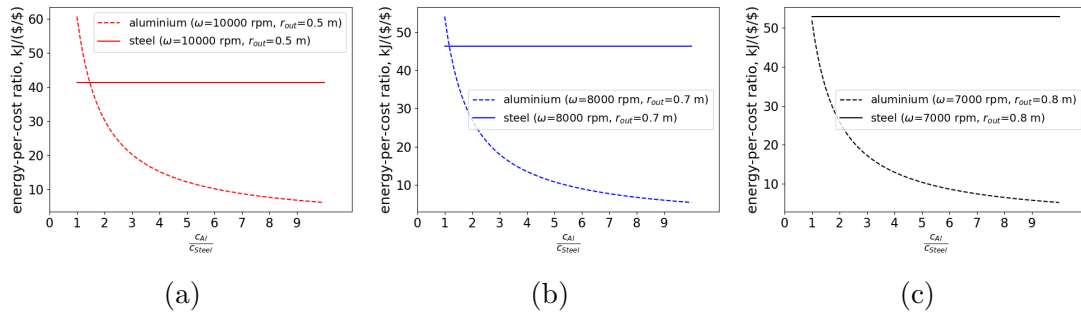


Figure 3.10: Plots of energy-per-cost ratio vs cost ratio of optimal steel and aluminium rotors with design specifications shown in Table 3.7

feasible than aluminium.

### 3.2.7 Post optimality analysis

A post optimal analysis was performed on some of the designs obtained in Section 3.2.4. The first order necessary conditions for optimality were checked by solving the KKT conditions, and were found to be satisfied for the two optimal designs reported in Table 3.5. The sensitivity of the optimal solution to the optimization convergence criterion was also checked. A hybrid optimization strategy was used in this study, with a global and a local optimization method used sequentially to find the global optimum. Thus, the sensitivity of the solution was studied with respect to the convergence criterion of the second-phase local optimization algorithm, which

used a relative change in objective function as the convergence criterion. It was found that convergence tolerances of  $10^{-2}$  or less (i.e. 1 % change in objective function) resulted in exactly the same optimal design. With a convergence tolerance of  $10^{-1}$  (i.e. 10 % change in objective function), the objective function value reduced by 0.4 %. Thus, the default tolerance of  $10^{-4}$  used in this study was found to be more than sufficient for convergence.

The sensitivity of the optimal rotor designs to rotor manufacturing tolerances was studied by perturbing the B-Spline control parameters, which were the optimization design variables. The optimal shape for design-1 reported in Table 3.5 was used in this analysis. When each of the eight B-spline control parameters were perturbed by 5 % of their optimal values, up to 1.2 % change in the kinetic energy was obtained in the perturbed design. This was accompanied by up to 1.1 % changes in the rotor mass and up to 2.8 % changes in the rotor stress  $\sigma_{vm}$ . The optimal design was found to be increasingly sensitive to the B-spline control parameters towards the outer edge of the rotor, i.e., the least sensitive parameter was  $h_1$  and the most sensitive parameter was  $h_8$ . This was expected, because the moment of inertia (and hence the kinetic energy) is higher at larger distances from the axis of rotation.

A similar sensitivity analysis was also performed with respect to the rotor design specifications ( $\omega$ ,  $r_{out}$ ) and the mesh refinement level of the numerical model used for shape optimization, which is recorded in Table 3.8. A 5 % variation in the operating speed was seen to change the objective function by 9 - 10 %. A 5 % variation in the rotor radius led to 18.5 - 21.5 % variations in the objective function value. Thus, the rotor design is quite sensitive to the maximum speed and rotor radius. On the other hand, a 5 % variation in the mesh size changed the value of the stress criterion by less than 0.2 %, so the optimal design was not too sensitive to variations in the mesh refinement level.

Table 3.8: Sensitivity of optimal solution to design parameters and mesh refinement

	$E$ , kWh	$\frac{\sigma_{VM}}{\sigma_y}$	$m$ , kg	$\omega$ , rpm	$r_{out}$ , m	$lc$ , m
Optimum	60.95	0.8707	3499	6000	1.0	0.01
0.95( $\omega$ )	55.37	0.7911	3499	<b>5700</b>	1.0	0.01
1.05( $\omega$ )	67.20	0.9599	3499	<b>6300</b>	1.0	0.01
0.95( $r_{out}$ )	49.64	0.7929	3158	6000	<b>0.95</b>	0.01
1.05( $r_{out}$ )	74.08	0.9522	3858	6000	<b>1.05</b>	0.01
0.95( $lc$ )	60.95	0.8706	3499	6000	1.0	<b>0.0095</b>
1.05( $lc$ )	60.95	0.8691	3499	6000	1.0	<b>0.0105</b>

### 3.2.7.1 Effect of gravity loads

The optimal rotor shapes obtained in the studies conducted in the previous sections used symmetry to reduce the axisymmetric numerical model domain size by half. This approach neglects the stress contributions of self weight as a result of gravity, which could be significant depending on the overall size and aspect ratio of the rotor. To understand how the introduction of gravity loads could affect the optimal designs, the optimal design for two of the rotors from Section 3.2.4 (design-1 at  $\omega=6000$  rpm,  $r_{out}=1$  m, and design-2 at  $\omega=10000$  rpm,  $r_{out}=0.5$  m) were simulated with gravity loads on the complete 2D axisymmetric rotor model. Initially, the two designs were simulated at standstill, i.e., with only gravity loads and no inertial loads, as shown in Figure 3.11. The stresses developed in the rotor due to gravity alone were well below the stresses developed during normal operation, and the highest stress concentration was seen to appear at the interface of the shaft and the rotor rim at the bottom of the flywheel, which was expected. Figure 3.12 depicts the stress distributions in the two rotors at the designed operating speed, simulated using the full mesh with gravity loads, as well as the original reduced mesh which neglects gravity loads. The maximum stresses at the design speed were seen to increase by 1.36 % and 6.73 %, respectively for the two designs evaluated in this study. Thus, depending on

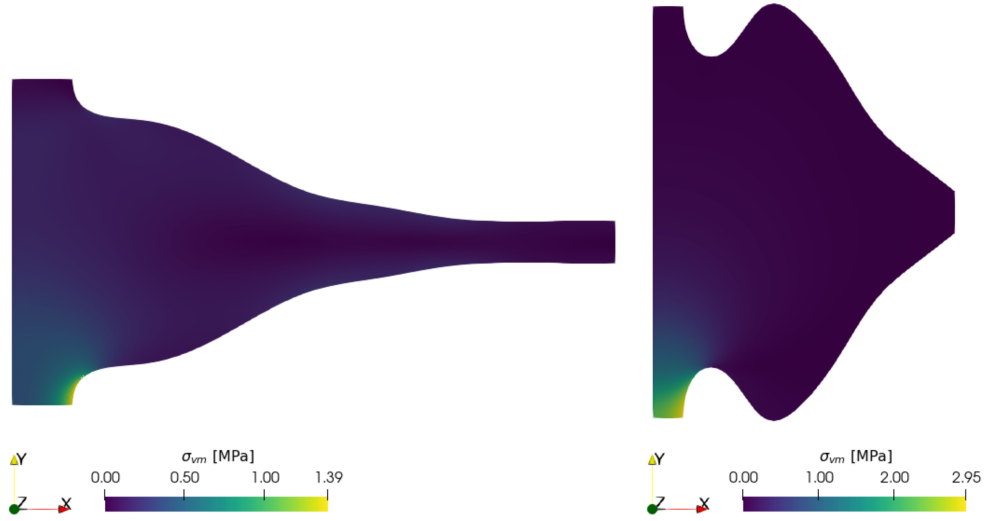


Figure 3.11: Stress distribution at standstill in optimal rotors for design-1 (left) at  $\omega=0$  rpm,  $r_{out}=1$  m and design-2 (right) at  $\omega=0$  rpm,  $r_{out}=0.5$  m (right)

the chosen FESS design specifications and aspect ratio, it might be necessary to consider the gravity load of the rotor during the design phase. Gravity loads could also be included during the optimization phase by using the entire 2D rotor mesh for simulations. Further, the use of two separate B-Spline functions to approximate the upper and lower rotor surfaces would help to determine if the optimal shape is influenced by the gravity load as well as the additional degrees of freedom due to the use of two separate shape approximations. This larger design space could be used to mitigate any high stresses caused by gravity loads, or in general, to try and achieve a more uniform stress distribution.

### 3.3 Summary

This chapter studied the relevance of choosing an ideal combination of interdependent FESS design parameters such as operating speed, rotor radius, rotor material and standby losses in the design of optimally shaped metal rotors for grid scale energy storage. An open-source rotor shape optimization framework was implemented integrating a 2D axisymmetric numerical rotor model with a shape optimization frame-

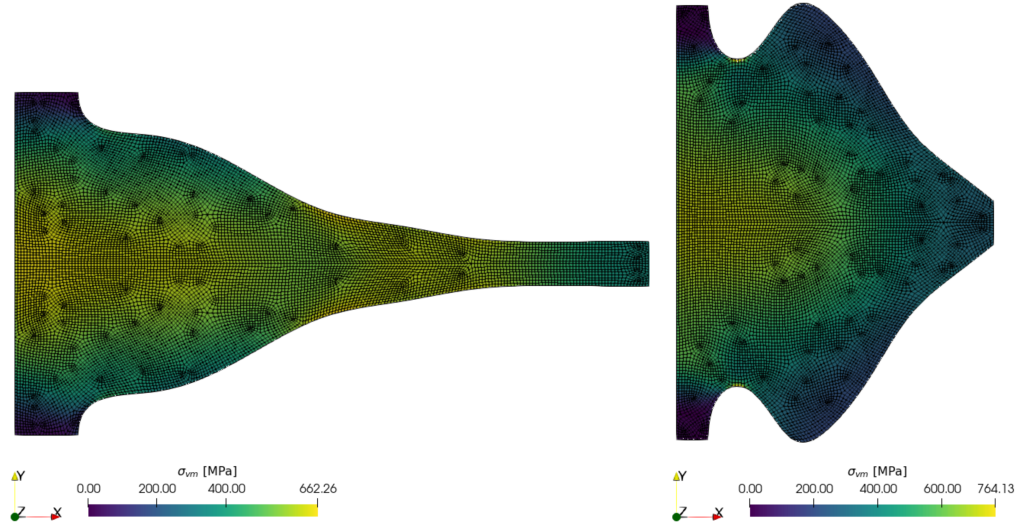


Figure 3.12: Stress distribution with gravity in optimal rotor for design-1 (left) at  $\omega=6000$  rpm,  $r_{out}=1$  m and design-2 (right) at  $\omega=10000$  rpm,  $r_{out}=0.5$  m

work. The software was used to evaluate and improve two rotor designs, which were based on two existing commercial FESS specifications. A hybrid sequential optimization strategy combining a global and a local method was chosen for the FESS rotor shape optimization studies because of the existence of multiple local optima in the shape optimization problems that were solved. The use of this hybrid sequential method for designing optimally shaped rotors was done for the first time in this study, and it provided a good tradeoff between robustness and computational cost of optimization. The global method, used in the first phase, ensured reliable convergence to the vicinity of the optimum, while the local method used in the second phase allowed the optimizer to quickly converge to the optimal designs.

The simultaneous effect of operating speed and rotor radius on the optimal rotor shape and its energy capacity was determined using a parametric study based approach. For a given mass and allowable stress, the two initial rotor designs were optimized for maximum energy capacity by optimizing the rotor shape at several speed - radius combinations. A response surface was plotted for the parametric study and it was found that flywheels with a large aspect ratio ( $r>h$ ) and relatively low

speeds had the best energy storage capacity. The energy storage capacity was seen to reduce as the designed rotor radius was reduced and the design speed was increased. This was true for both initial designs, where 21% and 46% improvements in the energy storage performance could be achieved by choosing the best combination of rotor shape, speed and radius. A study conducted to determine the normalized effects of the rotor shape, speed and radius on the improvements in rotor energy capacity determined that no significant improvements could be achieved by performing only shape optimization of the two initial designs. The effect of choosing optimal operating speed or rotor radius while keeping the shape fixed (i.e., a constant thickness disk) resulted in a reduction of 3.3 to 8.9% in the energy capacity of design-1, and small improvements of 2.5-7.9% in the energy capacity of design-2. Thus it was seen that the three design parameters were strongly correlated and only a suitable combination of these parameters could offer significant design improvements. Two optimally shaped rotor designs based on the Temporal (design-1) specifications - one operating at a low speed with a flat disc profile, and another high speed tall rotor were used to study the effect of the FESS design specifications on the standby power losses due to self discharge. It was seen that the low speed rotor with a large radius had a lower self discharge, which could be an important factor to be considered during the FESS design stage.

The effect of using a different rotor material on the optimal rotor designs was investigated for a few different combinations of rotor radii and operating speeds. It was seen that, for the same energy capacity, optimally shaped aluminium rotors had a higher specific energy content than corresponding steel rotors at lower rotor radii and high speeds, and vice-versa for higher rotor radii and low speeds. A cost analysis was also done to understand how the cost ratio of the two rotor materials being considered for the design could affect the choice of material. It was found that aluminium rotors with smaller radii and operating at high speeds become more feasible than steel for a cost ratio  $\frac{C_{Al}}{C_{Steel}} = 1.45$ . As the rotor radii were increased, steel was seen to become

more feasible than aluminium.

The sensitivity of the design to manufacturing tolerances, design specifications ( $\omega$ ,  $r_{out}$ ), mesh refinement levels in the numerical model and gravity loads was assessed. While the sensitivity of the optimal designs to the mesh refinement level was found to be low, the design was sensitive to manufacturing tolerances arising from small changes in the rotor radius or the B-spline control parameters that determined the thickness of the rotor at the outer rim. Since the numerical model of the rotor used symmetry to reduce the domain size, the effect of gravity loading was not accounted for in the parametric studies. Thus, the sensitivity of the optimal design to gravity loads was also studied, and was found to be dependent on the chosen rotor speed, radius and optimal shape.

# Chapter 4

## Topology optimization of grid-scale FESS<sup>†</sup>

### Preface

In this chapter, a novel stress-constrained flywheel topology optimization formulation based on specific energy maximization is proposed. The use of the specific energy as the main objective eliminates the need for a volume fraction constraint and accounts for material costs. The new specific energy formulation is compared with kinetic energy maximized designs at various volume fractions and is found to select the volume fraction that results in the best improvement in the specific energy capacity of the rotor. A P-norm aggregated stress constraint is used in this formulation to ensure a physically viable design without any detachment of the rotor rim from the shaft, while also preventing material failure. The optimization framework is used to study the influence of design specifications such as the operating speed, maximum stress, rotational symmetry, and choice of material on the optimal topology and energy capacity. The effects of charge-discharge rates or acceleration loads on the shear stresses in the optimal topology are also investigated, to determine the ramp times that are achievable with the optimized designs.

---

<sup>†</sup>Parts of this chapter have been submitted for publication in: Vaishnavi Kale, Niels Aage, and Marc Secanell. *Journal of Energy Storage*

## 4.1 Methodology

This chapter uses two different formulations to design optimal energy storage rotors. In the first approach, the kinetic energy of the flywheel rotor is maximized subject to a volume fraction constraint and a P-norm aggregated von Mises stress constraint. The optimization problem is formulated as:

$$\begin{aligned}
 \max E_{\text{kin}}(\hat{\boldsymbol{\rho}}) &= \frac{1}{2}I(\hat{\boldsymbol{\rho}})\omega^2 \\
 \text{w.r.t } \hat{\boldsymbol{\rho}} &= \{\hat{\rho}_1, \hat{\rho}_2, \dots, \hat{\rho}_N\} \\
 \text{s.t. } KU &= F \\
 f(\hat{\boldsymbol{\rho}}) &: \frac{V(\hat{\boldsymbol{\rho}})/V_0}{\alpha} - 1 \leq 0 \\
 g(\hat{\boldsymbol{\rho}}, \mathbf{u}) &: \frac{\tilde{\sigma}_{pm}}{\sigma_y} - 1 \leq 0 \\
 0.0 &\leq \hat{\rho}_e \leq 1.0
 \end{aligned} \tag{4.1}$$

where  $E(\hat{\boldsymbol{\rho}})$  is the kinetic energy of the rotor,  $f(\hat{\boldsymbol{\rho}})$  is the total volume fraction constraint, and  $g(\hat{\boldsymbol{\rho}}, \mathbf{u})$  is the P-norm aggregated von Mises stress constraint. The volume fraction constraint aims to remove material from the initial domain, and the stress constraint prevents material failure. Here  $\hat{\boldsymbol{\rho}} = \{\hat{\rho}_1, \hat{\rho}_2, \dots, \hat{\rho}_N\}$  are the filtered and projected normalized design densities which are used to solve the numerical model.

The second approach tries to remove the dependence of the optimal design on a predetermined volume fraction. Here, the specific energy  $e_{\text{kin}}$  of the rotor is maximized subject to a P-norm aggregated von Mises stress constraint to prevent material failure, which is formulated as shown below:

$$\begin{aligned}
 \max e_{\text{kin}}(\hat{\boldsymbol{\rho}}) &= \frac{\frac{1}{2}I(\hat{\boldsymbol{\rho}})\omega^2}{m(\hat{\boldsymbol{\rho}})} \\
 \text{w.r.t } \hat{\boldsymbol{\rho}} &= \{\hat{\rho}_1, \hat{\rho}_2, \dots, \hat{\rho}_N\} \\
 \text{s.t. } KU &= F \\
 g(\hat{\boldsymbol{\rho}}, \mathbf{u}) &: \frac{\tilde{\sigma}_{pm}}{\sigma_y} - 1 \leq 0 \\
 0.0 &\leq \hat{\rho}_e \leq 1.0
 \end{aligned} \tag{4.2}$$

The main components of the topology optimization framework are:

1. Numerical model to determine the deformations in the flywheel and corresponding optimization responses
2. Adjoint solver for response gradient computations
3. Filtering mechanism for length scale control and checkerboard pattern prevention
4. MMA gradient-based optimizer

The methodology used to implement these components is outlined in the following discussion.

#### **4.1.1 Flywheel numerical model**

Assuming that the flywheel rotates at a constant speed, a 2D plane stress quasi-static numerical model of the flywheel rotor is used in this study. The constitutive law for isotropic materials is used, since the study utilizes metal rotor materials. Linear elastic governing equations are used to predict the deformation and stress distribution in the flywheel rotor. The derivation of the weak form of the linear elastic numerical model used here can be found in Appendix D.1. The rotor geometry and boundary conditions are seen in Figure 4.1(a). The central shaft and the rotor are assembled by means of a press-fit assembly, which can be approximated by a Neumann-type boundary condition  $\Gamma_2$ , and the boundary  $\Gamma_1$  at the outer rim is treated as a stress-free boundary for the topology optimization phase. Rotational symmetry is used to reduce the size of the computational domain, which is approximated by the line-of-symmetry boundaries  $\Gamma_3$ . The open-source mesh generation tool GMsh [115] is used to parametrize this geometry and generate the unstructured quadrilateral mesh seen in Figure 4.1(b). The inner and outer rings are considered fixed portions of the topology, and the region between these two rims is treated as the topology optimization domain.

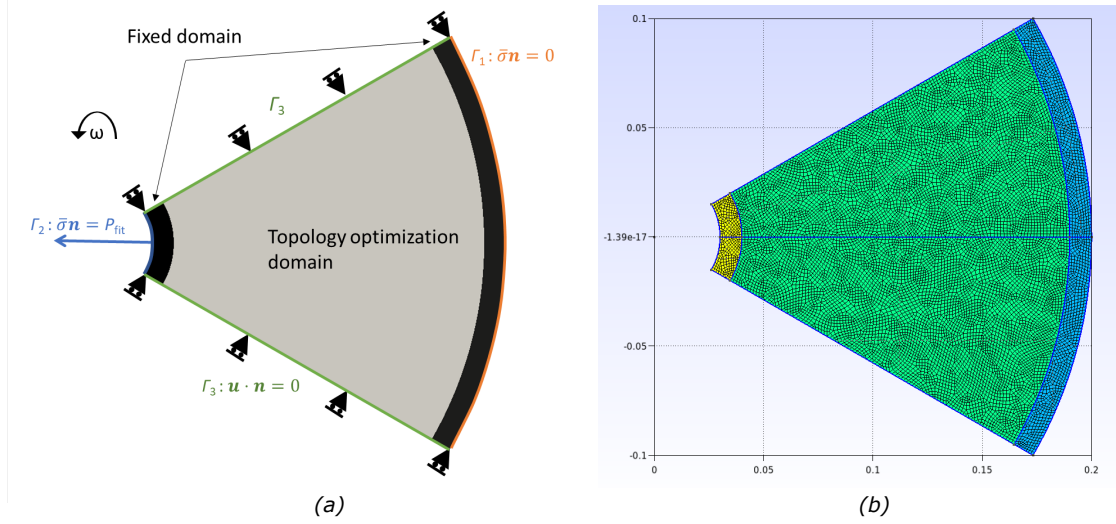


Figure 4.1: a) 2D rotor domain and boundary conditions and b) unstructured mesh using rotational symmetry of  $N=6$

Thus, the boundary conditions for this FEM problem may be represented as:

$$\begin{aligned}
 \underline{\sigma} \mathbf{n} &= 0 \quad \forall \Gamma_1 \\
 \underline{\sigma} \mathbf{n} &= P_{fit} \quad \forall \Gamma_2 \\
 \mathbf{u} \cdot \mathbf{n} &= 0 \quad \forall \Gamma_3
 \end{aligned} \tag{4.3}$$

In the density-based topology optimization approach, the mesh element densities are optimization design variables, and the material properties are interpolated using the solid isotropic material with penalization (SIMP) approach. The Young's modulus of the material for intermediate densities, i.e.,  $\hat{\rho}_e \in (0, 1)$  is interpolated as:

$$E_e = E_{\min} + \hat{\rho}_e^p (E_0 - E_{\min}) \tag{4.4}$$

where  $E_0$  is the Young's modulus of the solid material,  $E_e$  is the Young's modulus of the  $e^{th}$  mesh element with a density of  $\hat{\rho}_e$  and  $E_{\min}$  is chosen as a very small number, i.e.,  $10^{-9} E_0$ , to ensure that the system matrix is invertible even when the density of the mesh elements approaches zero ( $\hat{\rho}_e = 0$ ). This definition of the Young's modulus also affects the local stiffness matrix  $K_e$  calculated over each cell, as:

$$\mathbf{k}_{ij}^e = \int_{\Omega_e} \left( \phi_{k,k}^i \lambda_e \phi_{l,l}^j + \phi_{k,l}^i \mu_e \phi_{k,l}^j + \phi_{k,l}^i \mu_e \phi_{l,k}^j \right) d\Omega_e \tag{4.5}$$

where  $i, j$  are the indices over the number of DoFs per dimension,  $k, l$  are indices over the number of dimensions,  $\phi$  is the shape function approximation and  $\lambda_e, \mu_e$  are the modified Lamè's parameters, defined as:

$$\lambda_e = \frac{E_e \nu}{(1 + \nu)(1 - 2\nu)} \quad (4.6)$$

$$\mu_e = \frac{E_e}{2(1 + \nu)} \quad (4.7)$$

The rotational load applied on each element in the flywheel mesh is :

$$f^e = (\hat{\rho}_e^p \rho_0) \omega^2 r \underline{e}_r \quad (4.8)$$

where  $\hat{\rho}_e$  is the filtered and projected design density of each mesh element,  $\rho_0$  is the density of the solid material,  $\omega$  is the angular velocity, and  $r$  is the distance from the central axis of rotation. The inertial load is converted to the cartesian coordinate system, as  $f^e = (\hat{\rho}_e^p \rho_0) \omega^2 r \cos \theta \underline{e}_x + (\hat{\rho}_e^p \rho_0) \omega^2 r \sin \theta \underline{e}_y$ , and contributes to the local forcing vector  $\mathbf{f}_i^e$ , shown below:

$$\mathbf{f}_i^e = \int_{\Omega_e} \left( \phi_m^i f_m^e \right) d\Omega_e \quad (4.9)$$

where  $i$  is an index over the DoFs per dimension,  $m$  is an index over the number of dimensions and  $e$  is an index over mesh elements. This quasi-static centrifugal load, as well as the kinetic energy of the rotor are proportional to the square of the angular velocity  $\omega$ , whereas the mass or volume fraction of the rotor are independent of this term. As a result, any variation of the angular velocity will affect the kinetic energy and mass differently, resulting in a different specific energy. It is important to understand the influence of this factor on the optimal topology as well.

The quasi-static numerical model is also modified to include an acceleration term in the forcing vector, which mainly impacts the shear stresses  $\sigma_{r\theta}$  in the rotor. The additional acceleration load applied on each element in the flywheel mesh is

$$f_\theta^e = -(\hat{\rho}_e^p \rho_0) \dot{\omega} r \underline{e}_\theta \quad (4.10)$$

where  $\dot{\omega} = \frac{\Delta\omega}{\Delta t}$  is the angular acceleration experienced by the flywheel. The acceleration load is converted to the Cartesian coordinate system, as  $f_{\theta}^e = (\hat{\rho}_e^p \rho_0) \dot{\omega} r \sin \theta_{e_x} - (\hat{\rho}_e^p \rho_0) \dot{\omega} r \cos \theta_{e_y}$ . The local forcing vector,  $\mathbf{f}_i^e$ , for the combined centrifugal and acceleration load is:

$$\mathbf{f}_i^e = \int_{\Omega_e} \left( \phi_m^i (f_m^e + f_{\theta m}^e) \right) d\Omega_e \quad (4.11)$$

Since acceleration loads affect the circumferential direction deformations in the rotor, rotational symmetry boundary conditions, i.e.,  $(\mathbf{u} \cdot \mathbf{n} = 0)$  cannot be used with the acceleration loads, and the entire 2D rotor domain must be used when acceleration loads are applied. So, this additional acceleration load is only used in the post-optimality analysis presented in Section 4.2.3 to investigate the effects of acceleration loads on the stresses developed in the optimal rotor topology.

## 4.1.2 Post-processing and adjoint sensitivity analysis

The solution of the numerical model described previously was used to compute the optimization responses and their analytical gradients, which are described below.

### 4.1.2.1 Post-processing

#### Kinetic energy

The kinetic energy of the flywheel, which is the optimization objective for the formulation defined in equation (4.1), is calculated as:

$$E_{\text{kin}}(\hat{\rho}) = \frac{1}{2} I(\hat{\rho}) \omega^2 \quad (4.12)$$

where  $\omega$  is the angular velocity of the flywheel, and  $I(\hat{\rho})$  is its moment of inertia, which (assuming rotation about the Z-axis) is defined as:

$$I(\hat{\rho}) = \sum_{e=1}^N I_e = \sum_{e=1}^N \left( (\hat{\rho}_e^p \rho_0) \left\| x_{e,c}^2 + y_{e,c}^2 \right\| v_e \right) \quad (4.13)$$

where  $x_{e,c}$ ,  $y_{e,c}$  are the Cartesian coordinates of the centroid of the  $e^{\text{th}}$  mesh element w.r.t the central axis of rotation,  $\rho_0$  is the solid density of the material and  $v_e$  is the element volume.

### Specific energy

The specific energy maximization objective defined in equation (4.2) essentially combines two optimization objectives, i.e., maximizing the kinetic energy and minimizing the rotor mass or volume fraction. It is defined as a ratio of the rotor's total kinetic energy to its mass, and can be computed as:

$$e_{\text{kin}}(\hat{\boldsymbol{\rho}}) = \frac{E_{\text{kin}}(\hat{\boldsymbol{\rho}})}{m(\hat{\boldsymbol{\rho}})} = \frac{I(\hat{\boldsymbol{\rho}})\omega^2}{2m(\hat{\boldsymbol{\rho}})} \quad (4.14)$$

where the moment of inertia  $I$  is calculated as shown previously in equation (4.13), and the flywheel mass  $m(\hat{\boldsymbol{\rho}})$  is defined as:

$$m(\hat{\boldsymbol{\rho}}) = \sum_{e=1}^N ((\hat{\rho}_e^p \rho_0) v_e) \quad (4.15)$$

### Volume fraction constraint

The volume fraction constraint is defined as :

$$\frac{V(\hat{\boldsymbol{\rho}})}{V_0} \leq \alpha \quad (4.16)$$

where  $V(\hat{\boldsymbol{\rho}}) = \sum_{e=1}^N \hat{\rho}_e v_e$  is the volume of the topology,  $V_0 = \sum_{e=1}^N v_e$  is the volume of the entire domain,  $\alpha$  is the prescribed maximum volume fraction, and  $v_e$  is the volume of each mesh element. The above equation is rearranged into the standard inequality format used in optimization, as shown below:

$$f(\hat{\boldsymbol{\rho}}) : \frac{V(\hat{\boldsymbol{\rho}})}{\alpha V_0} - 1 \leq 0 \quad (4.17)$$

### P-norm aggregated stress constraint

The stress measure used here is developed based on the implementation adopted by De Leon et al. [118]. The von Mises stress failure criterion which can be used to predict failure in isotropic metals is:

$$\sigma_{vm}^{max} \leq \sigma_y \quad (4.18)$$

where  $\sigma_{vm}^{max}$  is the maximum von Mises stress in the domain, and  $\sigma_y$  is the maximum allowable stress. This constraint uses the `max` function, which is neither continuous nor differentiable. So a P-norm aggregated local stress constraint is used instead. The presence of intermediate densities causes very high stresses and prevents the formation of holes in the topology, causing problems with convergence, therefore the stress constraints need to be relaxed. To achieve this goal, the relaxed local stress at the centroid of each mesh element  $e$  is used. Its value is obtained using the stress relaxation scheme proposed by Le et al [86], shown below:

$$\sigma_e = \hat{\rho}_e^q \sigma_{vm}^e \quad (4.19)$$

Using this relaxed stress measure  $\sigma_e$ , the P-norm aggregated stress measure  $\sigma_{pn}$  is written as:

$$\sigma_{pn} = \left( \sum_{e=1}^N v_e \sigma_e^P \right)^{\frac{1}{P}} = \left( \sum_{e=1}^N v_e (\hat{\rho}_e^q \sigma_{vm}^e)^P \right)^{\frac{1}{P}} \quad (4.20)$$

The new stress measure  $\sigma_{pn}$  must be normalized to bring it to the same order of magnitude as  $\sigma_{vm}^{max}$ . The normalized P-norm stress measure  $\tilde{\sigma}_{pn}$  is:

$$\tilde{\sigma}_{pn} = c \sigma_{pn} \quad (4.21)$$

The normalization parameter  $c$  is updated at each iteration  $n$  using the rule:

$$c^{(n)} = \alpha^{(n)} \frac{\sigma_{vm}^{max(n-1)}}{\sigma_{pn}^{(n-1)}} + (1 - \alpha^{(n)}) c^{(n-1)} \quad (4.22)$$

where  $\alpha^{(n)}$  is an the update parameter. Thus, the normalized P-norm aggregated relaxed stress constraint in the standard form is expressed as:

$$g(\hat{\boldsymbol{\rho}}, \mathbf{u}) : \frac{\tilde{\sigma}_{pn}}{\sigma_y} - 1 \leq 0 \quad (4.23)$$

#### 4.1.2.2 Sensitivity Analysis

The gradients of the optimization responses w.r.t the design variables  $\hat{\boldsymbol{\rho}}$  need to be determined analytically. While some of the responses are dependent only on the

design variables  $\hat{\rho}$ , some are also dependent on the FEM solution variable  $\mathbf{u}$ . Such gradients are computed using an adjoint solver. The use of the adjoint solver (vs a direct solver) reduces the number of matrix inversions needed to calculate analytical gradients, provided that the number of optimization responses is less than the number of design variables. Since the topology simulations have very large number of mesh elements, using an adjoint solver can reduce computational overhead for calculating these gradients. Below, a detailed explanation is provided for the analytical gradients of the responses w.r.t the optimization design variables.

### Kinetic energy

The gradient of the kinetic energy as defined in equation (4.12) is:

$$\frac{dE_{\text{kin}}}{d\hat{\rho}_e} = \frac{\partial E_{\text{kin}}}{\partial \hat{\rho}_e} + \frac{\partial E_{\text{kin}}}{\partial \mathbf{u}} \frac{\partial \mathbf{u}}{\partial \hat{\rho}_e} \quad (4.24)$$

where the partial derivative w.r.t the design variables,  $\frac{\partial E_{\text{kin}}}{\partial \hat{\rho}}$ , can be written as:

$$\frac{\partial E_{\text{kin}}}{\partial \hat{\rho}_e} = \frac{1}{2} \frac{\partial I(\hat{\rho})}{\partial \hat{\rho}_e} \omega^2 \quad (4.25)$$

and the partial derivatives of the moment of inertia using the definition in equation (4.13) is:

$$\frac{\partial I}{\partial \hat{\rho}_e} = (p\hat{\rho}_e^{p-1}\rho_0) \left\| x_{e,c}^2 + y_{e,c}^2 \right\| v_e \quad (4.26)$$

and the partial derivative w.r.t the solution variables,  $\frac{\partial E_{\text{kin}}}{\partial \mathbf{u}}$  is zero, because of the assumption of small deformations in the linear elastic model. As a result, the second term is zero, and the response gradient is:

$$\frac{dE_{\text{kin}}}{d\hat{\rho}_e} = \frac{1}{2} \omega^2 \left( (p\hat{\rho}_e^{p-1}\rho_0) \left\| x_{e,c}^2 + y_{e,c}^2 \right\| v_e \right) \quad (4.27)$$

### Specific energy

The gradient of the specific energy (4.14) response w.r.t design densities is defined as:

$$\frac{de_{\text{kin}}}{d\hat{\rho}_e} = \frac{1}{2} \omega^2 \frac{\left( m \frac{\partial I}{\partial \hat{\rho}_e} - I \frac{\partial m}{\partial \hat{\rho}_e} \right)}{m^2} \quad (4.28)$$

where the moment of inertia  $I$  and its derivative  $\frac{\partial I}{\partial \hat{\rho}_e}$  are calculated as shown previously in equations (4.13),(4.26) respectively, and the partial derivative of flywheel mass  $m(\hat{\boldsymbol{\rho}})$  defined in equation (4.15) w.r.t the design densities can be defined as:

$$\frac{\partial m(\hat{\boldsymbol{\rho}})}{\partial \hat{\rho}_e} = (p\hat{\rho}_e^{p-1}\rho_0)v_e \quad (4.29)$$

### Volume fraction constraint

The sensitivity of the volume fraction constraint,  $f(\hat{\boldsymbol{\rho}})$ , defined in Equation (4.17) w.r.t design variables  $\hat{\boldsymbol{\rho}}$  is:

$$\frac{df(\hat{\boldsymbol{\rho}})}{d\hat{\rho}_e} = \frac{1}{\alpha V_0} \sum_{i=1}^N \delta_{ei} v_i = \frac{v_e}{\alpha V_0} \quad (4.30)$$

where  $\delta_{ei}$  is the Dirac function. The adjoint formulation is also not needed in this case because the constraint  $f(\hat{\boldsymbol{\rho}})$  only depends on the design variables  $\hat{\boldsymbol{\rho}}$ , and is independent of the solution vector  $\mathbf{u}$ .

### P-norm aggregated stress constraint

The sensitivity of the P-norm aggregated relaxed stress constraint  $g(\hat{\boldsymbol{\rho}}, \mathbf{u})$  defined in Equation (4.23) w.r.t design variables  $\hat{\rho}_e$  is:

$$\frac{dg(\hat{\boldsymbol{\rho}}, \mathbf{u})}{d\hat{\rho}_e} = \frac{\partial g}{\partial \hat{\rho}_e} + \frac{\partial g}{\partial \mathbf{u}} \frac{\partial \mathbf{u}}{\partial \hat{\rho}_e} \quad (4.31)$$

Here, the adjoint solver is used to avoid having to perform a large number of matrix inversions. The sensitivity of the stress constraint using the adjoint approach,  $\frac{dg}{d\hat{\rho}_e}$ , and the corresponding adjoint vectors,  $\lambda$ , are shown below. Detailed derivations for these expressions are in Appendix D.2.

$$\begin{aligned} \frac{dg}{d\hat{\rho}_e} &= \frac{\partial g}{\partial \hat{\rho}_e} + \lambda^T \left( \frac{\partial K}{\partial \hat{\rho}_e} \mathbf{u} - \frac{\partial F}{\partial \hat{\rho}_e} \right) \\ \lambda &= -(K^T)^{-1} \frac{\partial g}{\partial \mathbf{u}} \end{aligned} \quad (4.32)$$

where the partial derivative w.r.t the design variables  $\frac{\partial g}{\partial \hat{\rho}_e}$  is:

$$\frac{\partial g}{\partial \hat{\rho}_e} = \frac{1}{\sigma_y} c \left( \frac{1}{P} \sigma_{sum}^{\frac{1}{P}-1} \right) \left( P v_e \sigma_e^{P-1} \right) \left( q \hat{\rho}_e^{q-1} \sigma_{vm,e} \right), \quad (4.33)$$

the partial derivative of the local stiffness matrix defined in equation (4.5) w.r.t the design variables is:

$$\frac{\partial \mathbf{k}_{ij}^e}{\partial \hat{\rho}_e} = p \hat{\rho}_e^{p-1} \mathbf{k}_{ij}^0, \quad (4.34)$$

where  $k_{ij}^0$  is the original local stiffness matrix, and the partial derivative of the local rhs term defined in equation (4.9) w.r.t the design variables is:

$$\frac{\partial \mathbf{f}_i^e}{\partial \hat{\rho}_e} = p \hat{\rho}_e^{p-1} \mathbf{f}_i^0 \quad (4.35)$$

where  $f_i^0$  is the original local rhs vector. The partial derivative w.r.t the solution variable  $\frac{\partial g}{\partial \mathbf{u}_e}$  is:

$$\frac{\partial g}{\partial \mathbf{u}_e} = \frac{1}{\sigma_y} c \left( \frac{1}{P} \sigma_{sum}^{\frac{1}{P}-1} \right) \left( P v_e \sigma_e^{P-1} \right) \left( \hat{\rho}_e^q \frac{\partial \sigma_{vm,e}}{\partial \mathbf{u}_e} \right) \quad (4.36)$$

where  $\sigma_{sum}$  is defined as the term inside the brackets seen in Equation (4.20) as:

$$\sigma_{sum} = \sum_e v_e \sigma_e^P \quad (4.37)$$

and the term  $\frac{\partial \sigma_{vm,e}}{\partial \mathbf{u}_e}$  can be evaluated using the definition of the von Mises stress in terms of the deviatoric stress. The von Mises stress at the centroid of element  $e$  is defined as:

$$\sigma_{vm,e} = \sqrt{\sigma_e^{(c)} \mathbf{V} \sigma_e^{(c)}} \quad (4.38)$$

where  $\sigma_e^{(c)}$  is the vector form (Voight notation) of the stress tensor computed at the element centroid, and can be computed as usual in the post-processing step, i.e.,  $\sigma_e^{(c)} = \mathbf{C} \mathbf{B} \mathbf{u}_e$  and  $\mathbf{V}$  is an auxiliary matrix, used to transform the centroid stress  $\sigma_e^{(c)}$  to the deviatoric stress tensor. The 2D auxiliary matrix is defined as:

$$\mathbf{V} = \begin{bmatrix} 1 & -\frac{1}{2} & 0 \\ -\frac{1}{2} & 1 & 0 \\ 0 & 0 & 3 \end{bmatrix} \quad (4.39)$$

Thus, the term  $\frac{\partial \sigma_{vm,e}}{\partial \mathbf{u}_e}$  is defined as:

$$\frac{\partial \sigma_{vm,e}}{\partial \mathbf{u}_e} = \frac{1}{\sigma_{vm,e}} \mathbf{B}^T \mathbf{C} \mathbf{V} \sigma_e^{(c)} \quad (4.40)$$

### 4.1.3 Filtering

#### 4.1.3.1 Density filtering

In order to provide length scale control and to resolve numerical instabilities such as checkerboard patterns, the density filtering approach proposed by Bruns and Tortorelli [85] is commonly used in the stress constrained topology optimization literature [86]. The filtered element densities are defined as:

$$\tilde{\rho}_e = \frac{\sum_{f \in N_e} w_f v_f \rho_f}{\sum_{f \in N_e} w_f v_f} \quad (4.41)$$

where the filtered density measure  $\tilde{\rho}_e$  for mesh element  $e$  is defined by a weighted distribution of the element densities over the neighbourhood  $N_e$  of the element. For each element  $e$ , the filtering weight  $w_f$  is based on the distance from the centroid of  $e$  to the centroid of the neighboring element  $f$ , within a fixed radius  $r_e$  of the centroid of  $e$ . The filter kernel is scaled by the element volume  $v_f$  for unstructured meshes. The filter weights for a linear decay or conical distribution are defined as:

$$w_f = \left(1 - \frac{\sqrt{(x_f - x_e)^2 + (y_f - y_e)^2}}{r_e}\right) \mathcal{H}\left(1 - \frac{\sqrt{(x_f - x_e)^2 + (y_f - y_e)^2}}{r_e}\right) \quad (4.42)$$

#### 4.1.3.2 Projection filtering

The density filter can result in excessive blurring of the topology and an additional volume preserving projection or Heaviside filter (applied sequentially after the density filter) is usually applied to overcome this difficulty. The projected densities are expressed as:

$$\hat{\rho}_e = \frac{\tanh(\beta h) + \tanh(\beta(\tilde{\rho}_e - h))}{\tanh(\beta h) + \tanh(\beta(1 - h))} \quad (4.43)$$

where  $\beta$  is the slope of the projection filter, which is continuously updated,  $h$  is the filter threshold,  $\rho_e$  is the output of the density filter, and  $\hat{\rho}_e$  is the projected density. This filter and the continuous update scheme have been used previously in literature to obtain discrete optimal designs. De Leon et al. [118] used this scheme and found

that using a constant slope  $\beta$  took too long to converge, and on the other hand, if  $\beta$  was updated too quickly, the solution could diverge. Thus the update interval  $\beta_{update}$  and maximum slope  $\beta_{max}$  were determined heuristically. A study by Li and Khandelwal [99] determined that a 2x slope update in the initial iterations followed by a linear slope update after the emergence of a solid structure ensured convergence of the design. A similar continuous slope update strategy has also been used in this study. Further, the projection filter is made volume-preserving to improve the convergence of the design by preventing instabilities at slope update iterations. In order to preserve the volume of the design, the volume fractions of the topology before and after the projection filter must be equal, i.e.,  $\sum \hat{\rho}_e v_e = \sum \tilde{\rho}_e v_e$ . This is achieved by updating the filter threshold  $h$  at each optimization iteration using a 1D line search to preserve the volume fraction from the density filtered design.

#### 4.1.3.3 Filtered sensitivities

The overall sensitivities for each of the optimization responses  $\phi$  w.r.t the optimization design variables  $\boldsymbol{\rho}$  are computed using the chain rule as:

$$\frac{d\phi}{d\rho_e} = \frac{\partial\phi}{\partial\hat{\rho}_e} \frac{\partial\hat{\rho}_e}{\partial\tilde{\rho}_e} \frac{\partial\tilde{\rho}_e}{\partial\rho_e} \quad (4.44)$$

where the gradient of responses w.r.t filtered densities  $\tilde{\rho}_e$  is:

$$\frac{\partial\phi}{\partial\tilde{\rho}_e} = \frac{\partial\phi}{\partial\hat{\rho}_e} \frac{\partial\hat{\rho}_e}{\partial\tilde{\rho}_e} = \frac{\partial\phi}{\partial\hat{\rho}_e} \left( \frac{\beta \operatorname{sech}^2(\beta(\tilde{\rho}_e - h))}{\tanh(\beta h) + \tanh(\beta(1 - h))} \right) \quad (4.45)$$

and the gradient of responses w.r.t unfiltered densities  $\rho_e$  is:

$$\frac{\partial\phi}{\partial\rho_e} = \frac{\partial\phi}{\partial\tilde{\rho}_e} \frac{\partial\tilde{\rho}_e}{\partial\rho_e} = \sum_{f \in N_e} \frac{w_f v_f \left( \frac{\partial\phi}{\partial\tilde{\rho}_e} \right)}{w_f v_f} \quad (4.46)$$

#### 4.1.4 Optimization

The gradient based MMA algorithm by Svanberg [119] is used to optimize the topology. The  $l_2$ -norm of the KKT residual and the percentage of gray elements in the

topology are used as convergence criteria in this study. The percentage gray elements are calculated using the measure of discreteness [87], defined as:

$$M_{nd} = \frac{\sum_{e=1}^N 4\rho_e(1 - \rho_e)}{N} \times 100\% \quad (4.47)$$

### 4.1.5 Implementation

A block diagram of the topology optimization framework is shown in Figure 4.2, with the main components described above, as well as the output from each stage. The unstructured quadrilateral meshes used in the rotor topology optimization studies performed in this study were generated using the open-source script based meshing tool GMesh [115]. The numerical model, adjoint solver and filters were implemented in C++ in the OpenFCST toolbox [112], which uses the open-source deal.ii finite element libraries [113]. An open-source C++ MMA solver [120] based on the implementation by Aage and Lazarov [121] was adapted for use in the implemented framework.

## 4.2 Results and discussion

### 4.2.1 Flywheel rotor model validation

The results obtained from the implemented linear elastic numerical model of the flywheel with a SIMP power law modification to the equations were validated against a 1D plane-stress axisymmetric flywheel model implemented in a previous work by the authors [117], by comparing the stress distributions and deformation of the rotor in the radial direction in a uniform thickness, solid disk. The parameters used in these simulations can be found in Table 4.1. Figure 4.3 plots the radial deformation  $u_r$  as well as radial stress  $\sigma_{rr}$  and hoop stress  $\sigma_{\theta\theta}$  from the analytical and 2D numerical rotor models, which shows a good agreement between the results. This numerical model is used in the remaining topology optimization simulations.

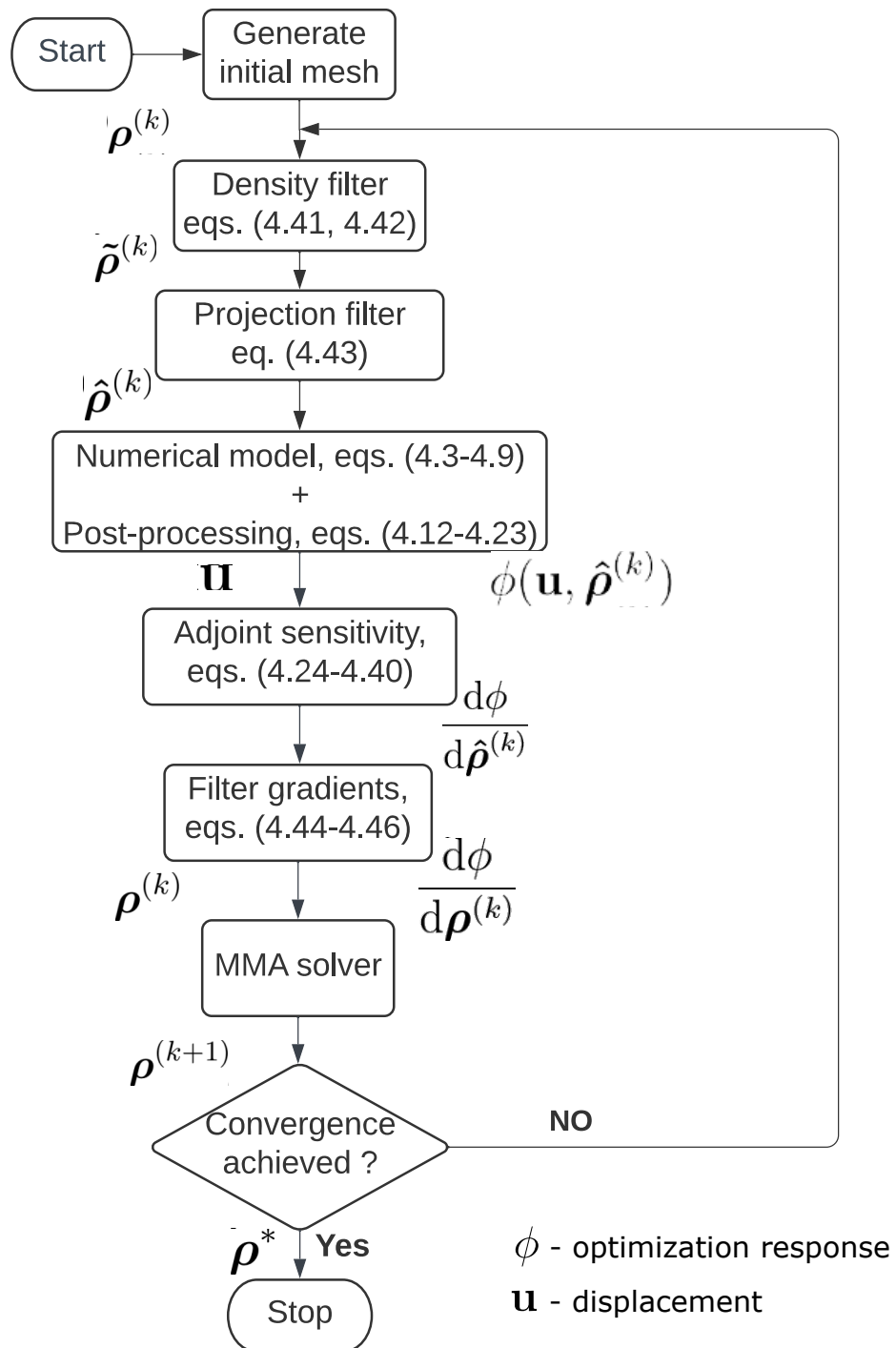


Figure 4.2: Flowchart of the rotor topology optimization framework

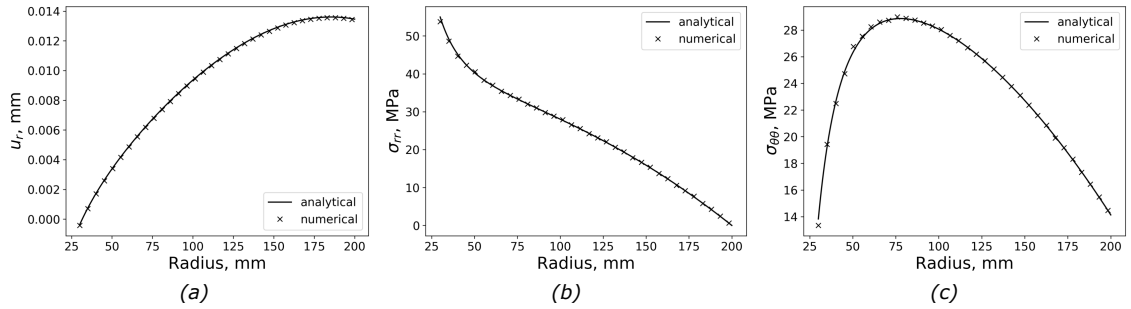


Figure 4.3: Validation of 2D plane stress numerical model of the rotor by comparison to 1D solutions of a) radial deformation  $u_r$ , b) radial stress  $\sigma_{rr}$ , and c) circumferential stress  $\sigma_{\theta\theta}$

Table 4.1: Parameters used to validate 2D plane stress numerical flywheel model using 1D solution

Parameter	Value
Inner radius ( $r_i$ ), m	0.03
Outer radius ( $r_o$ ), m	0.2
Fit pressure ( $P_{fit}$ ), MPa	55
Young's modulus ( $E$ ), GPa	210
Poisson's ratio ( $\nu$ )	0.3
Density, kg/m <sup>3</sup>	7850
Speed ( $\omega$ ), rpm	5000
FEM solver	UMFPACK

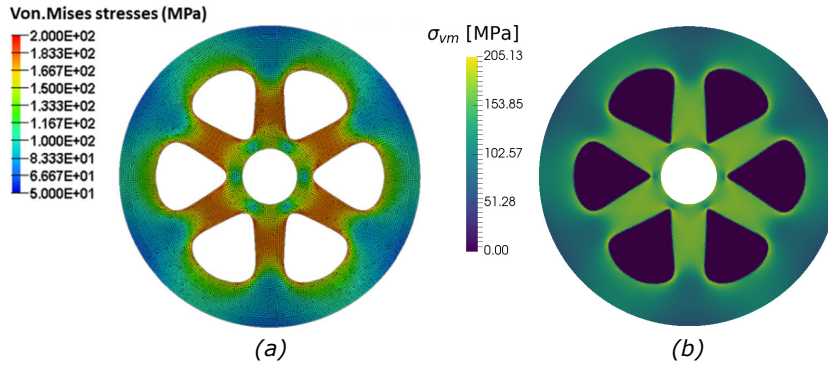


Figure 4.4: Validation of rotor topology optimization framework, a) literature design (reproduced from ref [68] with permission) and b) simulated design

## 4.2.2 Benchmarking of the topology framework

In order to ensure that the topology optimization framework was implemented correctly, the optimal rotor topology problem presented by Jiang and Wu [68] was reproduced. The kinetic energy of the rotor was maximized subject to maximum stress and volume fraction constraints. Finite difference tests were used to validate the analytical gradients of the optimization responses used in this study by comparison to numerically computed gradients, which can be found in Appendix D.3. Figure 4.4 and Table 4.2 show that there is good agreement between the literature and simulated optimal topologies, although the maximum stress is seen to be slightly higher in the simulated design. This is because the literature result was obtained after the extraction of a smooth final design from the optimal topology at post-processing. Moreover, the maximum stress developed in the uniform thickness rotor is also higher in the simulated design compared to reference [68], indicating differences in the computation of the stress measures in the reference and simulated designs. This, however, could not be verified as the reference article did not specify how the stress constraint was computed. Details about the simulation parameters used in the validation simulations, rotor mesh and convergence plots of the optimization responses can be found in Appendix D.4.

Table 4.2: Comparison of literature and simulated rotor designs for constant thickness and topology optimized designs

Study	Rotor design	$E_{\text{kin}}$ , J	$m$ , kg	$e_{\text{kin}}$ , J/kg	$\sigma_{\text{max}}$ , MPa	$\frac{\Delta e_{\text{kin}}}{e_{\text{kin}}^0}$ , % *
Literature [68]	Uniform thickness	139872	15.23	9184	146	-
	Optimal topology	113534	10.82	10493	200	+14.3
Simulated	Uniform thickness	140020	15.23	9194	162	-
	Optimal topology	111062	10.55	10527	213	+14.5

\*  $e_{\text{kin}}^0$  is the specific energy of uniform thickness rotor

### 4.2.3 Rotor topology optimization for kinetic energy maximization under volume fraction and stress constraints

Optimal rotor topologies were designed for the FESS demonstrator experimental setup in reference [108] using the optimization formulations described in Equation (4.1). The parameters used to perform this topology optimization can be found in Table 4.3. The optimal rotor was designed for an operating speed of 5,000 rpm, using an isotropic material, 4340-Steel. Rotational symmetry was used to reduce the size of the computational domain. Figure 4.5 shows the optimal topology and stress distribution in the rotor, which was optimized for maximum energy capacity, with constraints on the maximum stress (65 MPa) and volume fraction (70%). The convergence histories of the optimization objective and constraints and the gray regions in the optimization domain can be seen in Figure 4.6. The optimal design satisfies the volume and stress constraints, both of which are active. The optimal topology design as seen in Table 4.4 improves the specific energy of the uniform thickness disk flywheel by 12.79%, by removing material from the region between the shaft and the rim and forming connecting spokes. The influence of several FESS design parameters on the optimal rotor topology and its energy capacity is studied in the next sections.

The mesh independence of the optimal solutions obtained in the study was verified by using a different mesh refinement level for topology optimization. Figure 4.7 compares the optimal designs obtained with different mesh refinement levels of 1.5

Table 4.3: Topology optimization parameters for kinetic energy maximization of flywheel rotor using 2D plane stress numerical model

Parameter set	Parameter	Value
Material Properties	Young's modulus ( $E$ ), GPa	210
	Poisson's ratio ( $\nu$ )	0.3
	Solid density ( $\rho$ ), kg/m <sup>3</sup>	7850
Flywheel model	Rotor height, m	0.05
	Shaft boundary condition	Neumann (press-fit)
	Angular velocity ( $\omega$ ), rpm	5000
	Inner radius ( $r_{shaft}$ ), m	0.03
	Outer radius ( $r_{out}$ ), m	0.2
	Fixed rims thickness ( $t_{rim}$ ), m	0.01
SIMP parameters	penalty ( $p$ )	3
	$\rho_0$	0.55
	$E_{min}$ , GPa	1
MMA parameters	$a$	0.0
	$c$	1000.0
	$d$	0.0
	$\gamma^{(+)}$	1.2
	$\gamma^{(-)}$	0.7
	move limit	0.03
Density filter	filter radius $r_{filt}$ , m	0.035
	distribution	linear decay / conical
Projection filter	threshold ( $h$ )	1D line search
	initial slope ( $\beta_0$ )	1
	maximum slope ( $\beta_{max}$ )	100
	update interval	25
Mesh parameters	Rotational symmetry (N)	6
	elements	11988
Volume fraction constraint	Maximum volume fraction ( $\alpha$ ), %	70
Stress constraint aggregation	$\sigma_y$ , MPa	65
	P-norm ( $P$ )	8.0
	Stress relaxation ( $q$ )	0.5

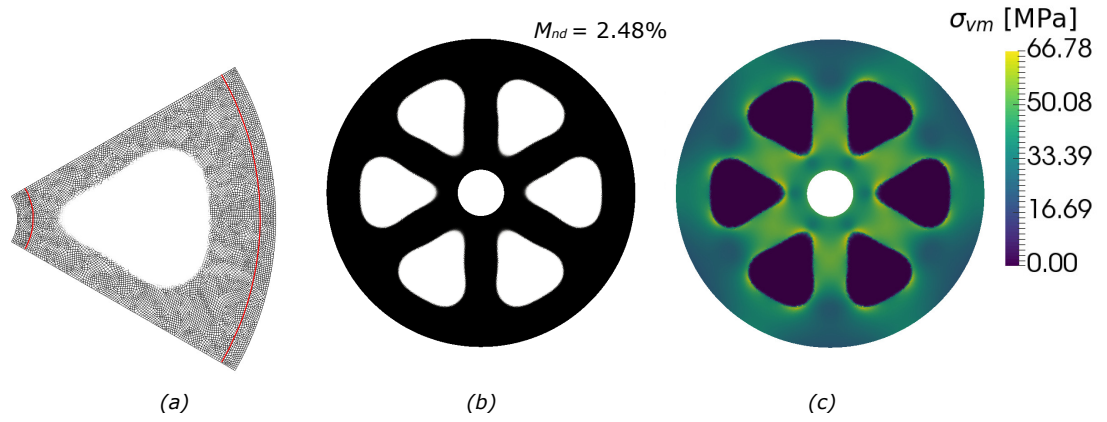


Figure 4.5: a) Optimal topology, b) full rotor topology, and c) stress distribution in the topology optimized energy storage flywheel

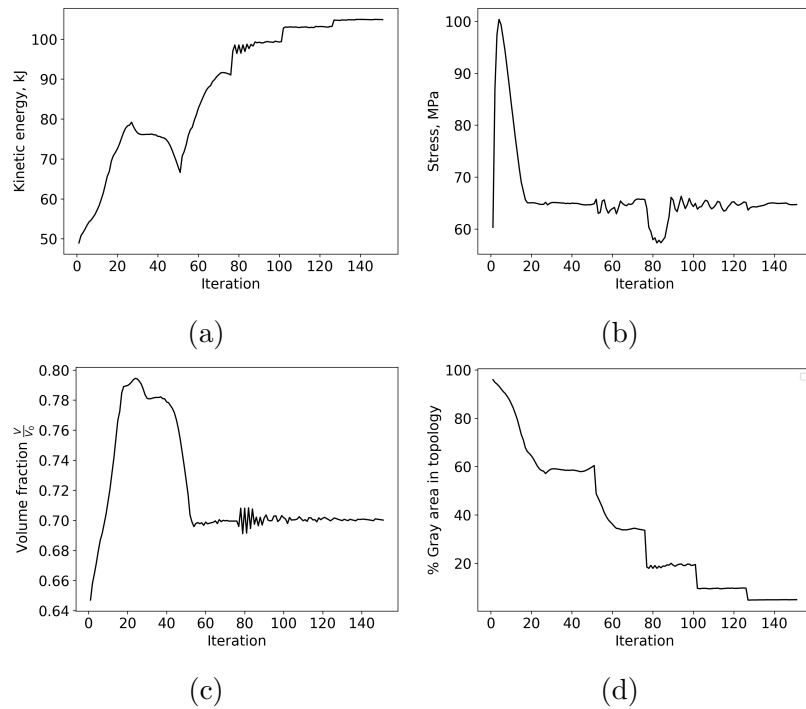


Figure 4.6: Convergence histories of a) kinetic energy, b) P-norm stress, c) volume fraction, and d) % gray region in the optimal energy storage flywheel topology

Table 4.4: Comparison of original uniform thickness disk-type and optimal topology flywheels

Rotor design	$E_{\text{kin}}, \text{ J}$	$m, \text{ kg}$	$e_{\text{kin}}, \text{ J/kg}$	$\frac{\Delta e_{\text{kin}}}{e_{\text{kin}}^0} \times 100, \text{ \%}$ *
Uniform thickness	135144.2	48.21	2803.05	0
Optimal topology	105851.4	33.48	3161.63	+12.79

\*  $e_{\text{kin}}^0$  is the specific energy of uniform thickness rotor

mm, 3.0 mm and 6.0 mm. Good agreement was observed between the solutions, and therefore it can be concluded that the optimal solution is mesh independent.

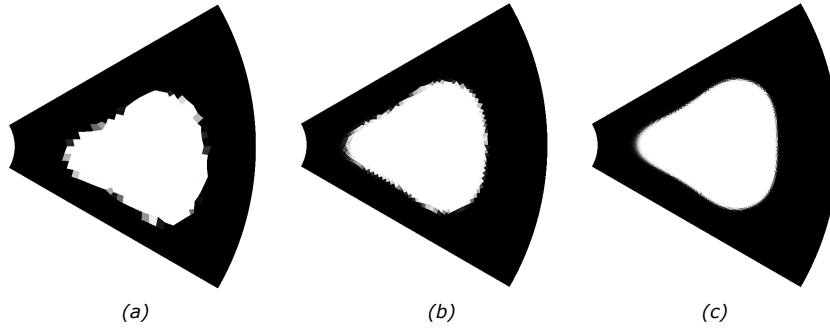


Figure 4.7: Optimal rotor topology obtained with mesh element sizes of a) 6 mm (coarse mesh), b) 3 mm (medium mesh), and b) 1.5 mm (fine mesh)

The optimal rotor design and the corresponding stress distribution at a constant operating speed was unaffected by the choice of inner radius  $r_i$ , which can be an important consideration for manufacturing of the flywheel, especially for assembly with the central shaft. This is because, the necessary fit pressure  $P_{fit}$ , which is used as a boundary condition in the numerical model used in this study, can only be achieved by the correct choice of shaft-rotor interference. As the shaft radius is increased, a larger interference is necessary to generate the same fit pressure. In this case, since the topology is unaffected by the bore radius, the designer is free to choose the value of  $r_i$  that can be manufactured using available tools. Detailed results from the parametric study to investigate the influence of bore radius on the optimal rotor design can be found in Appendix D.5.

In short duration energy storage applications, frequent charge-discharge cycles result in frequent acceleration and deceleration of the FESS, which could also affect the overall stress distribution in the flywheel. Tsai and Cheng [81] used tangential loads at eight equidistant points along the outer rim of the rotor to approximate acceleration induced loads in the quasi-static numerical model of the rotor. However, the results obtained using this approach could not be validated against the known analytical solution for acceleration induced stresses in a constant thickness rotor [40]. So a different approach was used in this study to investigate the influence of acceleration or deceleration related stresses on the FESS rotor, as described in equation (4.10). The stresses and deformations in the rotor using the additional acceleration load were in agreement with the analytical solution [40].

The stress distributions in the uniform thickness rotor and the optimal topology were investigated by considering different time intervals for the flywheel to go from its rated speed to standstill, as shown in Table 4.5. For a ramp-down time of 1 s or slower, the acceleration load did not significantly increase the overall stress in either the uniform thickness rotor or the optimized topology rotor. However, for very short ramp-down times ( $< 0.1$  s), the acceleration load accounted for 19.6% and 32.8% increases in the predicted von Mises stresses over constant speed operation in the two rotor designs. While the highest shear stresses in the uniform rotor were developed at the interface to the central shaft, the optimized topology had the highest shear stress concentrations near the spokes, as seen in Figure 4.8. Thus, the influence of acceleration loads is most likely not important in most FESS applications unless the FESS is required to have sub-second charge discharge cycles, which might only be realistic for extreme scenarios and would require a large electrical machine. The acceleration-related stresses are also influenced by the ratio of rotor radii  $\frac{r_i}{r_o}$  [40], and are known to increase significantly as this ratio decreases. Thus, a smaller bore size can negatively affect the design if high acceleration loads are expected.

Table 4.5: Comparison of stresses developed in the original uniform thickness disk-type and optimal topology flywheels under acceleration loads

Rotor design	$\dot{\omega}$ , rad/s <sup>2</sup>	$\Delta t$ , s	$\sigma_{vm}^{max}$ , MPa	$\sigma_{r\theta}$ , MPa
Uniform thickness	0	-	45.74	1.56
	523.59	1.0	45.86	3.27
	5235.9	0.1	54.70	18.66
Optimal topology	0	-	65.56	42.26
	523.59	1.0	67.24	40.90
	5235.9	0.1	87.07	56.15

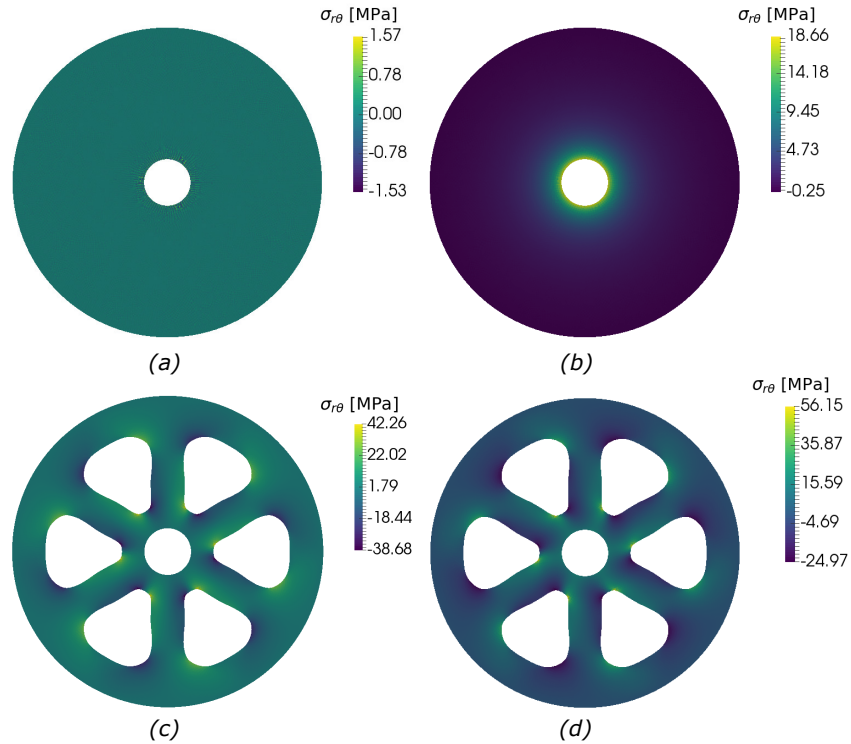


Figure 4.8: Shear stress distributions  $\sigma_{r\theta}$  in constant speed operation of uniform thickness rotors with a)  $\dot{\omega}=0$  rad/s<sup>2</sup>, b)  $\dot{\omega}=5235.9$  rad/s<sup>2</sup>, and optimal topology rotors with c)  $\dot{\omega}=0$  rad/s<sup>2</sup>, d)  $\dot{\omega}=5235.9$  rad/s<sup>2</sup>

#### 4.2.3.1 Effect of maximum stress limit

The effect of the maximum stress limit used in the global stress constraint on the optimal topology was studied by varying the upper limit on the stress constraint between 55 and 85 MPa. Figure 4.9 compares the optimal rotor topologies and corresponding stress distributions obtained at various maximum stress values. As the maximum stress limit was increased from 55 to 65 and 75 MPa, the shape of the holes or features in the rotor topology remained the same, but they moved inwards towards the central shaft. This caused the moment of inertia and consequently the kinetic energy of the rotor to increase, as more material was distributed towards the outer rim of the rotor. Since the holes moved inwards, the thickness of the spokes reduced, which resulted in a higher peak stresses. This is consistent with the finding by Jiang and Wu [68], where they determined that an increase in the maximum allowable stress resulted in material being redistributed towards the outer rim, and that the highest stresses always occurred in the ribs or spokes. However, the improvement in energy capacity peaked at a maximum stress limit of 75 MPa, and then reduced slightly for 85 MPa, as seen in Table 4.6. Thus, beyond a certain limit, an increase in the maximum stress limit did not significantly improve the specific energy of the design. This is because both the operating speed and the prescribed volume fraction were constrained or fixed, so it was not possible to achieve a rotor design with a higher specific energy by moving the holes any closer to the center. Also, as the maximum stress was increased, the optimizer could not find a physically viable design, since it was able to meet the stress criterion with a trivial solution of a detached rim without any spokes, which has the highest kinetic energy possible.

#### 4.2.3.2 Effect of maximum volume fraction

The effect of volume fraction on the optimal topology was studied by varying the upper limit on the volume fraction constraint between 60 and 80%. Figure 4.10 compares the optimal rotor topologies and corresponding stress distributions obtained

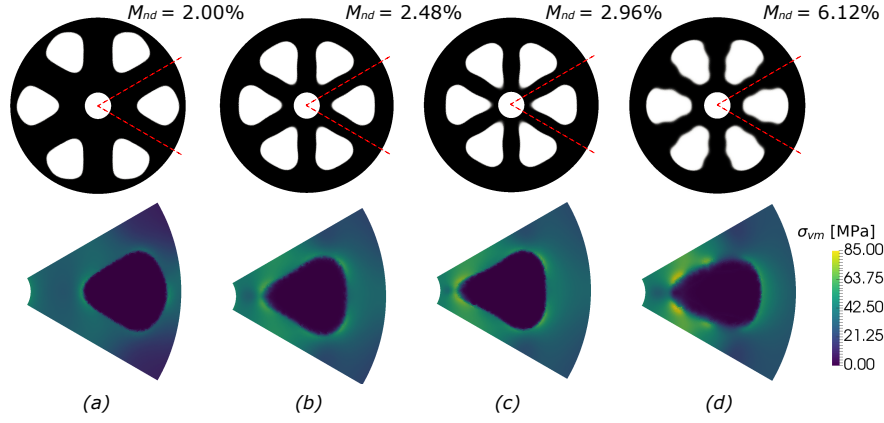


Figure 4.9: Optimal rotor topologies and corresponding stress distributions obtained at different maximum stresses: a) 55 MPa, b) 65 MPa, c) 75 MPa, and d) 85 MPa

Table 4.6: Comparison of optimal rotor topologies for various maximum stresses

Design	$\sigma_y$ , MPa	$E_{kin}$ , J	$m$ , kg	$e_{kin}$ , J/kg	$\tilde{\sigma}_{pn}$ , MPa	$\frac{V}{V_0}$	$\frac{\Delta e_{kin}}{e_{kin}^0}$ , % *
Uniform	-	135,144	48.21	2803.1	48.76	1.0	0
Optimal	55	93,590	33.79	2769.7	54.92	0.709	-1.19
	65	105,851	33.48	3161.6	64.22	0.699	+12.79
	75	108,692	33.19	3274.8	73.52	0.699	+16.83
	85	104,806	32.62	3213.1	86.76	0.701	+14.63

\*  $e_{kin}^0$  is the specific energy of uniform thickness rotor

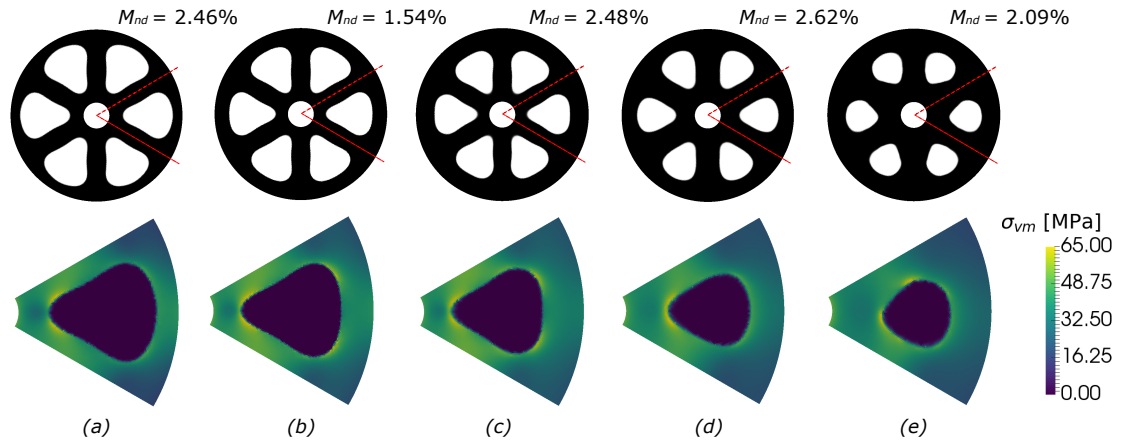


Figure 4.10: Optimal rotor topologies and corresponding stress distributions obtained at different prescribed volume fractions of a) 60%, b) 65%, c) 70%, d) 75% and e) 80%

at various limiting values of volume fraction. It is seen that the general shape of the features does not change much as the volume fraction is increased, and material is added mainly by increasing the thickness of the outer rim and spokes connecting the inner shaft to the outer rim. Table 4.7 compares the energy capacities of the different designs, which shows that there is an optimal volume fraction of 70% which provides the best improvement in specific energy of the design. This seems to indicate that the imposition of a volume fraction constraint unnecessarily reduces the design space, preventing the search for a truly optimal design. Given that in many applications, such as flywheels used for grid stability and transportation, the energy per unit cost or unit mass is the most critical parameter and not a specific volume fraction, a specific energy maximization formulation is clearly better suited for design, while the volume fraction is allowed to vary.

#### 4.2.4 Rotor topology optimization for maximum specific energy under stress constraints

It is evident from the parametric studies that investigated the effects of prescribed volume fraction on the optimal topology and energy capacity, that it does not make sense to impose a volume fraction constraint while trying to maximize the kinetic

Table 4.7: Comparison of optimal rotor topologies for various prescribed volume fractions

Design	$\alpha$ , %	$E_{\text{kin}}$ , J	$m$ , kg	$e_{\text{kin}}$ , J/kg	$\tilde{\sigma}_{pn}$ , MPa	$\frac{V}{V_0}$	$\frac{\Delta e_{\text{kin}}}{e_{\text{kin}}^0}$ , % *
Uniform	-	135,144	48.21	2803.1	48.76	1.0	0
	60	86,897	28.43	3056.51	64.48	0.599	+9.04
	65	97,599	31.06	3142.4	65.97	0.650	+12.10
Optimal	70	105,851	33.48	3161.6	64.22	0.699	+12.79
	75	107,119	35.64	3005.8	63.67	0.749	+7.23
	80	114,240	38.52	2965.9	64.07	0.807	+5.81

\*  $e_{\text{kin}}^0$  is the specific energy of uniform thickness rotor

energy with stress constraints, because some volume fractions are better than others at producing rotor designs with the best energy density. Thus, the volume fraction constraint was removed from the original formulation and the specific energy was maximized instead, thereby allowing the optimizer to search a larger design space.

The specific energy maximization approach effectively combined two objectives, i.e. maximizing the kinetic energy and minimizing the mass of the rotor. In order to understand how the objectives, i.e., specific energy and kinetic energy were influenced by the design densities, a sweep of the two functions with respect to the density of a single mesh element was plotted, as seen in Figure 4.11. A solid uniform disk rotor was used in this study, where the density of a single mesh element was varied. The element was chosen at two different locations along the radius, as seen in Figure 4.11(a). The kinetic energy had an increasing trend for both locations along the radius, however it was more sensitive to the mesh element that was near the outer rim. On the other hand, the specific energy had different trends for the two elements. Either removing material from the inner regions or adding material at the outer region was seen to improve the specific energy. Note that the magnitude of the variations in the two objective functions are small because these were based on density variations for a

Table 4.8: Comparison of optimal topologies at 5000 rpm, obtained with kinetic energy and specific energy formulations

Formulation	$E_{\text{kin}}, \text{J}$	$m, \text{kg}$	$e_{\text{kin}}, \text{J/kg}$	$\bar{\sigma}_{pn}, \text{MPa}$	$\frac{V}{V_0}$	$\frac{\Delta e_{\text{kin}}}{e_{\text{kin}}^0}, \%$ *	Iterations	Time, s
Eq. (4.1)	105,851	33.48	3161.6	64.22	0.699	+12.79	151	615
Eq. (4.2)	101,018	31.13	3244.8	64.92	0.646	+15.76	401	1119

\*  $e_{\text{kin}}^0$  is the specific energy of uniform thickness rotor

single mesh element.

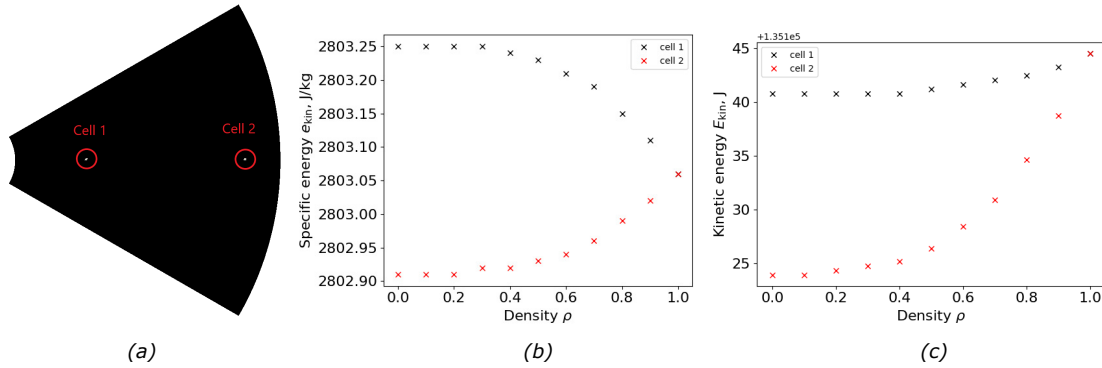


Figure 4.11: a) Location of mesh elements used for density sweep, and variation of b) specific energy and c) kinetic energy with density of the chosen mesh element

Figure 4.12 (a) and (d) depict the optimal topologies and corresponding rotor stress distributions obtained using the kinetic energy and specific energy maximization formulations respectively described in equations (4.1) and (4.2), with an operating speed of 5000 rpm, rotational symmetry of 6 and maximum stress limit of 65 MPa. For the kinetic energy formulation, the volume fraction constraint was set to 0.7, since this volume fraction resulted in the best specific energy improvement. Table 4.8 compares the energy ratings of the two designs. The newly proposed optimization formulation in equation (4.2) was able to achieve a higher specific energy by changing the volume fraction of the material. This was an improvement over the kinetic energy formulation, where the choice of volume fraction constraint limit was artificial and based on a parametric study.

Since the specific energy formulation searched a larger design space, it was more

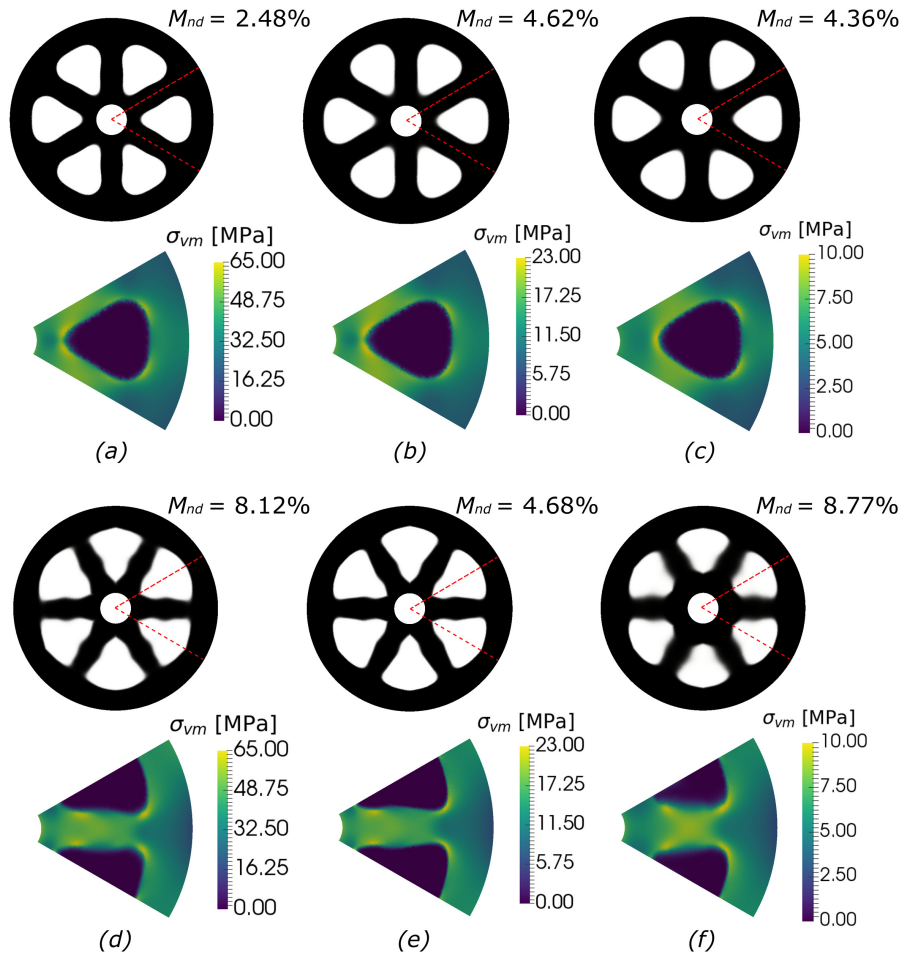


Figure 4.12: Stress distribution in the optimal rotor topology at 5000 rpm using steel with a) max  $E_{kin}$ , d) max  $e_{kin}$ , formulations, using aluminium with b) max  $E_{kin}$ , e) max  $e_{kin}$  formulations, and using PEEK with c) max  $E_{kin}$ , f) max  $e_{kin}$  formulations

challenging and required more iterations to converge. The stress relaxation parameter  $q$  had to be increased from the original value of 0.5 to 1.0 in the initial iterations, and the MMA asymptotes' increment and decrement limits ( $\gamma^{(+)}$ ,  $\gamma^{(-)}$ ) and solver move limit also had to be decreased to allow the problem to converge. Finally, a volume preserving projection filter was also needed to converge to an optimal design and prevent large variations in the maximum stress constraint during optimization iterations. The volume preserving approach ensured that the volume of the design before and after the projection filter was the same by varying the threshold using a 1D line search. Figure 4.13 compares the convergence of the specific energy formulation using the original Heaviside filter with a constant threshold to the volume preserving Heaviside filter.

Despite these measures, the discreteness measure  $M_{nd}$  convergence tolerance of 5% that was used in the kinetic energy formulations could not always be achieved with the specific energy formulations, as seen in Figure 4.12. As a result, slightly larger convergence tolerances were used in the specific energy based rotor designs. The effect of visible gray regions in the specific energy formulation was further investigated by using body-fitted meshes generated by extracting the solid regions of the domain to analyze the optimal designs. In designs where the geometry was extracted using a density threshold of 50%, up to 23% increase in the peak stress was observed, whereas choosing a higher density threshold of 90% increased the peak stress in the designs by up to 400%. The details of this study are presented in Appendix D.6 and further justify the need for convergence to a fully discrete design. In the future, the design discreteness and convergence could be improved with the use of a robust approach using a combination of eroded, blueprint and dilated designs, albeit at the cost of an increased number of FEM computations per optimization iteration [122]. In addition to the robust formulation, the use of an Augmented Lagrangian formulation for the treatment of stress constraints in a localized manner [123] could also improve the stress distribution and convergence of designs with the specific energy formulation.

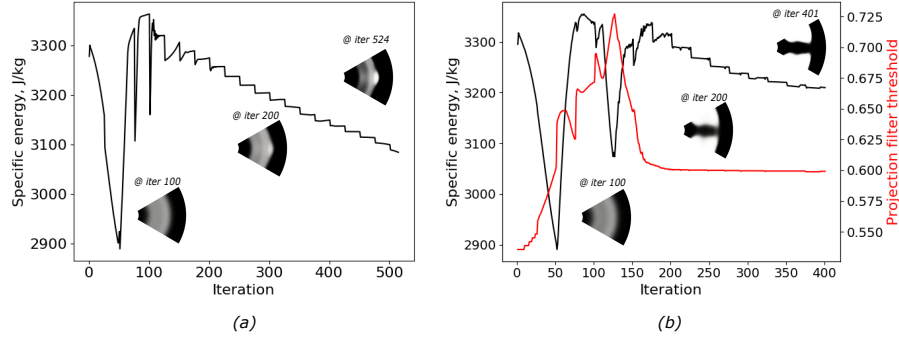


Figure 4.13: Convergence of the topology based on the specific energy formulation using a Heaviside filter with a) fixed threshold, and b) volume preserving threshold obtained with a line search

#### 4.2.4.1 Effect of rotor material

To understand the influence of choice of rotor material on the optimal topology, both the kinetic and specific energy formulations were used to determine optimal rotor designs using two additional materials, i.e, aluminium-2024 ( $E = 73$  GPa,  $\nu = 0.33$ ,  $\rho = 2800$  kg/m<sup>3</sup>), which was used by for flywheel design by Tsai and Cheng [81] and polyether ether ketone (PEEK) ( $E = 4.5$  GPa,  $\nu = 0.38$ ,  $\rho = 1310$  kg/m<sup>3</sup>) which was used in the study by Lottes et al. [82]. Rotational symmetry with  $N = 6$  was used, and the original operating speed of 5000 rpm was chosen for this study. The maximum allowable stress was different for each material, to account for the difference in their properties ( $E_0$ ,  $\rho$ ,  $\nu$ ,  $\sigma_y$ ). The results of this study, seen in Table 4.9 show that even though the kinetic energy and mass of the designs are very different, the optimal topologies obtained with steel and aluminium are nearly identical when using the same formulation, which could be a result of the scaling of their properties ( $E$ ,  $\rho$ ). For the PEEK rotor topology, where  $E$ ,  $\rho$  do not scale identically, the design shows a different volume fraction and topology as well as a smaller improvement in the specific energy over the uniform thickness disk.

For all three materials, the designs obtained using the specific energy formulation had rotor spokes with a slight bulge in the middle, which was not observed in the

Table 4.9: Comparison of optimal topologies for different rotor materials at 5000 rpm

Material	Formulation	$E_{\text{kin}}$ , J	$m$ , kg	$e_{\text{kin}}$ , J/kg	$\tilde{\sigma}_{pm}$ , MPa	$\frac{V}{V_0}$	$\frac{\Delta e_{\text{kin}}}{e_{\text{kin}}^0}$ , % *
Steel	Uniform disk	135,144	48.21	2803.1	48.76	1.0	0
	Eq. (4.1)	105,851	33.48	3161.6	64.22	0.699	+12.79
	Eq. (4.2)	101,018	31.13	3244.8	64.92	0.646	+15.76
Aluminium	Uniform disk	48,204	17.19	2803.1	17.80	1.0	0
	Eq. (4.1)	37,120	11.72	3166.2	22.96	0.699	+12.95
	Eq. (4.2)	36,119	11.18	3230.7	23.33	0.650	+15.25
PEEK	Uniform disk	22,548	8.04	2803.1	7.14	1.0	0
	Eq. (4.1)	16,745	5.486	3052.19	9.95	0.699	+8.9
	Eq. (4.2)	17,742	5.66	3135.1	9.98	0.703	+11.8

\*  $e_{\text{kin}}^0$  is the specific energy of uniform thickness rotor

kinetic energy maximized designs. One possible explanation for this difference is that specific energy formulation is effectively a multi-objective optimization problem that tries to simultaneously maximize the kinetic energy and minimize the mass of the rotor by maximizing the energy to mass ratio. The kinetic energy of the rotor is more sensitive to mesh element densities that are furthest away from the central axis, while the mass or volume fraction is independent of the distance from the central axis, and the highest stresses are expected to develop around the thin beams or holes. The bulges in the rotor spokes observed in the specific energy formulation help to improve the specific energy of the design by putting material in areas with a higher moment of inertia, which do not have high stresses and by searching a larger design space than the kinetic energy formulation.

#### 4.2.4.2 Effect of operating speed

The effect of the operating speed on the optimal topology was studied by varying the angular velocity to different values between 4000 and 6000 rpm. Figure 4.14 compares the optimal topologies and corresponding rotor stress distributions obtained at various

speeds, using both kinetic (maximum volume fraction = 70%) and specific energy formulations. Table 4.10 compares the energy capacities of the two formulations with the constant thickness rotor operated at the corresponding speed. The maximum stresses developed in the constant thickness rotor,  $\tilde{\sigma}_{pm}$ , are highest at low speeds, because of the interference fitting pressure applied at the interface to the shaft. As the speed increases,  $\tilde{\sigma}_{pm}$  reaches its lowest value of 47.28 MPa at a speed of 5500 rpm, before increasing at the higher speed of 6000 rpm. Thus, the pressure at the shaft-rotor assembly interface plays an important role in determining the energy storage characteristics at a specified speed.

At low speeds, since the stresses developed due to the centrifugal load were not too high, the shape of the holes between the rotor spokes was more elongated in both optimization formulations, in order to move more mass towards the outer rim thereby increasing the kinetic energy. As the operating speed increased, more material was added closer to the central shaft, and the holes in the topology moved outward to try and satisfy the stress constraint. This was accompanied by an increase in the specific energy of the optimal topology rotors compared to the uniform thickness rotor, and this improvement was seen to be the highest for  $\omega=5000$  rpm. However, there was a limiting speed, beyond which the kinetic energy formulation could not find feasible solutions that satisfied both stress and volume fraction constraint. For instance, the optimal topology rotor designed for 6000 rpm had a 5.3% decrease in specific energy over the constant thickness rotor operated at the same speed, and the volume fraction exceeded the prescribed value of 70%. Using the specific energy formulation, the volume fraction was automatically adjusted to be higher than 70% for low and high speeds, thereby achieving a truly optimal design. Overall, the specific energy formulation was able to achieve better improvements in the specific energy because it could vary the volume fraction to suit the chosen operating speed and stress distribution.

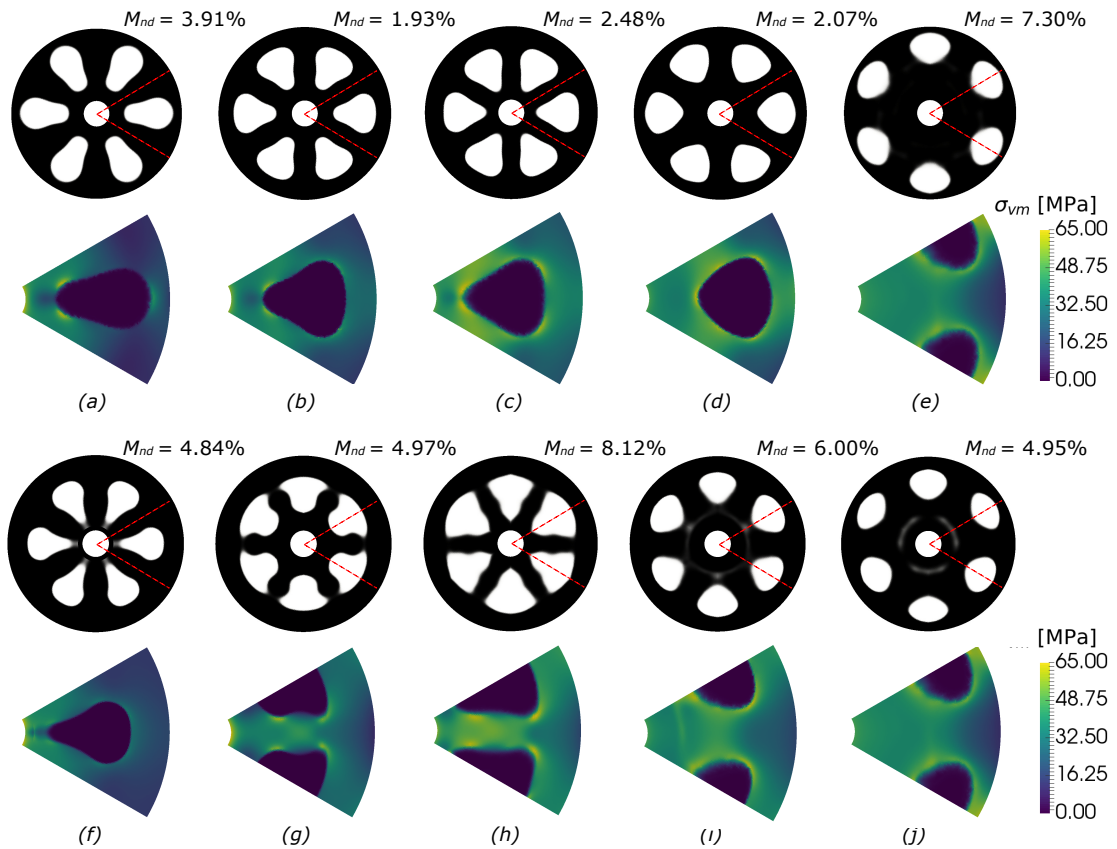


Figure 4.14: Optimal rotor topology and corresponding stress distributions obtained with kinetic energy and specific energy formulations respectively at different operating speeds: a),f) 4000 rpm, b),g) 4500 rpm, c),h) 5000 rpm, d),i) 5500 rpm and e),j) 6000 rpm

Table 4.10: Comparison of optimal rotor topologies for various operating speeds

Speed $\omega$ , rpm	Design	$E_{\text{kin}}$ , J	$m$ , kg	$e_{\text{kin}}$ , J/kg	$\tilde{\sigma}_{pm}$ , MPa	$\frac{V}{V_0}$	$\frac{\Delta e_{\text{kin}}}{e_{\text{kin}}^0}$ , % <sup>1</sup>
4000	Uniform	86,495	48.21	1794.0	60.24	1.0	0
	Eq. (4.1)	63,592	32.97	1928.8	64.57	0.699	+7.50
	Eq. (4.2)	72,548	36.36	1995.37	64.90	0.77	+11.22
4500	Uniform	109,471	48.21	2270.5	53.66	1.0	0
	Eq. (4.1)	82,917	33.34	2487.0	64.84	0.699	+9.53
	Eq. (4.2)	87,036	34.37	2532.04	64.96	0.73	+11.52
5000	Uniform	135,144	48.21	2803.1	48.76	1.0	0
	Eq. (4.1)	105,851	33.48	3161.6	64.22	0.699	+12.79
	Eq. (4.2)	101,018	31.13	3244.8	64.92	0.646	+15.76
5500	Uniform	163,530	48.21	3391.8	47.28	1.0	0
	Eq. (4.1)	116,511	33.34	3494.6	63.94	0.699	+3.03
	Eq. (4.2)	128,825	36.14	3565.52	65.37	0.77	+5.12
6000	Uniform	194,615	48.21	4036.5	50.76	1.0	0
	Eq. (4.1)	135,924	35.56	3822.4	64.04	0.765 <sup>2</sup>	-5.3
	Eq. (4.2)	150,748	37.33	4037.49	64.04	0.795	+0.0

<sup>1</sup>  $e_{\text{kin}}^0$  is the specific energy of uniform thickness rotor

<sup>2</sup> Volume constraint violated

#### 4.2.4.3 Effect of rotational symmetry

Rotational symmetry was used to reduce the optimization domain size from the original disc shape. For example, a symmetry  $N=5$  corresponds to a circular section of  $\frac{360}{N} = 72^\circ$ . The effect of using different rotor meshes obtained with different circular symmetries on the optimal topology was studied by varying  $N$  between 5 and 9. Figure 4.15 compares the optimal rotor designs and corresponding stress distributions obtained using both kinetic and specific energy optimization formulations with various circular sections and Table 4.11 compares the energy capacity improvements offered by the different designs.

The use of rotational symmetry of 6 or 7 resulted in the best design improvement when using the kinetic energy formulation. On the other hand, the specific energy formulation was able to achieve higher overall design improvements for all circular symmetries. While there is relatively little variation in the energy capacity of the designs, this parameter can be relevant for manufacturing and is thus useful to consider while designing the optimal topology.

### 4.3 Summary

This work explored several topology optimization formulations to design optimal energy storage flywheels for grid-scale FESS. To solve the different formulations, a density based topology optimization [124] framework was implemented with the SIMP power law to interpolate the material properties at intermediate densities. A density filter [85] was used for length scale control and to prevent checkerboard patterns in the final design, followed by a Heaviside projection filter [122] with a continuous slope update scheme, which was used to converge to a discrete topology. The threshold of the projection filter was determined by a 1D line search, to ensure stability and prevent large changes in the volume fraction at slope update intervals. The gradient-based MMA algorithm by Svanberg [119] was used to optimize the rotor topology. An ad-

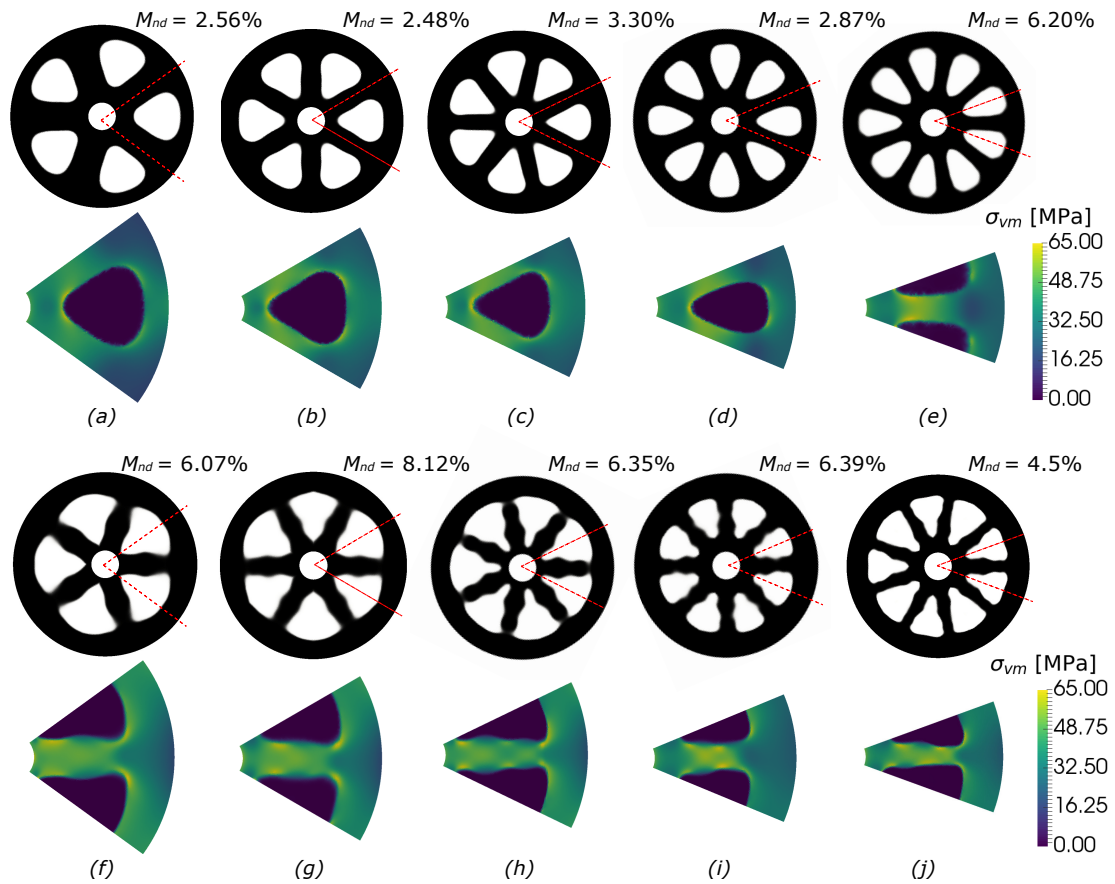


Figure 4.15: Optimal rotor topologies and corresponding stress distributions obtained with kinetic energy and specific energy formulations respectively using different circular symmetries: a),f) N=5, b),g) N=6, c),h) N=7, d),i) N=8, and e),j) N=9

Table 4.11: Comparison of optimal rotor topologies for various circular symmetries

Symmetry $N$	Design	$E_{\text{kin}}, \text{ J}$	$m, \text{ kg}$	$e_{\text{kin}}, \text{ J/kg}$	$\tilde{\sigma}_{pm}, \text{ MPa}$	$\frac{V}{V_0}$	$\frac{\Delta e_{\text{kin}}}{e_{\text{kin}}^0}, \%$ *
-	Uniform	135,144	48.21	2803.1	48.76	1.0	0
5	Eq. (4.1)	99,651	33.23	2998.72	64.85	0.699	+6.98
	Eq. (4.2)	104,347	31.80	3281.01	64.94	0.669	+17.05
6	Eq. (4.1)	105,851	33.48	3161.6	64.22	0.699	+12.79
	Eq. (4.2)	101,018	31.13	3244.8	64.92	0.646	+15.76
7	Eq. (4.1)	104,795	33.09	3166.8	64.96	0.699	+12.97
	Eq. (4.2)	100,070	30.99	3228.62	65.02	0.668	+15.18
8	Eq. (4.1)	101,430	33.19	3055.5	63.94	0.699	+9.0
	Eq. (4.2)	109,624	34.84	3146.41	65.33	0.735	+12.24
9	Eq. (4.1)	100,589	32.62	3084.0	67.49	0.70	+10.02
	Eq. (4.2)	102,841	32.03	3210.20	65.72	0.683	+14.5

\*  $e_{\text{kin}}^0$  is the specific energy of uniform thickness rotor

joint approach was used to determine the analytical sensitivities of the optimization responses.

Using a maximum kinetic energy topology optimization formulation with fixed volume fraction and stress constraints, a FESS rotor with 12% improvement in the specific energy over a uniform rotor was obtained by reducing 30% of the mass. When the maximum stress limit was varied without changing the operating speed or volume fraction limits, it was seen that the shape of the holes between the spokes remained more or less similar, but the position along the radius changed. As the maximum stress limit was increased, the holes in the rotor moved inwards and resulted in an improvement in the moment of inertia by moving material towards the outer rim of the rotor. The use of very large maximum stresses resulted in a trivial detached-rim design, since the stress constraint could be satisfied without creating connecting spokes or ribs between the shaft and the outer rim. A parametric study on volume fraction showed the constraint value limited the design space and led to sub-optimal

designs. Therefore, a novel specific energy maximization formulation with a stress constraint was proposed and shown to allow the optimizer to determine the ideal volume fraction which led to the best specific energy improvement, however, at the cost of introducing more intermediate densities in the optimized designs.

The effect of other relevant FESS design parameters, such as rotor material, operating speed, and rotational symmetry, on the optimal designs obtained with both kinetic and specific energy formulations was investigated. The design obtained with two different rotor material, aluminium and PEEK, was compared with the original steel rotor designed with kinetic and specific energy formulations. In general, while the energy content and mass of the rotors that used steel and aluminium were different, the specific energy and optimal topology were nearly identical. The PEEK rotor had a slightly different topology and a higher volume fraction, which was attributed to the fact that the PEEK material properties  $E$  and  $\rho$  scaled differently compared to steel and aluminium.

At low speeds, the optimal topologies using both formulations had elongated holes and the material was distributed towards the outer rim to achieve a higher moment of inertia. When the operating speed was increased, the material was redistributed in the area surrounding the central shaft and the holes between the spokes became more rounded. The specific energy formulation achieved better design improvements than the kinetic energy formulation by using higher volume fractions at low and high speeds, and lower volume fractions at intermediate speeds. The interaction between the stresses developed in the rotor due to the interference fit shaft-rotor assembly and the centrifugal loads was not trivial, and it influenced the optimal topology and volume fractions at different speeds.

Different circular symmetries were used to reduce the size of the computational domain, while keeping the operating speed, volume fraction and stress limits constant. The specific energy formulation was able to use different volume fractions and improve the energy capacity of the rotor to a similar extent, so the choice of rotational

symmetry could be based mainly on manufacturing or other considerations.

The acceleration related stresses were seen to be only significant when considering short duration charge-discharge cycles of less than 0.1 s, which are unlikely to be a design requirement in FESS applications unless very short ramp times are required to provide storage for fault protection and frequency regulation. If needed, the inclusion of acceleration loads in the topology optimization problem might help to achieve designs that can better handle these stresses as well.

# Chapter 5

## Augmented Lagrangian approach for locally stress constrained rotor topology optimization

### Preface

The 2D topology optimization studies discussed previously in Chapter 4 used a P-norm aggregated global stress measure in the optimization formulation. It was seen that the use of this global stress constraint allowed the optimizer to find feasible designs that satisfied the stress constraints, but the obtained designs also had some stress concentrations in bottleneck regions, which have potential for improvement by using some means to improve the overall stress distribution. The Augmented Lagrangian approach can be used to enforce stress constraints locally in the mesh elements, thereby allowing greater control over the stresses in localized parts of the rotor topology. This chapter discusses a new topology optimization framework based on the Augmented Lagrangian approach, and compares the results obtained using this method with the previous formulations that used global stress constraints.

### 5.1 Methodology

The overall methodology for topology optimization described in Chapter 4 was utilized in this study, including the proposed SIMP modifications to the numerical model

in Section 4.1.1, and the density and projection (Heaviside) filters described in Section 4.1.3. The optimization formulation, including objectives and local stress constraints, and the adjoint sensitivity analysis are discussed below.

### 5.1.1 Optimization formulation

While the specific energy formulation proposed in Chapter 4 was effective, it also had convergence issues and remnant gray regions in the optimized designs. On the other hand, the kinetic energy maximization approach with a volume fraction constraint imposed an artificial volume constraint that resulted in sub-optimal designs with low specific energy. Thus, this chapter uses a multi-objective formulation with local stress constraints to design optimal energy storage rotors, where the kinetic energy of the flywheel rotor is maximized and the total mass of the rotor is minimized simultaneously, subject to local stress constraints. While the multi-objective formulation also introduces an artificial weight on the two objective, i.e., kinetic energy and mass, it allows for the creation of a Pareto front which can be used to select the best rotor based on design requirements. The optimization problem is formulated as:

$$\begin{aligned}
& \max E_{\text{kin}}(\hat{\boldsymbol{\rho}}), \min m(\hat{\boldsymbol{\rho}}) \\
& \text{w.r.t } \hat{\boldsymbol{\rho}} = \{\hat{\rho}_1, \hat{\rho}_2, \dots, \hat{\rho}_N\} \\
& \text{s.t. } KU = F \\
& g_j^{(k)}(\hat{\boldsymbol{\rho}}, \mathbf{u}) = \frac{\sigma_i^j(\hat{\boldsymbol{\rho}}, \mathbf{u})}{\sigma_y} - 1.0 \leq 0 \quad \forall j = 1, 2, \dots, N \\
& 0.0 \leq \hat{\rho}_e \leq 1.0
\end{aligned} \tag{5.1}$$

where  $E(\hat{\boldsymbol{\rho}})$  is the kinetic energy of the rotor,  $m(\hat{\boldsymbol{\rho}})$  is the total rotor mass, and  $g_j(\hat{\boldsymbol{\rho}}, \mathbf{u})$  is the von Mises stress constraint at the  $j^{\text{th}}$  mesh element, which checks for material failure,  $\sigma_i^j(\hat{\boldsymbol{\rho}}, \mathbf{u})$  is the relaxed von Mises stress at element  $j$  and  $\sigma_y$  is the maximum allowable stress at mesh elements. Here  $\hat{\boldsymbol{\rho}} = \{\hat{\rho}_1, \hat{\rho}_2, \dots, \hat{\rho}_N\}$  are the filtered and projected normalized design densities which are used to solve the numerical model.

As the above problem has as many stress constraints as the number of mesh elements,  $N$ , the use of the adjoint solver to calculate sensitivities alone cannot suffi-

ciently reduce the computational cost of the problem, since the adjoint solver requires as many matrix inversions as the number of constraints. As a result, the Augmented Lagrangian (AL) formulation is used to solve the local stress constrained rotor topology problem.

### 5.1.2 Augmented Lagrangian function

This approach combines the objective function and all the stress constraints in the original formulation from Equation (5.1) into a single Augmented Lagrangian function which can be treated as an unconstrained optimization problem [103]:

$$\underset{\hat{\rho}}{\text{minimize}} \mathcal{L}_{\mu^{(k)}}(\hat{\rho}, \mathbf{u}) = f^{(k)}(\hat{\rho}) + \frac{1}{N} \sum_{j=1}^N \left[ \lambda_j^{(k)} h_j^{(k)}(\hat{\rho}, \mathbf{u}) + \frac{\mu^{(k)}}{2} h_j^{(k)}(\hat{\rho}, \mathbf{u})^2 \right] \quad (5.2)$$

where  $f^{(k)}(\hat{\rho})$  is the objective function evaluated at iteration  $k$ , and  $h_j^{(k)}(\hat{\rho}, \mathbf{u})$  is the local stress constraint at mesh element  $j$ ,  $\lambda_j^{(k)}$  is the Lagrange multiplier corresponding to the  $j^{\text{th}}$  stress constraint and  $\mu^{(k)}$  is the penalty coefficient used to convert the inequality constrained formulation into an unconstrained form. In the AL approach, the estimate of the Lagrange multipliers  $\lambda_j^{(k)}$  improves with each iteration, thus helping to avoid a very large increase in the penalty  $\mu^{(k)}$  with iterations, which can potentially make the problem ill-conditioned.

The unconstrained Lagrange function is minimized at each iteration of the AL method using the MMA algorithm. Once the MMA solver generates a new design guess, the Lagrange multipliers  $\lambda^{(k)}$  and penalty function  $\mu^{(k)}$  are updated using the rule [103],

$$\begin{aligned} \lambda_j^{(k+1)} &= \lambda_j^{(k)} + \mu^{(k)} h_j^{(k)} \\ \mu^{(k+1)} &= \min \left( \alpha \mu^{(k)}, \mu_{max} \right) \end{aligned} \quad (5.3)$$

where  $\alpha$  is the penalty multiplier and  $\mu_{max}$  is the maximum penalty. The convergence of the problem is known to be sensitive to the choice of  $\alpha$ ,  $\mu_{max}$  and the initial penalty  $\mu^{(0)}$ , so a calibration study is necessary to determine these parameters [103, 104, 123]

for the rotor problem. The constraints in the Lagrange function are normalized by the number of mesh elements  $N$  to improve convergence of the topology.

The two objective functions in the multi-objective problem, the one that maximizes the kinetic energy, and the one that minimizes the mass, are combined into a single objective,  $f^{(k)}(\hat{\boldsymbol{\rho}})$ , using a weighted sum approach shown in Equation (5.4),

$$f^{(k)}(\hat{\boldsymbol{\rho}}) = -w_{ke} \frac{E_{\text{kin}}(\hat{\boldsymbol{\rho}})}{E_{\text{kin}}^0} + w_m \frac{m(\hat{\boldsymbol{\rho}})}{m^0} \quad (5.4)$$

where the energy  $E_{\text{kin}}(\hat{\boldsymbol{\rho}}, \mathbf{u})$  and mass  $m(\hat{\boldsymbol{\rho}})$  are normalized using the energy  $E_{\text{kin}}^0$  and mass  $m^0$  of a uniform thickness rotor respectively, and  $w_{ke}$  and  $w_m$  are the weights used to combine the two objectives, which are chosen such that  $w_{ke} + w_m = 1.0$ , and their values control the trade-off between the two objectives, allowing us to obtain a Pareto set of solutions for varying weights. The negative sign for the energy objective converts the maximization problem to a minimization problem.

Constraints  $h_j^{(k)}(\hat{\boldsymbol{\rho}}, \mathbf{u})$  are defined at each mesh element  $j$ , which convert the inequality constraints  $g_j^{(k)}(\hat{\boldsymbol{\rho}}, \mathbf{u})$  to equality constraints which can be used in the Augmented Lagrangian function [103]:

$$h_j^{(k)}(\hat{\boldsymbol{\rho}}, \mathbf{u}) = \max \left( g_j^{(k)}(\hat{\boldsymbol{\rho}}, \mathbf{u}), -\frac{\lambda_j^{(k)}}{\mu^{(k)}} \right) \quad (5.5)$$

$$\text{where } g_j^{(k)}(\hat{\boldsymbol{\rho}}, \mathbf{u}) = \frac{\sigma_i^j(\hat{\boldsymbol{\rho}}, \mathbf{u})}{\sigma_y} - 1.0 \leq 0 \quad \forall j = 1, 2, \dots, N$$

The relaxed von Mises stresses at mesh elements are defined as:

$$\sigma_i^j(\hat{\boldsymbol{\rho}}, \mathbf{u}) = \rho_j^q \sigma_{vm,j} \quad (5.6)$$

where  $\sigma_{vm,j}$  is the von Mises stress computed at the centroid of element  $j$ . It is defined as discussed previously in Equations (4.38), (4.39).

### 5.1.3 Sensitivity analysis

The gradient of the AL function  $\mathcal{L}_{\mu^{(k)}}(\hat{\boldsymbol{\rho}}, \mathbf{u})$  defined in Equation (5.2) w.r.t design variable  $\hat{\rho}_e$  is:

$$\frac{d\mathcal{L}_{\mu^{(k)}}}{d\hat{\rho}_e} = \frac{\partial \mathcal{L}_{\mu^{(k)}}}{\partial \hat{\rho}_e} + \lambda^T \left( \frac{\partial K}{\partial \hat{\rho}_e} \mathbf{u} - \frac{\partial F}{\partial \hat{\rho}_e} \right) \quad (5.7)$$

where the adjoint vector  $\lambda$  is defined as:

$$\lambda = -(K^T)^{-1} \frac{\partial \mathcal{L}_{\mu^{(k)}}}{\partial \mathbf{u}} \quad (5.8)$$

Detailed derivations for the above expressions of adjoint sensitivity and adjoint vectors are in Appendix D.2. The definitions of  $\frac{\partial K}{\partial \hat{\rho}_e}$  and  $\frac{\partial F}{\partial \hat{\rho}_e}$  are from Equations (4.34), (4.35) respectively. The first term  $\frac{\partial \mathcal{L}_{\mu^{(k)}}}{\partial \hat{\rho}_e}$  in Equation (5.7) can be calculated as:

$$\frac{\partial \mathcal{L}_{\mu^{(k)}}}{\partial \hat{\rho}_e} = \frac{\partial f^{(k)}(\hat{\boldsymbol{\rho}})}{\partial \hat{\rho}_e} + \frac{1}{N} \sum_{j=1}^N \left[ \left( \lambda_j^{(k)} + \mu^{(k)} h_j^{(k)}(\hat{\boldsymbol{\rho}}, \mathbf{u}) \right) \frac{\partial h_j^{(k)}(\hat{\boldsymbol{\rho}}, \mathbf{u})}{\partial \hat{\rho}_e} \right] \quad (5.9)$$

where partial derivative  $\frac{\partial f^{(k)}(\hat{\boldsymbol{\rho}})}{\partial \hat{\rho}_e}$  is

$$\frac{\partial f^{(k)}(\hat{\boldsymbol{\rho}})}{\partial \hat{\rho}_e} = - \left( \frac{w_{ke}}{E_{\text{kin}}^0} \right) \frac{\partial E_{\text{kin}}(\hat{\boldsymbol{\rho}})}{\partial \hat{\rho}_e} + \left( \frac{w_m}{m^0} \right) \frac{\partial m(\hat{\boldsymbol{\rho}})}{\partial \hat{\rho}_e} \quad (5.10)$$

where partial derivatives of the kinetic energy  $E_{\text{kin}}$  and mass  $m$  are calculated using Equations (4.25), (4.29) respectively.

The partial derivative  $\frac{\partial h_e^{(k)}}{\partial \hat{\rho}_e}$  in Equation (5.9) can be written as:

$$\frac{\partial h_e^{(k)}}{\partial \hat{\rho}_e} = \begin{cases} 0 & , \text{ if } g_e^{(k)}(\hat{\boldsymbol{\rho}}, \mathbf{u}) < -\frac{\lambda_e^{(k)}}{\mu^{(k)}} \\ q \hat{\rho}_j^{q-1} \frac{\sigma_{vm,e}}{\sigma_y} & , \text{ otherwise} \end{cases} \quad (5.11)$$

Next, in order to calculate the adjoint vector in Equation (5.8), the term  $\frac{\partial \mathcal{L}_{\mu^{(k)}}}{\partial \mathbf{u}}$  can be simplified as:

$$\frac{\partial \mathcal{L}_{\mu^{(k)}}}{\partial \mathbf{u}} = \sum_{j=1}^N \left( \lambda_j^{(k)} + \mu^{(k)} h_j^{(k)}(\hat{\boldsymbol{\rho}}, \mathbf{u}) \right) \frac{\partial h_j^{(k)}}{\partial \mathbf{u}} \quad (5.12)$$

since the objective function  $f^{(k)}(\hat{\boldsymbol{\rho}})$  is independent of the solution  $\mathbf{u}$ . Here  $\frac{\partial h_j^{(k)}}{\partial \mathbf{u}_j}$  is calculated as:

$$\frac{\partial h_j^{(k)}}{\partial \mathbf{u}_j} = \begin{cases} 0 & , \text{ if } g_j^{(k)}(\hat{\boldsymbol{\rho}}, \mathbf{u}) < -\frac{\lambda_j^{(k)}}{\mu^{(k)}} \\ \frac{1}{\sigma_y} \hat{\rho}_j^q \frac{\partial \sigma_{vm,j}}{\partial \mathbf{u}_j} & , \text{ otherwise} \end{cases} \quad (5.13)$$

where  $\frac{\partial \sigma_{vm,j}}{\partial \mathbf{u}_j}$  is determined using the definition of the von Mises stress at the cell centroid from Equation (4.40).

### 5.1.4 Optimization solver

The above optimization problem is solved using a version of MMA tailored to explicitly solve unconstrained problems, as described in reference [103]. The key difference from the MMA solver used in Chapter 4 is that the minimizer of the approximate convex-subproblem can be found explicitly in this case, which makes it more computationally efficient.

### 5.1.5 Implementation

A block diagram of the Augmented Lagrangian topology optimization framework is shown in Figure 5.1. The unstructured quadrilateral meshes used in the rotor topology optimization studies performed in this study were generated using the open-source script based meshing tool Gmsh [115]. The numerical model, adjoint solver and filters were implemented in C++ in the OpenFCST toolbox [112], which uses the open-source deal.ii finite element libraries [113]. An open-source C++ MMA solver [120] was adapted for use in the implemented framework, based on the implementation of the unconstrained MMA solver by Giraldo-Londoño and Paulino [103].

## 5.2 Results and Discussion

The Augmented Lagrangian framework described in Figure 5.1 was used to solve the multi-objective problem seen in equation (5.2) to simultaneously maximize the kinetic energy and minimize the mass of the rotor, while subject to local stress constraints that were enforced at every mesh element. The two optimization objectives were normalized and combined using a weighted sum approach as seen in equation (5.4).

Table 5.1 contains the simulation parameters used for this study, including how the Lagrange multipliers  $\lambda_j^{(k)}$  and penalty  $\mu^{(k)}$  were initialized or updated at iterations ( $k$ ). The weights  $w_{ke}$  and  $w_m$  used to combine the energy and mass objectives were systematically varied to find several optimal solutions for the multi-objective

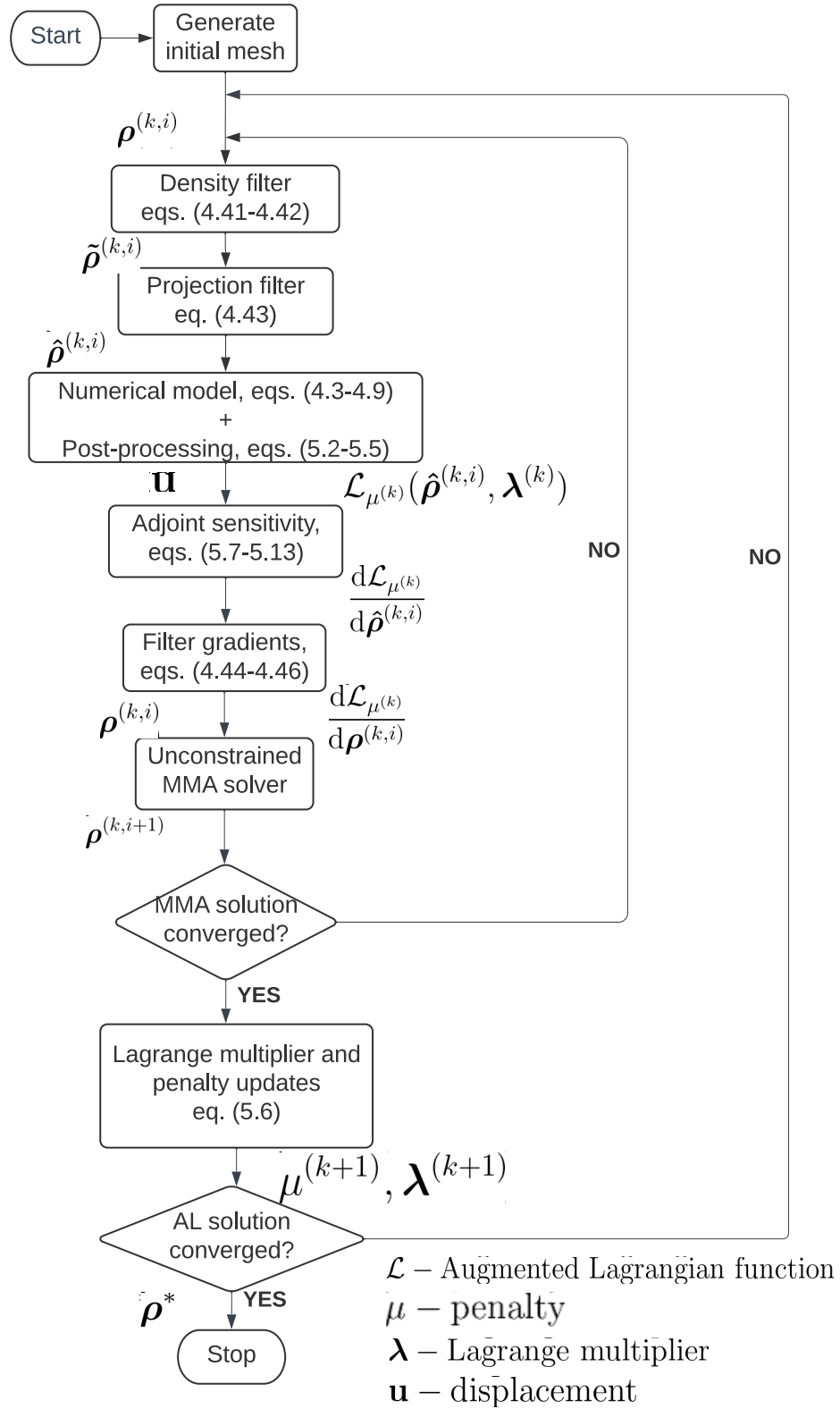


Figure 5.1: Flowchart of the Augmented Lagrangian approach for rotor topology optimization

problem.

### 5.2.1 Pareto-optimal solutions

The optimal solutions obtained using several different combinations of the objective weights were used to generate a Pareto-plot of the optimal rotor designs. Figures 5.2 and 5.3 contain the optimal topologies and corresponding stress distributions obtained with different weight combinations. For  $w_{ke} \geq 0.45$ , the optimization resulted in a solid disk, since the mass minimization objective was nearly ignored. Table 5.2 contains the corresponding specific energy, maximum stress, and other relevant details about the Pareto optimal designs. The remnant gray regions in the design were measured using the previously defined measure of discreteness  $M_{nd}$  (Equation (4.47)), which was required to be below 5% for convergence. Overall, the convergence of the Augmented Lagrangian formulation was better than the specific energy formulation, although a few designs had slightly higher than the acceptable remnant gray regions, which could be further improved by using a robust approach.

Figure 5.4 plots the Pareto-optimal solutions obtained with the linearly weighted multi-objective formulation to maximize the kinetic energy and minimize the mass. A Pareto-front of non-dominated designs is seen to emerge, with several possible energy-mass combinations. Although all non-dominated designs are equally optimal with respect to the optimization formulation, there is a large variation in the specific energy of the designs. Figure 5.4 also reports the specific energy of the designs with a colorbar, and it is evident that the designs with the highest specific energy all have a mass between 27 and 29 kg, resulting in volume fractions in the range of 55 to 65%. The specific energy of the designs reduced both at lower and higher volume fractions or rotor masses, which was also observed in the parametric study with respect to volume fractions conducted in Section 4.2.3.2.

While the Pareto front clearly indicates that certain volume fractions result in designs with a higher specific energy, it also allows the designer to choose a certain

Table 5.1: Optimization parameters for Augmented Lagrangian approach for local stress-constrained topology optimization of flywheel

Parameter set	Parameter	Value
Material Properties	Young's modulus ( $E$ ), GPa	210
	Poisson's ratio ( $\nu$ )	0.3
	Solid density ( $\rho$ ), kg/m <sup>3</sup>	7850
Flywheel model	Rotor height, m	0.05
	Shaft boundary condition	Neumann (press-fit)
	Angular velocity ( $\omega$ ), rpm	5000
	Inner radius ( $r_{shaft}$ ), m	0.03
	Outer radius ( $r_{out}$ ), m	0.2
SIMP parameters	Fixed rims thickness ( $t_{rim}$ ), m	0.01
	Penalty ( $p$ )	3
	Initial guess ( $\rho_0$ )	0.6
MMA parameters	Minimum Young's modulus ( $E_{min}$ ), GPa	1
	$a$	0.0
	$c$	1000.0
	$d$	0.0
Density filter	Move limit	0.01
	Filter radius ( $r_{filt}$ ), m	0.035
Projection filter	Distribution	linear decay / conical
	Threshold ( $h$ )	0.5
	Initial slope ( $\beta_0$ )	1
	Maximum slope ( $\beta_{max}$ )	100
	Update factor	2.0
Mesh parameters	Update interval	25
	Circular symmetry ( $N$ )	6
Augmented Lagrangian	Elements	11988
	Maximum allowable stress ( $\sigma_y$ ), MPa	65
	Stress relaxation ( $q$ )	0.5
	Initial Lagrange multipliers ( $\lambda_j^0$ )	0.0
	Initial penalty ( $\mu^0$ )	10.0
	Maximum penalty ( $\mu_{max}$ )	50000.0
	Penalty multiplier ( $\alpha$ )	1.1

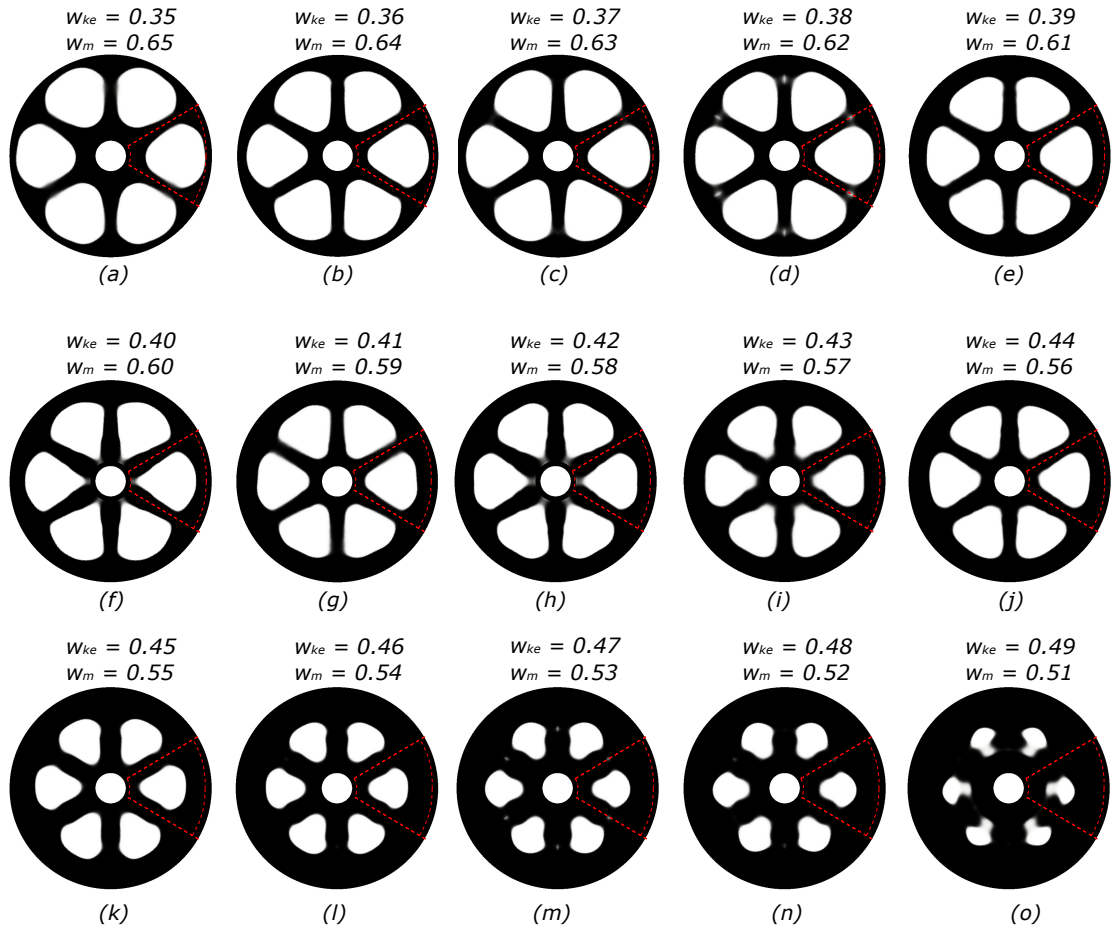


Figure 5.2: Optimal topologies obtained using the multi-objective (max energy, min mass) and the Augmented Lagrangian approach with local stress constraints, using several combinations of objective function weights  $w_{ke}$  and  $w_m$

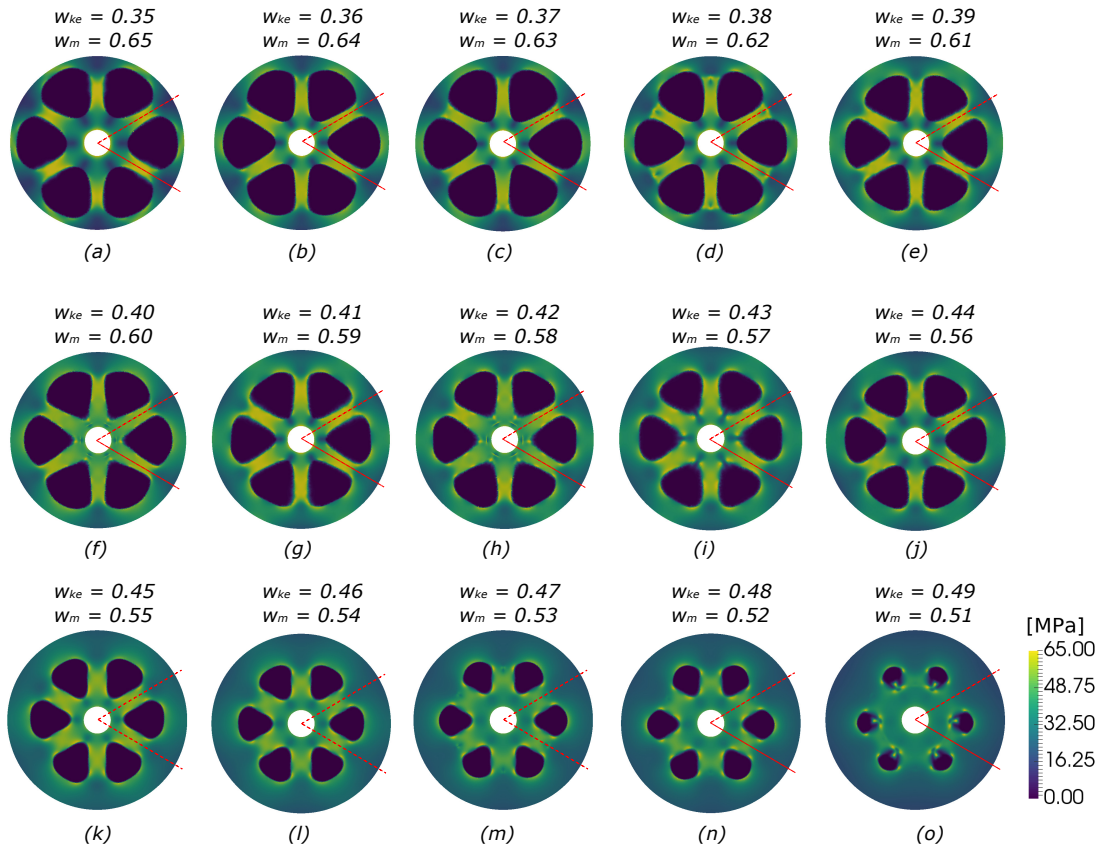


Figure 5.3: Stress distributions in the optimal rotors obtained using the multi-objective (max energy, min mass) and the Augmented Lagrangian approach with local stress constraints, using several combinations of objective function weights  $w_{ke}$  and  $w_m$

Table 5.2: Comparison of non-dominated optimal rotor designs obtained with different objective function weights for the multi-objective Augmented Lagrangian formulation

$w_{ke}$	$w_m$	$E_{\text{kin}}, \text{ J}$	$m, \text{ kg}$	$e_{\text{kin}}, \text{ J/kg}$	$\sigma_{pn}, \text{ MPa}$	$\frac{V}{V_0}$	$M_{nd}, \%$
0.35	0.65	65,927	22.05	2989.09	65.59	0.48	5.00
0.36	0.64	74,683	23.31	3204.05	64.99	0.50	3.27
0.37	0.63	72,821	22.77	3198.59	66.10	0.51	4.28
0.38	0.62	77,979	24.11	3233.83	65.08	0.54	5.26
0.39	0.61	90,607	27.26	3324.24	66.75	0.58	4.64
0.40	0.60	89,625	27.09	3308.79	64.98	0.58	4.76
0.41	0.59	96,507	28.68	3364.37	65.99	0.63	5.21
0.42	0.58	95,579	28.82	3316.85	68.09	0.62	5.88
0.43	0.57	100,536	30.60	3285.52	65.00	0.67	6.17
0.44	0.56	98,156	29.72	3303.04	64.98	0.63	4.11
0.45	0.55	111,372	34.69	3210.51	64.93	0.73	3.85
0.46	0.54	117,762	37.61	3131.54	64.99	0.79	3.07
0.47	0.53	119,358	39.01	3059.68	64.87	0.82	3.17
0.48	0.52	120,701	39.58	3049.55	64.99	0.83	3.47
0.49	0.51	127,355	43.18	2949.40	65.03	0.91	4.44
1.00	0.00	135,144	48.21	2803.10	48.76	1.00	0.0

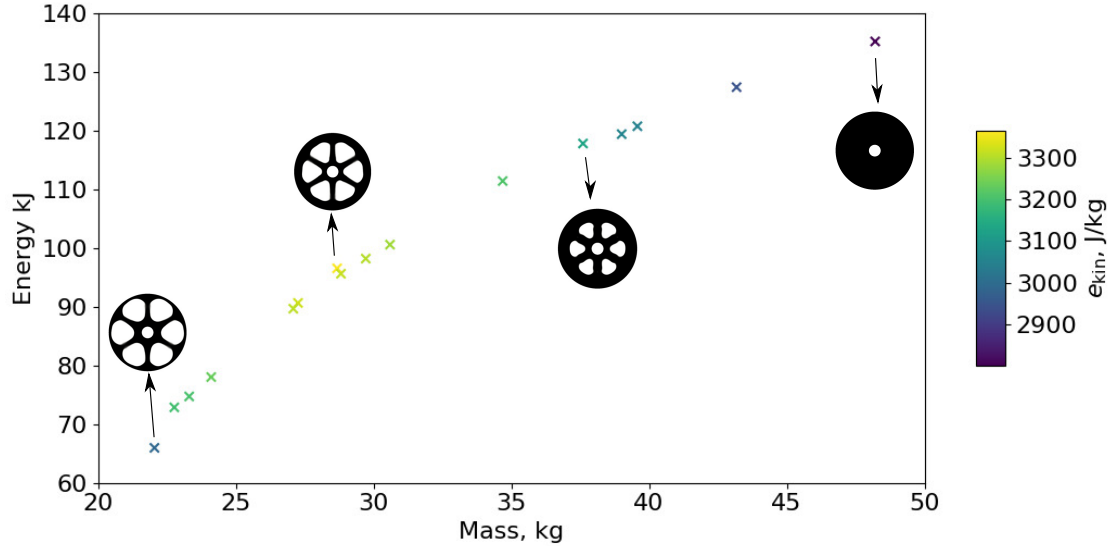


Figure 5.4: Pareto optimal designs for the multi-objective rotor design problem using the Augmented Lagrangian approach

rotor design depending on the design specifications on the minimum energy capacity or maximum rotor weight. Different criteria, such as specific energy, energy-per-cost, or total energy capacity could be used for selecting the best rotor design for different FESS applications such as transportation or grid-scale storage. For example, for transportation applications one might tend to choose lightweight rotors, while ensuring a reasonably high specific energy. On the other hand, rotors with slightly higher weights and a reasonably high specific energy could benefit grid-scale applications that use low-cost rotor materials.

### 5.2.2 Local vs global stress constraints

The designs obtained with the Augmented Lagrangian approach with local stress constraints were compared to those obtained using the global P-norm stress constraint. While the local stress-constrained approach used a multi-objective formulation to maximize the energy and minimize the mass seen in equation (5.2), the reference global stress constrained formulations used here are the kinetic energy formulation from equation (4.1) and the specific energy formulation from equation (4.2).

Table 5.3: Comparison of optimal 2D rotor designs obtained using global P-norm and local (Augmented Lagrangian) stress constraints

Approach	$\frac{V}{V_0}$	$E_{\text{kin}}, \text{ J}$	$m, \text{ kg}$	$e_{\text{kin}}, \text{ J/kg}$	$\sigma_{pn}, \text{ MPa}$	$\frac{\Delta e_{\text{kin}}}{e_{\text{kin}}^0}, \text{ \%}^*$	$M_{nd}, \text{ \%}$
Uniform disk	1.0	135,144	48.21	2803.1	48.76	-	-
Global, KE formulation	0.65	97,599	31.06	3142.4	65.97	+12.10	1.54
Global, SE formulation	0.65	101,018	31.13	3244.8	64.92	+15.76	8.12
Local	0.63	100,536	30.60	3285.52	65.00	+17.21	6.17

\*  $e_{\text{kin}}^0$  is the specific energy of uniform thickness rotor

Figure 5.5 compares the equivalent global and local stress constrained designs with similar rotor masses. The global stress constrained designs with kinetic energy (with volume fraction of 65%) and specific energy maximization formulations were seen to be closest in terms of rotor mass, to the MOO formulation designs with objective weights of ( $w_{ke} = 0.43$ ,  $w_m = 0.57$ ). The geometry obtained with local stress constraints had a thicker outer rim and thinner spokes when compared to the global stress constrained design with the kinetic energy formulation. On the other hand, the specific energy formulation and the local stress constrained design had a similar bulge in the spokes of the optimal designs. The local stress constrained designs had a much more uniform stress distribution than both global stress designs, which likely resulted in the differences in the geometry. The local stress design also had an overall higher specific energy rotor than the global stress designs, as seen in Table 5.3.

As seen from the discreteness measure  $M_{nd}$  for the three designs in Figure 5.5(d-f), the kinetic energy formulation with a global stress constraint resulted in the most discrete design, followed by the MOO formulation with local stresses, and the specific energy formulation with global stress constraint. This resulted in some noise at the edges, which could be improved in the future using a robust formulation to achieve better convergence.

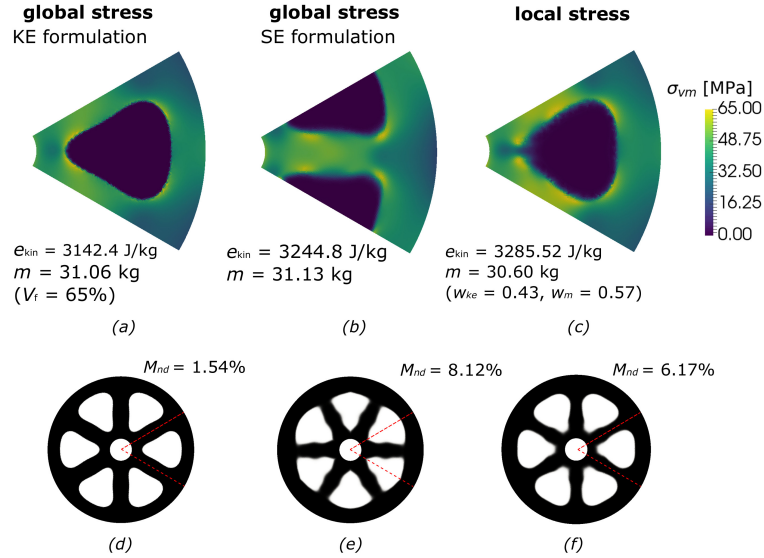


Figure 5.5: Comparison of stress distributions and flywheel topologies for designs obtained with a),d) global stress constrained  $E_{kin}$  formulation, b),e) global stress constrained  $e_{kin}$  formulation, and c),f) local stress constrained MOO formulation

### 5.3 Summary

The local stress constrained optimization formulation with an Augmented Lagrangian approach was evaluated to try and achieve a better stress distribution in the optimal topology. A multi-objective formulation was used to maximize the kinetic energy and minimize the rotor mass, subject to local stress constraints, using a weighted sum approach to combine the two objectives. A Pareto-front of optimal designs with different energy and mass combinations was obtained. Certain weight combinations resulted in designs with a volume fraction of 55-65% and the highest specific energy. Comparing the locally stressed optimal designs to the global stress constrained designs from the original formulation, the former resulted in a more uniform stress distribution compared to the P-norm global stress constraint, where undesirable local stress concentrations could be seen at narrow bottleneck regions. The local stress constraints also improved the specific energy of the optimal design to a larger extent than the global stress constraints.

# Chapter 6

## Modified robust approach for 3D rotor topology optimization

### Preface

The new specific energy formulation for rotor design proposed in Chapter 4 removed the dependence of the optimization on an artificial volume fraction constraint. However, using the specific energy as the objective function made the optimization problem harder to converge and additional measures were needed to reduce remnant gray elements from the optimal design. A volume preserving projection filter was used to improve the convergence of the stress-constrained problem, with a 1D line-search for determining the filter threshold at each optimization iteration. However, the resulting rotor designs still had gray regions which could not be completely eliminated. A modified robust strategy was investigated in this chapter, to explore its feasibility for solving the specific energy formulation for rotor design and achieving better discreteness of the optimal design. This strategy was then used to optimize the 3D topology of the flywheel. The optimal 3D designs were compared with 2D topology optimized designs from Chapters 4 and 5 and shape optimized designs using the framework from Chapter 3.

## 6.1 Methodology

This study aims at achieving a fully discrete topological design with the specific energy flywheel optimization formulation in Chapter 4, by taking inspiration from the robust design approach proposed by Wang et al. [122], which was able to achieve better convergence for stress-constrained problems using three different structures to predict the stresses in the design. In particular they solved three different FEM problems at each optimization iteration, i.e., a dilated, blueprint and eroded design obtained by using three different threshold values for the projection filter. In this work, to reduce the additional computational expense of the robust approach proposed in reference [122], a modified robust approach similar to the one proposed by Andreasen et al. [125] is used, that evaluates the optimization objective and constraint on the dilated and eroded designs respectively, and evaluates the blueprint design only at fixed intervals to update the constraint target. A block diagram of the modified robust topology optimization framework is shown in Figure 6.1.

The overall methodology for topology optimization described in Chapter 4 was reused in this study, including the proposed SIMP modifications to the numerical model described in Section 4.1.1, the optimization responses and adjoint sensitivity analysis from Section 4.1.2, and the density filtering stage described in Section 4.1.3. The modified robust optimization formulation and its implementation are described below.

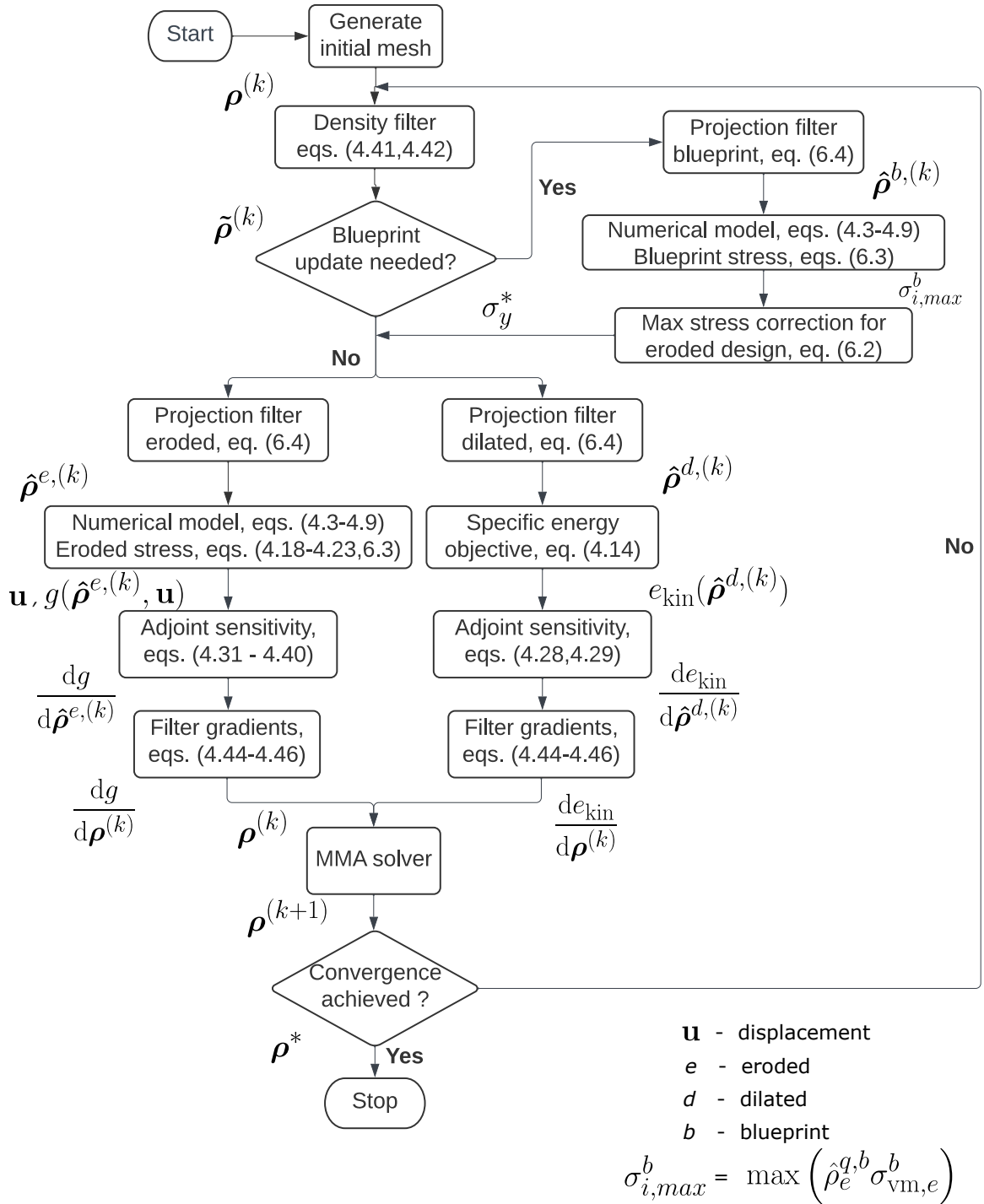


Figure 6.1: Flowchart of the modified robust approach for rotor topology optimization

### 6.1.1 Modified robust formulation

The modified robust approach is used to solve the following specific energy formulation,

$$\begin{aligned}
\max e_{\text{kin}}(\hat{\boldsymbol{\rho}}^d) &= \frac{\frac{1}{2}I(\hat{\boldsymbol{\rho}}^d)\omega^2}{m(\hat{\boldsymbol{\rho}}^d)} \\
\text{w.r.t } \hat{\boldsymbol{\rho}} &= \{\hat{\rho}_1, \hat{\rho}_2, \dots, \hat{\rho}_N\} \\
\text{s.t. } K^e U^e &= F^e \\
g(\hat{\boldsymbol{\rho}}^e, \mathbf{u}) &: \frac{\tilde{\sigma}_{pn}^e}{\sigma_y^*} - 1 \leq 0 \\
0.0 &\leq \hat{\rho}_i^e \leq 1.0
\end{aligned} \tag{6.1}$$

where the superscripts  $d$  and  $e$  on the design densities refer to the dilated and eroded designs.

At each optimization iteration, the stress constraint,  $g(\hat{\boldsymbol{\rho}}^e, \mathbf{u})$ , is evaluated on the eroded design, and the specific energy objective,  $e_{\text{kin}}(\hat{\boldsymbol{\rho}}^d)$ , is evaluated using the dilated design. Since the objective function is independent of the FEM solution, a single FEM evaluation per iteration is sufficient to solve this problem. The eroded design is expected to have higher stresses, so the maximum allowable stress for the eroded design,  $\sigma_y^*$ , is periodically re-estimated using the blueprint stresses, as follows:

$$\sigma_y^* = \frac{\tilde{\sigma}_{pn}^e}{\sigma_{i,\max}^b} \sigma_y \tag{6.2}$$

where  $\sigma_y$  refers to the maximum allowable stress in the rotor. Here, the eroded normalized P-norm stress,  $\tilde{\sigma}_{pn}^e$ , and the maximum relaxed von Mises stress in the blueprint design,  $\sigma_{i,\max}^b$  are calculated as:

$$\begin{aligned}
\tilde{\sigma}_{pn}^e &= c \left( \sum_{i=1}^N v_i (\hat{\rho}_i^{q,e} \sigma_{\text{vm},i}^e)^P \right)^{\frac{1}{P}} \\
\sigma_{i,\max}^b &= \max \left( \hat{\rho}_i^{q,b} \sigma_{\text{vm},i}^b \right)
\end{aligned} \tag{6.3}$$

where  $c$  is the normalization parameter,  $q$  is the stress relaxation term, and  $\sigma_{\text{vm},i}$  is the von Mises stress calculated at the centroid of element  $i$ . The blueprint stresses,  $\sigma_{i,\max}^b$ ,

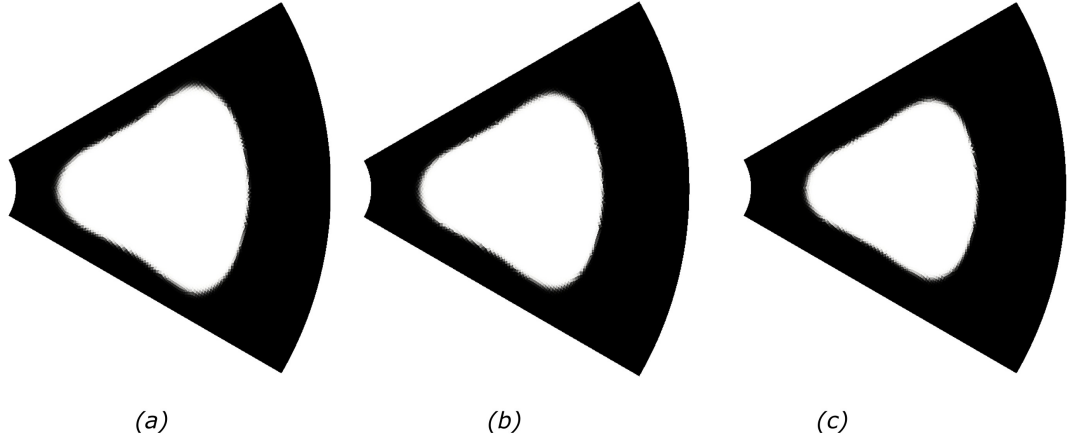


Figure 6.2: Projected density maps for an example 2D topology depicting: a) eroded ( $\hat{\rho}^e$ ), b) blueprint ( $\hat{\rho}^b$ ), and c) dilated ( $\hat{\rho}^d$ ) designs

are calculated using the projected design density variables  $\hat{\rho}^b$ , which are obtained using a projection filter threshold of 0.5. These are only evaluated from time to time, with the frequency chosen heuristically for each simulation (e.g., once in every 20 iterations), and need not be computed at all optimization iterations. As an example, Figure 6.2 shows the three projected density maps (eroded, blueprint, and dilated) for a 2D rotor topology. While the eroded and dilated density maps are utilized to compute responses and their gradients at every optimization iteration, the blueprint density map is only used to provide a stress correction update.

The projected densities for the eroded designs,  $\hat{\rho}^e$  are calculated using

$$\hat{\rho}_i^e = \frac{\tanh(\beta h^e) + \tanh(\beta(\tilde{\rho}_i - h^e))}{\tanh(\beta h^e) + \tanh(\beta(1 - h^e))} \quad (6.4)$$

where  $h^e$  is the eroded threshold, and its value is between  $(h^b, 1.0]$ . Similarly, the dilated design  $\hat{\rho}^d$  is computed using Equation (6.4), but using a dilated threshold  $h^d$ , that is typically chosen as  $1.0 - h^e$ . The blueprint threshold  $h^b$  is chosen as 0.5 to ensure that the volume fraction of the design is preserved. Broadly speaking, the thresholds for the three designs are chosen such that  $0 < h^d < h^b (= 0.5) < h^e < 1.0$ .

### 6.1.2 3D numerical model

The flywheel numerical model described in Section 4.1.1 is dimension independent and is reused here. The flywheel geometries used in the 3D simulations can be seen in Figure 6.3(a) where mid-plane symmetry along the z-axis is used to reduce the height of the mesh to half, and Figure 6.3(b), where the full height of the rotor is considered for analysis. The reduced mesh in Figure 6.3(a) is used for a majority of the 3D studies conducted, whereas the mesh with the full rotor height in Figure 6.3(b) is used to study the effect of computational domain size on the optimal topology. In both cases, rotational symmetry is used to further reduce the size of the computational domain. The inner and outer rings are considered fixed portions of the topology, and the region between these two rims is treated as the topology optimization domain. The open-source mesh generation tool Gmsh [115] is used to parametrize this geometry and generate the unstructured hexahedral mesh seen in Figure 6.3(c), which also depicts the boundary conditions for the problem. An average element side length of 3 mm is used to generate the mesh.

Similarly, the optimization responses described in Section 4.1.2 are also reused here, with the only exception being the definition of the Auxiliary matrix,  $V$ , used to calculate the von Mises stresses,  $\sigma_{vm}$ , at the centroids of the mesh elements. The 3D auxiliary matrix is:

$$\mathbf{V} = \begin{bmatrix} 1 & -\frac{1}{2} & -\frac{1}{2} & 0 & 0 & 0 \\ -\frac{1}{2} & 1 & -\frac{1}{2} & 0 & 0 & 0 \\ -\frac{1}{2} & -\frac{1}{2} & 1 & 0 & 0 & 0 \\ 0 & 0 & 0 & 3 & 0 & 0 \\ 0 & 0 & 0 & 0 & 3 & 0 \\ 0 & 0 & 0 & 0 & 0 & 3 \end{bmatrix} \quad (6.5)$$

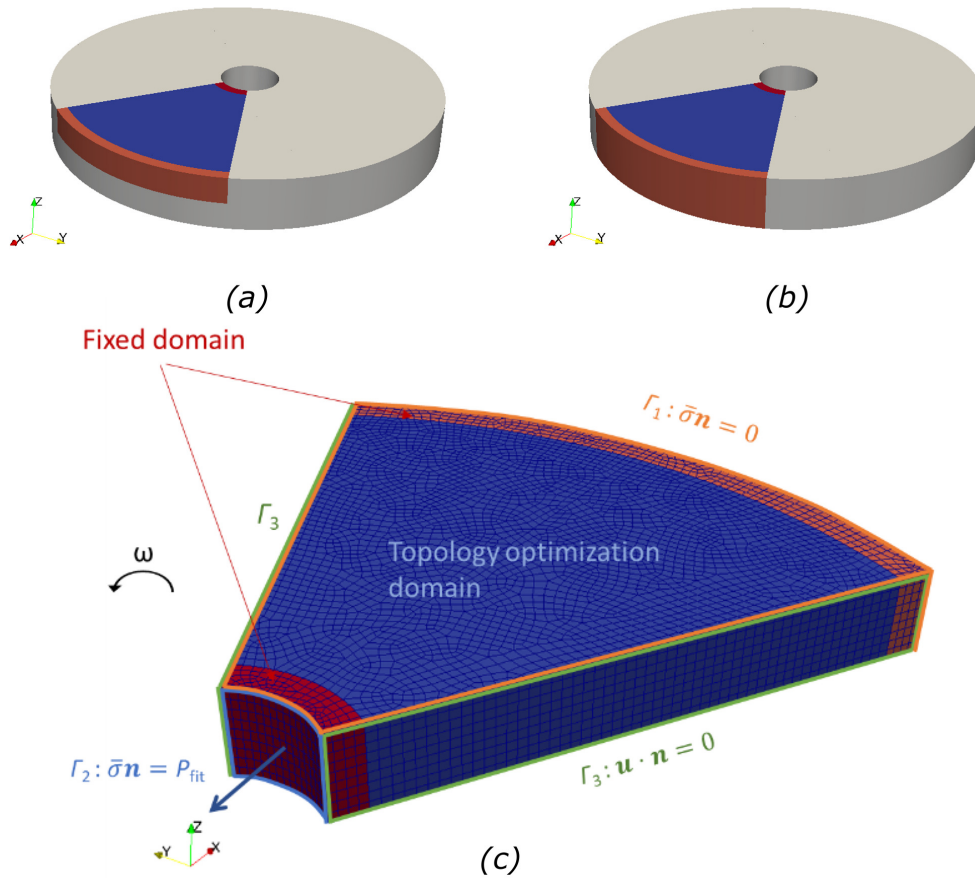


Figure 6.3: a) 3D rotor domain using a) half the rotor height  $H/2$ , b) full rotor height  $H$ , and c) unstructured hexahedral mesh using rotational symmetry ( $N=6$ ), with corresponding boundary conditions

### 6.1.3 Solver

The above optimization problem is solved using the MMA solver for inequality constrained problems that was previously discussed in Section 4.1.4.

## 6.2 Results and discussion

### 6.2.1 2D robust design compared to conventional design

Initially, the 2D rotor topology was optimized using the proposed modified robust approach and compared to results from Chapter 4 that were obtained using the conventional topology optimization method. Table 6.1 contains the simulation parameters used for this study, including the projection filter thresholds for the eroded and dilated designs and the target stress correction update interval used in the modified robust approach.

Figure 6.2 shows the optimal eroded, blueprint and dilated designs obtained with respective projection filter thresholds of 54, 50 and 46%. The convergence histories of the optimization responses and the measure of discreteness convergence criterion can be seen in Figure 6.4. Figure 6.4(a) plots the convergence of the specific energy objective evaluated on the dilated designs, with the actual specific energy evaluated using the blueprint design every 20 iterations being slightly higher. Similarly, Figure 6.4(b) plots the convergence of the eroded P-norm stress,  $\tilde{\sigma}_{pn}^e$ , as well as the blueprint stress measure,  $\sigma_{i,\max}^b$ , computed on the blueprint design every 20 iterations. While the maximum allowable stress for the blueprint stress,  $\sigma_y$ , is fixed throughout, the maximum stress for the eroded design,  $\sigma_y^*$ , is periodically corrected, and is seen to increase or decrease depending on the ratio  $\tilde{\sigma}_{pn}^e/\sigma_{i,\max}^b$ . The correction allows the blueprint design to converge to a feasible optimal topology.

The optimal solutions for the specific energy formulation obtained using the modified robust approach versus the volume preserving approach can be seen in Figure 6.5 and Table 6.2. Comparing the discreteness measure  $M_{nd}$  for the two designs, the

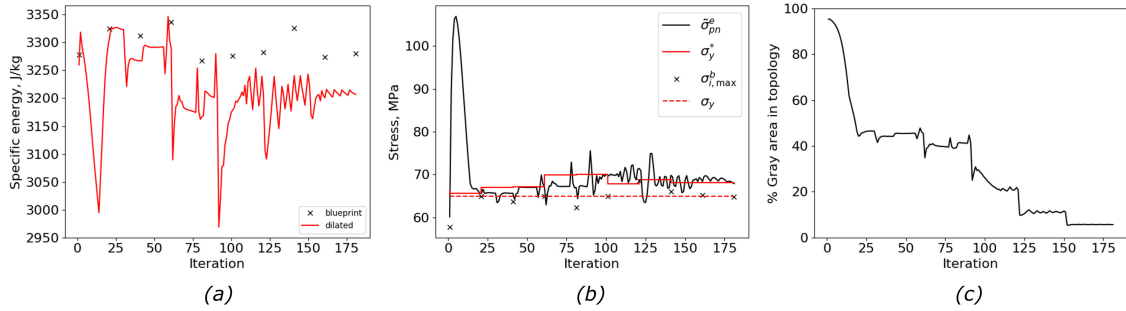


Figure 6.4: Convergence plots of the a) specific energy objective, b) stress constraint and c) convergence criterion in the modified robust approach

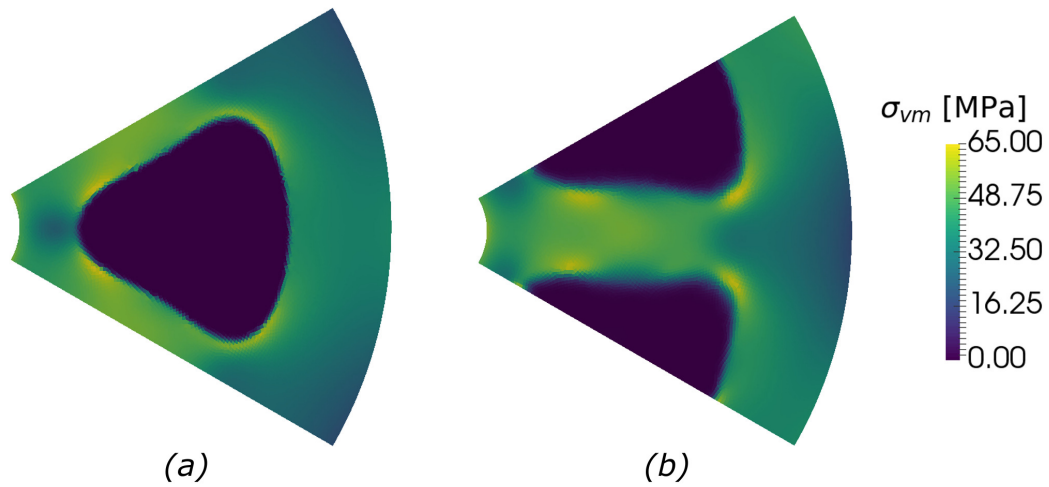


Figure 6.5: Optimal topology obtained using a) the robust approach and b) the volume preserving approach

modified robust approach allowed the design to converge to a higher degree than the volume preserving approach, while also achieving convergence in fewer iterations. The computational cost of each iteration was similar in both cases, since both the modified robust formulation and the conventional approach used a single FEM evaluation per iteration. Both designs had similar volume fractions and energy capacities. Thus, this approach can be used to improve the convergence, robustness and discreteness of the specific energy formulation for rotor design. These improvements enabled us to evaluate 3D rotor topologies with the specific energy formulation.

Table 6.1: Topology optimization parameters for specific energy maximization of flywheel rotor using modified robust approach

Parameter set	Parameter	Value
Material Properties	Young's modulus ( $E$ ), GPa	210
	Poisson's ratio ( $\nu$ )	0.3
	Solid density ( $\rho$ ), kg/m <sup>3</sup>	7850
Flywheel model	Rotor height, m	0.05
	Shaft boundary condition	Neumann (press-fit)
	Angular velocity ( $\omega$ ), rpm	5000
	Inner radius ( $r_{shaft}$ ), m	0.03
	Outer radius ( $r_{out}$ ), m	0.2
	Fixed rims thickness ( $t_{rim}$ ), m	0.01
SIMP parameters	Penalty ( $p$ )	3
	Initial design ( $\rho_0$ )	0.55
	Minimum Young's modulus ( $E_{min}$ ), GPa	1
MMA parameters	$a$	0.0
	$c$	1000.0
	$d$	0.0
	$\gamma^{(+)}$	1.2
	$\gamma^{(-)}$	0.7
	Move limit	0.03
Density filter	Filter radius ( $r_{filt}$ ), m	0.035
	Distribution	linear decay / conical
Projection filter	Threshold ( $h$ )	1D line search
	Initial slope ( $\beta_0$ )	1
	Maximum slope ( $\beta_{max}$ )	100
	Update interval	25
Mesh parameters	Rotational symmetry ( $N$ )	6
	Elements	11988
Stress constraint aggregation	$\sigma_y$ , MPa	65
	P-norm ( $P$ )	8.0
	Stress relaxation ( $q$ )	1.0
Modified Robust approach	$h^e$	0.54
	$h^b$	0.5
	$h^d$	0.46
	Blueprint correction interval	20 iters

Table 6.2: Comparison of optimal 2D rotor designs obtained using a) the robust approach and b) the volume preserving approach, with the specific energy formulation

Approach	$E_{\text{kin}}, \text{J}$	$m, \text{kg}$	$e_{\text{kin}}, \text{J/kg}$	$\sigma_{pn}, \text{MPa}$	$\frac{V}{V_0}$	$\frac{\Delta e_{\text{kin}}}{e_{\text{kin}}^0}, \%$ *	Iterations	$M_{nd}, \%$
Robust	104,573	31.98	3269.43	65.08	0.674	+16.63	181	2.83
Volume preserving	101,018	31.13	3244.8	64.92	0.646	+15.76	401	8.12

\*  $e_{\text{kin}}^0$  is the specific energy of uniform thickness rotor

## 6.2.2 3D Rotor topology

The 3D topology of the rotor was optimized using the implemented robust specific energy optimization framework and simulation parameters in Table 6.1. A coarser mesh with a global element size of 3 mm (compared to 1.5 mm for 2D) was chosen for this study. This was to allow the use of the MUMPS direct solver for the 3D simulation. As the mesh is refined, the use of an iterative solver becomes critical for 3D topology simulations. Although CG is the solver of choice for symmetric positive definite problems like the linear elastic equations, the global matrix becomes ill-conditioned for topology simulations because of the presence of holes and intermediate densities. Multigrid preconditioners are needed to then solve the 3D problems with iterative solvers. This was outside the scope of this thesis, and as a result, the 3D studies reported here are all performed using direct solvers without preconditioners.

The 3D topology was identical to the 2D design in the  $r-\theta$  plane, and had relatively little to no geometrical variations in the  $z$ -direction, as seen in Figure 6.6. Table 6.3 compares the energy capacity, mass and stresses developed in the two designs, which indicates that the 3D design has a slightly lower specific energy, due to a slightly higher volume fraction than the optimal 2D design. Both designs converged to a high level of discreteness (measured as a % value by  $M_{nd}$ ). The corresponding DoFs and total time for simulation are also recorded in Table 6.3, with the coarser 3D mesh requiring four times the number of DoFs used in the 2D design. This study suggested that there was no added benefit of using the 3D domain with more DoFs and an additional dimension. However, it is possible that the obtained design is a

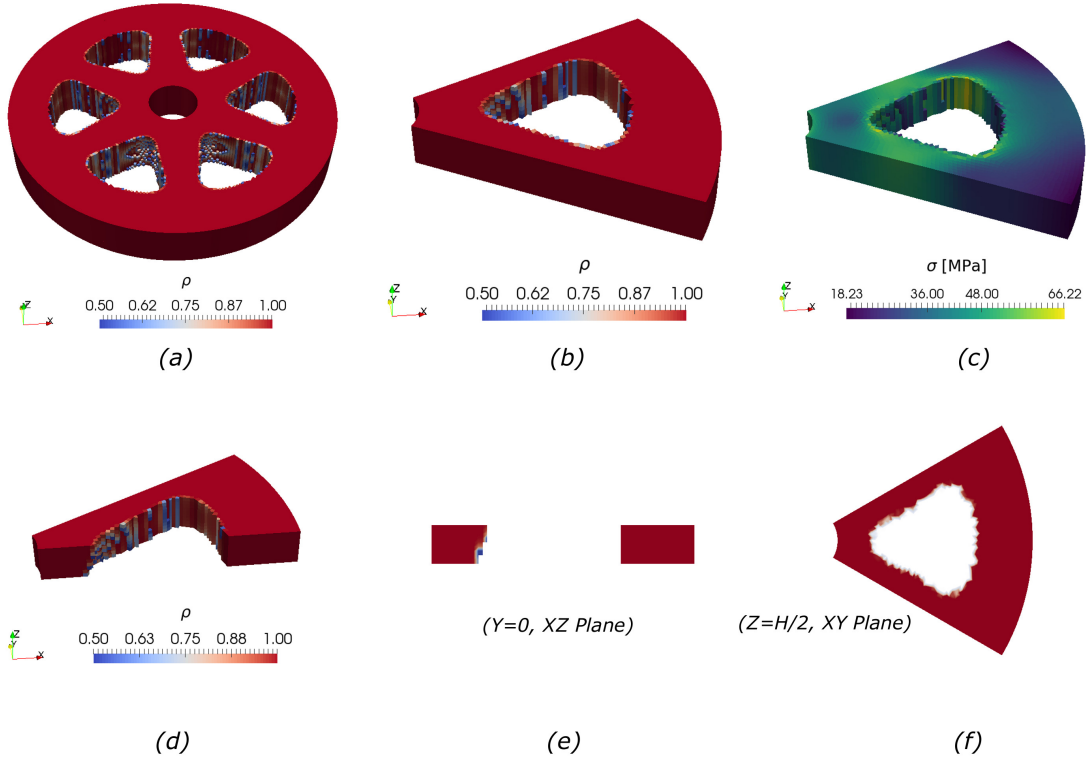


Figure 6.6: a) Full 3D topology, b) optimal topology ( $\rho > 0.5$ ), c) stress distribution, d) clipped view of 3D topology, e)  $r$ - $z$  plane slice of 3D topology, f)  $r$ - $\theta$  plane slice of 3D topology

local optimum resulting from the use of a density filter radius similar to the height of the rotor mesh used in the study, i.e., 35 mm vs 25 mm. Therefore, studies were performed where the density filter radius, mesh refinement and computational domain size (E.g., using the full rotor height or different circular section to offset filter effects) were changed to understand their influence on the optimal design.

Table 6.3: Comparison of optimal 2D and 3D rotor topologies obtained with the robust specific energy formulation in Eq. (6.1)

Dimension	$E_{\text{kin}}$ , J	$m$ , kg	$e_{\text{kin}}$ , J/kg	$V_f$	$\bar{\sigma}_{pm}$ , MPa	$M_{nd}$ , %	DoFs	Time, s (4 cores)
2D	104,573	31.98	3269.43	0.674	65.08	2.83	23976	758
3D	110,129	35.11	3136.33	0.735	65.28	1.57	98730	18137

### 6.2.2.1 Effect of density filter radius

When the density filter radius from the 2D simulations was varied in the range 10 mm to 35 mm, some geometrical variations in the z-direction and corresponding design improvements started to emerge. For filter radii of 10-25 mm, a mesh with element size ( $lc$ ) of 2 mm was used, whereas for the studies with filter sizes 30 and 35 mm, coarser mesh with element size ( $lc$ ) of 3 mm had to be used to achieve convergence.

Figure 6.7 and Table 6.4 contain the optimal topologies and designs for different density filter radii. It is seen that for smaller density filters, the optimal topology does not have any spokes, and a nearly axisymmetric design is obtained. The design somewhat resembles the designs obtained using shape optimization. With a filter radius of 25 mm, spokes start to emerge in the 3D design, with differences in the thickness along the Z-direction. For the largest filter radius of 35 mm, the design has very little variation in the Z-direction, as the filter size is larger than the height of the rotor in the Z-direction (=25 mm). Therefore, two very different optimal topologies were obtained, that either resembled the shape optimized designs from Chapter 3, or the designs with spokes in the  $r-\theta$  plane that were obtained in Chapters 4 and 5. Both options exhibited similar specific energy capacities and had similar rotor weights.

Table 6.4: Effect of density filter radius on the optimal 3D rotor topology obtained with the robust specific energy formulation

$r_{filt}$ , mm	$lc$ , mm	$E_{kin}$ , J	$m$ , kg	$e_{kin}$ , J/kg	$\tilde{\sigma}_{pn}$ , MPa	$M_{nd}$ , %
10	2	111,611	35.56	3138.60	65.61	1.96
15	2	107,302	33.38	3214.11	67.18	1.57
20	2	108,832	34.16	3185.77	64.05	2.36
25	2	109,018	34.01	3205.14	64.16	3.95
30	2	119,833	40.48	2960.08	65.37	1.16
35	3	110,129	35.11	3136.33	65.28	1.57

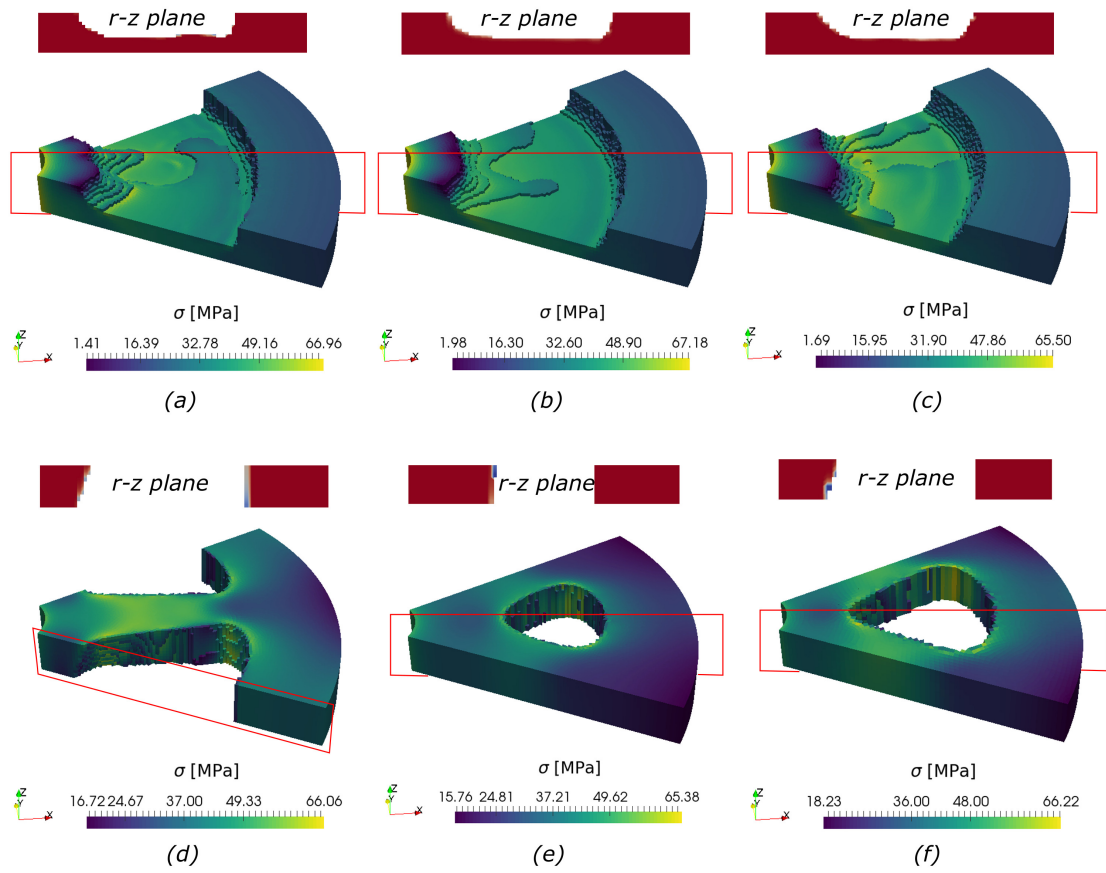


Figure 6.7: Optimal stress distribution in the 3D topology and corresponding  $r - z$  plane rotor profiles obtained using filter radius of a) 10 mm, b) 15 mm, c) 20 mm, d) 25 mm, e) 30 mm, f) 35 mm.

### 6.2.2.2 Effect of domain size

The previous studies that used a smaller density filter radius (10 - 20 mm) had a variable thickness design with no spokes, and larger filter radii (25 mm - 35 mm) resulted in a geometry with spokes, as well as some thickness variations along the height of the rotor. In order to investigate why the filter radius influenced the optimal topology, the size of the computational domain used for analysis was varied in two ways. In the first study, the rotational symmetry,  $N$ , used to determine the size of the  $r - \theta$  domain was changed from 6 (60° section) to 9 (40° section). Secondly, since symmetry in the  $z$ -direction was also used to reduce the size of the domain, the effect of using the full rotor height for analysis was also investigated.

Figure 6.8 shows the optimal 3D topologies obtained with rotational symmetries of  $N=6$  and  $N=9$ , with the same mesh size ( $lc = 2.0$  mm) and density filter radius ( $r_{filt} = 15$  mm). The emergence of spokes is more evident in the  $N=9$  topology, since the filter size is of the same order as the size of the section. Table 6.5 compares the two designs, which are very similar in terms of specific energy content as well.

Further, the chosen combination of mesh size,  $lc$ , and density filter,  $r_{filt}$ , was also seen to affect the optimal 3D topology for a given rotational symmetry. For instance, Figure 6.9 depicts three different topologies obtained with  $N=9$ . In Figure 6.9(a) and (b), the density filter radius  $r_{filt}$  was fixed at 10 mm, and the element size was varied from 1.5 to 2.0 mm, which significantly changed the optimal topology, although the specific energy of the two designs was similar. Whereas, in Figure 6.9(b) and (c), the density filter radius was varied from 10 to 15 mm, with a fixed mesh element size of 2.0 mm, which did not change the optimal topology to the same degree as the change in mesh size. A comparison of the specific energies and stresses in the three designs is in Table 6.6, which indicates that all three designs converged to a high degree of discreteness. Thus the influence of other design parameters such as angular speed and rotor height will also be investigated to determine the ideal choice of density filter

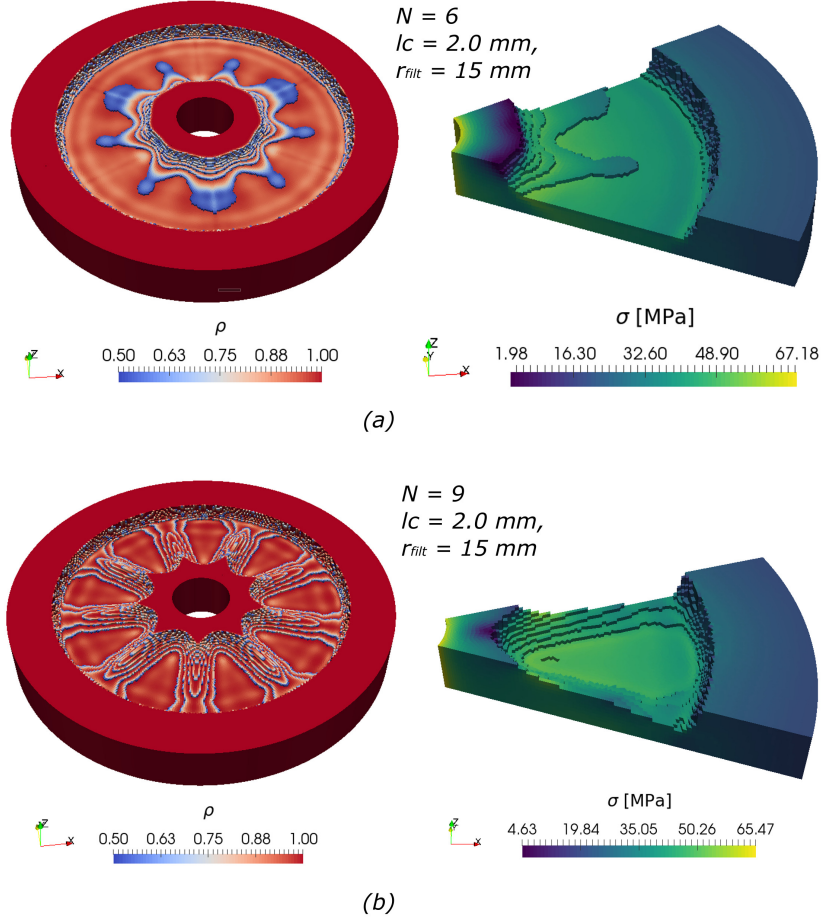


Figure 6.8: Optimal 3D topologies obtained using rotational symmetry of a)  $N = 6$ , and b)  $N = 9$ .

radius that is suitable for designing rotors at all operating conditions.

The 3D topology was also optimized using the entire height of the rotor, instead of using a plane of symmetry to reduce the z-direction thickness by half. The results of this study can be seen in Figure 6.10 and Table 6.7. The optimal topology obtained with using the full height of the rotor had spokes rather than the optimal shape profile obtained with the reduced domain of height  $H/2$ , and also had a lower specific energy. However, the design with the full height was simulated with a coarser mesh ( $lc = 3.0$  mm) due to limitations on the memory and computational speed that could be achieved with the existing CG solver.

Table 6.5: Effect of rotational symmetry on the optimal 3D rotor topology obtained with the robust specific energy formulation

$N$	$r_{filt}$ , mm	$lc$ , mm	$E_{kin}$ , J	$m$ , kg	$e_{kin}$ , J/kg	$\tilde{\sigma}_{pn}$ , MPa	$M_{nd}$ , %
6	15	2.0	107,302	33.38	3214.11	67.18	1.57
9	15	2.0	107,917	33.65	3206.75	64.87	2.49

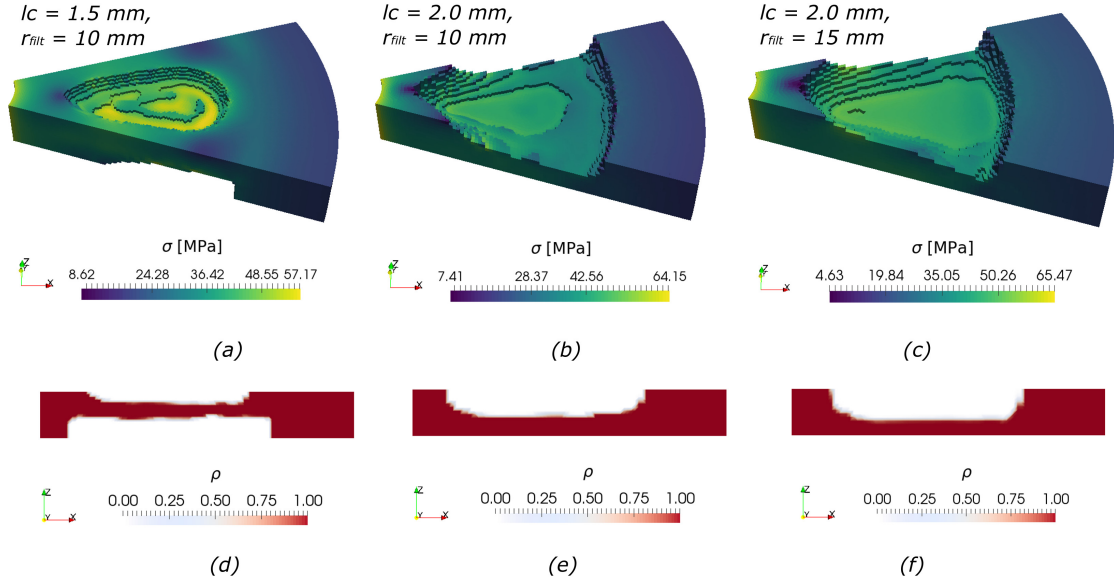


Figure 6.9: Optimal 3D topology ( $N=9$ ) and  $r - z$  plane views obtained using a),d)  $lc=1.5$  mm and  $r_{filt}=10$  mm, b),e)  $lc=2.0$  mm and  $r_{filt}=10$  mm, and c),f)  $lc=2.0$  mm and  $r_{filt}=15$  mm,

Table 6.6: Effect of rotational symmetry on the optimal 3D rotor topology obtained with the robust specific energy formulation

$r_{filt}$ , mm	$lc$ , mm	$E_{kin}$ , J	$m$ , kg	$e_{kin}$ , J/kg	$\tilde{\sigma}_{pn}$ , MPa	$M_{nd}$ , %
10	1.5	111,422	35.70	3120.61	61.26	2.03
10	2.0	111,190	35.19	3158.91	64.99	1.31
15	2.0	107,917	33.65	3206.75	64.87	2.49

Table 6.7: Effect of Z-direction symmetry on the optimal 3D rotor topology obtained with the robust specific energy formulation

$z$ -symmetry	$r_{filt}$ , mm	$lc$ , mm	$E_{kin}$ , J	$m$ , kg	$e_{kin}$ , J/kg	$\tilde{\sigma}_{pn}$ , MPa	$M_{nd}$ , %
$H/2$	20	2.0	108,832	34.16	3185.77	64.05	2.36
$H$	20	3.0	118,081	39.68	2975.55	66.34	1.22

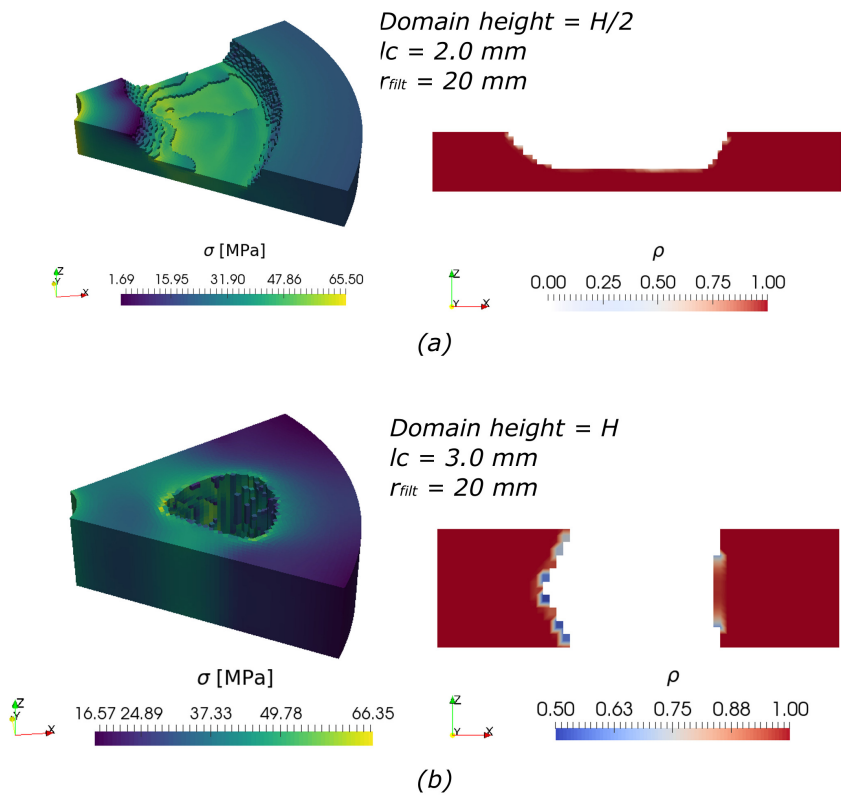


Figure 6.10: Optimal 3D topologies obtained using Z-direction symmetry of a)  $H/2$ , and b)  $H$ .

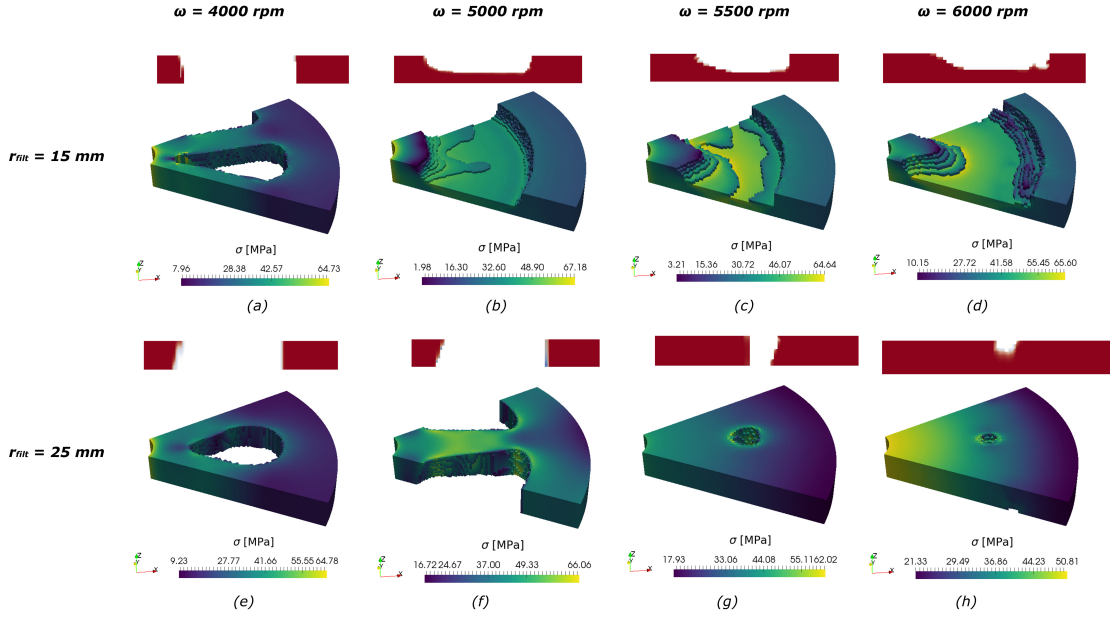


Figure 6.11: Optimal 3D topologies and  $r-z$  plane views obtained using two different density filter radii of 15 and 25 mm, with operating speeds of a),e)  $\omega = 4000$  rpm, b),f)  $\omega = 5000$  rpm, c),g)  $\omega = 5500$  rpm, and d),h)  $\omega = 6000$  rpm

### 6.2.2.3 Effect of operating speed on optimal topology

The effect of operating speed on the optimal 3D topology was studied by using two different density filter radii of 15 mm and 25 mm, which were seen to be representative of the two distinct rotor topologies obtained previously. Figure 6.11 and Table 6.8 show the optimal topologies for operating speeds in the range 4000 to 6000 rpm. Overall, the designs obtained with the smaller filter radius of 15 mm resulted in higher or equal specific energy designs compared to the 25 mm filter radius at all operating speeds. For higher speed of 5500 and 6000 rpm, the designs with  $r_{filt}=25$  mm were sub-optimal designs with a much lower specific energy than corresponding designs with  $r_{filt}=15$  mm, and they approached a constant thickness disk. Therefore, a smaller density filter was seen to increase the design space. On the other hand, at low operating speeds such as 4000 RPM, the design with  $r_{filt}=15$  mm had more spokes than the other designs, again resulting in a higher specific energy.

Table 6.8: Effect of operating speed and choice of density filter radius on the optimal 3D rotor topology obtained with the robust specific energy formulation

$\omega$ , rpm	$r_{filt}$ , mm	$lc$ , mm	$E_{kin}$ , J	$m$ , kg	$e_{kin}$ , J/kg	$\tilde{\sigma}_m$ , MPa	$M_{nd}$ , %
4000	15	3	70,047	34.11	2053.46	64.72	1.23
5000	15	2	107,302	33.38	3214.11	67.18	1.57
5500	15	3	129,702	34.21	3791.24	64.63	2.44
6000	15	3	144,780	32.79	4414.42	65.59	3.02
4000	25	3	73,686	37.08	1986.77	64.78	2.77
5000	25	2	109,018	34.01	3205.14	64.16	3.95
5500	25	3	160,744	47.08	3414.89	62.02	0.72
6000	25	3	193,296	47.87	4037.40	50.81	0.67

#### 6.2.2.4 Effect of rotor height on optimal topology

The effect of rotor height (or size) on the optimal 3D topology was investigated. A rotational symmetry of  $N=6$  and  $z$ -direction symmetry was used to reduce the size of the domain. Figure 6.12 and Table 6.9 contain the optimal topologies obtained using three different rotor heights of 40, 50, and 60 mm. For a density filter radius of  $r_{filt}=25$  mm, all three design look nearly identical, with a slight variation in the shape of the spokes along the  $z$ -direction. The specific energy of the three designs is also similar, whereas the kinetic energy and mass scale proportional to the height. This indicates that the rotor height could be used to scale the design to meet specific requirements on the minimum kinetic energy or maximum rotor weight.

Table 6.9: Effect of rotor height on the optimal 3D rotor topology obtained with the robust specific energy formulation

$H$ , mm	$r_{filt}$ , mm	$lc$ , mm	$E_{kin}$ , J	$m$ , kg	$e_{kin}$ , J/kg	$\tilde{\sigma}_m$ , MPa	$M_{nd}$ , %
40	25	3	87,616	27.69	3163.64	65.35	2.24
50	25	2	109,018	34.01	3205.14	64.16	3.95
60	25	3	131,957	41.62	3170.78	67.39	2.03

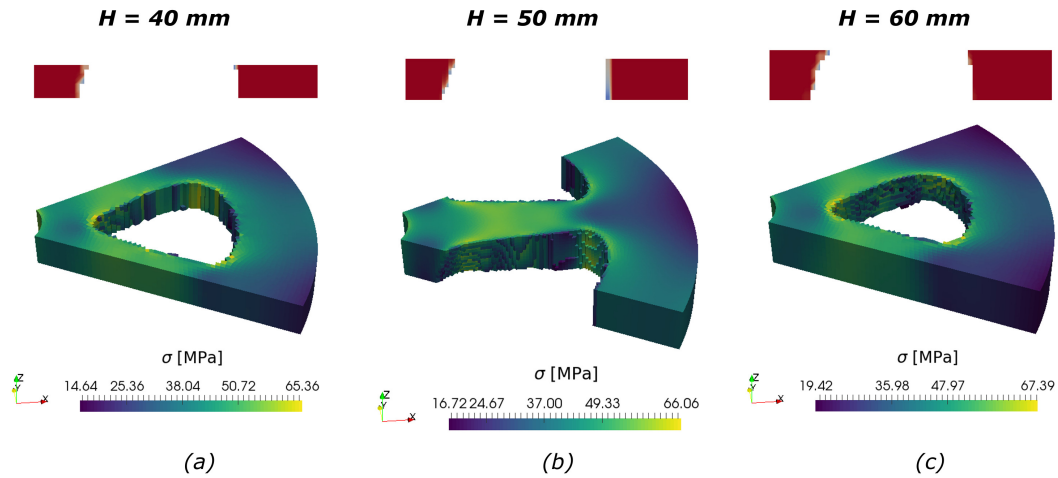


Figure 6.12: Optimal 3D topologies and  $r - z$  plane views obtained with different rotor heights of a)  $H = 40$  mm, b)  $H = 50$  mm, and c)  $H = 60$  mm

### 6.2.3 3D topology vs shape optimization

The two 3D designs obtained using topology optimization (with density filter,  $r_{filt}$ , set to 15 mm and 25 mm) were compared to a design obtained with the 2D axisymmetric rotor shape optimization framework from Chapter 3. In order to ensure the designs were equivalent, the inner and outer rims of the parameterized geometry used for the shape study were fixed. The thickness of the rotor between the fixed rims was approximated using a B-Spline function with eight control parameters, as shown in Figure 6.13(c). The optimization formulation described in Equation 3.17 was used, with the maximum stress,  $\sigma_y$ , set to 65 MPa, and the maximum rotor mass,  $m_{design}$ , being 33 kg to keep the design comparable to the 3D topology designs.

Figure 6.13 and Table 6.10 compare the shape optimized design with the two distinct topology designs obtained using the 3D robust specific energy formulation. The shape optimized design is somewhat similar to the topology design-2 shown in Figure 6.13(b) in terms of overall material and stress distribution, although it has a smoother thickness profile compared to the topology optimized design. Based on these results, either 2D shape optimization or 2D topology optimization are sufficient to achieve optimal rotor designs, with the selection of one method over the other

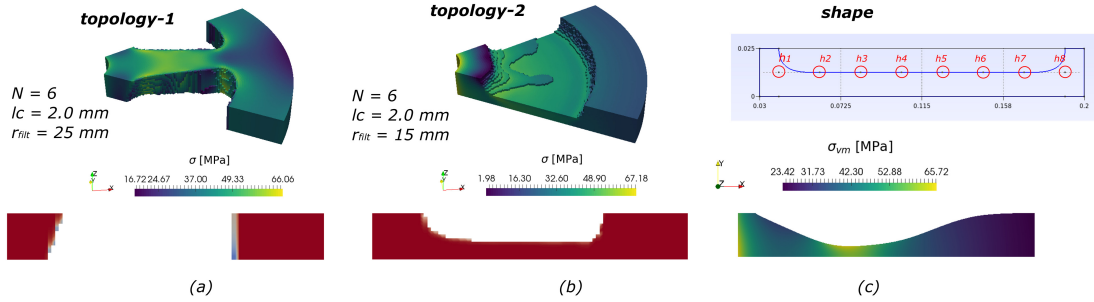


Figure 6.13: Comparison of optimal rotor geometry obtained using a) topology optimization, and b) shape optimization

being the manufacturing method. For the shape optimized designs, manufacturing complexity would be in the form of variations in the rotor thickness, and on the other hand, the design with spokes would require holes to be cut out into the circular cross-section of the rotor.

Table 6.10: Comparison of optimal rotor geometry obtained using topology optimization, and shape optimization

Method	$r_{filt}$ , mm	$lc$ , mm	$E_{kin}$ , J	$m$ , kg	$e_{kin}$ , J/kg	$\tilde{\sigma}_{pn}$ , MPa	$M_{nd}$ , %
Topology-1	25	2	109,018	34.01	3205.14	64.16	3.95
Topology-2	15	2	107,302	33.38	3214.11	67.18	1.57
Shape	-	1.5	107,987	32.84	3288.27	64.99	-

### 6.3 Summary

A modified robust approach was evaluated to improve the discreteness of the specific energy formulation for rotor topology optimization. It was found to achieve a more discrete design as compared to the volume-preserving approach used in Chapter 4. The modified robust approach used a single FEM evaluation per optimization iteration, compared to the traditional robust approach that would normally require three FEM evaluations per iteration. This made the modified robust approach a viable alternative to the volume preserving approach, as it also resulted in better and faster convergence to a discrete design.

The modified robust approach was subsequently used to design the 3D topology of the rotor. The optimal rotor topology was found to be sensitive to the choice of density filter radius. Two distinct rotor designs emerged when two different ranges of density filter radius were used for design. Topologies with lower filter radii ( $r_{filt} \leq 20$  mm) resulted in a design similar to the shape optimized rotor from Chapter 3. On the other hand, topologies with spokes were obtained with large filter radii ( $r_{filt} \geq 25$  mm), which were also seen in the 2D topology studies presented in Chapters 4 and 5, but with variations in the spoke thickness in the  $z$ -direction.

Since rotational and translational symmetry were used to reduce the size of the topology optimization domain, the effect of these parameters on the optimal design was also studied. Using a different circular section resulted in the gradual appearance of spoke-like formations in the topology without any holes. The use of the entire rotor height was also seen to influence the type of optimal design obtained, but this was likely due to the choice of a coarser mesh for the simulation that used the full rotor height. In the future, efforts will be directed towards reducing the memory and computational costs of topology optimization iterations so that large 3D simulations with fine meshes can be performed.

The effect of design parameters such as operating speed and rotor height on the 3D topology was also studied. A range of operating speeds between 4000 and 6000 rpm were used, along with two density filter radii of 15 and 25 mm for each speed. The lower filter radius resulted in higher specific energy designs for all speeds, while the larger filter radius resulted in designs that approached constant thickness rotors at high speeds. The optimal topologies obtained with three different rotor heights of 40, 50, and 60 mm were also evaluated with  $r_{filt} = 25$  mm. All three designs yielded similar looking topologies with similar energy densities. This indicated that the 3D rotors with spokes could be scaled to an appropriate height in order to scale the total energy capacity or weight of the rotor.

The two distinct 3D topologies obtained with the robust method were compared

with a shape optimized design based on the framework described in Chapter 3. All three designs had a similar specific energy, total energy and weight. The shape optimized design resembled one of the topology optimized designs in terms of stress and material distribution.

# Chapter 7

## Conclusions and future work

The optimal design of cost-effective and energy efficient FESS remains a challenge due to the high cost and low energy capacity of rotor materials used for rotor design. The interactions between several design parameters such as operating speed, rotor size and topology, and choice of material play an important role in determining the energy capacity and overall cost of the FESS. Advancements in large scale stress constrained topology optimization using numerical simulations are enabling complex 3D structural designs that can be manufactured with additive manufacturing techniques. The overall objective of this thesis was to develop an optimization framework that used numerical optimization techniques to design cost effective flywheel energy storage systems with improved energy storage characteristics. Such a unified framework would enable FESS designers or end users to determine the best FESS architecture, operating conditions and overall geometry or topology for their specific application.

This thesis presented an open-source optimization framework integrated with numerical rotor models of varying degrees of complexity that could be used to improve the energy capacity of the FESS rotor by optimizing its size, shape or topology, while using suitable rotor materials that minimized the cost or weight of the FESS. A 1D rotor model integrated with the DAKOTA optimization library [109] was implemented to allow for the analysis and optimization of several metal, composite or hybrid rotors with single or multiple press-fit rims. A 2D axisymmetric numerical

rotor model with a fully parameterized geometry was integrated with the DAKOTA library to enable rotor shape optimization. A density-based topology optimization framework integrated with 2D / 3D linear elastic numerical rotor model was implemented to allow the design of complex 3D rotor topologies. The numerical framework was developed as part of the open-source package OpenFCST [112].

The FESS literature contained many studies optimizing the rotor for either composite or metal flywheel rotors, however, a question that had not been addressed was - which material is more appropriate for different applications? To answer this question, optimal rotors with different materials were optimized based on different performance indices such as maximizing the kinetic energy, specific energy or energy-per-cost, that reflect the type of storage application. A number of composite and metal rotor materials with a constant thickness rotor profile were analyzed in this study. It was found that the choice of optimal material depended on the performance criterion being used. While composite rotors performed better in terms of specific energy, metal rotors had a better energy per cost. The total kinetic energy of both composite and metal rotors of a constant thickness were comparable. Press-fitted multi-rim composite rotors with specific material sequences could outperform single rim composite and metal flywheels, in terms of total energy or specific energy. However, when energy-per-cost was used as the performance criterion, multi-rim rotors offered no significant advantage over single-rim rotors. Therefore, the rest of this thesis focused on the optimal design of metal rotor FESS, which were generally more cost effective than composite rotors.

The next question was to determine what was the optimal rotor geometry that could improve the energy storage characteristics of low-cost metal flywheels. While most previous studies had designed optimally shaped rotors at fixed speeds and rotor radii, the simultaneous influence of rotor shape, speed, size and choice of rotor material had not been investigated. A framework to simultaneously optimize the rotor shape and multiple design specifications like speed, size and materials was de-

veloped [126], integrating a 2D axisymmetric numerical rotor model with a shape parametrization approach and an optimization toolbox. 21% to 46% improvements in the energy storage performance could be achieved by choosing the best combination of rotor shape, speed and radius. It was found that flywheels with the same weight, constructed with a large aspect ratio ( $r>h$ ) and operated at relatively low speeds of 6000 rpm had a higher energy capacity than low aspect ratio ( $h>r$ ) designs operated at high speeds of 10000 rpm. The low speed, flat rotor with a large radius had a lower self discharge than high-speed, tall rotors - which could be an important factor to be considered during the FESS design stage. The choice of rotor material also influenced the optimal speed-radius-shape combinations. For the same energy capacity, lower rotor radii and high speed optimally shaped aluminium rotors had a higher specific energy content than corresponding steel rotors, and vice-versa for higher rotor radii and low speeds.

Only one stress-constrained topology optimization study for flywheel design was found in literature [68], and it used a volume fraction constraint to remove material from the topology domain. In this thesis, it was determined via preliminary parametric studies, that the use of a volume fraction constraint for a stress-constrained energy maximization problem lead to suboptimal designs. Therefore a novel specific energy based formulation was proposed without a volume fraction constraint, and was shown to allow the optimizer to determine the ideal volume fraction which led to the best specific energy improvement. However, due to its non-convex nature, the specific energy objective was generally harder to converge than the kinetic energy problem, and strategies such as projection filter slope continuation and volume-preserving projection filter were adopted to achieve discrete optimal designs with the new formulation. The effect of other relevant FESS design parameters, such as speed, rotational symmetry, and materials, on the optimal designs obtained with both kinetic and specific energy formulations was investigated. The specific energy formulation achieved better design improvements than the kinetic energy formulation by using higher volume

fractions at low and high speeds, and lower volume fractions at intermediate speeds. While the kinetic energy formulation was sensitive to the choice of rotational symmetry used to reduce the computational domain size, the specific energy formulation was able to use different volume fractions and improve the energy capacity of the rotor to a similar extent; thus the choice of rotational symmetry could be based mainly on manufacturing or other considerations. The specific energy and optimal rotor topology obtained with different materials was identical if the material properties,  $E$  and  $\rho$ , scaled proportionally. The effect of acceleration related stresses on the optimal topologies were studied and determined to be significant only when considering extremely short duration charge-discharge cycles of less than 0.1 s.

Global stress measures were used in previous topology optimization literature on flywheel design [68] as well as other rotating disk applications such as motors [97, 98] and turbines [95, 96]. This thesis proposed the use of local stress constraints in the topology optimization formulation using an Augmented Lagrangian approach, to achieve a more uniform stress distribution in the optimal design. A multi-objective formulation was explored to maximize the kinetic energy and minimize the rotor mass, with a weighted sum approach to combine the two objectives, and subject to local stress constraints applied locally at all mesh elements. The multi-objective formulation was an alternative approach to the specific energy formulation, which also explored a larger design space compared to the conventional approach with constraints on the stresses and the volume fraction. A Pareto-front of optimal designs with different energy and mass combinations was obtained, and it demonstrated that designs with a volume fraction of 55-65% had the highest specific energy content. The locally stressed optimal designs resulted in a more uniform stress distribution compared to the P-norm aggregated global stress constraint used previously, where undesirable stress concentrations could be seen at narrow bottleneck regions.

The use of 3D topology optimization for flywheel design was relatively unexplored in literature, with a single study [82] that used a compliance based formulation with-

out any stress constraints. In this thesis, a modified robust approach was proposed to improve the discreteness of the specific energy formulation so that it could be used for 3D rotor design. The optimal 3D rotor topology was found to be sensitive to the choice of density filter radius. Two distinct rotor designs emerged when two different ranges of density filter radius were used for design. Topologies with lower filter radii ( $r_{filt} \leq 20$  mm) resulted in a design similar to the shape optimized rotor designs. On the other hand, topologies with spokes were obtained with large filter radii ( $r_{filt} \geq 25$  mm), which were similar to the 2D topology studies, but with additional variations in the spoke thickness in the  $z$ -direction. The two distinct 3D topologies obtained with the robust method were compared with a shape optimized rotor design. While all three designs had a similar specific energy, total energy capacity and weight, the shape optimized design closely resembled one of the topology optimized designs in terms of stress and material distribution. Further research in this area could be directed towards combining the designs obtained from the shape and topology optimization frameworks to achieve better design improvements, by using the optimally shaped rotor as a initial domain for 3D topology optimization. This could improve the specific energy of the system even further by optimizing material usage in the interior regions of the rotor, while maintaining a uniform stress distribution due to the smooth thickness profile of the shape optimized design.

## 7.1 Contributions

In terms of numerical methods and optimization, the contributions of this thesis are:

- the development of an open-source shape optimization framework integrated with a linear elastic numerical model and a parametrized meshing tool.
- the development of an adjoint solver for sensitivity analysis, which was vital for solving topology optimization problems with a large number of design variables.

- the development of an open-source and modular density-based topology optimization framework integrated with a linear elastic numerical model, with direct and adjoint solvers for sensitivity analysis. The modular nature of this toolbox is a key strength and differentiator, which makes it easy to add new optimization formulations, perform adaptive mesh refinement, or extend to multi-physics problems.
- the development of an Augmented Lagrangian framework to incorporate local stress constraints that can quickly achieve a more uniform stress distributions in complex geometries, compared to global stress constrained methods.
- the development of a modified robust topology optimization framework to achieve better convergence for problems with non-convex optimization objectives

The tools developed were integrated within an open-source framework, OpenFCST [112], based on the deal.ii finite element libraries [113], and were validated using benchmarking data from literature.

In terms of advancing the knowledge of the field, the key contributions of this work are:

- providing a comparative study of several optimal metal and composite rotor FESS, and establishing a means to determine the ideal FESS rotor material for an application based on different performance metrics such as specific energy, total energy and energy-per-cost.
- showing the importance of simultaneously optimizing operating speed, rotor size and shape in order to achieve larger improvements in the energy capacity of metal FESS rotors.
- demonstrating the use of a novel topology optimization formulation based on the specific energy objective and eliminating the need for a volume constraint to remove material from the topology design domain.

- demonstrating the use of a multi-objective formulation with an Augmented Lagrangian approach for local stress constraints in achieving a Pareto-front and designs with a more uniform stress distribution and subsequently, higher improvements in the design.
- demonstrating the use of a modified robust topology optimization formulation for achieving optimal rotor topologies with a high level of discreteness.

This study is the first unified approach for the design of energy storage rotors for FESS applications using a combination of several numerical models and optimization strategies.

## 7.2 Future work

The shape optimization framework developed in OpenFCST is currently integrated with 2D axisymmetric structural problems with a linear elastic model. This framework could be extended to account for large deformations and non-isotropic materials, which would allow for the analysis and shape optimization of FESS rotors with a larger set of materials. It would also allow for the use of the shape optimization framework for other multi-physics problems within the OpenFCST framework.

The density-based topology optimization framework in OpenFCST is currently integrated with 2D and 3D structural problems using a linear elastic numerical model. The future applications of this framework include performing multi-physics topology optimization simulations which would enable the addition of non-structural optimization responses into the optimization formulation. This will allow the use of this framework for designing novel porous microstructures used in electrochemical systems such as fuel cells and electrolyzers. Some other natural extensions to the topology optimization framework would be to implement a fully robust framework to account for manufacturing tolerances in the optimized designs, as well as a multigrid solver to solve very large 3D problems with millions of DoFs.

# Bibliography

- [1] *Climate action tracker*, <https://climateactiontracker.org/global/temperatures/>, Accessed: 2019-01-31.
- [2] *Climate action tracker eu*, [https://climateactiontracker.org/documents/505/CAT\\_2018-12-06\\_ScalingUp\\_EU\\_FullReport.pdf](https://climateactiontracker.org/documents/505/CAT_2018-12-06_ScalingUp_EU_FullReport.pdf), Accessed: 2019-01-31.
- [3] *Climate action tracker india*, <https://climateactiontracker.org/countries/india/>, Accessed: 2019-01-31.
- [4] *Natural resources canada*, <https://www.nrcan.gc.ca/energy/electricity-infrastructure/about-electricity/7359>, Accessed: 2019-01-31.
- [5] X. Luo, J. Wang, M. Dooner, and J. Clarke, “Overview of current development in electrical energy storage technologies and the application potential in power system operation,” *Applied energy*, vol. 137, pp. 511–536, 2015.
- [6] C. K. Das, O. Bass, G. Kothapalli, T. S. Mahmoud, and D. Habibi, “Overview of energy storage systems in distribution networks: Placement, sizing, operation, and power quality,” *Renewable and Sustainable Energy Reviews*, vol. 91, pp. 1205–1230, 2018.
- [7] *International energy agency*, <https://www.iea.org/tcep/energyintegration/energystorage/>, Accessed: 2019-01-31.
- [8] *National energy board market snapshot*, <http://www.neb-one.gc.ca/nrg/ntgrtd/mrkt/snpsht/2016/07-03bttrsdmmttstng-eng.html>, Accessed: 2019-01-30.
- [9] J. G. Bitterly, “Flywheel technology: Past, present, and 21st century projections,” *IEEE Aerospace and Electronic Systems Magazine*, vol. 13, no. 8, pp. 13–16, 1998.
- [10] R. F. Post and S. F. Post, “Flywheels,” *Scientific American*, vol. 229, no. 6, pp. 17–23, 1973.
- [11] R. F. Post, T. Fowler, and S. F. Post, “A high-efficiency electromechanical battery,” *Proceedings of the IEEE*, vol. 81, no. 3, pp. 462–474, 1993.
- [12] B. Bolund, H. Bernhoff, and M. Leijon, “Flywheel energy and power storage systems,” *Renewable and Sustainable Energy Reviews*, vol. 11, no. 2, pp. 235–258, 2007.

- [13] K. Mongird *et al.*, “Energy storage technology and cost characterization report,” Pacific Northwest National Lab.(PNNL), Richland, WA (United States), Tech. Rep., 2019.
- [14] H. Chen, T. N. Cong, W. Yang, C. Tan, Y. Li, and Y. Ding, “Progress in electrical energy storage system: A critical review,” *Progress in natural science*, vol. 19, no. 3, pp. 291–312, 2009.
- [15] P. Ralon, M. Taylor, A. Ilas, H. Diaz-Bone, and K Kairies, “Electricity storage and renewables: Costs and markets to 2030,” Tech. Rep., 2017.
- [16] M. A. Skinner, “Characterization of passive discharge losses in a flywheel energy storage system,” M.S. thesis, University of Alberta, 2017.
- [17] M Krack, M Secanell, and P Mertiny, “Cost optimization of hybrid composite flywheel rotors for energy storage,” *Structural and Multidisciplinary Optimization*, vol. 41, no. 5, pp. 779–795, 2010.
- [18] S. Jiang, H. Wang, and S. Wen, “Flywheel energy storage system with a permanent magnet bearing and a pair of hybrid ceramic ball bearings,” *Journal of Mechanical Science and Technology*, vol. 28, no. 12, pp. 5043–5053, 2014.
- [19] A. Filatov, P. McMullen, K. Davey, and R. Thompson, “Flywheel energy storage system with homopolar electrodynamic magnetic bearing,” *CEM Publications*, 2006.
- [20] T. M. Mulcahy *et al.*, “Flywheel energy storage advances using hts bearings,” *IEEE Transactions on Applied superconductivity*, vol. 9, no. 2, pp. 297–300, 1999.
- [21] G. Genta, *Kinetic energy storage: theory and practice of advanced flywheel systems*. Butterworth-Heinemann, 2014.
- [22] S. K. Ha, H.-M. Jeong, and Y.-S. Cho, “Optimum design of thick-walled composite rings for an energy storage system,” *Journal of Composite Materials*, vol. 32, no. 9, pp. 851–873, 1998.
- [23] S. Arnold, A. Saleeb, and N. Al-Zoubi, “Deformation and life analysis of composite flywheel disk systems,” *Composites part B: engineering*, vol. 33, no. 6, pp. 433–459, 2002.
- [24] M. Krack, M. Secanel, and P. Mertiny, “Advanced optimization strategies for cost-sensitive design of energy storage flywheel rotors,” *JOURNAL OF ADVANCED MATERIALS*, vol. 43, no. 2, pp. 65–78, 2011.
- [25] M. Mittelstedt, C. Hansen, and P. Mertiny, “Design and multi-objective optimization of fiber-reinforced polymer composite flywheel rotors,” *Applied Sciences*, vol. 8, no. 8, p. 1256, 2018.
- [26] S. K. Ha, D.-J. Kim, and T.-H. Sung, “Optimum design of multi-ring composite flywheel rotor using a modified generalized plane strain assumption,” *International Journal of Mechanical Sciences*, vol. 43, no. 4, pp. 993–1007, 2001.

- [27] M. Krack, M. Secanell, and P. Mertiny, “Cost optimization of a hybrid composite flywheel rotor with a split-type hub using combined analytical/numerical models,” *Structural and Multidisciplinary Optimization*, vol. 44, no. 1, pp. 57–73, 2011.
- [28] M Holland, “Radial-displacement solution for a rotating disc with a hyperbolic thickness profile,” *Journal of Strain Analysis*, vol. 7, no. 1, pp. 7–8, 1972.
- [29] A. Stodola, *Dampf-und Gasturbinen. Mit einem Anhang über die Aussichten der Wärmekraftmaschinen: Nachtrag zur 5*. Springer-Verlag, 2013.
- [30] F. Manna, “Rotating discs of unconventional profile,” *Meccanica*, vol. 3, no. 4, pp. 274–282, 1968.
- [31] K.-Y. Yeh and R. Han, “Analysis of high-speed rotating disks with variable thickness and inhomogeneity,” *Journal of applied mechanics*, vol. 61, no. 1, pp. 186–191, 1994.
- [32] P. Singh and H. Chaudhary, “Shape optimization of the flywheel using the cubic b spline curve,” in *Advances in Engineering Design*, Springer, 2019, pp. 805–813.
- [33] P. Singh and H. Chaudhary, “Optimal shape synthesis of a metallic flywheel using non-dominated sorting jaya algorithm,” *Soft Computing*, pp. 1–12, 2019.
- [34] M Berger and I Porat, “Optimal design of a rotating disk for kinetic energy storage,” *Journal of applied mechanics*, vol. 55, no. 1, pp. 164–170, 1988.
- [35] G. Kress, “Shape optimization of a flywheel,” *Structural and Multidisciplinary Optimization*, vol. 19, no. 1, pp. 74–81, 2000.
- [36] S. J. Kim, K. Hayat, S. U. Nasir, and S. K. Ha, “Design and fabrication of hybrid composite hubs for a multi-rim flywheel energy storage system,” *Composite structures*, vol. 107, pp. 19–29, 2014.
- [37] S. K. Ha, J. H. Kim, and Y. H. Han, “Design of a hybrid composite flywheel multi-rim rotor system using geometric scaling factors,” *Journal of composite materials*, vol. 42, no. 8, pp. 771–785, 2008.
- [38] S. Tang, “Note on acceleration stress in a rotating disk,” *International Journal of Mechanical Sciences*, vol. 12, no. 2, pp. 205–207, 1970.
- [39] J. W. Phillips and M. Schrock, “Note on shear stresses in accelerating disks of variable thickness,” *International Journal of Mechanical Sciences*, vol. 13, no. 5, pp. 445–449, 1971.
- [40] S. Reid, “On the influence of acceleration stresses on the yielding of disks of uniform thickness,” *International Journal of Mechanical Sciences*, vol. 14, no. 11, pp. 755–763, 1972.
- [41] T. Y. Reddy and H Srinath, “Effect of acceleration stresses on the yielding of rotating disks,” *International Journal of Mechanical Sciences*, vol. 16, no. 8, pp. 593–596, 1974.

- [42] M. E. Amiryar and K. R. Pullen, “Analysis of standby losses and charging cycles in flywheel energy storage systems,” *Energies*, vol. 13, no. 17, p. 4441, 2020.
- [43] S. Gurusurthy, A. Sharma, S. Sarkar, and V. Agarwal, “Apportioning and mitigation of losses in a flywheel energy storage system,” in *2013 4th IEEE International Symposium on Power Electronics for Distributed Generation Systems (PEDG)*, IEEE, 2013, pp. 1–6.
- [44] M. Schneider and S. Rinderknecht, “System loss measurement of a novel outer rotor flywheel energy storage system,” in *2019 IEEE International Electric Machines & Drives Conference (IEMDC)*, IEEE, 2019, pp. 1379–1385.
- [45] *Beacon Power webpage*, <http://beaconpower.com/carbon-fiber-flywheels/>, Accessed: 2017-07-07.
- [46] *LEVISYS webpage*, <http://www.levisys.com/en/technologie.html>, Accessed: 2017-07-07.
- [47] *Stornetic GmbH webpage*, <http://stornetic.com/>, Accessed: 2017-07-07.
- [48] *Powerthru webpage*, <http://www.power-thru.com/>, Accessed: 2017-07-07.
- [49] *Calnetix webpage*, <https://www.calnetix.com/>, Accessed: 2017-07-07.
- [50] *Amber Kinetics webpage*, <http://amberkinetics.com/>, Accessed: 2017-07-07.
- [51] *Temporal Power webpage*, <http://temporalpower.com/>, Accessed: 2017-07-07.
- [52] *ActivePower webpage*, <http://www.activepower.com/en-US>, Accessed: 2017-07-07.
- [53] *ABB Powerstore webpage*, [https://library.e.abb.com/public/e13f1d26d87e9167c1257c37002e38bf/9AKK100580A2551\\_Powerstore\\_Brochure\\_EN\\_HR\\_\(Dic2013\).pdf](https://library.e.abb.com/public/e13f1d26d87e9167c1257c37002e38bf/9AKK100580A2551_Powerstore_Brochure_EN_HR_(Dic2013).pdf), Accessed: 2017-07-07.
- [54] *Piller webpage*, <http://www.piller.com/en-GB/205/energy-storage>, Accessed: 2017-07-07.
- [55] *Energiestro webpage*, <http://www.energiestro.net/>, Accessed: 2017-07-07.
- [56] H. Liu and J. Jiang, “Flywheel energy storage—an upswing technology for energy sustainability,” *Energy and buildings*, vol. 39, no. 5, pp. 599–604, 2007.
- [57] S. K. Ha, H.-I. Yang, and D.-J. Kim, “Optimal design of a hybrid composite flywheel with a permanent magnet rotor,” *Journal of composite materials*, vol. 33, no. 16, pp. 1544–1575, 1999.
- [58] S. K. Ha, H. H. Han, and Y. H. Han, “Design and manufacture of a composite flywheel press-fit multi-rim rotor,” *Journal of reinforced plastics and composites*, vol. 27, no. 9, pp. 953–965, 2008.
- [59] S. K. Ha, S. J. Kim, S. U. Nasir, and S. C. Han, “Design optimization and fabrication of a hybrid composite flywheel rotor,” *Composite Structures*, vol. 94, no. 11, pp. 3290–3299, 2012.

- [60] M. Krack, M. Secanell, and P. Mertiny, “Rotor design for high-speed flywheel energy storage systems,” in *Energy Storage in the Emerging Era of Smart Grids*, InTech, 2011.
- [61] T. Hinterdorfer, A. Schulz, H. Sima, S. Hartl, and J. Wassermann, “Topology optimization of a flywheel energy storage rotor using a genetic algorithm,” in *Proceedings of the 14th International Symposium on Magnetic Bearings, Linz, Austria*, 2014, pp. 11–14.
- [62] A. C. Arvin and C. E. Bakis, “Optimal design of press-fitted filament wound composite flywheel rotors,” *Composite structures*, vol. 72, no. 1, pp. 47–57, 2006.
- [63] S. Wen and S. Jiang, “Optimum design of hybrid composite multi-ring flywheel rotor based on displacement method,” *Composites Science and Technology*, vol. 72, no. 9, pp. 982–988, 2012.
- [64] S. Bhavikatti and C. Ramakrishnan, “Optimum shape design of rotating disks,” *Computers & Structures*, vol. 11, no. 5, pp. 397–401, 1980.
- [65] D. Eby, R. Averill, B. Gelfand, W. Punch, O. Mathews, and E. Goodman, “An injection island ga for flywheel design optimization,” in *5th European Congress on Intelligent Techniques and Soft Computing EUFIT*, vol. 97, 1997, pp. 687–691.
- [66] D. Eby, R. Averill, W. F. Punch, and E. D. Goodman, “Evaluation of injection island ga performance on flywheel design optimisation,” in *Adaptive Computing in Design and Manufacture*, Springer, 1998, pp. 121–136.
- [67] L. Jiang, W. Zhang, G. Ma, and C. Wu, “Shape optimization of energy storage flywheel rotor,” *Structural and Multidisciplinary Optimization*, vol. 55, no. 2, pp. 739–750, 2017.
- [68] L. Jiang and C. Wu, “Topology optimization of energy storage flywheel,” *Structural and Multidisciplinary Optimization*, vol. 55, no. 5, pp. 1917–1925, 2017.
- [69] M. A. Arslan, “Flywheel geometry design for improved energy storage using finite element analysis,” *Materials & Design*, vol. 29, no. 2, pp. 514–518, 2008.
- [70] P. Singh and H. Chaudhary, “Optimal design of the flywheel using nature inspired optimization algorithms,” *Open Agriculture*, vol. 3, no. 1, pp. 490–499, 2018.
- [71] L. Pedrolli, A. Zanfei, S. Ancellotti, V. Fontanari, and M. Benedetti, “Shape optimization of a metallic flywheel using an evolutive system method: Design of an asymmetrical shape for mechanical interface,” *Proceedings of the Institution of Mechanical Engineers, Part C: Journal of Mechanical Engineering Science*, vol. 232, no. 2, pp. 217–230, 2018.
- [72] A. Uyar, A. Arikoglu, G. Komurgoz, and I. Ozkol, “Thermoelastic analysis and multi-objective optimal design of functionally graded flywheels for energy storage systems,” *Engineering Optimization*, pp. 1–18, 2019.

- [73] E. Ghotbi and A. K. Dhingra, “A bilevel game theoretic approach to optimum design of flywheels,” *Engineering Optimization*, vol. 44, no. 11, pp. 1337–1350, 2012.
- [74] J.-S. Liu, G. Parks, and P. Clarkson, “Topology/shape optimisation of axisymmetric continuum structures—a metamorphic development approach,” *Structural and Multidisciplinary Optimization*, vol. 29, no. 1, pp. 73–83, 2005.
- [75] J. Huang and G. M. Fadel, “Heterogeneous flywheel modeling and optimization,” *Materials & Design*, vol. 21, no. 2, pp. 111–125, 2000.
- [76] G. Bugada, J. J. Ródenas, and E. Oñate, “An integration of a low cost adaptive remeshing strategy in the solution of structural shape optimization problems using evolutionary methods,” *Computers & Structures*, vol. 86, no. 13-14, pp. 1563–1578, 2008.
- [77] R Rao, “Jaya: A simple and new optimization algorithm for solving constrained and unconstrained optimization problems,” *International Journal of Industrial Engineering Computations*, vol. 7, no. 1, pp. 19–34, 2016.
- [78] G Genta, “Spin tests on medium energy density flywheels,” *Composites*, vol. 13, no. 1, pp. 38–46, 1982.
- [79] M. P. Bendsøe, “Topology optimization,” in *Encyclopedia of Optimization*, Springer, 2001, pp. 2636–2638.
- [80] R. A. Lopes, F. V. Stump, and E. C. N. Silva, “Topology optimization of three dimensional structures under self-weight and inertial forces,” in *6th world congress of structural and multidisciplinary optimization. Rio de Janeiro, Brazil*, Citeseer, 2005, pp. 5–6.
- [81] T. Tsai and C. Cheng, “Topology optimization of flywheel rotors using simp method: A preliminary study,” in *Advanced Materials Research*, Trans Tech Publ, vol. 579, 2012, pp. 427–434.
- [82] L. M. Lottes, N. Kaiser, N. Goossens, H. W. Oelze, and C. Braxmaier, “Tomares-topology optimization of an additive manufactured reaction flywheel designed for an earth-observation satellite,” *CEAS Space Journal*, 2021.
- [83] M. P. Bendsøe, “Optimal shape design as a material distribution problem,” *Structural optimization*, vol. 1, no. 4, pp. 193–202, 1989.
- [84] O. Sigmund, “A 99 line topology optimization code written in matlab,” *Structural and multidisciplinary optimization*, vol. 21, no. 2, pp. 120–127, 2001.
- [85] T. E. Bruns and D. A. Tortorelli, “Topology optimization of non-linear elastic structures and compliant mechanisms,” *Computer methods in applied mechanics and engineering*, vol. 190, no. 26-27, pp. 3443–3459, 2001.
- [86] C. Le, J. Norato, T. Bruns, C. Ha, and D. Tortorelli, “Stress-based topology optimization for continua,” *Structural and Multidisciplinary Optimization*, vol. 41, no. 4, pp. 605–620, 2010.

- [87] O. Sigmund, “Morphology-based black and white filters for topology optimization,” *Structural and Multidisciplinary Optimization*, vol. 33, no. 4-5, pp. 401–424, 2007.
- [88] P. Duysinx and M. P. Bendsøe, “Topology optimization of continuum structures with local stress constraints,” *International journal for numerical methods in engineering*, vol. 43, no. 8, pp. 1453–1478, 1998.
- [89] E. Lee, K. A. James, and J. R. Martins, “Stress-constrained topology optimization with design-dependent loading,” *Structural and Multidisciplinary Optimization*, vol. 46, no. 5, pp. 647–661, 2012.
- [90] G. A. da Silva, A. T. Beck, and O. Sigmund, “Stress-constrained topology optimization considering uniform manufacturing uncertainties,” *Computer Methods in Applied Mechanics and Engineering*, vol. 344, pp. 512–537, 2019.
- [91] M. Collet, L. Noël, M. Bruggi, and P. Duysinx, “Topology optimization for microstructural design under stress constraints,” *Structural and Multidisciplinary Optimization*, vol. 58, no. 6, pp. 2677–2695, 2018.
- [92] G. Cheng and X. Guo, “ $\varepsilon$ -relaxed approach in structural topology optimization,” *Structural optimization*, vol. 13, no. 4, pp. 258–266, 1997.
- [93] R. Yang and C. Chen, “Stress-based topology optimization,” *Structural optimization*, vol. 12, no. 2, pp. 98–105, 1996.
- [94] R. A. Lopes, F. V. Stump, and E. C. N. Silva, “Topology optimization of three dimensional structures under self-weight and inertial forces,” in *6th world congress of structural and multidisciplinary optimization. Rio de Janeiro, Brazil*, Citeseer, 2005, pp. 5–6.
- [95] B. Wang *et al.*, “A preliminary design method for axisymmetric turbomachinery disks based on topology optimization,” *Proceedings of the Institution of Mechanical Engineers, Part C: Journal of Mechanical Engineering Science*, p. 09 544 062 211 039 529, 2021.
- [96] B. Wang, G. Wang, Y. Shi, L. Huang, and K. Tian, “Stress-constrained thermo-elastic topology optimization of axisymmetric disks considering temperature-dependent material properties,” *Mechanics of Advanced Materials and Structures*, pp. 1–17, 2021.
- [97] F. Guo and I. P. Brown, “Simultaneous magnetic and structural topology optimization of synchronous reluctance machine rotors,” *IEEE Transactions on Magnetics*, vol. 56, no. 10, pp. 1–12, 2020.
- [98] A. Credo, G. Fabri, M. Villani, and M. Popescu, “Adopting the topology optimization in the design of high-speed synchronous reluctance motors for electric vehicles,” *IEEE Transactions on Industry Applications*, vol. 56, no. 5, pp. 5429–5438, 2020.
- [99] L. Li and K. Khandelwal, “Volume preserving projection filters and continuation methods in topology optimization,” *Engineering Structures*, vol. 85, pp. 144–161, 2015.

- [100] J. K. Guest, A. Asadpoure, and S.-H. Ha, “Eliminating beta-continuation from heaviside projection and density filter algorithms,” *Structural and Multidisciplinary Optimization*, vol. 44, no. 4, pp. 443–453, 2011.
- [101] D. Munro and A. Groenwold, “Local stress-constrained and slope-constrained sand topology optimisation,” *International Journal for numerical methods in engineering*, vol. 110, no. 5, pp. 420–439, 2017.
- [102] J Paris, F Navarrina, I Colominas, and M Casteleiro, “Global versus local statement of stress constraints in topology optimization of continuum structures,” *Computer aided optimum design in engineering X/Ed. by S. Hernandez, CA Brebbia. Southampton*, pp. 13–23, 2007.
- [103] O. Giraldo-Londoño and G. H. Paulino, “Polystress: A matlab implementation for local stress-constrained topology optimization using the augmented lagrangian method,” *Structural and Multidisciplinary Optimization*, vol. 63, no. 4, pp. 2065–2097, 2021.
- [104] G. A. da Silva, N. Aage, A. T. Beck, and O. Sigmund, “Local versus global stress constraint strategies in topology optimization: A comparative study,” *International Journal for Numerical Methods in Engineering*, vol. 122, no. 21, pp. 6003–6036, 2021.
- [105] M. Beckers, “Topology optimization using a dual method with discrete variables,” *Structural Optimization*, vol. 17, no. 1, pp. 14–24, 1999.
- [106] K. Svanberg, “The method of moving asymptotes—a new method for structural optimization,” *International journal for numerical methods in engineering*, vol. 24, no. 2, pp. 359–373, 1987.
- [107] E Moses, M. Fuchs, and M Ryvkin, “Topological design of modular structures under arbitrary loading,” *Structural and Multidisciplinary Optimization*, vol. 24, no. 6, pp. 407–417, 2002.
- [108] G. Ertz, “Development, manufacturing and testing of a multi-rim (hybrid) flywheel rotor,” Diploma Thesis, Institut für Dynamik und Schwingungen, Germany and University of Alberta, Canada, 2014.
- [109] B. M. Adams *et al.*, “Dakota, a multilevel parallel object-oriented framework for design optimization, parameter estimation, uncertainty quantification, and sensitivity analysis: Version 5.0 user’s manual,” *Sandia National Laboratories, Tech. Rep. SAND2010-2183*, 2009.
- [110] *Autodesk helius composite*, <https://knowledge.autodesk.com/support/helius-composite/learn-explore/caas/CloudHelp/cloudhelp/2015/ENU/ACMPDS/files/GUID-2B4538D7-227F-4C9F-891F-785F90CA10CA-htm.html>, Accessed: 2017-11-01.
- [111] V. Kelner, F. Capitanescu, O. Léonard, and L. Wehenkel, “A hybrid optimization technique coupling an evolutionary and a local search algorithm,” *Journal of Computational and Applied Mathematics*, vol. 215, no. 2, pp. 448–456, 2008.

- [112] M. Secanell *et al.*, “Openfcst: An open-source mathematical modelling software for polymer electrolyte fuel cells,” *ECS Transactions*, vol. 64, no. 3, pp. 655–680, 2014.
- [113] D. Arndt *et al.*, “The deal.II library, version 8.5,” *Journal of Numerical Mathematics*, vol. 25, no. 3, pp. 137–146, 2017. DOI: 10.1515/jnma-2016-1045.
- [114] H.-S. Oh and R. Batra, “Locations of optimal stress points in higher-order elements,” *Communications in numerical methods in engineering*, vol. 15, no. 2, pp. 127–136, 1999.
- [115] C. Geuzaine and J.-F. Remacle, “Gmsh: A 3-d finite element mesh generator with built-in pre-and post-processing facilities,” *International journal for numerical methods in engineering*, vol. 79, no. 11, pp. 1309–1331, 2009.
- [116] G. Chiandussi, G. Bugada, and E. Oñate, “A simple method for automatic update of finite element meshes,” *Communications in Numerical Methods in Engineering*, vol. 16, no. 1, pp. 1–19, 2000.
- [117] V Kale and M Secanell, “A comparative study between optimal metal and composite rotors for flywheel energy storage systems,” *Energy Reports*, vol. 4, pp. 576–585, 2018.
- [118] D. M. De Leon, J. Alexandersen, J. S. O Fonseca, and O. Sigmund, “Stress-constrained topology optimization for compliant mechanism design,” *Structural and Multidisciplinary Optimization*, vol. 52, no. 5, pp. 929–943, 2015.
- [119] K. Svanberg, “The method of moving asymptotes—a new method for structural optimization,” *International journal for numerical methods in engineering*, vol. 24, no. 2, pp. 359–373, 1987.
- [120] *GitHub - jdumas/mma: A self-contained C++ implementation of MMA and GCMMA.* — *github.com*, <https://github.com/jdumas/mma>, [Accessed 01-May-2022].
- [121] N. Aage and B. S. Lazarov, “Parallel framework for topology optimization using the method of moving asymptotes,” *Structural and multidisciplinary optimization*, vol. 47, no. 4, pp. 493–505, 2013.
- [122] F. Wang, B. S. Lazarov, and O. Sigmund, “On projection methods, convergence and robust formulations in topology optimization,” *Structural and multidisciplinary optimization*, vol. 43, no. 6, pp. 767–784, 2011.
- [123] G. A. da Silva, N. Aage, A. T. Beck, and O. Sigmund, “Three-dimensional manufacturing tolerant topology optimization with hundreds of millions of local stress constraints,” *International Journal for Numerical Methods in Engineering*, vol. 122, no. 2, pp. 548–578, 2021.
- [124] O. Sigmund and K. Maute, “Topology optimization approaches,” *Structural and Multidisciplinary Optimization*, vol. 48, no. 6, pp. 1031–1055, 2013.

- [125] C. S. Andreasen, M. O. Elingaard, and N. Aage, “Level set topology and shape optimization by density methods using cut elements with length scale control,” *Structural and Multidisciplinary Optimization*, vol. 62, no. 2, pp. 685–707, 2020.
- [126] V. Kale, M. Thomas, and M. Secanell, “On determining the optimal shape, speed, and size of metal flywheel rotors with maximum kinetic energy,” *Structural and Multidisciplinary Optimization*, vol. 64, no. 3, pp. 1481–1499, 2021.
- [127] H. Ledbetter, *Physical Properties Data Compilations Relevant to Energy Storage*. National Bureau of Standards, 1982.

# Appendix A: Literature data

## A.1 Literature on flywheel rotor sizing and material optimization

Table A.1 contains information about flywheel rotor optimization studies from literature. A variety of optimization objectives, design variables, constraints and optimization algorithms and strategies have been used to design optimal FESS rotors.

Table A.1: Literature on optimal rotor design for FESS using tailored material properties

Reference	Objective	Design Variables	Constraints	Parameters	Model	Strategy
Krack et al. [17]	$\max \frac{E_{kin}}{\text{cost}}$	$\omega, t_1$	Tsai-Wu	materials	1D PSS & 3D	multistart NIPM multistrategy EA+NIPM
Ha et al. [22]	$\max \omega^2$	$\omega, \{\phi_j, \delta_j\}_{j=1}^{n_{rims}}$	Tsai-Wu	-	1D	SLP/MFD GS/polynomial search
Krack et al. [24]	$\max \frac{E_{kin}}{\text{cost}}$	$\omega, \{\frac{t_j}{t_{all}}, \phi_j\}_{j=1}^{n_{rims}}$	Tsai-Wu	-	1D PSS & 3D	multistart NIPM multistrategy EA+NIPM
Mittelstedt et al. [25]	$\max \{E_{kin}, \text{productivity}\}$ & min cost	$\omega, n_{rims}, \{t_j, \delta_j, material_j\}_{j=1}^{n_{rims}}$	M $\sigma$ FT, M $\epsilon$ FT, Tsai-Wu	-	1D PSS	GA+SQP
Ha et al. [26]	$\max E_{kin}$	$\{t_j\}_{j=1}^{n_{rims}}$	Tsai-Wu	$\Delta T$ , materials	1D MPGS & PSS, 3D FEM	Modified MFD
Krack et al. [27]	$\max \frac{E_{kin}}{\text{cost}}$	$\omega, \frac{t_1}{t_{all}}, t_{hub}$	M $\sigma$ FT	hub type	1D PSS & 3D FEM	NIPM (single/ sequential / surrogate models)
Ha et al. [57]	$\max(E_{kin})$	$r_o, r_i, \{t_j\}_{j=1}^{n_{rims}}$	Tsai-Wu	material sequence	1D PSS	Modified MFD
Ha et al. [58]	$\max(e_{kin})$	$\{t_j, \delta_j\}_{j=1}^{n_{rims}}$	Tsai-Wu, M $\sigma$ FT	assembly, no. of rims, curing temperature	1D PSS	not reported
Ha et al. [59]	$\min(R_{max}^*)$	$\{t_j, V_f^j\}_{j=1}^{n_{rims}}$	M $\sigma$ FT	assembly	1D PSS	SQP
Arvin and Bakis [62]	$\max e_{kin}$	$\omega, \{t_j\}_{j=1}^{n_{rims}}$	M $\sigma$ FT, Tsai-Wu	rims, $T_{sf}$	1D PSS	SA
Wen & Jiang [63]	$\max(E_{kin} \text{ or } \frac{E_{kin}}{m})$ or $\frac{E_{kin}}{V} \text{ or } \frac{E_{kin}}{\text{cost}}$	$\omega, r_o, r_i, \{t_1, \dots, t_j, \dots, t_n\}$	M $\sigma$ FT, delamination, press-fit	acceleration, gravity	1D PSS	NIPM+SQP

## A.2 Literature on FESS rotor shape optimization

Table A.2 contains the optimization formulations used in literature for flywheel rotor shape optimization. A variety of optimization objectives, shape approximation functions, constraints and optimization algorithms and strategies have been used to design optimally shaped FESS rotors.

Table A.2: Literature on optimal metal rotor design using shape optimization

Reference	Objective	Design Variables	Constraints	Parameters	Geometry	Rotor model	Strategy
Singh & Chaudhary [32, 70]	$\max E_{kin}$	$\{h_j\}_{j=1}^{n_{baptine}}$	$\sigma_{VM}^{max} \leq \sigma_{design}, m \leq m_{design}$	-	annular disk	2D FDM	JAYA global method
Singh & Chaudhary [33]	$\max E_{kin}$ & $\min \sigma_{vm}^{max}$	$\{h_j\}_{j=1}^{n_{baptine}}$	$\sigma_{VM}^{max} \leq \sigma_{design}, m \leq m_{design}$	-	annular disk	2D axisymmetric FDM	non-dominated sorted Jaya
Berger & Porat. [34]	$\max e_{kin}$	$h_1(r), h_2(r), h_3(r), h_4(r)$	$\sigma_r^{max} \leq \sigma_{design}, \sigma_\theta^{max} \leq \sigma_{design}$	$\omega$	solid disk	2D axisymmetric	-
Kress [35]	$\min \int_r (\sigma - \bar{\sigma})^2 dr$	$h_e(r) \forall e$ (elements)	$m = m_{design}, E_{kin} = E_{kin}^{design}$	$r_{in}, r_{out}$	annular disk	modified 0D, 2D axisymmetric FEM	method of feasible directions
Bhavikatti & Ramakrishnan [64]	a) $\min (\sigma_\theta^{max} - \sigma_\theta^{min})$ b) $\min \int_r (\sigma - \bar{\sigma})^2 dr$ c) $\min (\int_r (\sigma - \bar{\sigma})^2 dr, V)$	5 <sup>th</sup> degree polynomial shape fn.	$\sigma_r \geq \sigma_\theta^{min}$	$\omega, p$	annular disk	2D axisymmetric FEM	improved move limit seq lin programming
Eby & Averill [65]	$\max e_{kin}$	$h_e(r) \forall e$ (elements)	-	-	solid disk	1D & 2D axisymmetric FEM	injection island genetic algorithm
Jiang et al. [67]	a) $\max e_{kin}$ b) $\max E_{kin}$	$\{h_j\}_{j=1}^{n_{baptine}}$	a) $\sigma_{VM}^{max} \leq \sigma_{design}, h_j^L \leq h_j \leq h_j^U$ b) $\sigma_{VM}^{max} \leq \sigma_{design}, h_j^L \leq h_j \leq h_j^U,$ $m = m_{design}$	-	a) solid disk b) solid and annular disks	2D axisymmetric FEM	downhill simplex
Pedrolli et al. [71]	$\min m$	$\{h_j\}_{j=1}^{n_{baptine}}$	$s(\sigma_{VM}) = 0, \sigma_{VM}^{max} = \sigma_{design},$ $I = I_{design}$	$\omega, E_{kin}^{design}, r_{out}, \rho, \sigma_y$	solid disk	2D axisymmetric FEM	evolutionary algorithm (multi-member, elitist)
Uyar et al [72]	$\max E_{kin}^{avg}, \min m$	$\{h_j\}_{j=1}^{n_{baptine}}, \text{material}_j$	$\sigma_{VM}^{max} \leq \sigma_{design}, \omega_{max} \leq \omega_{design},$ $m \leq m_{design}$	$\omega_{design}, \text{material}_j, r_{out}$	annular disk	2D axisymmetric GDQM, & FEM	non-dominated sorting genetic algorithm II

Table A.2: (Continued) Literature on optimal metal rotor design using shape optimization

Reference	Objective	Design Variables	Constraints	Parameters	Geometry	Rotor model	Strategy
Ghotbi & Dhingra [73]	$\max E_{kin}$ & $\min C$	Fourier coefficients ( $s_0, a_i, b_i, i=1,2,3$ )	$\sigma_{VM}^{max} \leq \sigma_{design}, m \leq m_{design}$	-	annular disk	2D axisymmetric FDM	bi-level Stackelberg game
Liu et al. [74]	$\min m$	mesh elements	$\sigma_{VM}^{max} \leq \sigma_{design}$	-	annular disk	3D FEM	metamorphic development
Bugeda et al. [76]	$\min m$	60 shape parameters in ( $r - \theta$ ) plane	$\sigma_{VM}^{boundaries} \leq \sigma_{design}$	-	annular disk with spokes	2D plane-stress FEM	evolutionary algorithm
Present work [126]	$\max E_{kin}$	$\{h_j\}_{j=1}^{n_{bspline}}$	$\sigma_{VM}^{max} \leq \sigma_{design}, m \leq m_{design}$	$\omega, r_{out}, \text{material}$	solid disk	2D axisymmetric FEM	hybrid sequential (global + local)

## A.3 Literature on FESS rotor topology optimization

Table A.3 contains information about flywheel rotor topology or 3D geometry optimization studies from literature. A variety of optimization objectives, design variables, constraints and optimization algorithms and strategies have been used to design optimal FESS rotors.

Table A.3: Literature on topology optimization of flywheels used in energy storage applications

Reference	Optimization formulation		Numerical model	Load	Boundary Conditions	Solver
	Objective	Constraints				
Tsai and Cheng [81]	Torsional frequency					
	Moment of Inertia	Volume fraction	2D plane stress ( $r-\theta$ ), CAMD	Centrifugal force	Annular disk, zero displacement inner boundary	MMA
	Torsional frequency and Moment of Inertia (MOO)					
	Compliance			Centrifugal force and Acceleration load		
Jiang and Wu [68]	Moment of Inertia	Maximum von Mises stress, Volume fraction Mass,	2D plane stress ( $r-\theta$ ), SIMP,	Centrifugal force	Annular disk, zero displacement inner boundary	Not reported
Lottes et al. [82]	step 1. Shape parametric study with ranking based on 4 criteria	Form factor, Rankine stress criterion, Mass-specific angular momentum	2D axisymmetric ( $r-z$ )	Centrifugal force	Different shaft geometries were evaluated	
	step 2. Topology optimization Minimize compliance	Volume fraction	3D	Centrifugal force	Integrated shaft, fixed outer contour / shape	MMA
<i>Present work</i>	Kinetic energy	P-norm stress, Volume fraction	2D plane stress ( $r-\theta$ ) 3D	Centrifugal force, Acceleration load, Gravity load (3D)	Annular disk, Press-fit shaft	MMA
	Specific energy	P-norm stress	2D plane stress ( $r-\theta$ )	Centrifugal force and Acceleration load		

## A.4 Literature on topology optimization of rotors used in other applications

Table A.4 contains information about flywheel rotor topology or 3D geometry optimization studies from literature. A variety of optimization objectives, design variables, constraints and optimization algorithms and strategies have been used to design optimal rotors in other applications.

Table A.4: Literature on topology optimization of axisymmetric disks used in other applications

Application	Reference	Optimization formulation		Load	Model	Solver
		Objective	Constraints			
Hydrogenerator shaft	Lopes et al. [94]	Minimize Compliance	Volume fraction	Centrifugal load Radial load due to magnets	Linear elastic model, 2D plane stress ( $r-\theta$ ) and 3D	MMA
Theoretical	Moses et al. [107]	Minimize Compliance	Volume fraction	Acceleration load	Periodic cyclic structure, 2D plane stress ( $r-\theta$ )	Optimality criterion
Synchronous reluctance motor	Guo and Brown [97]	Maximize Average torque	Torque ripple, P-norm stress, Compliance	Magnetic load Centrifugal load	Magneto-structural model, 2D plane stress ( $r-\theta$ )	GCMMA
		MOO: Max Average torque, Min Compliance	Torque ripple, P-norm stress			
	Credo et al. [98]	Maximize Average torque	Torque ripple, Maximum stress, Mass, Phase voltage, Peak torque	Magnetic load, Centrifugal load	Magneto-structural model, 2D plane stress ( $r-\theta$ )	-
Compressor / turbine rotors	Wang et al. [95]	Minimize Mass	P-norm stress	Centrifugal load Radial load due to blades	Linear elastic model, 2D axisymmetric ( $r-z$ )	MMA
	Wang et al. [96]	Minimize Volume fraction	P-norm stress, Compliance	Centrifugal load Radial load due to blades, Thermal load	Thermo-elastic model, 2D axisymmetric ( $r-z$ )	MMA

# Appendix B: Rotor Materials

## B.1 Material Properties

Table B.1: Composite material properties [110]

Material	$V_f$	$E_\theta$	$E_r$	$G_{\theta r}$	$G_{rz}$	$\nu_{\theta r}$	$\nu_{rz}$	$\rho$	$\sigma_{\theta,T}^{ult}$	$\sigma_{\theta,C}^{ult}$	$\sigma_{r,T}^{ult}$	$\sigma_{r,C}^{ult}$	$\tau_{\theta r}^{ult}$	relative cost
		GPa	GPa	GPa	GPa									
AS4-3501-6	0.6	127	11.15	6.55	3.64	0.27	0.53	1.591	1950	1480	48	200	79	26.63
AS4-8552	0.58	135.1	9.63	4.95	3.35	0.30	0.43	1.577	2206	1531	80	259.9	114.5	26.69
E-Glass Epoxy	0.45	44.81	12.41	5.51	3.59	0.28	0.36	2.076	1035	620	48	137.8	68.9	18.72
IM7-8551-7	0.6	165.8	8.56	5.59	2.94	0.27	0.46	1.574	2560	1590	73	185	90	35.77
IM7-8552	0.57	139.7	11.39	4.75	3.89	0.32	0.46	1.588	2723	1689	111	215.9	119.9	35.77
Kevlar-49 Epoxy	0.45	75.84	5.51	2.06	1.54	0.34	0.47	1.384	1378	275	29	137.8	62	27.10
S-2 Glass Epoxy	0.45	55.84	17.92	6.20	3.89	0.27	0.35	1.993	1999	965	62	155	93	30.91
T300-BSL914C	0.6	138.1	11	5.43	3.57	0.28	0.54	1.559	1500	900	27	200	80.0	31.71
T300-PR319	0.6	128.9	5.706	1.33	1.84	0.32	0.55	1.562	1378	950	40	125	97	31.71

Table B.2: Isotropic material properties [127]

<b>Material</b>	E GPa	G GPa	$\nu$	$\rho$ g/cm <sup>3</sup>	Yield Strength MPa	relative cost /kg
Al-2024	73.1	27.1	0.332	2.77	417.8	3.84
Al-6061-T6	69.6	26.3	0.331	2.71	275	2.30
Al-7075-T6	71.8	26.8	0.33	2.79	465	3.07
Steel-4340	205.0	76.5	0.29	7.85	470	1.0
Steel-18Ni-300	190.0	66.3	0.318	8.04	758	1.53
Stainless-Steel-15-7	201.0	77.9	0.32	7.67	745	2.69
Stainless-Steel-440C	203.0	93.1	0.284	7.7	1220	1.26
Stainless-Steel-455	197.9	75.8	0.3	7.76	1489	2.30
Carbon-Steel-1020	206.2	80.0	0.288	7.84	429.6	1.76

# Appendix C: Shape optimization

## C.1 Mesh independence of axisymmetric rotor model

The mesh independence of the 2D axisymmetric model implementation described in Chapter 3 was checked using the convergence of the displacement and stress solutions with mesh refinement (h-refinement) and higher order approximations (p-refinement). An annular constant thickness rotor was used for this study, and the mesh with 120 elements used for simulations can be seen in Figure C.1. Figure C.2 shows the convergence of the maximum radial displacement  $u_r^{max}$  with h and p-refinement and Figure C.3 shows the convergence of maximum stresses  $\sigma_r^{max}$  in the axisymmetric rotor with both h and p-refinement. The % difference between subsequent solutions is calculated as shown in Equation (C.1), where  $x^n$  is the solution obtained with  $n$  refinement levels. The displacement solutions converge relatively quickly in both cases and a second-order approximation with a mesh of 120 elements is sufficient to ensure

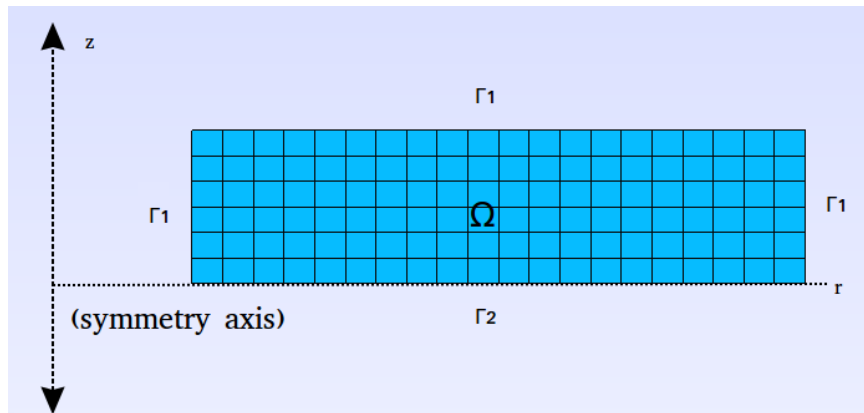


Figure C.1: Axisymmetric constant thickness rotor mesh for a) annular disk geometry with 20x6 elements and b) solid disk geometry with 40x6 elements

the accuracy of the displacement solution, but the stresses are not as accurate. This is because the stresses are calculated using the gradients of the displacement solutions, which are not necessarily continuous in the entire domain. The use of stresses obtained at Gauss quadrature points (one order lower than the order of quadrature used for numerical integration) instead of nodal stresses is seen to improve the convergence of the stress solution, which is expected as per the super-convergence theory [114]. Thus, a combination of h and p refinement is used to ensure the convergence of all the necessary solutions. Different mesh refinement strategies will be used in the shape and topology optimization studies. In shape optimization, the FEM domain and mesh is regenerated at every optimization iteration, so an adaptive re-meshing strategy will be used to ensure stress convergence, whereas the domain and mesh are fixed in topology optimization, thus a predetermined mesh refinement with either linear or quadratic solution approximations will suffice in these studies.

$$\% \text{difference} = \frac{x^n - x^{n-1}}{x^n} * 100 \quad (\text{C.1})$$

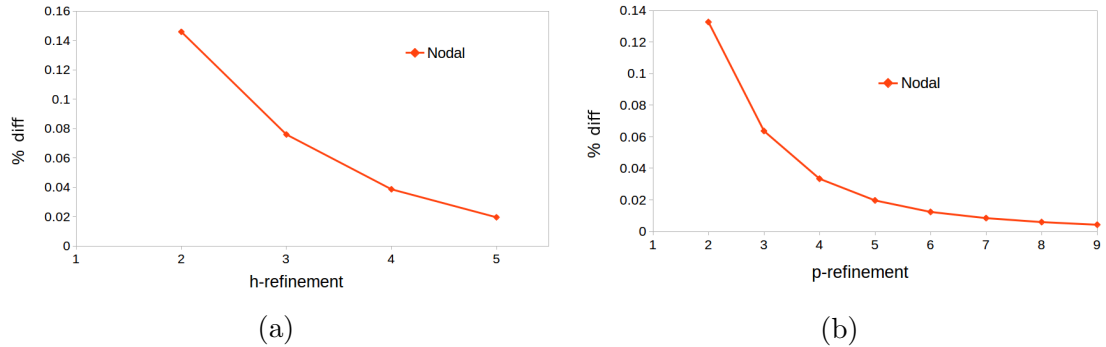


Figure C.2: Convergence of displacement  $u_r^{max}$  in the axisymmetric rotor model with a) h-refinement (first order approximations) and b) p-refinement (mesh with 120 elements).

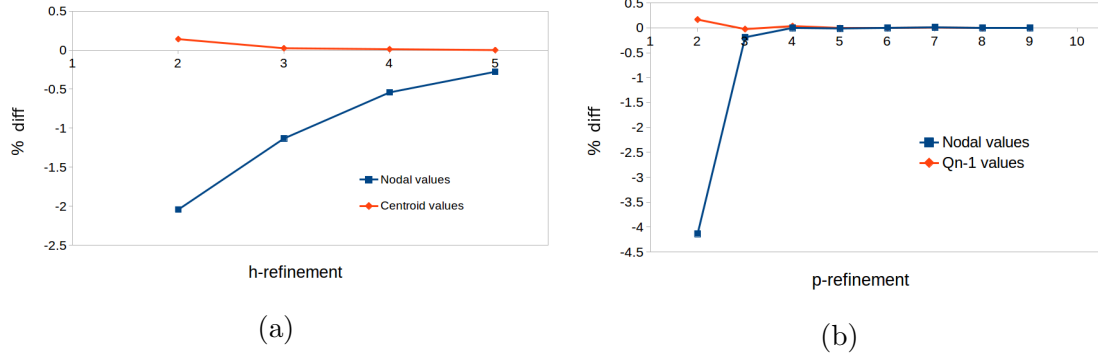


Figure C.3: Convergence of stress  $\sigma_r^{max}$  in the axisymmetric rotor model with a) h-refinement (first order approximations) and b) p-refinement (mesh with 120 elements).

## C.2 Optimal solutions for parametric studies to determine the effect of operating speed and rotor radius on the rotor design

Table C.1 shows the optimal solutions of the shape optimization problem which maximizes the rotor kinetic energy, based on design-1 (Temporal rotor) specifications, at different combinations of operating speed and rotor radius. The parameters varied in this study are  $r_{out} = 0.4 : 1.0$  m and  $\omega = 4000 : 10000$  rpm.

Table C.1: Kinetic energy in kWh for the optimal shaped rotors based on design-1

$r_{out}$ [m], $\omega$ [rpm]	4000	5000	6000	7000	8000	9000	10000
0.4	11.21	17.58	25.31	22.60	27.87	34.03	41.99
0.5	18.30	28.66	31.02	36.39	41.13	42.79	40.33
0.6	23.04	34.38	37.08	46.13	41.14	40.15	31.31
0.7	30.54	40.29	49.04	49.68	45.14	0.00	0.00
0.8	32.40	45.49	53.88	51.63	0.00	0.00	0.00
0.9	40.02	50.24	56.62	53.32	0.00	0.00	0.00
1	47.88	56.57	60.95	0.00	0.00	0.00	0.00

Table C.2 shows the optimal solutions of the shape optimization problem which maximizes the rotor kinetic energy, based on design-2 (Amber Kinetics) specifications, at

different combinations of operating speed and rotor radius. The parameters varied in this study are  $r_{out} = 0.4 : 1.0$  m and  $\omega = 4000 : 10000$  rpm.

Table C.2: Kinetic energy in kWh for the optimal shaped rotors based on design-2

$r_{out}$ [m], $\omega$ [rpm]	4000	5000	6000	7000	8000	9000	10000
0.4	6.95	11.11	15.94	22.22	19.00	23.85	25.81
0.5	11.56	18.20	20.71	24.67	30.06	32.29	29.72
0.6	14.81	19.78	22.50	31.77	34.57	33.17	31.51
0.7	17.70	25.40	33.18	36.60	38.37	32.88	0.00
0.8	19.51	32.00	36.52	41.24	41.80	0.00	0.00
0.9	27.27	34.70	41.23	44.61	0.00	0.00	0.00
1	32.23	43.04	47.68	0.00	0.00	0.00	0.00

### C.3 Optimal designs for parametric studies to determine the effect of operating speed and rotor radius on the rotor design

Table C.3 shows the optimal shape design parameters  $h(r)$  in m, for the shape optimization problem which maximizes the rotor kinetic energy, based on design-1 (Temporal rotor) specifications, at different combinations of operating speed and rotor radius.

Table C.3: Shape design parameters  $h(r)$  for optimal rotors in the parametric studies based on design-1

Parametric study	$h_1$	$h_2$	$h_3$	$h_4$	$h_5$	$h_6$	$h_7$	$h_8$
$r_{out} = 0.4$ m, $\omega = 4000$ rpm	0.03	0.03	0.03	0.03	0.03	0.03	0.80	1.81
$r_{out} = 0.4$ m, $\omega = 5000$ rpm	0.03	0.03	0.03	0.03	0.03	0.03	0.75	1.87
$r_{out} = 0.4$ m, $\omega = 6000$ rpm	0.03	0.03	0.03	0.03	0.03	0.03	0.76	1.87
$r_{out} = 0.4$ m, $\omega = 7000$ rpm	0.35	0.33	0.35	0.32	0.49	0.40	0.55	0.51
$r_{out} = 0.4$ m, $\omega = 8000$ rpm	0.35	0.36	0.36	0.61	0.33	0.46	0.51	0.42

$r_{out}=0.4\text{m}, \omega=9000\text{ rpm}$	0.45	0.39	0.49	0.47	0.42	0.51	0.37	0.44
$r_{out}=0.4\text{m}, \omega=10000\text{ rpm}$	0.41	0.49	0.52	0.40	0.45	0.37	0.46	0.46
$r_{out}=0.5\text{m}, \omega=4000\text{ rpm}$	0.03	0.03	0.03	0.03	0.03	0.03	0.04	1.73
$r_{out}=0.5\text{m}, \omega=5000\text{ rpm}$	0.03	0.03	0.03	0.03	0.03	0.03	0.03	1.75
$r_{out}=0.5\text{m}, \omega=6000\text{ rpm}$	0.10	0.08	0.09	0.10	0.21	0.26	0.50	0.49
$r_{out}=0.5\text{m}, \omega=7000\text{ rpm}$	0.21	0.19	0.19	0.20	0.25	0.35	0.29	0.40
$r_{out}=0.5\text{m}, \omega=8000\text{ rpm}$	0.26	0.34	0.27	0.26	0.34	0.25	0.21	0.32
$r_{out}=0.5\text{m}, \omega=9000\text{ rpm}$	0.34	0.33	0.31	0.53	0.43	0.21	0.16	0.12
$r_{out}=0.5\text{m}, \omega=10000\text{ rpm}$	0.45	0.44	0.48	0.71	0.41	0.13	0.05	0.05
$r_{out}=0.6\text{m}, \omega=4000\text{ rpm}$	0.03	0.03	0.04	0.03	0.05	0.12	0.30	0.65
$r_{out}=0.6\text{m}, \omega=5000\text{ rpm}$	0.07	0.05	0.04	0.05	0.05	0.13	0.39	0.49
$r_{out}=0.6\text{m}, \omega=6000\text{ rpm}$	0.18	0.14	0.17	0.23	0.13	0.17	0.24	0.25
$r_{out}=0.6\text{m}, \omega=7000\text{ rpm}$	0.21	0.21	0.21	0.22	0.20	0.15	0.23	0.18
$r_{out}=0.6\text{m}, \omega=8000\text{ rpm}$	0.34	0.21	0.52	0.32	0.24	0.12	0.06	0.08
$r_{out}=0.6\text{m}, \omega=9000\text{ rpm}$	0.38	0.31	0.67	0.49	0.08	0.09	0.04	0.03
$r_{out}=0.6\text{m}, \omega=10000\text{ rpm}$	0.37	0.21	0.88	0.15	0.05	0.03	0.03	0.03
$r_{out}=0.7\text{m}, \omega=4000\text{ rpm}$	0.03	0.03	0.03	0.03	0.03	0.09	0.20	0.48
$r_{out}=0.7\text{m}, \omega=5000\text{ rpm}$	0.10	0.10	0.09	0.11	0.06	0.10	0.19	0.31
$r_{out}=0.7\text{m}, \omega=6000\text{ rpm}$	0.17	0.16	0.17	0.14	0.10	0.10	0.16	0.21
$r_{out}=0.7\text{m}, \omega=7000\text{ rpm}$	0.21	0.23	0.22	0.23	0.16	0.13	0.07	0.08
$r_{out}=0.7\text{m}, \omega=8000\text{ rpm}$	0.28	0.24	0.53	0.27	0.08	0.07	0.03	0.04
$r_{out}=0.7\text{m}, \omega=9000\text{ rpm}$	0.29	0.18	0.62	0.11	0.05	0.03	0.03	0.03
$r_{out}=0.7\text{m}, \omega=10000\text{ rpm}$	0.25	0.24	0.53	0.17	0.06	0.03	0.03	0.03
$r_{out}=0.8\text{m}, \omega=4000\text{ rpm}$	0.05	0.04	0.09	0.03	0.10	0.12	0.14	0.19
$r_{out}=0.8\text{m}, \omega=5000\text{ rpm}$	0.12	0.11	0.10	0.07	0.07	0.12	0.11	0.16
$r_{out}=0.8\text{m}, \omega=6000\text{ rpm}$	0.17	0.16	0.19	0.13	0.08	0.07	0.11	0.09
$r_{out}=0.8\text{m}, \omega=7000\text{ rpm}$	0.22	0.21	0.35	0.14	0.09	0.07	0.04	0.04
$r_{out}=0.8\text{m}, \omega=8000\text{ rpm}$	0.24	0.23	0.45	0.10	0.05	0.03	0.03	0.03
$r_{out}=0.8\text{m}, \omega=9000\text{ rpm}$	0.23	0.23	0.42	0.11	0.04	0.03	0.03	0.03
$r_{out}=0.8\text{m}, \omega=10000\text{ rpm}$	0.21	0.21	0.34	0.10	0.05	0.03	0.03	0.03

$r_{out} = 0.9\text{m}, \omega = 4000 \text{ rpm}$	0.06	0.05	0.05	0.04	0.05	0.12	0.10	0.14
$r_{out} = 0.9\text{m}, \omega = 5000 \text{ rpm}$	0.13	0.13	0.08	0.11	0.07	0.10	0.05	0.10
$r_{out} = 0.9\text{m}, \omega = 6000 \text{ rpm}$	0.17	0.17	0.18	0.11	0.06	0.07	0.05	0.06
$r_{out} = 0.9\text{m}, \omega = 7000 \text{ rpm}$	0.20	0.23	0.26	0.10	0.05	0.03	0.03	0.03
$r_{out} = 0.9\text{m}, \omega = 8000 \text{ rpm}$	0.19	0.24	0.24	0.11	0.06	0.03	0.04	0.03
$r_{out} = 0.9\text{m}, \omega = 9000 \text{ rpm}$	0.21	0.24	0.22	0.09	0.05	0.03	0.03	0.03
$r_{out} = 0.9\text{m}, \omega = 10000 \text{ rpm}$	0.20	0.23	0.26	0.10	0.05	0.03	0.03	0.03
$r_{out} = 1\text{m}, \omega = 4000 \text{ rpm}$	0.07	0.07	0.05	0.05	0.04	0.09	0.05	0.13
$r_{out} = 1\text{m}, \omega = 5000 \text{ rpm}$	0.15	0.12	0.09	0.07	0.05	0.07	0.05	0.06
$r_{out} = 1\text{m}, \omega = 6000 \text{ rpm}$	0.20	0.22	0.15	0.07	0.06	0.03	0.03	0.04
$r_{out} = 1\text{m}, \omega = 7000 \text{ rpm}$	0.20	0.22	0.18	0.07	0.05	0.03	0.03	0.03
$r_{out} = 1\text{m}, \omega = 8000 \text{ rpm}$	0.19	0.23	0.16	0.09	0.05	0.03	0.03	0.03
$r_{out} = 1\text{m}, \omega = 9000 \text{ rpm}$	0.21	0.23	0.17	0.07	0.05	0.03	0.03	0.03
$r_{out} = 1\text{m}, \omega = 10000 \text{ rpm}$	0.19	0.23	0.19	0.08	0.05	0.03	0.03	0.03

Table C.4 shows the optimal shape design parameters  $h(r)$  in m, for the shape optimization problem which maximizes the rotor kinetic energy, based on design-2 (Amber Kinetics) specifications, at different combinations of operating speed and rotor radius.

Table C.4: Shape design parameters  $h(r)$  for optimal rotors in the parametric studies based on design-2

Parametric study	$h_1$	$h_2$	$h_3$	$h_4$	$h_5$	$h_6$	$h_7$	$h_8$
$r_{out} = 0.4 \text{ m}, \omega = 4000 \text{ rpm}$	0.03	0.03	0.03	0.03	0.03	0.14	0.53	0.98
$r_{out} = 0.4\text{m}, \omega = 5000 \text{ rpm}$	0.03	0.03	0.03	0.03	0.03	0.08	0.50	1.11
$r_{out} = 0.4\text{m}, \omega = 6000 \text{ rpm}$	0.03	0.03	0.03	0.03	0.03	0.10	0.48	1.10
$r_{out} = 0.4\text{m}, \omega = 7000 \text{ rpm}$	0.03	0.03	0.03	0.03	0.03	0.03	0.44	1.25
$r_{out} = 0.4\text{m}, \omega = 8000 \text{ rpm}$	0.20	0.18	0.17	0.21	0.38	0.22	0.33	0.36
$r_{out} = 0.4\text{m}, \omega = 9000 \text{ rpm}$	0.23	0.23	0.23	0.23	0.29	0.36	0.25	0.36

$r_{out}=0.4\text{m}, \omega=10000\text{ rpm}$	0.28	0.24	0.49	0.27	0.24	0.38	0.23	0.22
$r_{out}=0.5\text{m}, \omega=4000\text{ rpm}$	0.03	0.03	0.03	0.03	0.03	0.03	0.03	1.06
$r_{out}=0.5\text{m}, \omega=5000\text{ rpm}$	0.03	0.03	0.03	0.03	0.03	0.03	0.03	1.09
$r_{out}=0.5\text{m}, \omega=6000\text{ rpm}$	0.07	0.06	0.07	0.05	0.08	0.19	0.38	0.30
$r_{out}=0.5\text{m}, \omega=7000\text{ rpm}$	0.10	0.10	0.10	0.11	0.24	0.10	0.29	0.25
$r_{out}=0.5\text{m}, \omega=8000\text{ rpm}$	0.16	0.18	0.15	0.15	0.17	0.13	0.22	0.27
$r_{out}=0.5\text{m}, \omega=9000\text{ rpm}$	0.20	0.20	0.18	0.34	0.13	0.19	0.13	0.18
$r_{out}=0.5\text{m}, \omega=10000\text{ rpm}$	0.27	0.22	0.37	0.33	0.25	0.13	0.09	0.03
$r_{out}=0.6\text{m}, \omega=4000\text{ rpm}$	0.03	0.03	0.03	0.03	0.03	0.11	0.13	0.46
$r_{out}=0.6\text{m}, \omega=5000\text{ rpm}$	0.07	0.03	0.04	0.03	0.11	0.12	0.28	0.15
$r_{out}=0.6\text{m}, \omega=6000\text{ rpm}$	0.10	0.08	0.19	0.11	0.12	0.13	0.11	0.15
$r_{out}=0.6\text{m}, \omega=7000\text{ rpm}$	0.13	0.14	0.12	0.11	0.09	0.14	0.15	0.14
$r_{out}=0.6\text{m}, \omega=8000\text{ rpm}$	0.16	0.18	0.16	0.17	0.13	0.11	0.11	0.09
$r_{out}=0.6\text{m}, \omega=9000\text{ rpm}$	0.21	0.23	0.22	0.32	0.08	0.11	0.04	0.04
$r_{out}=0.6\text{m}, \omega=10000\text{ rpm}$	0.26	0.23	0.56	0.20	0.06	0.03	0.04	0.03
$r_{out}=0.7\text{m}, \omega=4000\text{ rpm}$	0.03	0.03	0.03	0.03	0.06	0.15	0.13	0.16
$r_{out}=0.7\text{m}, \omega=5000\text{ rpm}$	0.06	0.04	0.08	0.05	0.03	0.15	0.06	0.20
$r_{out}=0.7\text{m}, \omega=6000\text{ rpm}$	0.10	0.10	0.09	0.07	0.06	0.10	0.10	0.14
$r_{out}=0.7\text{m}, \omega=7000\text{ rpm}$	0.13	0.18	0.10	0.14	0.06	0.10	0.04	0.11
$r_{out}=0.7\text{m}, \omega=8000\text{ rpm}$	0.17	0.17	0.22	0.12	0.07	0.07	0.05	0.05
$r_{out}=0.7\text{m}, \omega=9000\text{ rpm}$	0.19	0.17	0.26	0.15	0.05	0.03	0.03	0.03
$r_{out}=0.7\text{m}, \omega=10000\text{ rpm}$	0.24	0.20	0.35	0.09	0.04	0.03	0.03	0.03
$r_{out}=0.8\text{m}, \omega=4000\text{ rpm}$	0.03	0.03	0.05	0.03	0.06	0.12	0.08	0.07
$r_{out}=0.8\text{m}, \omega=5000\text{ rpm}$	0.07	0.07	0.04	0.05	0.03	0.10	0.07	0.13
$r_{out}=0.8\text{m}, \omega=6000\text{ rpm}$	0.11	0.11	0.07	0.07	0.07	0.10	0.05	0.05
$r_{out}=0.8\text{m}, \omega=7000\text{ rpm}$	0.13	0.17	0.12	0.09	0.05	0.07	0.04	0.04
$r_{out}=0.8\text{m}, \omega=8000\text{ rpm}$	0.18	0.18	0.21	0.10	0.04	0.03	0.03	0.03
$r_{out}=0.8\text{m}, \omega=9000\text{ rpm}$	0.15	0.22	0.20	0.07	0.04	0.03	0.03	0.03
$r_{out}=0.8\text{m}, \omega=10000\text{ rpm}$	0.18	0.19	0.22	0.10	0.04	0.03	0.03	0.03
$r_{out}=0.9\text{m}, \omega=4000\text{ rpm}$	0.03	0.04	0.03	0.03	0.03	0.10	0.05	0.10

$r_{out} = 0.9\text{m}, \omega = 5000 \text{ rpm}$	0.07	0.05	0.09	0.04	0.03	0.07	0.06	0.05
$r_{out} = 0.9\text{m}, \omega = 6000 \text{ rpm}$	0.12	0.11	0.06	0.07	0.04	0.03	0.05	0.05
$r_{out} = 0.9\text{m}, \omega = 7000 \text{ rpm}$	0.16	0.18	0.10	0.07	0.04	0.03	0.03	0.03
$r_{out} = 0.9\text{m}, \omega = 8000 \text{ rpm}$	0.15	0.18	0.12	0.06	0.04	0.03	0.03	0.03
$r_{out} = 0.9\text{m}, \omega = 9000 \text{ rpm}$	0.14	0.18	0.11	0.07	0.04	0.03	0.03	0.03
$r_{out} = 0.9\text{m}, \omega = 10000 \text{ rpm}$	0.18	0.17	0.07	0.07	0.03	0.03	0.03	0.03
$r_{out} = 1\text{m}, \omega = 4000 \text{ rpm}$	0.03	0.03	0.03	0.03	0.03	0.07	0.05	0.07
$r_{out} = 1\text{m}, \omega = 5000 \text{ rpm}$	0.08	0.06	0.05	0.04	0.03	0.03	0.05	0.06
$r_{out} = 1\text{m}, \omega = 6000 \text{ rpm}$	0.12	0.11	0.07	0.05	0.04	0.03	0.03	0.04
$r_{out} = 1\text{m}, \omega = 7000 \text{ rpm}$	0.14	0.20	0.09	0.05	0.04	0.03	0.03	0.03
$r_{out} = 1\text{m}, \omega = 8000 \text{ rpm}$	0.20	0.21	0.18	0.07	0.05	0.03	0.03	0.03
$r_{out} = 1\text{m}, \omega = 9000 \text{ rpm}$	0.15	0.23	0.10	0.06	0.05	0.03	0.03	0.03
$r_{out} = 1\text{m}, \omega = 10000 \text{ rpm}$	0.16	0.19	0.09	0.07	0.04	0.03	0.03	0.03

# Appendix D: Topology optimization

## D.1 Weak form of linear elastic flywheel numerical model

The balance of linear momentum is the governing equation that is used to predict the stress-state of a solid object subject to various loads and boundary conditions. This equation can be stated as

$$\nabla \cdot \underline{\sigma} + \underbrace{\rho \mathbf{b}}_f = \rho \mathbf{a} \stackrel{0}{\implies} \nabla \cdot \underline{\sigma} + \mathbf{f} = 0, \quad (\text{D.1})$$

where  $\underline{\sigma}$  is the second-order stress tensor,  $\rho$  is the density of the material,  $\mathbf{b}$  is the vector of body forces, and  $\mathbf{a}$  is the vector of acceleration loads on the body. A quasi-static state is assumed here, thus the acceleration term is neglected in this analysis. Hooke's law is used to capture the stress-strain relationship, and can be expressed as

$$\underline{\sigma} = \underline{\underline{C}} : \underline{\varepsilon}, \quad (\text{D.2})$$

where  $\underline{\underline{C}}$  is the fourth-order elasticity tensor and  $\underline{\varepsilon}$  is the second-order strain tensor. A constitutive law may be used to determine the components of the elasticity tensor. For isotropic materials, the elasticity tensor is given by

$$\underline{\underline{C}} = \lambda \underline{I} \otimes \underline{I} + 2\mu \underline{I} \quad (\text{D.3})$$

where  $\lambda$  and  $\mu$  are Lamé's first and second parameter respectively, and can be obtained from the material properties using the following relations,

$$\begin{aligned}\lambda &= \frac{E\nu}{(1+\nu)(1-2\nu)} \quad \text{Lamé's first parameter ,} \\ \mu &= \frac{E}{2(1-\nu)} \quad \text{Lamé's second parameter .}\end{aligned}\tag{D.4}$$

where  $E$ ,  $\nu$  are the Young's modulus and Poisson's ratio respectively. The strain-displacement relation, assuming small deformations, can be expressed as:

$$\underline{\varepsilon} = \frac{1}{2} \left( \nabla \mathbf{u} + (\nabla \mathbf{u})^T \right)\tag{D.5}$$

where  $\mathbf{u}$  is the vector of displacements. The above equations form the basis for the linear elastic numerical models. The weak form of the governing equations described above is derived as follows. Let  $\bar{\mathbf{v}}$  be a vector-valued test function belonging to the Sobolev functional space  $H^1$ . Multiplying Equation (D.1) by  $\bar{\mathbf{v}}$  and integrating over the domain,  $\Omega$ ,

$$\int_{\Omega} \bar{\mathbf{v}} \cdot (\nabla \cdot \underline{\sigma} + \mathbf{f}) \, d\Omega = 0\tag{D.6}$$

The above equation can be simplified using Green's formula, i.e.,

$$\int_{\Omega} \bar{\mathbf{v}} \cdot (\nabla \cdot \underline{\sigma}) \, d\Omega = - \int_{\Omega} (\nabla \bar{\mathbf{v}}) : \underline{\sigma} \, d\Omega + \int_{\Gamma} \bar{\mathbf{v}} \cdot (\underline{\sigma} \mathbf{n}) \, d\Gamma\tag{D.7}$$

Thus, Equation (D.6) becomes:

$$\int_{\Omega} (\nabla \bar{\mathbf{v}}) : \underline{\sigma} \, d\Omega = \int_{\Omega} \bar{\mathbf{v}} \cdot \mathbf{f} \, d\Omega + \int_{\Gamma} \bar{\mathbf{v}} \cdot (\underline{\sigma} \mathbf{n}) \, d\Gamma\tag{D.8}$$

Interpreting the test function  $\bar{\mathbf{v}}$  as a virtual displacement vector, the following virtual strain form of the test function can be defined:

$$\bar{\underline{\varepsilon}} = \frac{1}{2} \left( \nabla \bar{\mathbf{v}} + \nabla \bar{\mathbf{v}}^T \right)\tag{D.9}$$

Then, the weak form of the 2D / 3D linear elastic model is developed using Equation (D.8) and can be written as:

$$\int_{\Omega} \bar{\underline{\varepsilon}} : \underline{\sigma} \, d\Omega = \int_{\Omega} \bar{\mathbf{v}} \cdot \mathbf{f} \, d\Omega + \int_{\Gamma} \bar{\mathbf{v}} \cdot \underline{\sigma} \mathbf{n} \, d\Gamma\tag{D.10}$$

The domain  $\Omega$  is discretized using a mesh with Lagrange quadrilateral (2D model) or hexahedral (3D model) elements. For each mesh element located at  $\Omega_e$ , the displacement vector  $\mathbf{u}$  is approximated as:

$$\begin{bmatrix} u_x \\ u_y \\ u_z \end{bmatrix} = \underbrace{\begin{bmatrix} \phi_1 & \dots & \phi_n & 0 & \dots & 0 & 0 & \dots & 0 \\ 0 & \dots & 0 & \phi_1 & \dots & \phi_n & 0 & \dots & 0 \\ 0 & \dots & 0 & 0 & \dots & 0 & \phi_1 & \dots & \phi_n \end{bmatrix}}_{\underline{N}} \begin{bmatrix} u_{x1} \\ \dots \\ u_{xn} \\ u_{y1} \\ \dots \\ u_{yn} \\ u_{z1} \\ \dots \\ u_{zn} \end{bmatrix} \quad (\text{D.11})$$

where  $u_x$ ,  $u_y$ ,  $u_z$  are the components of the solution vector  $\mathbf{u}$ ,  $n$  is the number of degrees of freedom (DoFs) per solution component approximation which is determined by the degree of polynomial approximation function used and  $\underline{N}$  is the matrix of shape function coefficients. Using the above definitions, the vector-valued test function  $\mathbf{v}$  and solution  $\mathbf{u}$  can be approximated as:

$$\mathbf{v} = N_{kp} v_p \mathbf{e}_k = \phi_k^{(i)} v_i \mathbf{e}_k \quad (\text{D.12})$$

$$\mathbf{u} = N_{lq} u_q \mathbf{e}_l = \phi_l^{(j)} u_j \mathbf{e}_l \quad (\text{D.13})$$

where  $i, j$  are the indices over the number of DoFs per dimension ( $n$ ),  $p, q$  are the indices over the total number of DoFs, and  $k, l$  are indices over the number of dimensions.

Substituting the expressions above on the weak form of the governing equation, the element-wise stiffness matrix,  $\mathbf{K}_e$ , forcing vector,  $\mathbf{f}_e$ , and boundary term,  $\mathbf{f}_b$ , can be obtained as follows,

$$\mathbf{K}_{ij}^e = \int_{\Omega_e} \left( \phi_{k,k}^i \lambda \phi_{l,l}^j + \phi_{k,l}^i \mu \phi_{k,l}^j + \phi_{k,l}^i \mu \phi_{l,k}^j \right) d\Omega_e \quad (\text{D.14})$$

where  $i, j$  are the indices over the number of DoFs per dimension,  $k, l$  are indices over the number of dimensions.

$$\mathbf{f}_i^e = \int_{\Omega_e} \left( \phi_m^i f_m \right) d\Omega_e \quad (\text{D.15})$$

where  $i$  is an index over the number of DoFs per dimension,  $m$  is an index over the number of dimensions.

$$\mathbf{f}_i^b = \int_{\Gamma_e} \left( \phi_m^i \sigma_{mr} n_r \right) \Gamma_e \quad (\text{D.16})$$

where  $i$  is an index over the number of DoFs per dimension and  $m, r$  are indices over the number of dimensions.

Here, the inertial load due to the rotation of the flywheel is imposed as a body force  $f_m = \rho\omega^2 r_m$  over the entire domain, and the outer surfaces of the flywheel are assumed to be stress free.

The linear elasticity numerical model is implemented in the Cartesian coordinate system to make the implementation generic i.e the same model can be used for 2D / 3D simulations.

The stresses and strains in the solid domain are obtained *a posteriori* from the displacement solutions of the numerical model, by using the relations outlined in Equations (D.2), (D.5).

## D.2 Adjoint sensitivity analysis

The adjoint form can be used to analytically determine the gradient of topology optimization responses with a reduced computational cost. The expression for the adjoint sensitivity is derived below.

The sensitivity of an optimization response,  $\phi(\hat{\boldsymbol{\rho}}, \mathbf{u})$  w.r.t design variable  $\hat{\rho}_e$  (using the chain rule) is:

$$\frac{d\phi(\hat{\boldsymbol{\rho}}, \mathbf{u})}{d\hat{\rho}_e} = \frac{\partial\phi}{\partial\hat{\rho}_e} + \frac{\partial\phi}{\partial\mathbf{u}} \frac{\partial\mathbf{u}}{\partial\hat{\rho}_e} \quad (\text{D.17})$$

The adjoint form of this equation can be used to avoid having to perform a large

number of matrix inversions. In this approach, the original response  $\phi$  can be rewritten as:

$$\phi(\hat{\boldsymbol{\rho}}, \mathbf{u}) = \phi(\hat{\boldsymbol{\rho}}, \mathbf{u}) + \lambda^T (K\mathbf{u} - F) \quad (\text{D.18})$$

where  $\lambda^T$  is an adjoint vector, and  $R = K\mathbf{u} - F = 0$  is the residual of the FEM solution. Using this new definition of the response, the gradient from Equation (D.17) can be rewritten as:

$$\frac{d\phi(\hat{\boldsymbol{\rho}}, \mathbf{u})}{d\hat{\rho}_e} = \frac{\partial\phi}{\partial\hat{\rho}_e} + \frac{\partial\phi}{\partial\mathbf{u}} \frac{\partial\mathbf{u}}{\partial\hat{\rho}_e} + \lambda^T \left( K \frac{\partial\mathbf{u}}{\partial\hat{\rho}_e} + \frac{\partial K}{\partial\hat{\rho}_e} \mathbf{u} - \frac{\partial F}{\partial\hat{\rho}_e} \right) \quad (\text{D.19})$$

Rearranging the terms,

$$\frac{d\phi}{d\hat{\rho}_e} = \frac{\partial\phi}{\partial\hat{\rho}_e} + \left( \frac{\partial\phi}{\partial\mathbf{u}} + \lambda^T K \right) \frac{\partial\mathbf{u}}{\partial\hat{\rho}_e} + \lambda^T \left( \frac{\partial K}{\partial\hat{\rho}_e} \mathbf{u} - \frac{\partial F}{\partial\hat{\rho}_e} \right) \quad (\text{D.20})$$

In the above equation, the adjoint vector  $\lambda$  can be chosen so that the second term becomes zero, i.e.,

$$\left( \frac{\partial\phi}{\partial\mathbf{u}} + \lambda^T K \right) \frac{\partial\mathbf{u}}{\partial\hat{\rho}_e} = 0 \quad (\text{D.21})$$

This results in the following definition of the adjoint sensitivity:

$$\frac{d\phi}{d\hat{\rho}_e} = \frac{\partial\phi}{\partial\hat{\rho}_e} + \lambda^T \left( \frac{\partial K}{\partial\hat{\rho}_e} \mathbf{u} - \frac{\partial F}{\partial\hat{\rho}_e} \right) \quad (\text{D.22})$$

where the adjoint vector  $\lambda$  is defined as:

$$\lambda = -(K^T)^{-1} \frac{\partial\phi}{\partial\mathbf{u}} \quad (\text{D.23})$$

### D.3 Finite difference tests for topology optimization responses

The analytical sensitivities of topology optimization responses were validated using finite difference tests. The sensitivity of the responses  $\phi(\rho)$  w.r.t one of the design variables was computed using finite differences, as shown in Eqn. (D.24).

$$\widetilde{\frac{\partial\phi(\rho)}{\partial\rho_i}} \approx \frac{\phi(\rho + e_i h) - \phi(\rho)}{h} \quad (\text{D.24})$$

The error or the relative difference between the above computed numerical gradient and the sensitivity obtained from the analytical expression, was calculated as follows:

$$\text{err}_\phi = \frac{\left| \frac{\partial \phi(\rho)}{\partial \rho_i} \right| - \widetilde{\left| \frac{\partial \phi(\rho)}{\partial \rho_i} \right|}}{\left| \frac{\partial \phi(\rho)}{\partial \rho_i} \right|} \quad (\text{D.25})$$

The density of a randomly chosen mesh element was varied using different step sizes,  $h$ , and the effect on the optimization response,  $\phi$ , was observed. Figure D.1 plots the errors in the analytical sensitivities of the kinetic energy and P-norm stress calculated using Eqn. (D.25), vs the finite difference step size,  $h$ , on a log scale. As the step size was reduced from  $10^{-1}$  to  $10^{-5}$ , the finite difference error approached zero at the same rate. The small increase in the finite difference error in the stress response in Figure D.1(b) for very small step sizes  $\leq 10^{-5}$  could be because the calculated numerical gradients of the stress were approaching machine precision at these step sizes. Thus, overall, the computed analytical sensitivities were sufficiently accurate and could be used in the optimization studies.

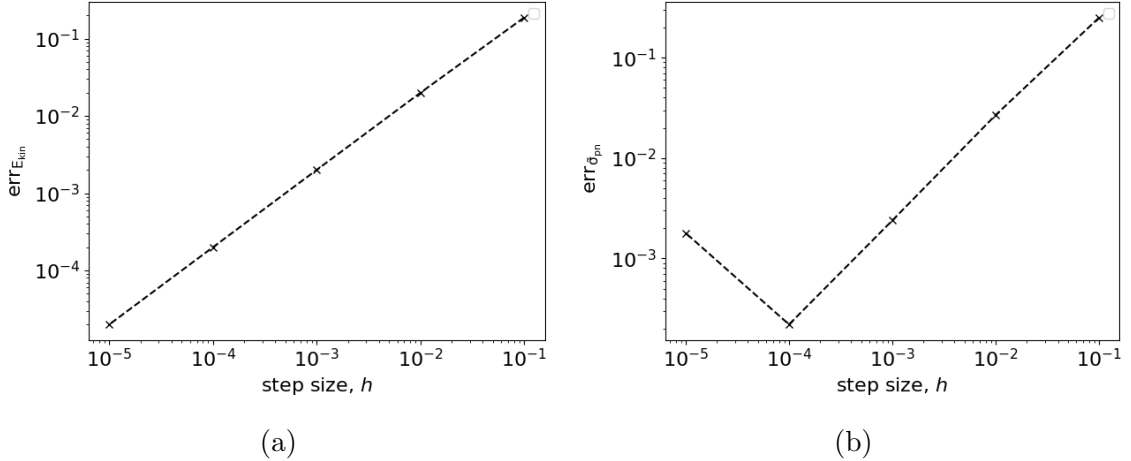


Figure D.1: Finite difference tests to validate the analytical sensitivity of a) kinetic energy and b) P-norm aggregated stress response

## D.4 Benchmarking of 2D rotor topology reported by Jiang and Wu [68]

The optimization problem solved in the benchmarking study is described below in Equation D.26.

$$\begin{aligned}
 \min \tilde{\sigma}_{pn} &= c \left( \sum_{e=1}^N v_e (\hat{\rho}_e^q \sigma_{vm}^e)^P \right)^{\frac{1}{P}} \\
 \text{w.r.t } \hat{\boldsymbol{\rho}} &= \{\hat{\rho}_1, \hat{\rho}_2, \dots, \hat{\rho}_N\} \\
 \text{s.t. } KU &= F \\
 f(\hat{\boldsymbol{\rho}}) &: \frac{V(\hat{\boldsymbol{\rho}})/V_0}{\alpha} - 1 \leq 0 \\
 g(\hat{\boldsymbol{\rho}}) &: \frac{E_{kin}(\hat{\boldsymbol{\rho}})}{E_{kin}^0} - 1 \leq 0 \\
 0.0 &\leq \hat{\rho}_e \leq 1.0
 \end{aligned} \tag{D.26}$$

where  $\tilde{\sigma}_{pn}$  is the normalized P-norm aggregated von Mises stress in the rotor,  $f(\hat{\boldsymbol{\rho}})$  is the volume fraction constraint and  $g(\hat{\boldsymbol{\rho}}, \mathbf{u})$  is the kinetic energy constraint. The literature study maximized the kinetic energy subject to constraints on the volume fraction and maximum stress. However, since there was a slight difference in the predicted maximum stress in the simulated uniform thickness rotor, the problem was solved as a stress minimization formulation instead.  $E_{kin}^0$  is the kinetic energy of the optimal rotor reported in the benchmark study.

Table D.1 contains the model and optimization related parameters used to benchmark the 2D rotor topology reported by Jiang and Wu [68].

Figure D.2 contains the 2D mesh, optimal topology and stress distribution obtained from the simulation of the benchmark problem from Equation D.26.

Figure D.3 contains the simulation convergence histories of the optimization objective, constraints, convergence criterion and the % of gray elements in the mesh for the benchmark problem from Equation D.26.

Table D.1: Topology optimization parameters for kinetic energy maximization of 2D rotor design reported in reference [68]

Parameter set	Parameter	Literature [68]	Simulation
Material Properties	Young's modulus $E$ , GPa	210	210
	Poisson's ratio $\nu$	0.3	0.3
	Solid density $\rho$ , kg/m <sup>3</sup>	7850	7850
Flywheel model	Numerical model	2D Plane stress	2D Plane stress
	Rotor height, m	0.001	0.001
	Shaft boundary condition	Dirichlet (zero displacement)	Neumann (press-fit)
	Angular velocity $\omega$ , rpm	2250	2250
	Inner radius $r_{shaft}$ , m	0.15	0.15
	Outer radius $r_{out}$ , m	0.80	0.80
	Fixed rims thickness $t_{rim}$ , m	0.05	0.05
SIMP parameters	penalty $p$	3	3
	$\rho_0$	<i>not reported</i>	0.55
	$E_{min}$	<i>not reported</i>	1
MMA parameters	$a$		0.0
	$c$	<i>not reported</i>	1000.0
	$d$		0.0
	move limit		0.03
Density filter	filter radius $r_{fit}$ , m	0.06	0.09
	distribution	<i>not reported</i>	linear decay / conical
Projection filter	threshold $h$		1D line search
	initial slope $\beta_0$		1
	maximum slope $\beta_{max}$	<i>not reported</i>	100
	update interval		25
Mesh parameters	N (cyclic symmetry)	6	6
	elements	19716	11731
Volume fraction constraint	Maximum volume fraction $\alpha$ , %	70	70
Stress constraint aggregation	$\sigma_{max}$ , MPa	200	minimized
	P-norm $P$	<i>not reported</i>	8.0
	Stress relaxation $q$	<i>not reported</i>	0.5

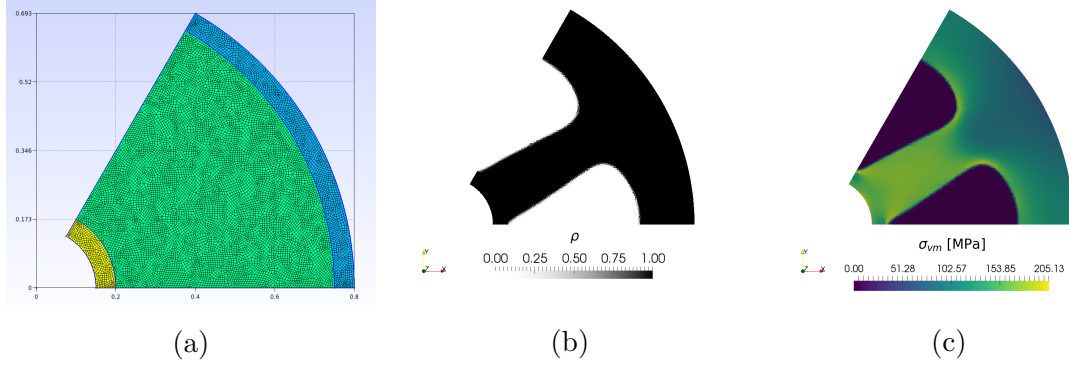


Figure D.2: a) 2D mesh, b) optimal topology and c) optimal stress distribution for the benchmarking problem described in Equation D.26

Table D.2: Comparison of optimal topologies for various rotor radius ratios

$r_i$ , mm	$E_{kin}$ , J	$m$ , kg	$e_{kin}$ , J/kg	$\sigma_{pn}$ , MPa	$\frac{V}{V_0}$
25	100239.9	33.58	2984.98	64.34	0.698
30	105851.4	33.48	3161.63	64.22	0.699
35	103418.7	33.06	3128.12	64.17	0.699

## D.5 Effect of bore size on optimal topology

The effect of varying the bore size on the optimal topology was studied by fixing the outer radius and varying the inner radius between 25 and 35 mm. Figure D.4 compares the optimal designs based on the kinetic energy formulation and corresponding rotor stress distributions obtained with various radius ratios. Only minor differences in the optimal topologies or stress distributions are obtained while using different inner radii. Table D.2 compares the energy capacity and other optimization responses for the designs. The mass of the rotors is slightly different because of the difference in the volume of the initial rotors. The specific energy of the rotors reduces as the inner radius  $r_i$  is decreased, because the difference in rotor mass is primarily added in the region closest to the shaft, which does not contribute significantly to the moment of inertia.

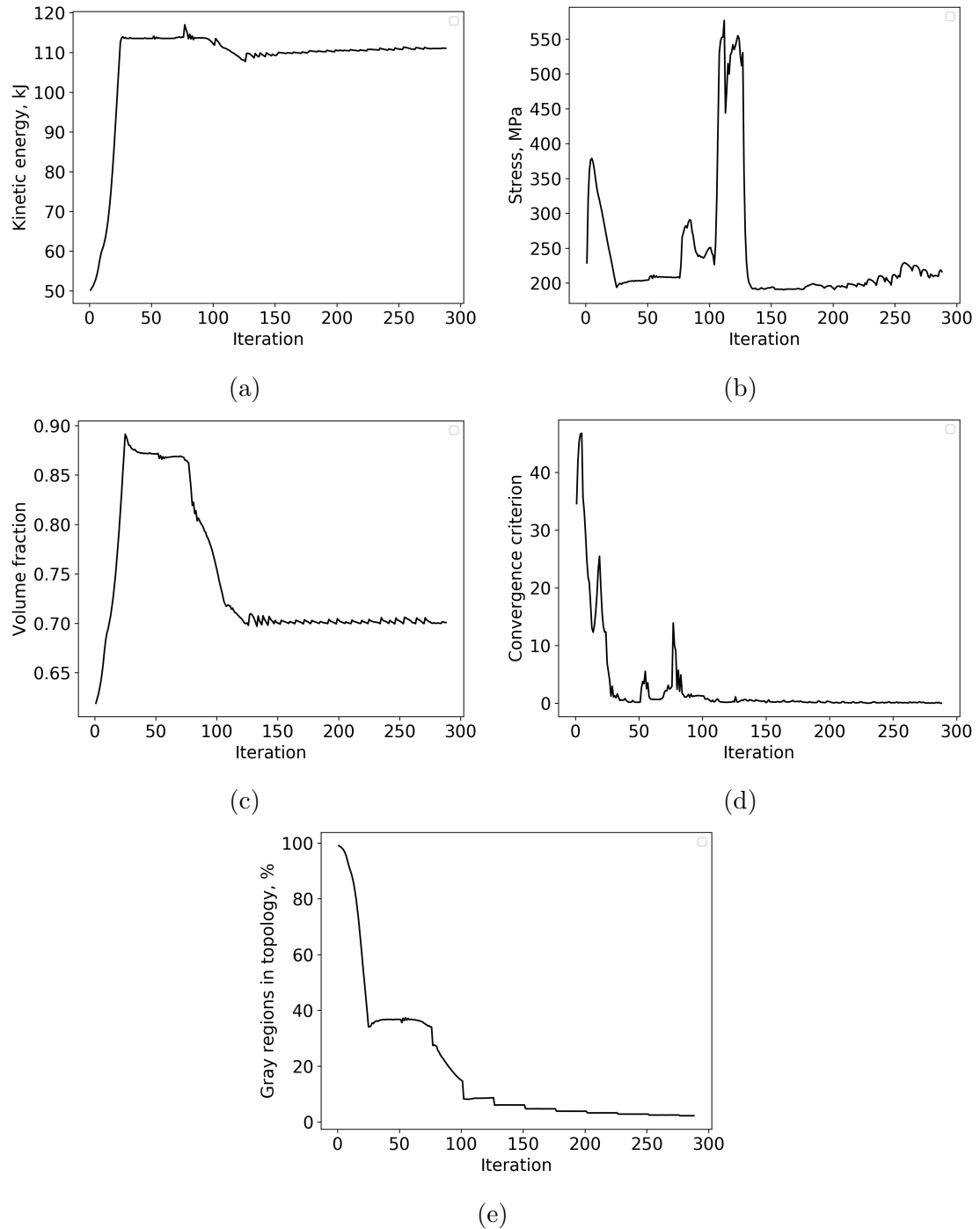


Figure D.3: Convergence histories of a) kinetic energy, b) P-norm stress, c) volume fraction, d) convergence criterion and e) % gray region in the topology for the benchmarking problem described in Equation D.26

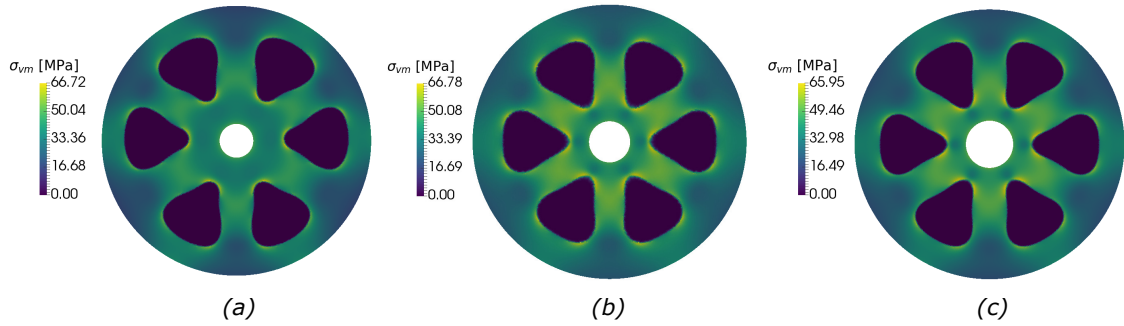


Figure D.4: Stress distributions in the optimal rotor topology obtained using different radius ratios, with inner radius of a) 25 mm, b) 30 mm, and c) 35 mm

## D.6 Post-optimality analysis on body fitted meshes

The specific energy maximized optimal designs presented in Figure 4.14 f), i), and j) were seen to have visible remnant gray regions. These topologies were post-processed to extract body fitted geometries with smooth boundaries. Two different design density thresholds of 50% and 90% were used to generate the body fitted meshes. The stress distributions in the post-processed designs are presented in Figure D.5.

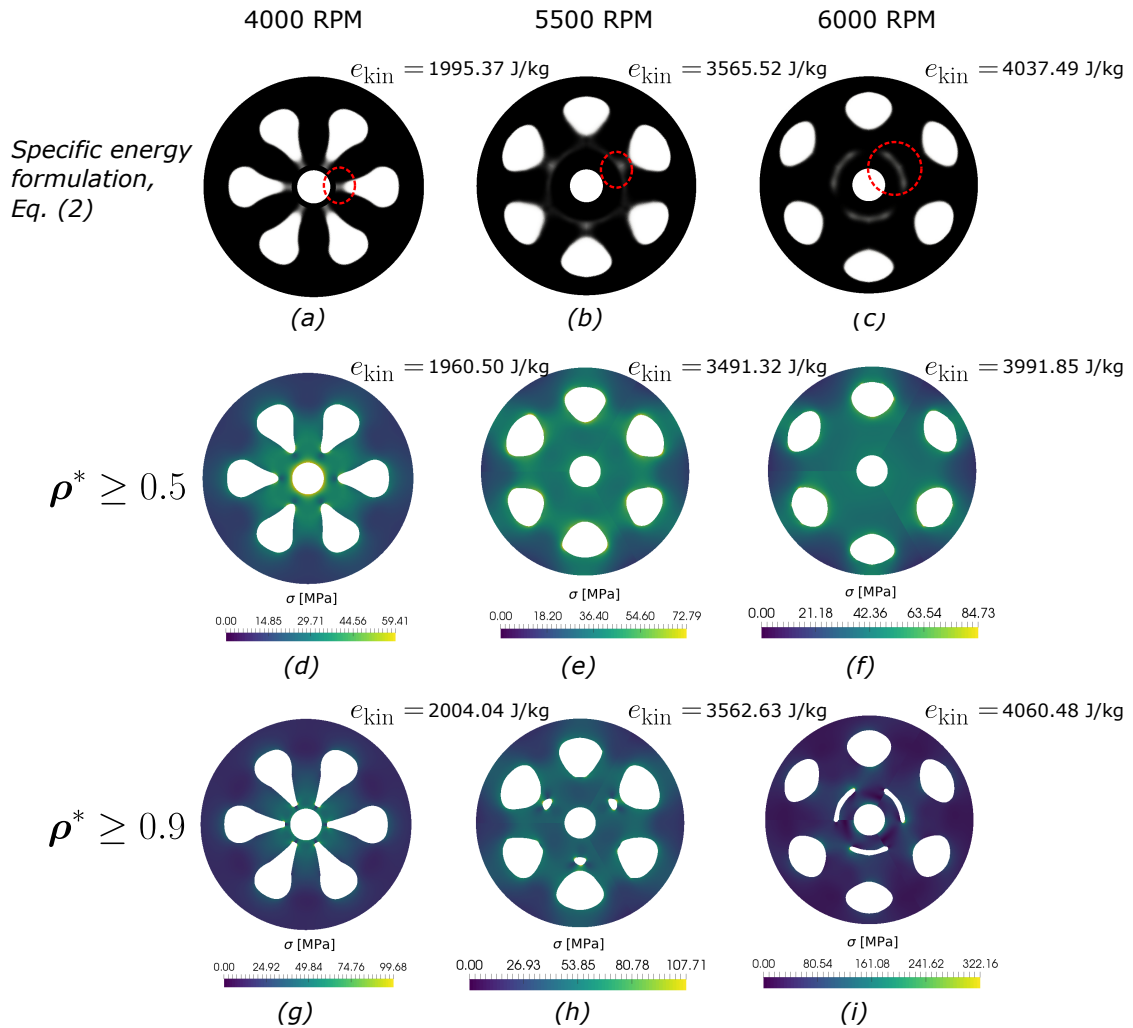


Figure D.5: Effect of using a body fitted mesh to analyze design with remnant gray regions: a-c) optimal topologies with visible gray regions, d-f) stress distribution in post-processed meshes with density threshold of 50%, and g-i) stress distribution in post-processed meshes with density threshold of 90%.